Abstract

Title of Dissertation:	HYPERSONIC TURBULENT BOUNDARY LAYERS WITH INTERACTIONS
	Vishal A. Bhagwandin Doctor of Philosophy, 2025
Dissertation directed by:	Professor M. Pino Martín Department of Aerospace Engineering

The Mach 10 Hollow-Cylinder Flare (HCF) and the Mach 6 BoLT-II hypersonic configurations were simulated and studied. Wall-Resolved Large Eddy Simulations (WRLES) with a high-bandwidth resolving WENO method and explicit third order Runge-Kutta time advancement was used to obtain detailed solutions of the flowfields, to include mean data, first and second order turbulent statistics and spectral content. The two configurations each presented a different set of flow physics which were interrogated using a variety of processing techniques.

Investigation of the low frequency dynamics in the corner shock-separation of the HCF revealed pairs of Görtler-type centrifugal instabilities across the span generated by the concavity of the separation streamline. This study provided strong qualitative and statistical evidence that the low frequency pulsations of the separation bubble and shockwave are driven by the Görtler-type centrifugal instabilities, which are in turn generated by streamline distortion caused by the separation bubble, thus creating a low-frequency feedback loop. That is, the unsteady shock-

separation dynamics, which are also responsible for the large pressure and heat flux fluctuations, are driven by instabilities intrinsic to the corner interaction itself.

This study provided new and important insight into the behavior of the turbulent velocity and thermodynamic correlations in the separation zone and post-shock nonequilibrium flow of the HCF. The nonequilibrium flowfield exhibits significant compression and mean strain with strong amplification of the Reynolds stresses, turbulent kinetic energy and their transport budgets, viz, production, viscous diffusion, turbulent diffusion, pressure diffusion, viscous dissipation, pressure strain and turbulent mass flux. The amplifications far exceeded that of supersonic and lower speed shock-boundary layer interaction flows, and often departed from canonical trends. Classical single-point closures used in lower-order RANS modeling of the Reynolds stress transport budgets, the turbulent kinetic energy transport budgets and turbulent heat flux were also evaluated a priori by comparing to the WRLES solution. While the models performed very well in the upstream equilibrium boundary layer, many performed poorly in the downstream post-shock nonequilibrium region, with few exceptions. The results herein have important implications in wall-bounded turbulence modeling which has typically been based on canonical non-hypersonic equilibrium flows, and to a lesser extent simple nonequilibrium flows.

A single flight condition during the descent phase of the BoLT-II hypersonic research vehicle was simulated using WRLES. For the unperturbed adiabatic wall case, flowfield solutions of the turbulent environment over the vehicle show multiple and distinct large-scale vortical instabilities on top of what is typically seen in broad-frequency turbulence. The downstream boundary layer was marked by high vorticity, temperature and skin friction. Wall normal extractions in key regions of the downstream boundary layer revealed broad-frequency turbulence as well as low frequency content in the energy spectra. An examination of the boundary layer velocity profile

showed a significant departure of the transformed velocity from classical turbulence similarity scaling. For the isothermal wall case, the inlet was perturbed according to acoustic wave theory to simulate turbulence in the freestream environment. The simulations predicted precipitous rises in the downstream wall shear stress and wall heat flux mainly in the central and outboard regions, indicative of transition-to-turbulence with a two-dimensional transition front. Except for some locations across the span, the predictions of wall shear stress and wall heat flux were generally lower than that reported from the inflight sensors. However, it was noted that the particular flight condition simulated in this study fell within a very unstable flight regime where the flow flip-flops multiple times between laminar and turbulent states producing inordinately large fluctuations in the wall heat flux as indicated by flight sensor data.

HYPERSONIC TURBULENT BOUNDARY LAYERS WITH INTERACTIONS

by

Vishal A. Bhagwandin

Dissertation submitted to the Faculty of the Graduate School of the
University of Maryland, College Park, in partial fulfillment
of the requirements for the degree of
Doctor of Philosophy
2025

Advisory Committee:
Professor M. Pino Martín, Chair/Advisor
Professor James Baeder
Professor Kenneth Yu
Professor Christopher Cadou
Professor Tobias von Petersdorff, Dean's Representative

© Copyright by
Vishal A. Bhagwandin
2025

Acknowledgments

Successful completion of this dissertation is due to the support of many too innumerable to list and to whom I am profoundly grateful. Foremost, my sincerest gratitude to my PhD advisor Dr. Pino Martín, without whose expertise, guidance and support none of this would be possible. Many thanks to my dissertation committee for their time and effort in evaluating this thesis and providing crucial feedback. A big thank you to the DoD SMART Scholarship program and the U.S. DEVCOM Army Research Laboratory (ARL) for partial sponsorship of my doctoral degree, and in particular my ARL colleagues Luke Strohm, Paul Weinacht and James DeSpirito for their unwavering support. I would also like to thank the Air Force Office of Scientific Research for partial funding of this research, and the DoD High Performance Computing Modernization Program and the UMD CRoCCo Laboratory for computational resources. Many thanks to my former labmates, Clara Helm and Nathan Grube, for their technical assistance on many occasions. Finally, a special thank you to my mom, dad, sisters and those close to me, shoutout to Elizabeth, for their moral support and encouragement over the years that led to this moment.

Table Of Contents

Acknowledgments ii

Table Of Contents iii

List Of Tables vi

List Of Figures vii

Chapter 1: Introduction 1

1.1 Motivation 1

1.2 Background 3

1.3 Scope 8

Chapter 2: Computational Methodology 11

2.1 LES Governing Equations 11

2.2 Flux Discretization 15

2.3 Time Integration 18

Chapter 3: HCF Computational Setup 19

3.1 Grid Generation 19

3.2 Freestream and Boundary Conditions 21

3.3 Turbulent Inflow Generation via Recycling-Rescaling Method 22

3.4 Inflow Turbulent Boundary Layer Assessment 25

3.4.1 Comparison Datasets 25

3.4.2 Mean Fields 26

3.4.3 Turbulence Fields 28

Chapter 4: HCF Mean Flow Analysis 33

4.1 Qualitative Flowfield Description 33

4.2 Mean Flowfield 35

4.3 Mean Wall Profiles: Skin Friction, Pressure and Heat Flux 39

4.4 Chapter Summary 44

Chapter 5: HCF Low Frequency Dynamics and the Centrifugal Instability 45

5.1 Introduction 45

5.2 Flowfield Processing 48

5.3 Low-Frequency Dynamics 49

5.3.1 Power Spectra and Lowpass Filtering 49

5.3.2 Lowpass Filtered 3D Flowfields 52
5.3.3 Görtler-type Centrifugal Instabilities 58
5.4 Vortex Dynamics 63
5.4.1 Vortex ID Methods: $\Gamma_{1,2}$ Criterion 63
5.4.2 Vortex ID Methods: λ_{ci} Criterion 65
5.4.3 $\Gamma_{1,2}$ + λ_{ci} Criteria Assessment 66
5.4.4 Vortex Center Detection and Strength 67
5.4.5 3D Vortex Visualization 68
5.5 Vortex Signals and Correlations with Separation Event 70
5.5.1 Tracking Mean Vortex Properties over Time 70
5.5.2 Time Correlation of Vortex Strength and Separation Point Motion 72
5.5.3 Time Correlation of Vortex Convection Velocity and Separation Point Motion 74
5.5.4 Estimate of Vortex Pitch 76
5.6 Chapter Summary 76
Chapter 6: HCF Turbulence Nonequilibrium 80
6.1 Introduction 80
6.2 The Reynolds Stress Transport and Turbulent Kinetic Energy Transport Equations 85
6.2.1 The Reynolds Stress Transport Equation 85
6.2.2 The Turbulent Kinetic Energy Transport Equation 87
6.3 Flowfield Processing 88
6.4 Reynolds Stresses and Turbulent Kinetic Energy 89
6.5 Reynolds Stress Anisotropy 94
6.6 Turbulent Kinetic Energy Transport Budgets 99
6.7 Reynolds Stress Transport Budgets 104
6.8 Viscous Dissipation 115
6.8.1 Dissipation Components 116
6.8.2 Dilatational Dissipation 120
6.8.3 Dissipation Tensor 124
6.9 Pressure Strain and Pressure Dilatation 131
6.9.1 Pressure Dilatation 131
6.9.2 Pressure Strain Tensor 137
6.10 Thermodynamic Fluctuations and Correlations 149
6.10.1 Density, Pressure and Temperature Fluctuations 149
6.10.2 The Strong Reynolds Analogies 152
6.10.3 Turbulent Heat Flux 160

6.11 Chapter Summary 167
Chapter 7: BoLT-II Hypersonic Vehicle 173
7.1 Introduction 173
7.2 Geometry and Flight Conditions 174
7.3 Methodology 176
7.3.1 Computational Domain and Grid Generation 176
7.3.2 Numerical Method 178
7.3.3 Initial Conditions 178
7.3.4 Boundary Conditions 179
7.4 Adiabatic Wall Case 181
7.4.1 General Flowfield 181
7.4.2 Boundary Layer Profiles: Mean Profiles 185
7.4.3 Boundary Layer Profiles: Signals and Spectra 188
7.5 Isothermal Wall Case 193
7.6 Chapter Conclusion 198
Chapter 8: Conclusion: Significance of Work 200
Appendix A 203
Appendix B 205
Bibliography 207

List Of Tables

Table 3.1. Cylinder-Flare Grid Specifications. 21
Table 3.2. Mach 10 Cylinder-Flare Freestream Conditions. 22
Table 3.3. Mach 10 Cylinder-Flare Turbulent Boundary Layer Inflow Reference. 22
Table 3.4. Mach 10 Turbulent Boundary Layer Comparison Datasets. 25
Table 3.5. Turbulence Stresses in Two Regions and comparisons with Archival DNS 31
Table 4.1. Mach 10 STBLI Comparison Datasets. 40
Table 5.1. Location Data for Selected Cross-Stream Planes. 49
Table 6.1. Downstream Amplification of Reynolds Stresses 93
Table 7.1. Simulated Flight Conditions. 175
Table 7.2. Downstream Boundary Layer (BL) Properties (Adiabatic Wall) 177
Table 7.3. Bolt-II Sensor Types and Locations. 195

List Of Figures

Figure 1.1. Mach 10 NASA X-43A Experimental Scramjet [1] (left) and Mach 5 Boeing X-51A Experimental Waverider [2] (right). 1

Figure 1.2. Illustration of flow interactions on a hypersonic vehicle (reproduced from Leishman 2022 [3]). 2

Figure 1.3. General SBLI Features, Mach 3 24° compression corner (reproduced from Wu et al. 2015 [4]). 7

Figure 1.4. Mach 10 HCF (left) with contours of streamwise velocity and density gradient, and Mach 6 BoLT-II (right) with surface contours of pressure fluctuation. Images are a preview of the LES solutions in this study. 8

Figure 2.1. Symmetric candidate stencil arrangement for computing SYMBO-WENO flux $\hat{f}^{+}_{i+1/2}$ at cell face $i + 1/2$ when $r = 3$. Figure reproduced from [45]. 16

Figure 3.1. Cylinder-Flare grid, coarsened for viewing. 20

Figure 3.2. Auxiliary cylinder inflow run and cylinder-flare SBLI run. 23

Figure 3.3. Auxiliary cylinder inflow run, mean contours of pressure (Pa). 24

Figure 3.4. Van Driest-transformed mean streamwise velocity. 27

Figure 3.5. Mean streamwise velocity, scaled by freestream value. 27

Figure 3.6. Mean temperature, scaled by freestream value. 28

Figure 3.7. Mean density, scaled by freestream value. 28

Figure 3.8. Turbulent streamwise velocity, scaled by u_τ. 30

Figure 3.9. Turbulent stresses and TKE, Morkovin scaled. 30

Figure 3.10. Turbulent stresses, scaled by TKE. 30

Figure 3.11. Turbulent temperature, density and pressure, scaled by freestream values. 32

Figure 4.1. Isosurface of modified density gradient, $\nabla\rho_{mod}$, colored by u-velocity. 34

Figure 4.2. Streamwise u-velocity just above wall with planes density gradient $\nabla\rho_{mod}$. 34

Figure 4.3. Instantaneous density gradient on streamwise plane and SBLI general features. 35

Figure 4.4. Favre-averaged flowfields, normalized by freestream values except for $\widetilde{M}$. 37

Figure 4.5. Favre-averaged wall-normal profiles, upstream (top row) and downstream (bottom row) of corner ($x/\delta_0 = 0$), normalized by freestream values. 37

Figure 4.6. Locations of wall normal data extractions plotted in Figure 4.5. Contours are mean density gradient. 38

Figure 4.7. Wall pressure, heat flux and shear stress. Left line plots are span-averaged and normalized. Right 3D contour plots are instantaneous snapshots in dimensional SI units..... 42

Figure 5.1. Wall normal extraction locations. Contours are mean turbulent kinetic energy. 49

Figure 5.2. Span-averaged separation point (top) and reattachment point (bottom) signals. 51

Figure 5.3. PSD of span-averaged separation (left) and reattachment (right) point signals. 51

Figure 5.4. Lowpass FIR filter design: filter window (left) and magnitude response (right)..... 51

Figure 5.5. Separation point signals in span-averaged bins of $2\delta_0$. 52

Figure 5.6. PSD of separation point signals in span-averaged bins of $2\delta_0$. 52

Figure 5.7. Instantaneous lowpassed-filtered turbulent wall shear stress τ' (Pa) and turbulent wall heat flux q' (W/m^2). 55

Figure 5.8. Instantaneous cross-stream planes of lowpassed- filtered streamwise turbulent momentum $\rho u'/\rho U_\infty$ with lowpassed wall shear stress τ' (Pa). Left image also shows cross-stream v-w velocity vector field..... 55

Figure 5.9. Zoom of instantaneous cross-stream plane $i = 280$ showing a pair of counter-rotating vortices. Contours are lowpassed- filtered streamwise turbulent momentum $\rho u'/\rho U_\infty$ with cross-stream v-w velocity vector field. 56

Figure 5.10. Isosurfaces of instantaneous lowpass-filtered streamwise turbulent momentum $\rho u'/\rho U_\infty$. A positive and a negative isosurface are chosen to highlight the low and high turbulent moment streaks, extending from just after separation to past reattachment. 56

Figure 5.11. Instantaneous cross-stream variations of (a) turbulent wall shear stress τ' (Pa), and (b & c) turbulent momentum $\rho u'/\rho U_\infty$ at various axial and wall normal locations..... 57

Figure 5.12. Wall normal locations on sample i280 plane for spanwise correlations of turbulent momentum $\rho u'/\rho U_\infty$. 57

Figure 5.13. Autocorrelation of turbulent momentum $\rho u'$ at various axial locations across the separated zone (left) and at various boundary layer heights at a single axial location just downstream of the corner..... 58

Figure 5.14. Illustrations of unstable Rayleigh circulation condition for a concave (left) and convex (right) wall, reproduced from [86]. 59

Figure 5.15. Illustrations of Görtler centrifugal instabilities: (left) streamwise vortex pairs on a concave wall, and (right) cross-stream momentum and induced rotation and mixing, reproduced from [41] & [91], respectively. 59

Figure 5.16. Streamlines labeled S1 & S2 across the separation bubble with contours of mean turbulent kinetic energy k/U_e^2 (top), streamline curvatures (middle), and corresponding Görtler indices (bottom). 62

Figure 5.17. Illustration of interrogation window S of point P for computing pseudo-circulation $\Gamma_{1,2}$. 64

Figure 5.18. Identification of vortex cores using the modified Γ_2 criterion (top left) and the modified λ_{ci} criterion (bottom left) for a sample lowpass filtered cross-stream plane cropped to width $4\delta_0$ (location shown right). 67

Figure 5.19. Vortex centers and strength on sample lowpass filtered cross-stream plane (cropped to width $4\delta_0$). 68

Figure 5.20. Isosurfaces of $|\Gamma_2| \approx 2/\pi$ showing an instantaneous snapshot of the streamwise centrifugal instabilities at the separated corner on the full $10\delta_0$ span. Also shown are lowpass filtered streamwise velocity contours u/U_∞ on a plane just above the wall and on a longitudinal plane on a spanwise boundary. 69

Figure 5.21. Sample vortex signals span-averaged over a $2\delta_0$ bin on plane i240: (from top) circulation Γ, swirl strength λ_{ci} and convection velocity U_c. 71

Figure 5.22. Cross-correlation of vortex circulation Γ and vortex swirl strength λ_{ci} in δ_0 spanwise bins. 71

Figure 5.23. Cross-correlation of vortex circulation Γ and vortex swirl strength λ_{ci} in $2\delta_0$ spanwise bins. 72

Figure 5.24. Sample signals of vortex strength fluctuation λ'_{ci} and separation point fluctuation X'_{sep} on plane i240 span-averaged over $2\delta_0$ bins and filtered to remove high-frequency noise. 73

Figure 5.25. Cross-correlation of vortex strength λ'_{ci} and separation point X'_{sep} in δ_0 spanwise bins. 73

Figure 5.26. Cross-correlation of vortex strength λ'_{ci} and separation point X'_{sep} in $2\delta_0$ spanwise bins. 73

Figure 5.27. Sample signals of convection velocity fluctuation U'_c and separation point fluctuation X'_{sep} on plane i240 span-averaged over $2\delta_0$ bins and filtered to remove high-frequency noise. . 75

Figure 5.28. Cross-correlation of convection velocity U'_c and separation point X'_{sep} in δ_0 spanwise bins. 75

Figure 5.29. Cross-correlation of convection velocity U'_c and separation point X'_{sep} in $2\delta_0$ spanwise bins. 75

Figure 6.1. Wall normal extraction locations annotated by streamwise location $x' = (x - x_c)/\delta_0$. Contours are instantaneous modified density gradient. 88

Figure 6.2. Reynolds stresses and TKE, scaled by upstream $u^2_{\tau,ref}$. 90

Figure 6.3. Reynolds stresses and TKE vs. z/δ_0 (left) and z^* (right), scaled by $u^2_{\tau,ref}$. 91

Figure 6.4. Reynolds stress anisotropy tensor vs. z/δ_0 (left) and z^* (right). 96

Figure 6.5. Reynolds stress anisotropy invariant map (Lumley triangles). 97

Figure 6.6. Turbulent kinetic energy transport budgets, normalized by viscous wall units. 100

Figure 6.7a. Reynolds stress transport budgets, location I. 111

Figure 6.8a. Reynolds stress transport budgets, location I, $\Pi_{ij}^{tot} = \Pi_{ij} + \mathcal{D}_{ij}^{p}$. 113

Figure 6.9. Dissipation components, in local wall units (left) and as a fraction of total dissipation (right). 119

Figure 6.10. Dilatational dissipation model assessment, versus z^* (left), M_t^2 (middle) and $M_t^4(Sk/\epsilon_s)^4 R_t^{-1}$ (right). 122

Figure 6.11. Dissipation tensor models, normalized by viscous wall units: Rotta (left), LRKY (middle), HJ (right). 129

Figure 6.12. Dissipation tensor models, normalized by $2/3\epsilon$: Rotta (left), LRKY (middle), HJ (right). 130

Figure 6.13. Pressure dilatation models. 136

Figure 6.14. Pressure dilatation model scalings at upstream equilibrium station I. 136

Figure 6.15a. Pressure strain tensor models at station I. 147

Figure 6.16. Density fluctuations. 151

Figure 6.17. Pressure fluctuations. 151

Figure 6.18. Temperature fluctuations. 152

Figure 6.19. SRA: Turbulent Prandtl number. 155

Figure 6.20. SRA: Phase relations. 157

Figure 6.21. SRA: Magnitude Relation. 159

Figure 6.22. Inner and outer turbulence timescales. 161

Figure 6.23. Turbulent Heat Flux. 164

Figure 6.24. Temperature gradients. 165

Figure 7.1. Full BoLT-II vehicle (left) and simulated top (Side A) half of the vehicle (right) with partial slices of the computational grid (coarsened for viewing). Note the grid encompasses the full upper half minus the nose. 175

Figure 7.2. Mach number and Reynolds number during BoLT-II ascent phase (left) and descent phase (right). Simulated flight condition denoted on right. Figure reproduced from Portoni & Dufrene 2023 [216]. 176

Figure 7.3. Normalized wall-normal spacing on experimental surface, Δz_w^+ (adiabatic wall). .. 178

Figure 7.4. FUN3D laminar adiabatic wall solution: pressure $p/(\rho_\infty a_\infty^2)$ on xz symmetry plane (top) and experimental surface (bottom left), and skin friction $\tau_w/(0.5\rho_\infty U_\infty^2)$ on experimental surface (bottom right). 179

Figure 7.5. Instantaneous surface contours: pressure P_w (Pa), temperature T_w (K) and shear stress τ_w (Pa). 183

Figure 7.6. Pressure contours P/P_∞ on a plane just above the surface and on slices across the span. 184

Figure 7.7. Streamwise velocity u/U_∞ on a plane just above the surface and on spanwise slices showing downstream development of flow. 184

Figure 7.8. Isosurface of Q-criterion colored by normalized vorticity magnitude $\omega\delta_0/U_\infty$. 185

Figure 7.9. Vorticity magnitude $\omega\delta_0/U_\infty$ with wall normal line extractions labeled P1-P8. ... 185

Figure 7.10. Van Driest transformed mean u-velocity u_{vd}^*, (red line), with theoretical viscous sublayer (blue line) and theoretical log law layer (green line). 186

Figure 7.11. Mean profiles of u, v, w, T, ρ, p normalized by boundary layer edge values. 188

Figure 7.12. Signals of u-velocity at sample location $z/\delta = 0.1$ in the boundary layer. 190

Figure 7.13. Energy spectra through the boundary layer vs. z/δ for probes P1-P8. 191

Figure 7.14. Energy spectra through the boundary layer vs. z^* for probes P1-P8. 191

Figure 7.15. Energy spectra at $z/\delta = 0.9$. 192

Figure 7.16. Wall pressure spectra. 192

Figure 7.17. Instantaneous wall pressure fluctuations p' (Pa) with no inlet disturbances (left) and with inlet pressure disturbances (right). Freestream disturbance: $(p'/\bar{p}_\infty)_{rms} = 0.5\%$. 195

Figure 7.18. Instantaneous surface contours: shear stress τ_w (Pa). 196

Figure 7.19. Instantaneous surface contours: heat flux q_w (W/m^2). 196

Figure 7.20. Instantaneous cross-stream shear stress τ_w (Pa) (top) and heat flux q_w (W/m^2) (bottom). Solid lines are from CFD, and square symbols are from flight experiment. 197

Figure 7.21. Heat flux tracking during flight from thermocouple sensor MT-A-3-2F, and comparisons with CFD. Reproduced from Wheaton & Dufrene 2023 [223]. This figure illustrates the unstable nature of the chosen point in the trajectory for the simulations herein. 197

Figure A.1. Reynolds stresses and TKE vs. z/δ (left) and z^* (right), Morkovin scaled. 203

Figure A.2. Reynolds stresses vs. z/δ_0 (left) and z^* (right), TKE scaled. 204

Figure B.1. Blending function f_ϵ assessment for dissipation tensor models at upstream equilibrium station I: Rotta (left), LRKY (middle), HJ (right). 206

Chapter 1: Introduction

1.1 Motivation

Hypersonic flight has seen several decades of progress, from the first hypersonic vehicle – the Mach 7 WAC Corporal rocket flown in 1949 – to the first crewed space flights on Vostok 1 and Freedom 7 in 1961. This progress continued with the Mach 6 North American X-15 manned research aircraft in 1961, the record breaking Mach 37 Apollo 10 manned space capsule, the Mach 10 NASA-43A research scramjet first flown in 2004 (Figure 1.1) and the Mach 5 Boeing X-51 experimental waverider first flown in 2013 (Figure 1.1). Additionally, a range of hypersonic cruise, glide and artillery systems are being developed in the defense sector. The technology however has been slow to mature due to a plethora of scientific challenges that are specific to hypersonic flight.



Figure 1.1. Mach 10 NASA X-43A Experimental Scramjet [1] (left) and Mach 5 Boeing X-51A Experimental Waverider [2] (right).

Vehicles in hypersonic flight, typically assumed to be at speeds of approximately Mach 5 and above, experience an extremity of complex flow physics. The strong shock wave formed around the vehicle lies close to the vehicle airframe and interacts in very complex ways with the fluid boundary layer in proximity to the surface. In the post-shock region temperature and pressure rises significantly, particularly in the nose region. High heat transfer to the vehicle surface can incur material warping and surface erosion. At high enough temperatures the flow experiences thermochemical nonequilibrium effects where vibrational excitation, dissociation and ionization

become significant and pose a challenge for current predictive methods. Shock interactions and plasma sheaths can interfere with guidance and telemetry devices. The thin compressed boundary layer may be laminar but is susceptible to transition-to-turbulence due to atmospheric disturbances penetrating the boundary layer and generating instabilities that are challenging to model. In transitional flow the surface heating tends to spike in the transition region to a value higher than that in the upstream laminar region or downstream turbulent region. In compression corners of the vehicle, such as on control surfaces and engine inlets and nozzles, strong shock interactions with the wall boundary layer can incur large-scale unsteady separation and high localized fluctuating pressure and heat loads. The precipitous fluctuations can incur buffeting and vibrations, and threaten both aerodynamic stability and structural integrity. Figure 1.2 illustrates some hypersonic flow interaction effects.

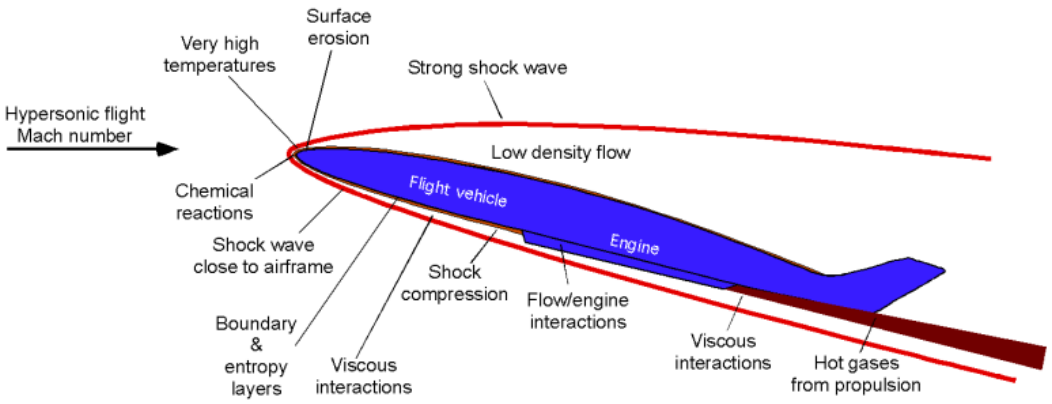


Figure 1.2. Illustration of flow interactions on a hypersonic vehicle (reproduced from Leishman 2022 [3]).

Design of hypersonic vehicles therefore requires accurate prediction of flow physics, which in turn necessitates understanding of the underpinning physical mechanisms, such as shock-boundary layer interactions (SBLI), flow separation dynamics, energy-dominant flow instabilities and viscous-inviscid interactions. Available prediction tools generally include analytical methods such as Newtonian theory, experiment such as wind tunnel and free flight testing, and simulation such

as computational fluid dynamics (CFD). Current prediction methods are often based on canonical two-dimensional descriptions of the flowfield and often at lower speeds. They are certainly challenged by the complex flow interactions in the hypersonic regime. The difficulty is exacerbated when three-dimensional flow gradients and cross-stream instabilities are present. To address the scientific challenges of hypersonic flight, geometries that are much simpler than a full scale system, but with just enough complexity to replicate one or more critical flow phenomena encountered in hypersonic flight, are often studied. Two such canonical configurations are studied in this thesis, each addressing a different set of flow phenomena, viz, the Mach 10 Hollow-Cylinder Flare (HCF) and the Mach 6 BoLT-II. A brief introduction to the flow phenomena and literature pertaining to these two hypersonic configurations are discussed next. Detailed discussions are deferred to later Chapters.

1.2 Background

The Navier-Stokes equations are a system of partial differential equations that express the conservation of mass, momentum and energy of fluid and describe the motion of that fluid. The Navier-Stokes are solved via iterative numerical procedures since no analytical solution exist. Numerical computation of turbulent flow fields has typically utilized Direct Numerical Simulation (DNS), Large Eddy Simulation (LES) and Reynold-Averaged Navier Stokes (RANS) methods. The main difference between these approaches is the treatment of turbulence. DNS offers the highest fidelity of fluid modeling in continuum mechanics, wherein all spatial and temporal scales of turbulence are resolved, but is very computationally expensive and currently may be suited for simple canonical problems but not practical application. LES, the method used in this work, resolves the largest scales of turbulence while modeling the smallest scales, and generally offers a

balance between accuracy and computational expense. A detailed discussion of the LES method is deferred to the next Chapter. The most common approach by far, particularly in the commercial sector, is RANS, which models all scales of turbulence and in doing so incurs significantly less computational cost than higher fidelity LES or DNS.

In RANS approaches, the main challenge is the treatment of the turbulent stresses or Reynolds stresses required to close the time-averaged Navier-Stokes equations. Modeling of the Reynolds stresses is most often based on the Boussinesq 1877 [5] eddy viscosity hypothesis which assumes similarity between momentum transfer caused by molecular stresses and momentum transfer caused by turbulent stresses. However, the physics of the two processes are fundamentally different and the hypothesis is not accurate for many types of flows. The Boussinesq relation fares poorly in flows with rapid changes in strain rate, high surface curvature, rotating flows, secondary motions and many three-dimensional flows. Nevertheless, RANS eddy viscosity models (EVM) have demonstrated widespread practical value in many engineering applications.

At a higher fidelity of RANS modeling is the transport of the Reynolds stress tensor itself, referred to as Reynolds Stress Transport (RST) modeling. RST models obviate the need for the Boussinesq relation. The conceptual advantage of RST models is the natural incorporation of non-local effects, history effects and sudden changes in strain rate, streamline curvature, rotation and body forces, whereas EVMs require empirical terms to model these effects. A more detailed discussion of RSTs is deferred to a later Chapter.

All RANS models, both EVMs and RSTs, contain multiple terms that require modeling and continues to be an active area of research. Models are semi-empirical in nature and have been calibrated and validated over the years with varying levels of success using theory, experiment, DNS and LES solutions of canonical flows such as wall-bounded flows (flat plates, channel flows,

pipe flows) and free shear flows (wakes, mixing layers, jets), among others. Many such early canonical studies were incompressible and have served as a guide for developing models for supersonic compressible flows. Extension of the models to hypersonic compressible flows is less studied, and even more so for nonequilibrium flows such as those with shock wave interactions. Part of the difficulty lies in the ability to obtain detailed turbulence statistics for model development with reliable accuracy from both experiment and numerical simulation. While experiments are key tools for system design and model validation, high-fidelity LES and DNS numerical solutions can be mined to obtain more detailed turbulence physics that complement experimental measurements, e.g., velocity and thermodynamic correlations and related higher-order moments.

High-speed shock wave interactions with solid boundaries have been study extensively for decades using theoretical, experimental and computational tools with notable progress reviews at various times, e.g., Zuo & Pirozzoli 2024 [6], Gaitonde & Adler 2023 [7], Sabnis & Zabinsky 2023 [8], Gaitonde 2015 [9], Gnoffo et al. 2013 [10], Roy & Blottner 2006 [11], Knight et al. 2003 [12], Andreopoulos et al. 2000 [13], Settles & Dolling 1992 [14], Settles & Dodson 1991/1994 [15][16], Fernholz et al. 1989 [17] and Fernholz & Finley 1981 [18]. Several classes of canonical shock-boundary layer interaction flows have been studied, including ramp compression corners, axisymmetric compression corners (as is the case in this work), impinging-wall-reflected shock interactions and fin-shock interactions, among others. Many studies provide mean data (such as velocity, pressure, wall heat flux and skin friction) but often limited turbulence data. Studies that use RANS methods rely on modeling of the full turbulence spectrum and can only provide time-averaged data. Unsteady RANS (URANS) can provide low-frequency unsteady data but cannot be

relied on for high-frequency turbulence statistics. Even for mean flow prediction, as discussed above, RANS models are known to be less reliable for flows with shock-boundary layer interactions in which nonequilibrium effects persist (Georgiadis et al. 2015 [19] and Debonis et al. 2012 [20]). Few studies provide the richer set of turbulence dynamics in the nonequilibrium separated and post-shock flow regions desired for turbulence model development and a priori model validation. Even fewer such studies exist for the hypersonic regime ($M \gtrsim 5$) in which compressibility and nonequilibrium effects become more important and need to be accounted for by models in order to capture the flow physics. Some studies that have reported SBLI turbulence statistics in some detail using LES or DNS include Helm & Martín 2022 [21], Priebe & Martín 2021 [22], Fang 2020 [23], Vyas et al. 2019 [24], Morgan et al. 2013 [25], Wu & Martín 2007 [26], Pirozzoli & Grasso 2006 [27], and Loginov et al. 2006 [28].

Shock-boundary layer interactions in compression corners are characterized by strong adverse pressure gradients, flow separation, shock oscillation, centrifugal instabilities, and high wall pressure, shear and heating. Figure 1.3 shows the salient features in a Mach 3 compression corner. The approaching undisturbed boundary layer is compressed by sudden change in direction of the flow at the corner. A 'primary' oblique shock wave is generated to account for the discontinuous change in flow conditions which occurs across the shock line. The shock wave imposes an adverse pressure gradient that may separate the flow producing a low-speed recirculating region at the corner referred to as the separation bubble. The bubble in turn imposes a secondary compression and reattachment shocks emanating from the incipient separation and reattachment points, respectively. The separation and reattachment shocks intersect the primary oblique shock forming a triple point. A shear layer also forms between the separation bubble and outer flow. The shear layer typically continues downstream of the flow reattachment. Temperatures and pressures rise

significantly in the corner interaction and downstream of reattachment. Downstream of the primary shock and reattachment, the boundary layer is thinner, highly compressed, highly strained and generally in a state of nonequilibrium.

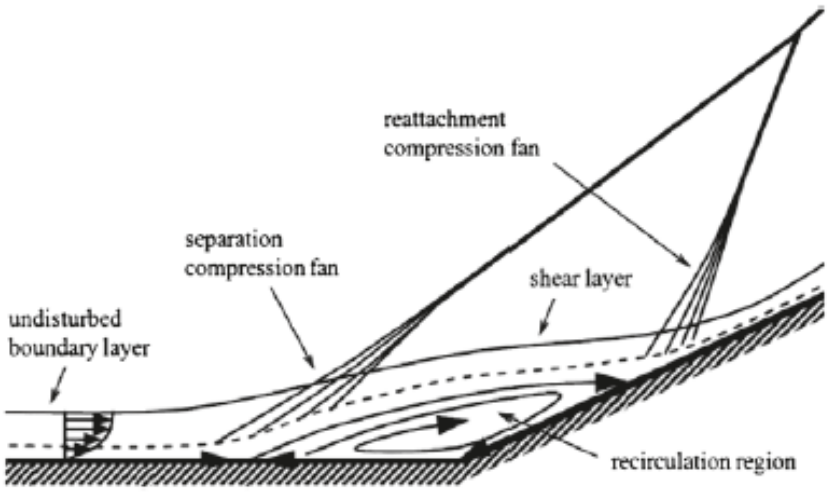


Figure 1.3. General SBLI Features, Mach 3 24° compression corner (reproduced from Wu et al. 2015 [4]).

The corner SBLI interaction is inherently unsteady across a broad range of frequencies. Previous works have identified a low-frequency event that dominates the energy in the separated corner. The driving mechanism of the dominant low-frequency event in high-speed separated compression corners has been a topic of research and debate for many decades. The low-frequency event consists of periodic contraction and dilation of the separation bubble that have been shown to be statistically linked to the separation shear layer and shock oscillations. Some studies suggested that the dynamics are driven by upstream boundary layer disturbances [30]-[33], while others suggest that the dynamics are driven by instabilities intrinsic to the shock-boundary layer corner interaction itself [34]-[39]. Furthermore, an inviscid centrifugal instability of a Görtler-type [40]-[41] was identified consisting of pairs of counter rotating vortices generated near separation and developing downstream [34]-[39]. It was hypothesized that the unsteadiness of the separation bubble are driven by the centrifugal instabilities and vice versa. The origin and statistical properties

of the centrifugal instabilities and their statistical correlation to the low-frequency separation event are however not well understood, particularly so at hypersonic Mach numbers.

1.3 Scope

Wall-Resolved Large Eddy Simulations (WRLES) of two hypersonic configurations are conducted and studied in this thesis, viz, the canonical Mach 10 Hollow-Cylinder Flare (HCF) and the Mach 6 BoLT-II test vehicle (see Figure 1.4). Many canonical flowfields studied in the existing literature are two-dimensional (e.g., plates, ramps, cones, ogives) in the sense that the flow is homogenous in the spanwise direction. The two configurations herein were chosen because of three-dimensional effects due to their shape and flow conditions. The axisymmetric HCF imposes spanwise relaxation of the flow on the flared section of the geometry and consists of spanwise periodic instability modes. The BoLT-II vehicle imposes a three-dimensional pressure field and consists of multiple instability modes.

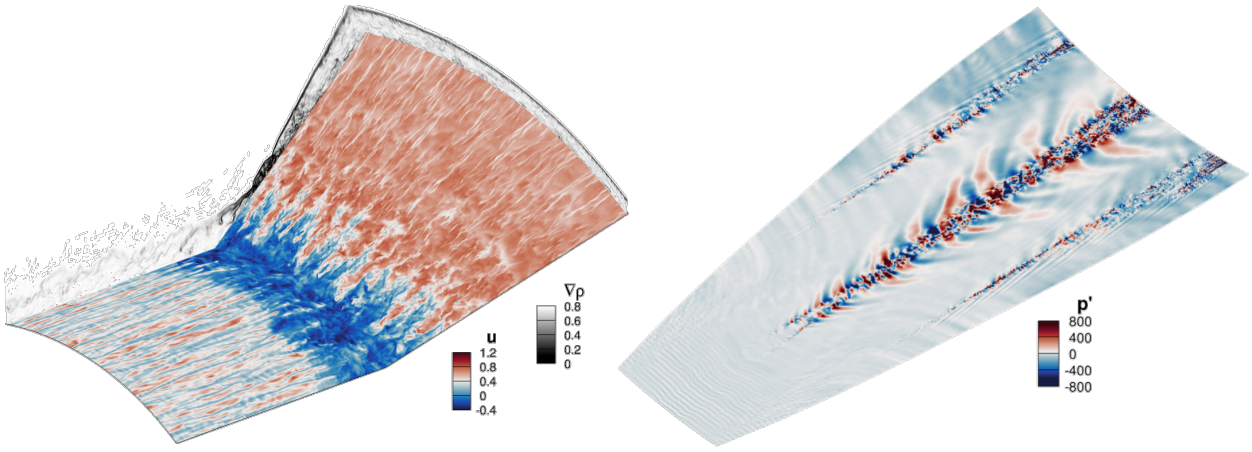


Figure 1.4. Mach 10 HCF (left) with contours of streamwise velocity and density gradient, and Mach 6 BoLT-II (right) with surface contours of pressure fluctuation. Images are a preview of the LES solutions in this study.

The Hollow-Cylinder Flare

Two key issues are addressed. The first is the corner shock-separation dynamics consisting of a high-energy low-frequency event identified in the spectra of the separation point motion and wall pressure signals. The low-frequency event is isolated via lowpass filtering of three-dimensional LES flow solutions. Centrifugal instabilities of a Görtler-type are identified in the lowpass filtered fields and extracted using a combination of topological and eigenvalue-based vortex ID methods which captures their size, strength, speed, direction of rotation, spanwise periodicity and streamwise extent across the separated region. Statistical correlations between the centrifugal instabilities and the unsteady separation dynamics are investigated. The objective is to provide strong visual and statistical evidence for the driving mechanisms of the unsteady shock-separation dynamics, a topic that has been debated for many years.

The second issue addresses the turbulence dynamics in the highly nonlinear shock-separated flowfield. The properties and transport mechanisms of the turbulent kinetic energy and the turbulent/Reynolds stresses are investigated. The applicability of classical similarity laws and semi-empirical closure models for the turbulence transport and turbulence heat flux, such as those typically used in RANS, are investigated a priori in the post-reattachment region following the primary shockwave on the flare where the flow is in a state of high compression, high strain and nonequilibrium. The objective is to provide detailed insight into the turbulence dynamics using the WRLES solutions in order to inform model development for lower-order EVMs and RSTs.

The BoLT-II Vehicle

BoLT-II is a hypersonic research vehicle aimed at studying boundary layer instabilities, laminar-turbulence transition, turbulence, aerothermal loads, aeroelasticity and various other

hypersonic phenomena. The geometry presents several challenging features, such as highly swept leading edges, surfaces with spanwise concavity, significant bow-shock curvature, highly three-dimensional flow, multiple vortical instabilities and multiple transition mechanisms. The objective is to simulate a single point in the flight trajectory, investigate the distribution of surface pressure, shear stress and heating, and interrogate the mean and spectral characteristics of the downstream three-dimensionally strained turbulent boundary layer.

Chapter 2: Computational Methodology

2.1 LES Governing Equations

Large Eddy Simulations (LES) are conducted using the CRoCCo code that has been extensively validated for DNS and LES [21],[26],[34],[42]-[50], including shock-boundary layer interaction configurations. The LES method resolves the larger energy-carrying scales of turbulence, while subgrid scale (SGS) models are used to approximate the smallest scale dynamics. This approach affords a significant reduction of the cost of DNS which seeks to resolve all scales of turbulence. The method is also significantly more accurate than Reynolds-Averaged Navier-Stokes (RANS) approaches which models all scales of turbulence.

The LES governing equations are obtained by applying the spatial lowpass filtering operation of Leonard [51] to the Favre-averaged Navier Stokes equations for conservation of mass, momentum, and total energy. A field variable f may be split into filtered $\bar{f}$ and sub-filtered f' components, viz,

$$f(\xi_i) = \bar{f}(\xi_i) + f'(\xi_i) \quad [1]$$

where ξ_i are spatial coordinates with subscript $i = 1,2,3$. The filtering operation is defined as the convolution,

$$\bar{f}(\xi_i) = \int_{D(\xi_i)} f(\xi_i') G(\xi_i, \xi_i'; \overline{\Delta}) d\xi_i' \quad [2]$$

where G is the filter kernel, $\overline{\Delta}$ is the smallest length scale retained by the filtering operation and D is the computational domain. In compressible flows it is convenient to use Favre-averaged field variables, defined as $\tilde{f} = \overline{\rho f}/\bar{\rho}$, to prevent additional terms from appearing on the right-hand side of the filtered governing equations. Applying the filtering operation to the Favre-averaged Navier Stokes equations results in,

$$\frac{\partial Q}{\partial t}+\frac{\partial F_j^C}{\partial \xi_j}+\frac{\partial F_j^V}{\partial \xi_j}=\frac{\partial F_j^{SGS}}{\partial \xi_j} \quad [3]$$

where Q is vector of conserved variables, F_j^C is the convective flux vector, F_j^V is the viscous flux vector, F_j^{SGS} is the unresolved SGS flux vector representing the smaller scales of motion that results from the filtering operation. The vectors are defined below. Subscripts $i,j,k = 1,2,3$ are Einstein summation notation where the numeric values represent the three body-fitted curvilinear/computational coordinate directions.

$$Q = J\begin{bmatrix}\bar{\rho}\\ \bar{\rho}\tilde{u}\\ \bar{\rho}\tilde{v}\\ \bar{\rho}\tilde{w}\\ \tilde{e}\end{bmatrix} \quad [4]$$

$$F_j^C = Jr_j\begin{bmatrix}\bar{\rho}\tilde{\mathcal{u}}_j\\ \bar{\rho}\tilde{u}\tilde{\mathcal{u}}_j+\bar{p}s_{j1}\\ \bar{\rho}\tilde{v}\tilde{\mathcal{u}}_j+\bar{p}s_{j2}\\ \bar{\rho}\tilde{w}\tilde{\mathcal{u}}_j+\bar{p}s_{j3}\\ (\tilde{e}+\bar{p})\tilde{\mathcal{u}}_j\end{bmatrix}, \quad F_j^V = -Jr_j\begin{bmatrix}0\\ \tilde{\sigma}_{1i}s_{ji}\\ \tilde{\sigma}_{2i}s_{ji}\\ \tilde{\sigma}_{3i}s_{ji}\\ \tilde{\sigma}_{ik}\tilde{u}_k s_{ji}-\tilde{q}_i s_{ji}\end{bmatrix}, \quad F_j^{SGS} = -Jr_j\begin{bmatrix}0\\ \tau_{j1}\\ \tau_{j2}\\ \tau_{j3}\\ \gamma c_v \mathcal{Q}_j+{}^1\!/_2\,\mathcal{J}_j-\mathcal{D}_j\end{bmatrix} \quad [5]$$

Auxiliary equations:

Velocity Vector: $\tilde{u}_i = [\tilde{u},\tilde{v},\tilde{w}]$ [6]

Contravariant Velocity Vector: $\tilde{\mathcal{u}}_j = \tilde{u}_i s_{ji}$ (note the use of script $\mathcal{u}$ vs. u) [7]

Total Energy: $\tilde{e} = c_v\bar{\rho}\tilde{T}+{}^1\!/_2\,\bar{\rho}\tilde{u}_i^2$ [8]

Viscous Stress Tensor: $\tilde{\sigma}_{ij} = 2\tilde{\mu}\tilde{S}_{ij}-{}^2\!/_3\,\tilde{\mu}\delta_{ij}\tilde{S}_{kk}$ [9]

Strain Rate Tensor: $\tilde{S}_{ij} = \frac{1}{2}\left(\frac{\partial \tilde{u}_i}{\partial x_j}+\frac{\partial \tilde{u}_j}{\partial x_i}\right)$ [10]

Viscosity Law:

Sutherland $\left(\tilde{T} \gtrsim 100K\right)$: $\tilde{\mu} = C_1\frac{\tilde{T}^{1.5}}{\tilde{T}+C_2}$ [11]

Keyes $\left(\tilde{T} \lesssim 100K\right)$: $\tilde{\mu} = C_3\frac{\tilde{T}^{0.5}}{1+\left(C_4/\tilde{T}\right)10^{-5/\tilde{T}}}$ [12]

Heat Flux Vector: $\tilde{q}_j = -\tilde{k}\dfrac{\partial \tilde{T}}{\partial x_j}, \qquad \tilde{k} = \tilde{\mu} c_p / Pr$ [13]

Ideal Gas Equation of State: $\bar{p} = \bar{\rho} R \tilde{T}$ [14]

Here $\bar{\rho}$ is density, c_v and c_p are the specific heats at constant volume and pressure respectively, $\tilde{\mu}$ is the dynamic viscosity, $\tilde{k}$ is the thermal conductivity, Pr is the molecular Prandtl number, R is the specific gas constant and $\bar{p}$ is the pressure computed using the ideal gas law for the equation of state. The fluid is assumed to be a Newtonian fluid in which the viscous stress tensor $\tilde{\sigma}_{ij}$ is linearly related to the strain rate tensor $\tilde{S}_{ij}$. Dynamic viscosity $\tilde{\mu}$ can be computed using Sutherland [52] or Keyes [53] depending on the local temperature where constants C_1, C_2, C_3 and C_4 depend on the fluid. The heat flux $\tilde{q}_j$ is modeled using Fourier's law of heat conduction.

The transformation from physical space in x_i to curvilinear space in ξ_i results in the appearance of the following quantities:

$$s_{ji} = \left[\frac{\partial \xi_j}{\partial x_i}\right] r_j^{-1}, \qquad r_j = \sqrt{\left(\frac{\partial \xi_j}{\partial x_1}\right)^2 + \left(\frac{\partial \xi_j}{\partial x_2}\right)^2 + \left(\frac{\partial \xi_j}{\partial x_3}\right)^2}, \qquad J = \det\left[\frac{\partial x_i}{\partial \xi_j}\right]$$

where s_{ji} is the matrix of partial derivatives of ξ_j normalized by r_j and J is the Jacobian determinant of the grid transformation. First order partial derivatives in physical space, such as that in $\tilde{S}_{ij}$ and $\tilde{q}_j$, may be transformed to curvilinear space via:

$$\frac{\partial}{\partial x_i} = \frac{\partial \xi_j}{\partial x_i}\frac{\partial}{\partial \xi_j}$$

The SGS source term vector F_i^{SGS} which represents the unresolved fine-scale turbulence contains the following terms defined as,

SGS Viscous Stress: $\tau_{ji} \equiv \bar{\rho}\left(\widetilde{u_i u_j} - \tilde{u}_i \tilde{u}_j\right)$ [15]

SGS Heat Flux: $Q_j \equiv \bar{\rho}\left(\widetilde{u_j T} - \tilde{u}_j \tilde{T}\right)$ [16]

SGS Turbulent Diffusion: $$\mathcal{J}_j \equiv \bar{\rho}\left(\widetilde{u_j u_k} u_k - \widetilde{u}_j \widetilde{u_k u_k}\right) \quad [17]$$

SGS Viscous Diffusion: $$\mathcal{D}_j \equiv \overline{\sigma_{ij} u_i} - \tilde{\sigma}_{ij} \widetilde{u}_i \quad [18]$$

The SGS terms are unclosed. The closure models are based on Martín, Piomelli & Candler 2000 [1]. The SGS viscous stress τ_{ji} is modeled using a one-coefficient dynamic mixed model consisting of an eddy viscosity term and a scale-similar term. The eddy viscosity term models the dissipative drain of energy associated with the turbulence energy cascade from the resolved scales to the unresolved scales. The eddy viscosity term approximates the anisotropic SGS stresses based on Smagorinsky 1963 [54]. The scale-similar term models the conservative exchange of energy between the smallest resolved scales and the SGSs. The scale-similar term is based on the assumption that the most active SGSs are closest to the LES filter cutoff frequency and is designed to seek the smallest resolved stresses to represent the SGS stresses. A similar dynamic mixed model formulation is used for the SGS heat flux $\mathcal{Q}_j$. The SGS turbulent diffusion $\mathcal{J}_j$ is modeled using the velocity-shear stress tensor correlation approximation of Kight et al. 1998 [55]. The SGS viscous diffusion $\mathcal{D}_j$ is not modeled herein as it is an order of magnitude smaller than the SGS heat flux (typically the most significant SGS term in the energy equation) and because current models are less well-developed [1]. The model equations are listed below in the transformed curvilinear coordinate system. The first terms of τ_{ji} and $\mathcal{Q}_j$ are the eddy viscosity-like terms and the second terms are the scale-similar terms.

SGS Viscous Stress: $$\tau_{ji} = -2C_1 \overline{\Delta}^2 \bar{\rho} |\tilde{S}| \left(\tilde{S}_{ij} - {}^1\!/_3\, \tilde{S}_{kk}\delta_{ij}\right) + \bar{\rho}\left(\widetilde{\widetilde{u}_i \widetilde{u}_j} - \widetilde{\widetilde{u}}_i \widetilde{\widetilde{u}}_j\right) \quad [19]$$

SGS Heat Flux: $$\mathcal{Q}_j = -C_2 \frac{\overline{\Delta}^2 \bar{\rho} |\tilde{S}|}{Pr_t} \frac{\partial \tilde{T}}{\partial \xi_j} + \bar{\rho}\left(\widetilde{\widetilde{u}_j \tilde{T}} - \widetilde{\widetilde{u}}_j \widetilde{\tilde{T}}\right) \quad [20]$$

SGS Turbulent Diffusion: $$\mathcal{J}_j = \widetilde{u}_k \tau_{jk} \quad [21]$$

Here $\tilde{\mathcal{S}}_{ij}$ (denoted using script $\mathcal{S}$ instead of S) is the coordinate-transformed strain rate tensor, $\left|\tilde{\mathcal{S}}\right| = \left(2\tilde{\mathcal{S}}_{ij}\tilde{\mathcal{S}}_{ij}\right)^{0.5}$ is the magnitude of $\tilde{\mathcal{S}}_{ij}$, Pr_t is the turbulent Prandtl number which can be fixed or dynamically varying, and (C_1, C_2) are dynamically varying coefficients. Further details on the SGS models, including the dynamic formulations of Pr_t, C_1 and C_2, can be found in Ref. [1]. The filter width is calculated as $\overline{\Delta} = \left(\overline{\Delta}_{\xi_1}\overline{\Delta}_{\xi_2}\overline{\Delta}_{\xi_3}\right)^{1/3}$ where $\overline{\Delta}_{\xi_i}$ are the local grid spacings in the three curvilinear coordinate directions. The filtered fields are obtained using the tophat filter kernel, which in one dimension is defined as,

$$\bar{f}_i = \frac{1}{2n}\left(f_{i-n/2} + 2\sum_{i-n/2+1}^{i+n/2+1} f_i + f_{i+n/2}\right) \qquad [22]$$

Here subscript i represents the central grid point in the local filter stencil and choice of n lies in $\{4, 8, 16, \ldots\}$.

2.2 Flux Discretization

The viscous fluxes are elliptic in nature and are therefore discretized using a standard 4th-order central differencing scheme. The convective fluxes are discretized using a 4th-order symmetric bandwidth-optimized weighted essentially non-oscillatory (SYMBO-WENO) scheme [43]-[47]. The linear and non-linear components of original WENO method proposed by Jiang & Shu 1996 [56] have been optimized to minimize dissipation while maximizing order of accuracy, bandwidth resolution and shock-capturing capability. The high-bandwidth-resolving SYMBO-WENO flux scheme can reproduce the turbulence intensities and spectral content of DNS to within a high degree of accuracy.

A convective flux f in one dimension is first split into two parts, viz,

$$f = f^+ + f^- \qquad [23]$$

where f^+ has a strictly non-negative derivative and f^- has a strictly non-positive derivative. This is done for upwinding, which is critical for hyperbolic conservation laws. The splitting is accomplished using the local lax-Friedrichs flux splitting method (also referred to as the Rusanov flux splitting method) [57]. The SYMBO-WENO scheme in one-dimension then approximates f^+ at a cell face $(i + 1/2)$ as the weighted sum of $(r + 1)$ candidate fluxes q_k^r, viz,

$$\hat{f}^+_{i+\frac{1}{2}} = \sum_{k=0}^{r} w_k q_k^r \qquad [24]$$

where $\hat{f}$ is the numerical approximation of f, the weights are w_k and i is the computational coordinate. The symmetric candidate stencil arrangement for a flux $\hat{f}^+_{i+1/2}$ is depicted in Figure 2.1 for $r = 3$. The corresponding stencil arrangement for flux $\hat{f}^-_{i+1/2}$ is the mirror image of Figure 2.1.

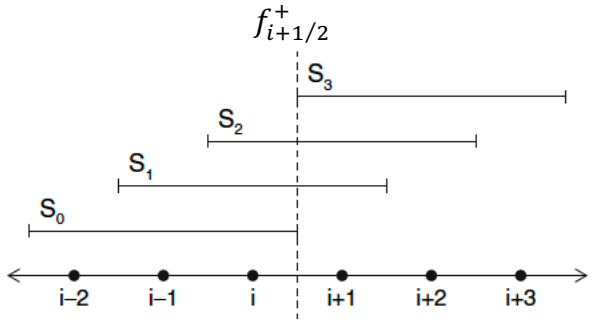


Figure 2.1. Symmetric candidate stencil arrangement for computing SYMBO-WENO flux $\hat{f}^+_{i+1/2}$ at cell face $(i + 1/2)$ when $r = 3$. Figure reproduced from [45].

The candidate fluxes q_k^r are rth-order accurate reconstructed polynomial interpolants computed at $(i + 1/2)$. The weights are given by,

$$w_k = \frac{\alpha_k}{\sum_{k=0}^{r-1} \alpha_k}, \qquad \alpha_k = \frac{C_k^r}{(\epsilon + IS_k)^p} \qquad [25]$$

where C_k^r are the optimal weights, IS_k is a smoothness measurement in the kth candidate stencil, p is an assigned 'adaptation sensitivity' exponent and ϵ is a small positive number ($\epsilon \ll 1$) to

prevent division by zero. In smooth regions of the flow, each candidate stencil is equally desirable, thus IS_k is small (on the order of ϵ) and the weights revert to the optimal weights C_k^r. This results in optimal order-of-accuracy and bandwidth resolution with minimal dissipation. When discontinuities (such as shocks) are present within a stencil k, the smoothness measurement IS_k is large and the weighting w_k of that stencil decreases to prevent interpolation across discontinuities. The modulation of the stencil weights via IS_k is referred to as WENO adaptation and constitutes the nonlinear part of the scheme. Computation and tabulation of the optimal weights C_k^r (the linear part of the scheme) can be found in Martín et al. 2006 [43]. The definitions of candidate fluxes q_k^r and smoothness measurement IS_k are based on Jiang & Shu's 1996 original paper [56] and can also be found in [43]. Typical values of assigned adaptation sensitivity exponent are $p = 1,2,3,4$ where higher values may be chosen for more severe shocks/discontinuities that exist in the flowfield.

To mitigate unnecessary adaptation which can introduce too much dissipation and compromise accuracy, an absolute limiter AL_{AL} and two relative limiters A_{RL} and B_{RL} are imposed on the stencil weights as follows:

$$w_k = \begin{cases} C_k^r, & \text{if } \max(IS_k) < A_{AL}^{TV} \\ w_k, & \text{otherwise} \end{cases} \quad [26]$$

$$w_k = \begin{cases} C_k^r, & \text{if } \max(TV_k)/\min(TV_k) < A_{RL}^{TV} \text{ and } \max(TV_k) < B_{RL}^{TV} \\ w_k, & \text{otherwise} \end{cases} \quad [27]$$

where TV_k is the total variation of flux f in candidate stencil k. Choices of A_{AL}^{TV}, A_{RL}^{TV} and B_{RL}^{TV} are problem dependent. Further details on optimization of the nonlinear adaptation mechanism can be found in Taylor, Wu & Martín 2007 [45] and Wu & Martín 2007 [26].

2.3 Time Integration

Accurate computation of turbulent and shock separated flows requires time advancement methods that resolve all relevant time scales. Time integration herein is performed using the low-storage 3rd-order explicit Runge-Kutta method of Williamson 1980 [58]. The maximum stable convective timestep Δt_c is based on the time it takes for a characteristic wave to traverse one grid spacing resulting in the Courant number stability condition, viz, $C_n = (|u_i| + a)\Delta t_c/|\Delta x_i| < 1$, from which the maximum Δt_c can be computed, where u_i is the local flow velocity, Δx_i is the local grid spacing and a is the speed of sound. The viscous timestep is computed via $\Delta t_v = \rho/(\mu \Delta x_i^2)$. The maximum stable timestep is then taken as the $\Delta t = \min(\Delta t_c, \Delta t_v)$. In practice, to maintain stability, the actual timestep was some fraction of Δt.

Chapter 3: HCF Computational Setup

3.1 Grid Generation

The three-dimensional (3D) hollow-cylinder flare (HCF) configuration consisted of a cylindrical section followed by a flared conical section. Figure 3.1 shows a coarsened view of the computational grid in xz- and xy-planes, where x, y & z are the cartesian streamwise, spanwise and wall normal coordinate directions respectively. The junction of the cylinder-flare was designated $x = 0$. The length along the cylinder and flared portions were $13\delta_0$ and $12\delta_0$ respectively. The flare angle to the x-axis was 34°. The inlet height was $7\delta_0$ at $x = -13\delta_0$. Utilizing the axisymmetry of the configuration, a 45° sector of the cylinder-flare geometry was modeled to conserve on grid points and computational time. The upstream cylinder section was constructed with a spanwise arclength of $10\delta_0$, where $\delta_0 = 0.018$ m is the reference turbulent boundary layer (BL) thickness near the inlet. This fixes the radius of the cylinder segment at ~$12.732\delta_0$. Grid details are summarized in Table 3.1 (labeled as "STBLI HCF"). Quantities with a '+' superscript have been normalized by the inner boundary layer viscous length scale $z_\tau = \nu_w/u_\tau$, where the friction velocity $u_\tau = \sqrt{\tau_w/\rho_w}$ is the inner boundary layer velocity length scale, and τ_w, ρ_w and ν_w are the shear stress, density and kinematic viscosity, respectively, at the wall.

The computational grid was obtained by first generating a 2D grid on the xz streamwise plane, as depicted on the left of Figure 3.1. The 2D xz-grid was then rotated 45° azimuthally using uniform angular spacing, as depicted in the inlet cross-section shown on the right of Figure 3.1, to obtain the full 3D computational domain. The 2D xz-grid was generated using analytical functions to ensure C1 and C2 continuity of the grid Jacobians in order to minimize numerical noise which can contaminate the flow when using low-dissipation high-bandwidth-resolving numerical flux

schemes. This was accomplished in two steps via a method similar to that found in Adams 1998 [59] and Martín et al. 2003 [60]. The first step is a linear transformation Φ_1 from physical coordinates (x, z) to intermediate coordinates (r, s). The second step is a nonlinear transformation Φ_2 consisting of hyperbolic functions from intermediate coordinates (r, s) to computational coordinates (ξ, ζ). This conceptually depicted in Eq. [28]. The linear transformation Φ_1 is shown in Eq [29], where subscripts l and u represent the functions that describe the lower and upper boundaries of the 2D xz-grid. Transformation Φ_2 is shown in Eq [30], where nonlinear functions $s(\xi)$ and r(ζ) are formulated such that the spatial distribution of the mesh can be controlled in the streamwise and longitudinal directions (for example, finer longitudinal spacing in the wall boundary layer, and finer streamwise spacing at the corner at $x = 0$). The functions $x_l(s)$, $x_u(s)$, $z_l(s)$, $z_u(s)$, $s(\xi)$ and $r(\zeta)$ are described in detail in Wu 2007 [61].

$$(x, z) \xrightarrow{\Phi_1} (r, s) \in [0,1] \xrightarrow{\Phi_2} (\xi, \zeta) \in [0,1] \qquad [28]$$

$$\Phi_1: \quad \begin{aligned} x(r, s) &= (1 - r)x_l(s) + rx_u(s) \\ z(r, s) &= (1 - r)z_l(s) + rz_u(s) \end{aligned} \qquad [29]$$

$$\Phi_2: \quad \begin{aligned} s &= s(\xi) \\ r &= r(\zeta) \end{aligned} \qquad [30]$$

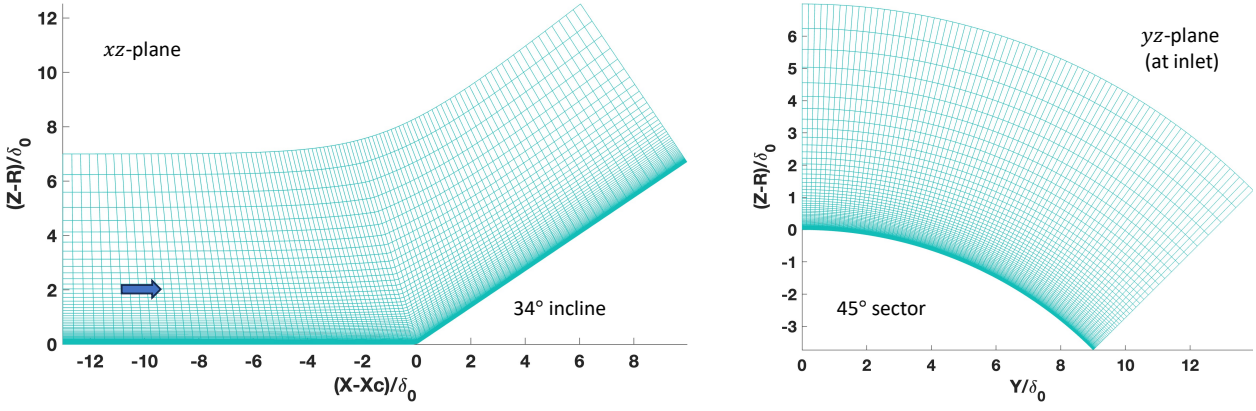


Figure 3.1. Cylinder-Flare grid, coarsened for viewing.

Table 3.1. Cylinder-Flare Grid Specifications.

	$N_x \times N_y \times N_z$ (grid points)	$L_x \times L_y \times L_z$ (units δ_0)	$\Delta x^+, \Delta y^+, \Delta z_w^+$ (units of z_τ)	z Stretch Factor	Points in BL
Auxiliary Cylinder BL	726 x 808 x 81 total 47.5M	30 x 10 x 7	20, 6, 0.5	1.08	50
STBLI HCF	800 x 808 x 100 total 64.6M	25 x 10 x7	20, 5, 0.2	1.1	67

L_x = streamwise distance along surface; L_y = spanwise arclength; L_z = wall normal inlet height.

3.2 Freestream and Boundary Conditions

The working fluid is nitrogen for which the ideal gas equation of state is assumed. The freestream conditions are shown in Table 3.2. The fluid temperature-kinematic viscosity relation is modeled using Keyes law [53] for temperatures below 100K and Sutherland's law [52] for temperatures above 100K. The walls of the cylinder and flare were modeled as a viscous no-slip isothermal wall at 300K. The resulting wall temperature to adiabatic recovery temperature ratio was $T_w/T_r \approx 0.32$. The turbulent boundary layer characteristics referenced at the inflow are summarized in Table 3.3. The Reynolds numbers are defined as $Re_\delta = U_\infty \delta/\nu_\infty$, $Re_{\delta^*} = U_\infty \delta^*/\nu_\infty$, $Re_\theta = U_\infty \theta/\nu_\infty$, $Re_\tau = u_\tau \delta/\nu_w$ and $Re^* = \sqrt{\rho_\infty/\rho_w}\ \mu_w/\mu_\infty Re_\tau$, where the length scales and wall conditions are referenced at the inlet station.

At the outlet and freestream boundaries supersonic extrapolation of flow was used. Rotational periodicity was implemented at the spanwise boundaries. The time-accurate turbulent inflow was generated using a separate auxiliary simulation (described in the next Section). The span-averaged and time-averaged turbulent boundary layer of the auxiliary run at a single axial downstream station (denoted as the rescaling station in the next Section) was used to initialize the entire computational domain of the HCF run.

Table 3.2. Mach 10 Cylinder-Flare Freestream Conditions.

M_∞	U_∞ (m/s)	ρ_∞ ($\mathrm{kgm^{-3}}$)	T_∞ (K)	T_w (K)	T_w/T_r	Re_x
9.60	1410.8	0.0326	53.8	300	0.32	1.22e+7

Table 3.3. Mach 10 Cylinder-Flare Turbulent Boundary Layer Inflow Reference.

δ_0 (mm)	δ_0^* (mm)	θ_0 (mm)	Re_δ	Re_{δ^*}	Re_θ	Re_τ	Re^*
18.0	12.7	0.562	2.54e+5	1.59e+5	7697	431	4830

3.3 Turbulent Inflow Generation via Recycling-Rescaling Method

The inflow turbulent boundary layer of the HCF was supplied by a separate auxiliary boundary-layer simulation. This run consisted of a cylinder (with no flare) with dimensions shown in Table 3.1 labeled to the left as "Auxiliary Cylinder BL" and freestream conditions shown in Table 3.2. Figure 3.2 illustrates the auxiliary cylinder boundary layer run and the HCF run. The downstream boundary layer at a specified axial location that was approximately one boundary layer thickness from the cylinder outlet, referred to as the 'rescaling station', was interpolated onto the inlet of the HCF at each timestep. Implementation-wise, at least four consecutive axial planes of the cylinder that included the rescaling station were interpolated onto the same number of consecutive axial planes at the inlet of the HCF run. This was necessary in order to populate the ghost planes of the HCF inlet, which are required for the stencils of the WENO flux scheme and the SGS spatial filter.

The auxiliary cylinder flow was initialized using an approximate turbulent boundary layer whose downstream Reynolds number at the rescaling station was less than the target Reynolds number of the HCF inlet. The cylinder flow was then established in two steps. The first step is periodic recycling of the boundary layer from the rescaling station to the inlet of the cylinder at each timestep. The cylinder boundary layer is thus allowed to evolve and grow until the Reynolds

number at the rescaling station reaches the target Reynolds number of the HCF inlet as specified in Table 3.3. The second step is to establish a statistically stationary boundary layer by rescaling the inlet boundary layer after the recycling procedure at each timestep. The recycling-rescaling procedure is described in detail in Xu & Martín 2004 [62]. The rescaling transformations are applied separately to the mean and turbulent fields and is done in a piecewise manner for the various inner and outer sublayers. The piecewise transformations are stitched together using smooth hyperbolic tangent functions. While the rescaling transformations are based on flat-plate turbulent boundary layer theory, they are applicable to the cylinder flow herein providing $\mathcal{O}(\delta/R) \ll 1$, where R is the cylinder radius. For the auxiliary cylinder run, $\delta/R \approx 0.08$. The rescaled boundary layer at the inlet of the cylinder is not an exact solution of the Navier-Stokes governing equations. However, small errors arising from the rescaling procedure are curtailed as the flow convects downstream. Turbulence eddies decorrelate as they convect the long length of the cylinder, thus minimizing any forcing that might be incurred by recycling the turbulence.

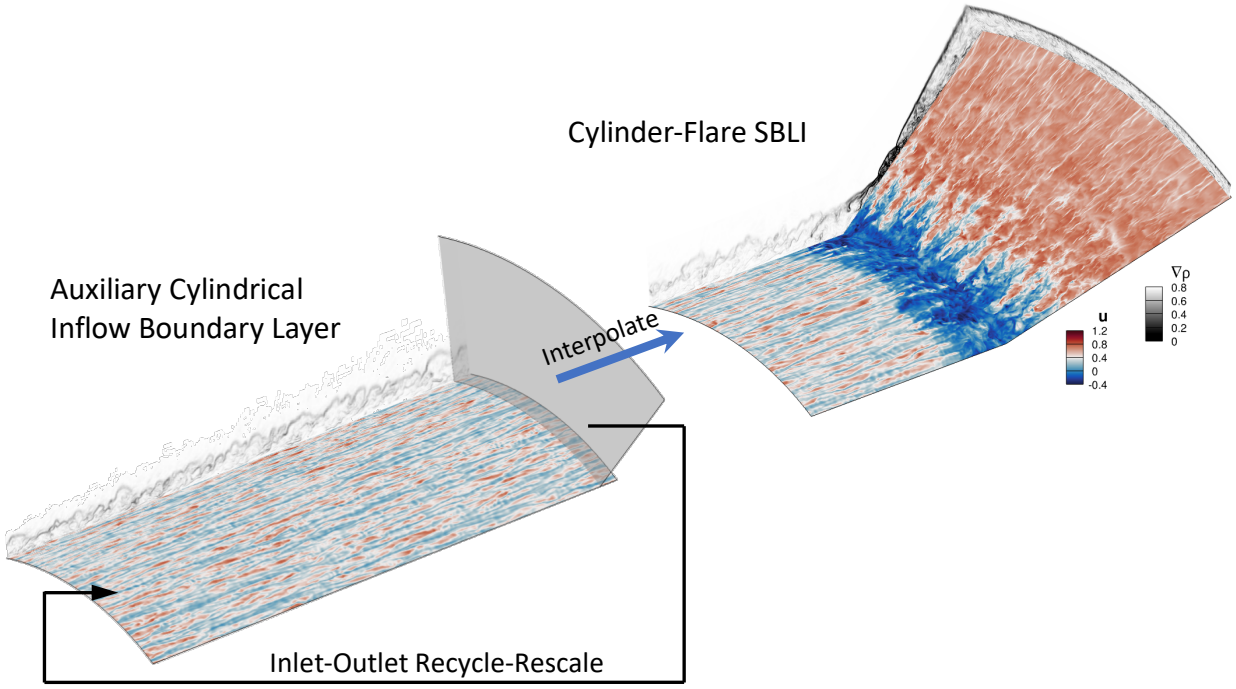


Figure 3.2. Auxiliary cylinder inflow run and cylinder-flare SBLI run.

During the auxiliary cylinder run, acoustic disturbances from the boundary layer penetrate the freestream. The periodic recycling of the boundary layer from the rescaling station to the inlet continuously amplifies these freestream disturbances. This effect can be observed in the mean freestream pressure in the top plot of Figure 3.3. The amplification is very gradual but reduces the flow quality over long run times. In order to damp the spurious disturbances, the flow at the inlet station of the cylinder is filtered prior to rescaling at each iteration according to,

$$\boldsymbol{Q}(x,y,z) = \bar{\boldsymbol{Q}}(z) + [1 - f(z)]\boldsymbol{Q}'(x,y,z) \qquad [31]$$

$$f(z) = 1 - \frac{1}{2}\left[1 - \tanh\left(c\frac{z - z_m}{z_e - z_s}\right)\right]$$

where $\boldsymbol{Q} = \{u, v, w, T, \rho\}$, $\bar{\boldsymbol{Q}}$ and $\boldsymbol{Q}'$ are the mean and turbulent fields of $\boldsymbol{Q}$, $f(z)$ is a filter function, z_s and z_e are approximate start and end wall normal locations in which the filter function transitions from $f = 0$ in the boundary layer to $f = 1$ in the freestream, $z_m = (k_s + k_e)/2$, and c is a chosen transition steepness parameter ($c \approx 1$). As a result the filter is active only in the freestream while the boundary layer is preserved over the duration of the run. The effect of the filter operation can be observed in the bottom plot of Figure 3.3 in which mean pressure disturbances in the freestream above the leading edge shock wave are significantly reduced.

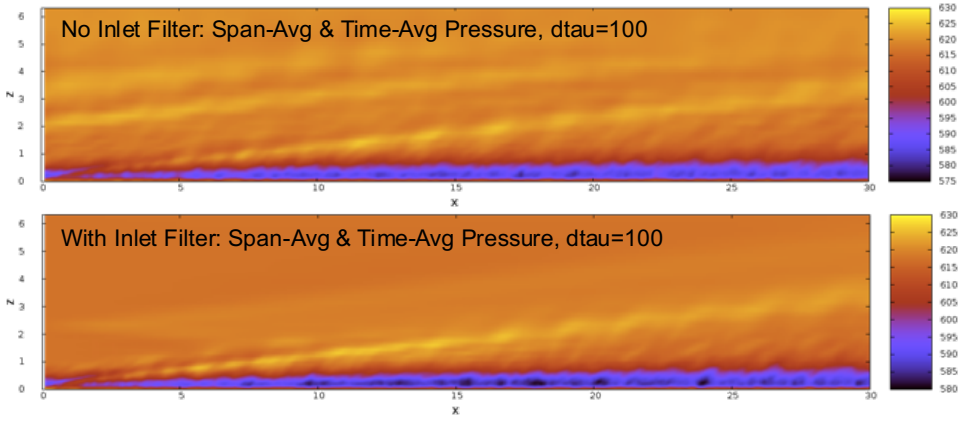


Figure 3.3. Auxiliary cylinder inflow run, mean contours of pressure (Pa).

3.4 Inflow Turbulent Boundary Layer Assessment

3.4.1 Comparison Datasets

Table 3.4. Mach 10 Turbulent Boundary Layer Comparison Datasets.

Case	M_∞	U_∞ (m/s)	T_∞ (K)	ρ_∞ (kg /m^3)	T_w (K)	$\frac{T_w}{T_r}$	δ_0 (mm)	δ (mm)	δ^* (mm)	θ (mm)	Re_δ	Re_{δ^*}	Re_θ	Re_τ	Re^*	Δx^+ Δy^+ Δz_w^+	L_x L_y L_z
Cylinder LES (Present Case)	9.60	1410.8	53.8	.0326	300	0.32	18.0	20.9	12.7	.562	2.54e+5	1.59e+5	7697	431	4830	20 6.0 .50	30 10 7
Plate LES, Helm & Martín 2021 [63]	9.05	1410.6	58.5	.0401	300	0.33	18.0	19.1	11.2	.585	2.62e+5	1.54e+5	8038	503	4958	27 11 .67	30 10 7
Plate DNS, Helm & Martín 2021 [63]	9.04	1410.7	58.6	.0403	300	0.33	18.0	17.9	10.5	.543	2.47e+5	1.45e+5	7486	495	4870	7.8 3.0 .31	30 10 10.5
Cylinder PIV, Brooks et al. 2018 [64],[65]	9.87	1467	53.0	.0400	300	0.31	-	23.3	12.5	.524	3.71e+5	1.99e+5	8346	706	-	-	-

Before assessing the quality of the inflow turbulent boundary layer, some datasets for comparison are first introduced. Table 3.4 shows three Mach 10 turbulent boundary layer datasets in addition to the present test case. Note that there are some differences in Reynolds numbers, which may have an effect when comparing results among the datasets. The first dataset is the present LES cylinder case. The second and third datasets are LES and DNS respectively of a flat plate [63] at similar run conditions and similar exterior dimensions (see last column). The last dataset is a hollow cylinder with 34° flare experiment conducted at Arnold Engineering Development Complex Hypervelocity Wind Tunnel Number 9 (T9) by Brooks et al. 2018 [64]. Note the distinction between δ_0 and δ. The former, δ_0, is the reference boundary layer thickness, while the latter, δ, is an actual 99% velocity boundary layer thickness measured at the far downstream location of the cylinder configuration. Note that the present cylinder LES has slightly higher grid resolution in all three coordinate directions then the flat plate LES case (refer to penultimate column). The flat plate DNS case has significantly higher grid resolution as expected

than the present cylinder LES case and serves as a test of grid convergence for the inflow boundary layer. As previously stated, the axisymmetric boundary layer of the cylinder can be compared to that of an equivalent flat plate providing $\delta/R \ll \mathcal{O}(1)$.

3.4.2 Mean Fields

For the present cylinder boundary layer, wall normal data is taken at the rescaling plane, which was ~$1\delta_0$ from the outflow of the cylinder. The data was span-averaged and time-averaged over $100\delta_0/U_\infty$, where δ_0/U_∞ is a boundary layer time scale representative of a large-eddy turnover time. Figure 3.4 shows the Van Driest II transformed mean streamwise velocity $\bar{u}_{vd}^+$ [66]. The present cylinder LES comparison with the flat plate DNS is excellent throughout the boundary layer. Comparison with the flat plate LES and the wind tunnel PIV is excellent in the laminar sublayer and buffer layer and reasonably good in the log layer. The cylinder LES result in the log layer has approximately the same slope as the law of the wall given by $u^+ = 1/\kappa \log(z^+) + C$, where $k = 0.41, C = 5.2$. The offset in data from the law of the wall resulting in a larger additive constant *C* can be attributed to wall cooling. This is characteristic of compressible boundary layers with wall heat transfer [49]. The differences in the outer wake layer are due to the variation in Reynolds numbers of the datasets.

Figure 3.5-Figure 3.7 show the mean profiles of streamwise velocity, temperature and density, normalized by freestream values. The profiles are characteristic of an equilibrium turbulent boundary layer. The streamwise velocity increases monotonically with a very steep gradient from the wall value to the freestream value. The temperature profile increases away from the isothermal cooled wall, peaking at ~7 times the freestream value in the viscous region, before decreasing monotonically to the freestream value. The peak is due to an equilibration between the colder freestream and the increase in thermal energy near the wall due to molecular dissipation of kinetic

energy. The density decreases away from the wall forming a minimum point at ~14% of the freestream value, then increases with multiple mild inflection points towards the freestream value. The minimum point in density approximately coincides with the maximum point in the mean temperature because the mean pressure through the undisturbed boundary layer is constant (not shown) and the fluid is assumed to follow the ideal gas equation of state. The comparisons with the flat plate DNS are generally excellent, with some small differences in the temperature and density profiles.

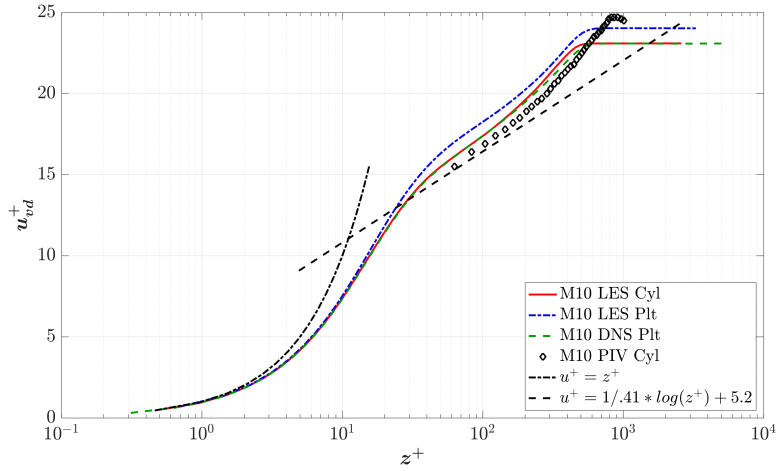


Figure 3.4. Van Driest-transformed mean streamwise velocity.

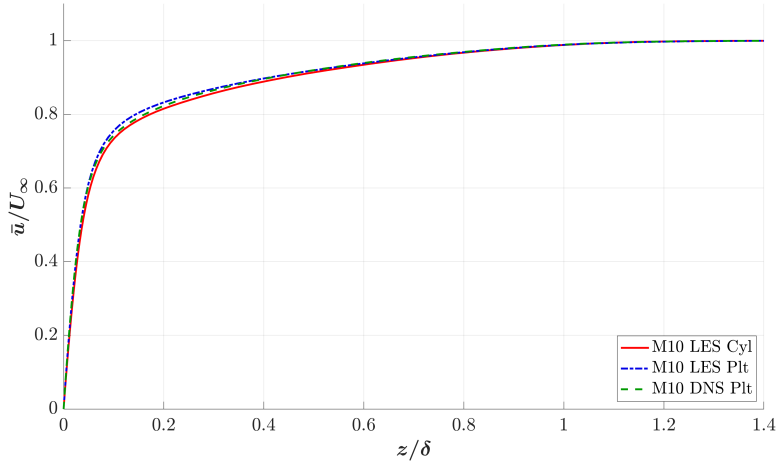


Figure 3.5. Mean streamwise velocity, scaled by freestream value.

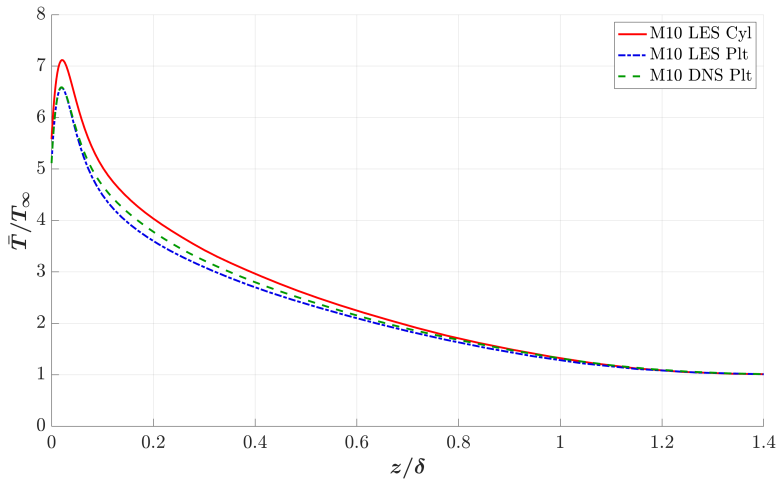


Figure 3.6. Mean temperature, scaled by freestream value.

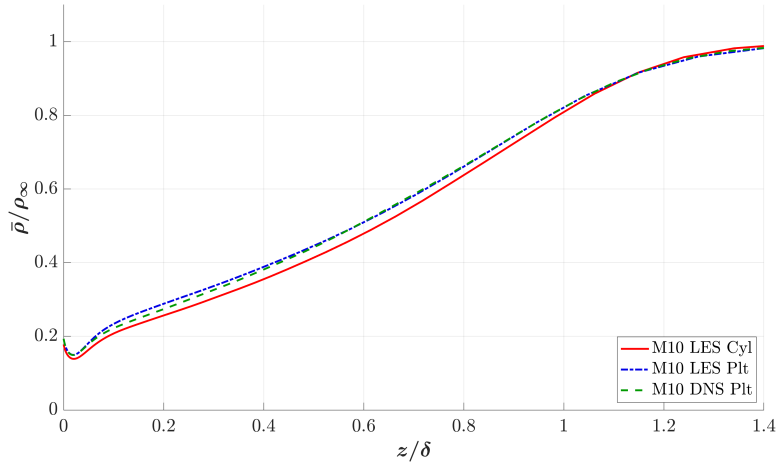


Figure 3.7. Mean density, scaled by freestream value.

3.4.3 Turbulence Fields

Figure 3.8 shows the root-mean-square (RMS) of turbulent streamwise velocity scaled by u_τ. The characteristic maximum is observed near the wall where turbulence production peaks in the buffer layer. The profile then shows an inflection point in the outer layer, after which the turbulence decreases to near zero in the freestream. The CFD datasets show excellent agreement. The PIV data follows the CFD trend up to $z/\delta = 0.2$. For $z/\delta > 0.2$, the PIV results start to flatten

eventually increasing for $z/\delta > 0.7$. The upward deviation of the PIV result is artificial and was due to particle biasing as noted by Brooks 2018 [65].

Figure 3.9 shows the Morkovin-scaled turbulent stresses (Reynolds stresses) and turbulent kinetic energy k. This scaling takes into account compressibility effects across Mach numbers by using the semilocal scaling factor $(\bar{\rho}/\bar{\rho}_w)^{.5}u_\tau^{-2}$ [67]-[68]. The profiles are representative of a canonical equilibrium turbulent boundary layer. There is a large peak in the normal stress $\widetilde{u''^2}$ close to the wall which approximately coincides with peak turbulence production and the strongest fluid ejection and sweep events. Following the peak, $\widetilde{u''^2}$ decreases to zero at the boundary layer edge. Normal stresses $\widetilde{v''^2}$, $\widetilde{w''^2}$ and shear stress $\widetilde{u''w''}$ are smaller in magnitude with peaks in the near wall region. Shear stresses $\widetilde{u''v''}$ and $\widetilde{v''w''}$, i.e., cross-correlations with $\widetilde{v''}$, are almost negligible (not shown). The growth in $\widetilde{u''^2}$ and $\widetilde{v''^2}$ from the wall is larger in magnitude than that of $\widetilde{w''^2}$ and $\widetilde{u''w''}$. This is consistent with a Taylor series analysis of the boundary condition for a canonical wall bounded flow where it can be shown that k, $\widetilde{u''^2}$ and $\widetilde{v''^2}$ increase as z^2, while $\widetilde{w''^2}$ and $\widetilde{u''w''}$ increase as z^4 and z^3, respectively, where z is normalized by boundary layer thickness. The shear stress $\widetilde{u''w''}$ is negative, as expected, due to momentum transfer of faster moving fluid away from the wall towards slower moving fluid near the wall. The comparisons with the flat plate DNS are excellent.

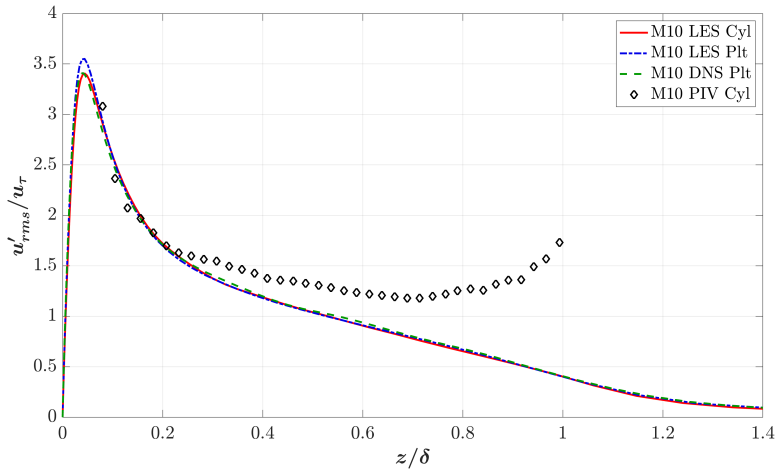


Figure 3.8. Turbulent streamwise velocity, scaled by u_τ.

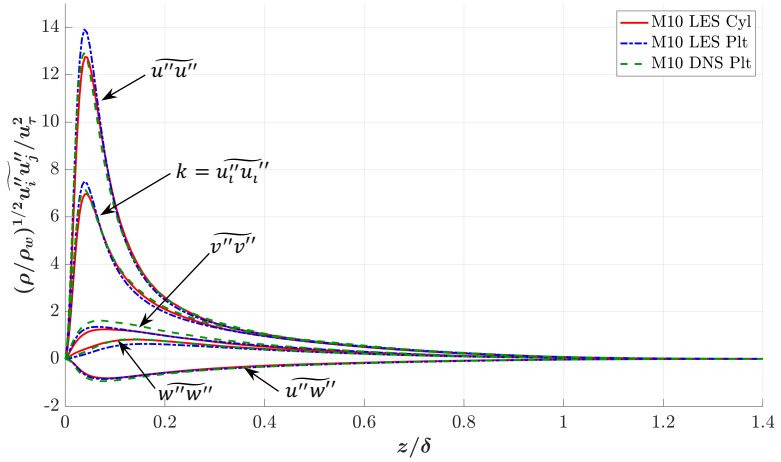


Figure 3.9. Turbulent stresses and TKE, Morkovin scaled.

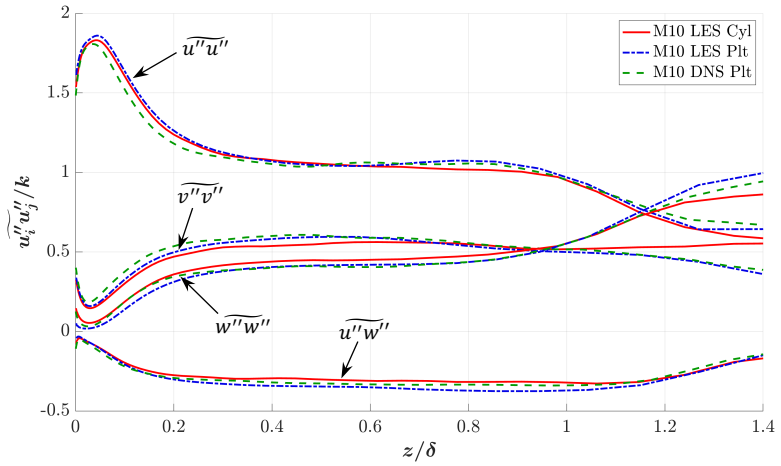


Figure 3.10. Turbulent stresses, scaled by TKE.

When scaled by TKE, Figure 3.10 shows that, following the near-wall magnitude peaks, the turbulent stresses are essentially uniform in the range $z/\delta \approx [0.25,0.95]$. The comparisons with the flat plate DNS are excellent. The relatively larger discrepancy for $z/\delta > 1.2$ is due to the stresses in the numerator and TKE in the denominator both approaching very small values in this region (as observed in Figure 3.9). Table 3.5 shows the values of the turbulent stresses in the present test case in two regions: (i) the near-wall viscous region where peak turbulence production occurs at $z/\delta \approx 0.05$ (or $z^* \approx 13$), and (ii) the mean value in the uniform region which falls in the log-law and outer layers. The values are benchmarked against the archival DNS of fully developed channel flow of Kim et al. 1987. The statistics compare remarkably well, especially in the uniform region.

Table 3.5. Turbulence Stresses in Two Regions and comparisons with Archival DNS

$\widetilde{u_i''u_j''}/k$	Near-Wall Region at Peak Production		Uniform Region in Outer Layer	
	Present Study	DNS of Kim et al. (1987)	Present Study	DNS of Kim et al. (1987)
$\widetilde{u''^2}/k$	1.82	1.70	1.03	1.02
$\widetilde{v''^2}/k$	0.15	0.26	0.58	0.59
$\widetilde{w''^2}/k$	0.03	0.04	0.39	0.39
$\widetilde{u''w''}/k$	-0.08	-0.12	-0.32	-0.29

Figure 3.11 shows RMS profiles of turbulent temperature, pressure and density, normalized by freestream values. Temperature fluctuations peak close to the wall where the turbulence production peaks in the buffer layer, then decrease to the freestream value. Density fluctuations decrease to a minimum of ~1.3% of ρ_∞ close to the wall and rises to a maximum of ~23% of ρ_∞ in the outer layer. Unlike incompressible flows, density fluctuations are nonzero in compressible flows and

play a role in turbulent mass transport, as will be demonstrated in later Chapters. Pressure fluctuations are a maximum at the wall reaching ~17% of p_∞, then gradually decreases to the freestream value. A common assumption in compressible boundary layers is that normalized pressure fluctuations are negligible relative to normalized density fluctuations leading to Morkovin's 1962 similarity hypotheses [67]. This may be a good approximation in supersonic flows, but not necessarily in hypersonic flows. Pressure fluctuations in the present case are generally on the same order of magnitude as density fluctuations, particularly so in the inner boundary layer. Pressure fluctuations in high speed flows have a strong dynamic influence on the transport of TKE and the Reynolds stresses through the covariances of the pressure fluctuations with strain rate fluctuations and velocity fluctuations, particularly in the near-wall viscous region. Note that the comparisons with the DNS flat plate are generally very good with some small differences in the temperature and density profiles.

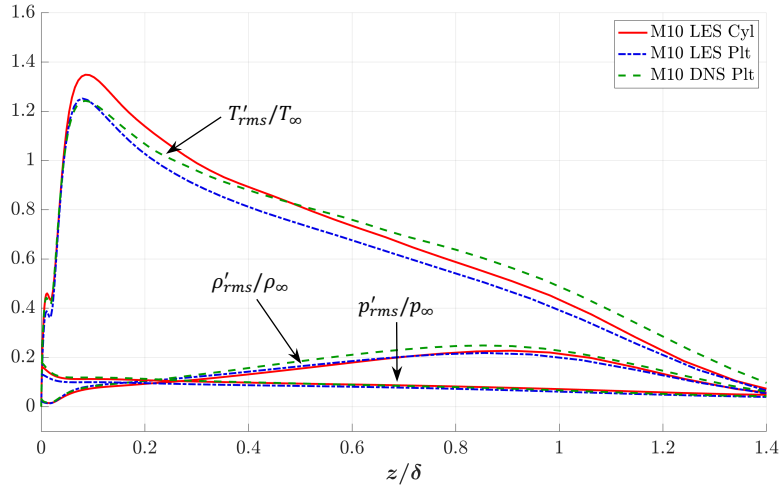


Figure 3.11. Turbulent temperature, density and pressure, scaled by freestream values.

Chapter 4: HCF Mean Flow Analysis

4.1 Qualitative Flowfield Description

Before analyzing the mean flow, the general features of the interaction are discussed using instantaneous flowfield solutions. Figure 4.1 and Figure 4.2 show 3D instantaneous flowfields of the cylinder-flare configuration. Figure 4.1 shows an isosurface of modified density gradient, $\nabla\rho_{mod} = 0.7$, where $\nabla\rho_{mod} = 0.8exp\,(-\nabla\rho/30)$, colored by contours of streamwise u-velocity (u/U_∞). Figure 4.2 shows streamwise u-velocity on a plane just above the wall and density gradient $\nabla\rho_{mod}$ on a longitudinal plane. The conical shock front downstream of the corner is clearly distinct. At the corner, the low-speed u-velocity (blue) contours highlight the region of separation. Large-scale turbulence eddies in the incoming boundary layer appear as $\mathcal{O}(\delta)$ bulges in the isosurface. The spatial scales of turbulence become larger above the separation region at the corner. Further downstream the bulges become distorted and leave an imprint of ripples on the shock sheet.

Figure 4.3 shows instantaneous density gradient (numerical Schlieren) on a streamwise xz-plane along with some general features of the shock-boundary layer interaction (SBLI). The ramp generates a strong oblique shock wave which induces an adverse pressure gradient that separates the flow at the corner. Low speed recirculating flow forms a separation bubble at the corner. Near the incipient separation point, the bubble induces a compression shock (referred to as the separation shock) that appears to be diffused and mostly embedded in the turbulent boundary layer. The separation shock coalesces with the foot of the main shock on the flare just downstream of reattachment. A shear layer forms across the separation bubble stemming from incipient separation to the foot of the main shock and is somewhat visible in Figure 4.3. Just downstream of the

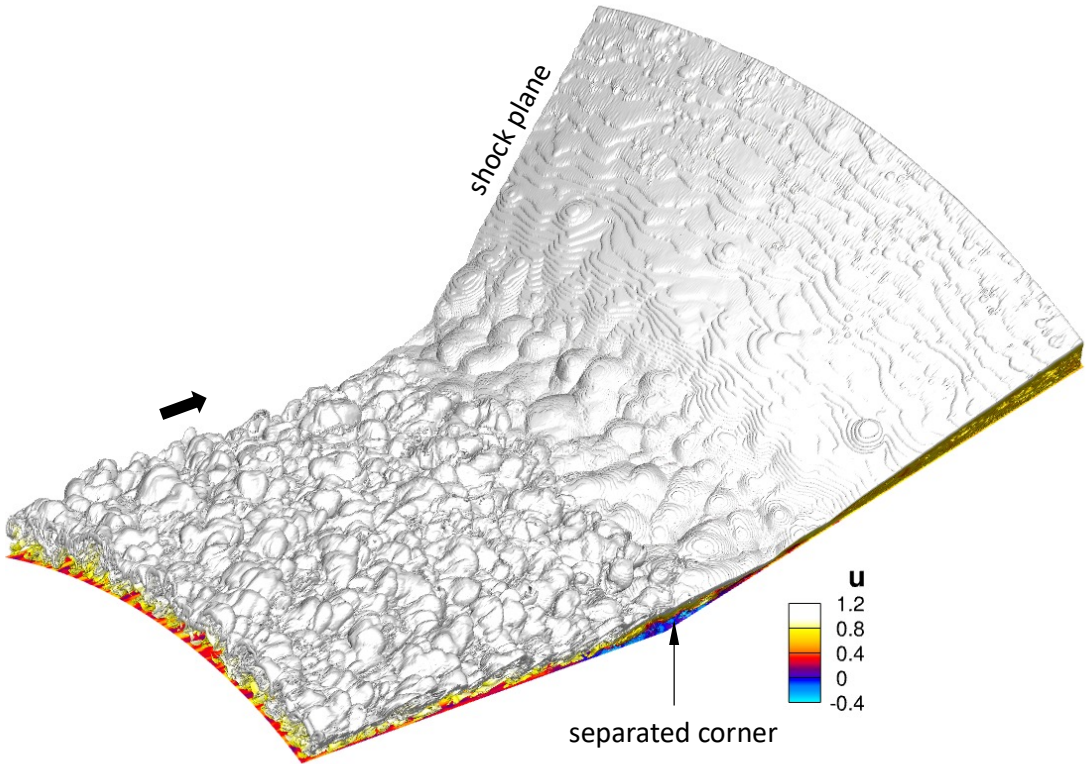


Figure 4.1. Isosurface of modified density gradient, $|\nabla\rho|_{mod}$, colored by u-velocity.

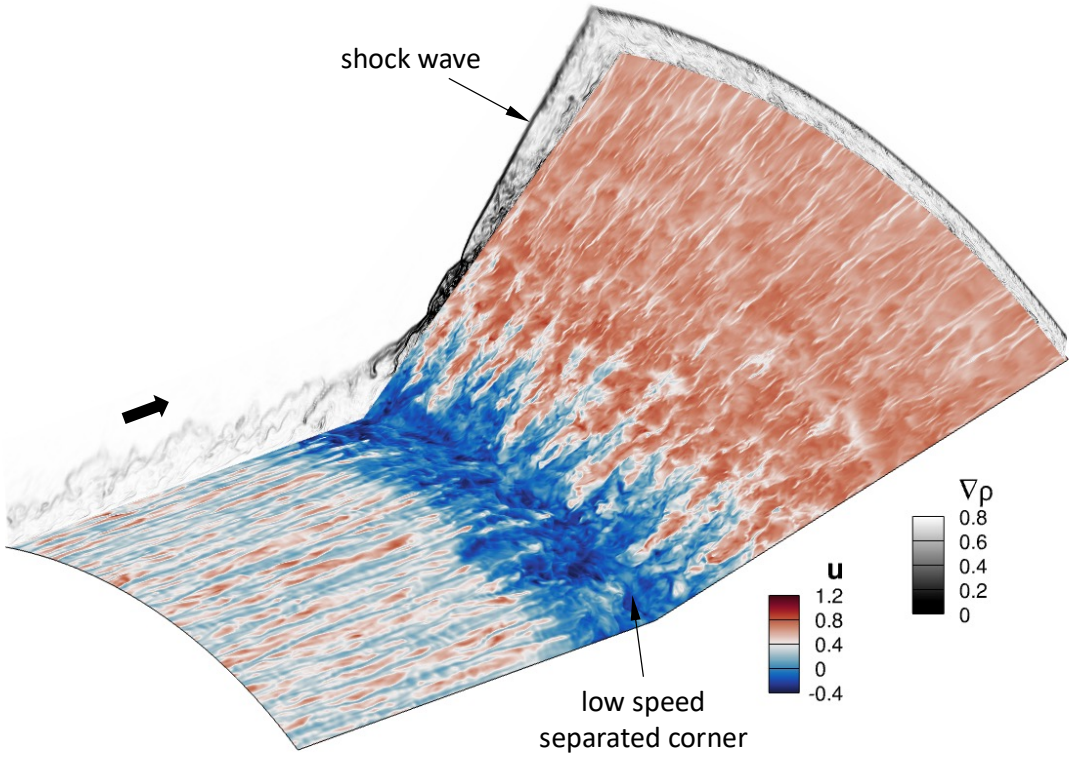


Figure 4.2. Streamwise u-velocity just above wall with planes density gradient $|\nabla\rho|_{mod}$.

reattachment point near the foot of the main shock the boundary layer is highly compressed. Here the turbulence structures become distorted. The effect leaves a ripple in the main shock (as observed in Figure 4.1). There is also a large spike in pressure and heat transfer in this region as will be shown in later Figures. These effects continue for some distance past the main shock, then relaxes further downstream.

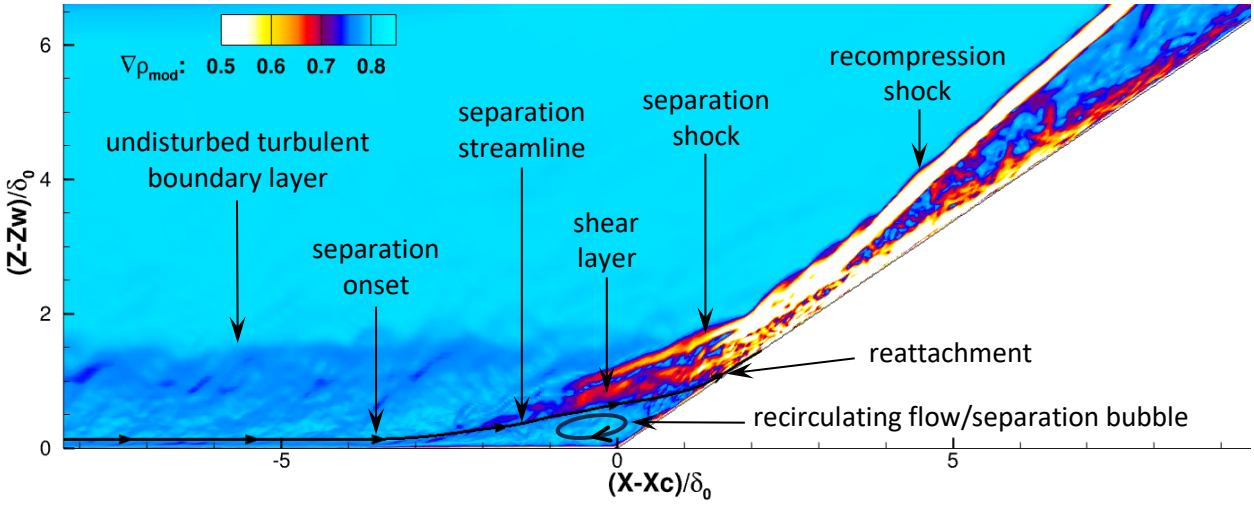


Figure 4.3. Instantaneous density gradient on streamwise plane and SBLI general features.

4.2 Mean Flowfield

All mean LES generated profiles are time-averaged over $\sim 1200\delta_0/U_\infty$, or 15ms, which approximately represents ~48 flowtimes through the domain. Using scales relevant to the interaction, this corresponds to $\sim 350 L_{sep}/U_\infty$, where L_{sep} and L_{sep}/U_∞ are the length scale and timescale, respectively, representative of the low-frequency separation dynamics, U_∞ is the freestream velocity, $L_{sep} = 3.34\delta_0$ is the mean distance from the compression corner ($x/\delta_0 = 0$) to the upstream separation point, and δ_0 is the incoming reference boundary layer thickness. Also, all mean profiles are span-averaged unless otherwise noted. Except for density and pressure, all mean profiles are represented using Favre-averaged variables.

Figure 4.4 shows mean streamwise contours with the mean separation streamline that demarcates the separation bubble. Figure 4.5 shows mean wall-normal profiles extracted at the locations indicated in Figure 4.6. Figure 4.6 also shows contours of the mean density gradient, which shares the same interaction features as that in Figure 4.3. The wall-normal profiles are plotted against normal distance z_n from the wall. The top row are profiles upstream of the corner, and the bottom row are profiles downstream of the corner. Included are the profiles at the mean separation point $x_{sep} = 3.34\delta_0$ and the mean reattachment point $x_{rea} = 0.83\delta_0$. The u and w velocities in Figure 4.5 have been rotated so that u is parallel to the wall and w is normal to the wall.

In the upstream undisturbed flow at $x/\delta_0 = -6.0$, the profiles are characteristic of an equilibrium turbulent boundary layer. The streamwise velocity in the upstream undisturbed boundary layer increases monotonically from the wall to the freestream. As the flow approaches the separated corner, an inflection point forms in the streamwise velocity profile. Past the separation point and within the separation bubble, flow reversal is evidenced by the negative streamwise velocity and its local negative maximum near the wall. Between separation and just before reattachment, a single inflection point in the streamwise velocity is observed. This inflection point is due to the shear layer that forms between the low-speed separation bubble and high-speed fluid above it. This separation shear layer is more visible in Figure 4.3. The inflection in the separation shear layer and its associated increase in vorticity (not shown) and turbulent kinetic energy (not shown) is typically associated with a Kelvin-Helmholtz type of instability in which the shear layer rolls up and generates vortical structures that convect downstream across the separation bubble. In the downstream flow past the corner, the streamwise velocity in the now thinner boundary layer attempts to relax back to an equilibrium state. However away from the wall

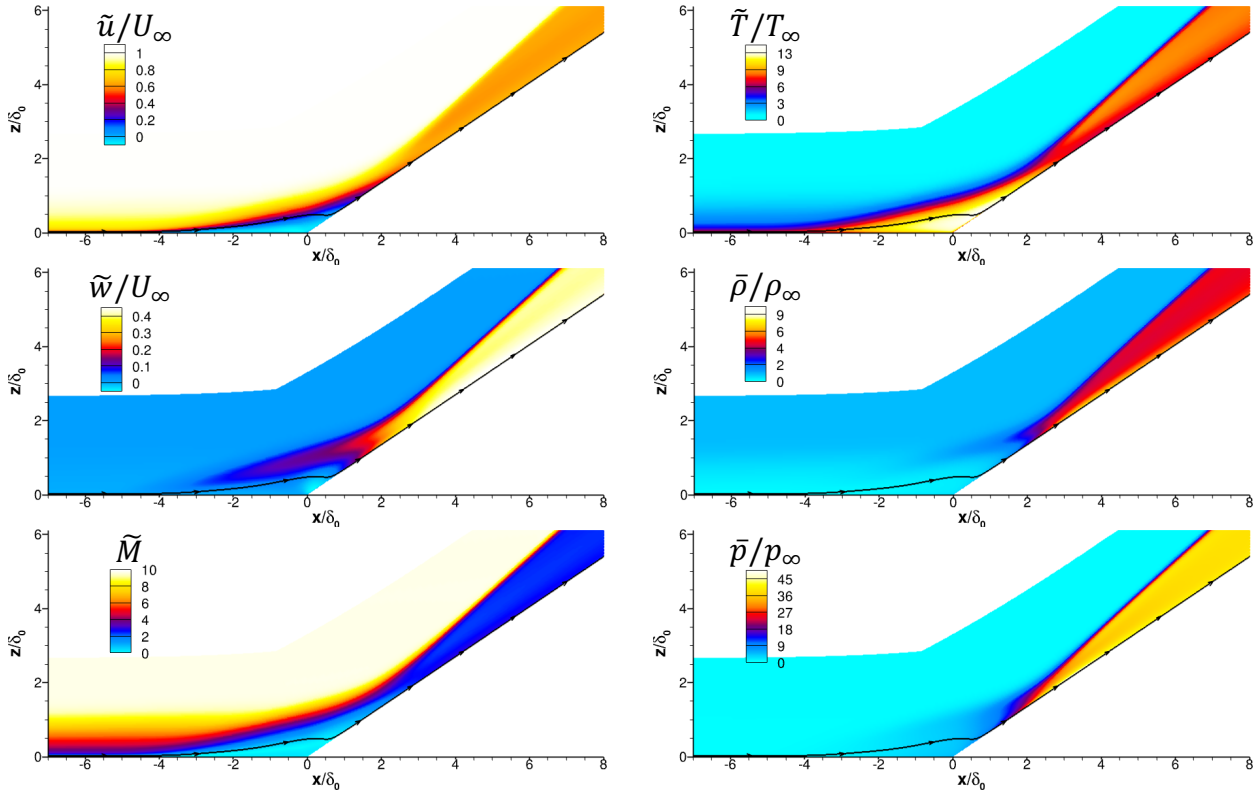


Figure 4.4. Favre-averaged flowfields, normalized by freestream values except for $\widetilde{M}$.

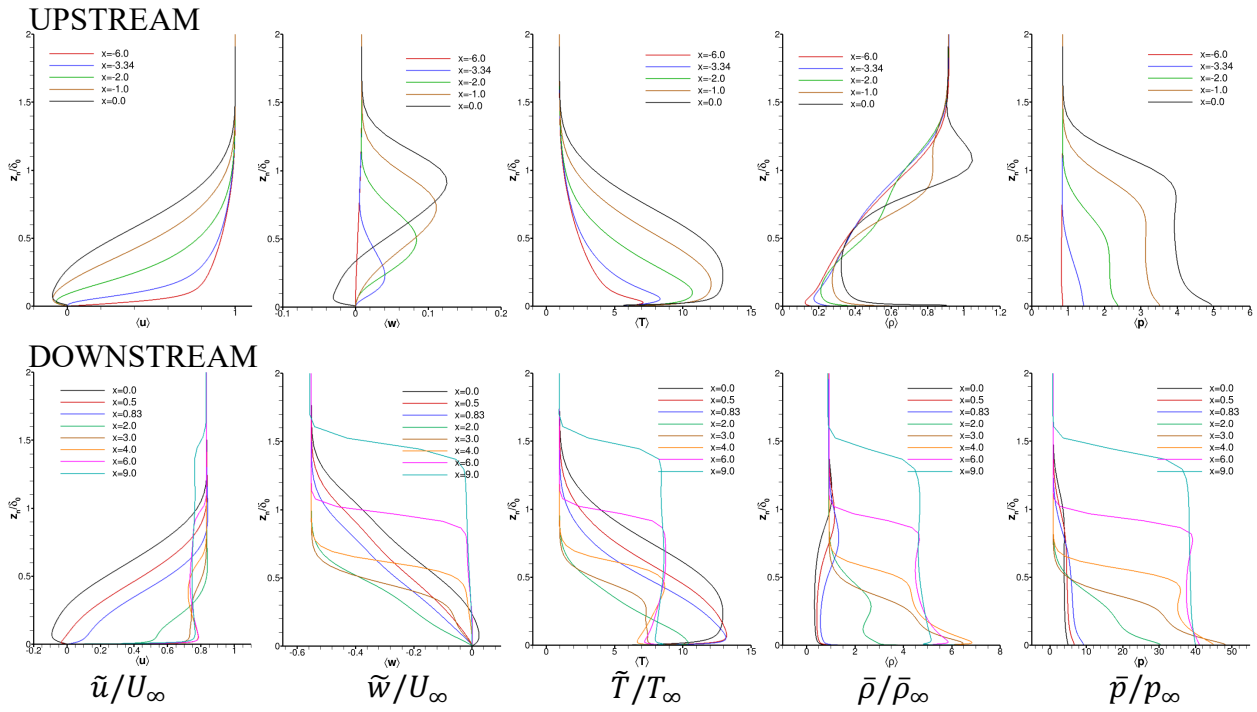


Figure 4.5. Favre-averaged wall-normal profiles, upstream (top row) and downstream (bottom row) of corner ($x/\delta_0 = 0$), normalized by freestream values.

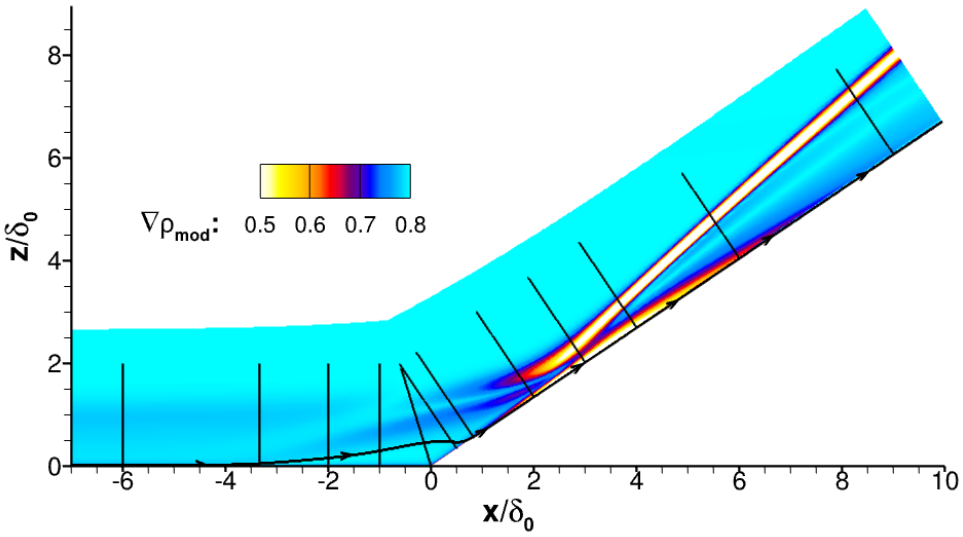


Figure 4.6. Locations of wall normal data extractions plotted in Figure 4.5. Contours are mean density gradient.

the flow must equilibrate with the shock jump conditions producing multiple inflection points in all variables in the post-shock flow. The shock jump, for example, can be observed at $x = 9.0\delta_0$ where the streamwise velocity profile drops from 1 to $\tilde{u}/U_\infty \approx 0.65$ in a small finite distance across the shock wave in the vicinity of $z_n \approx 1.4\delta_0$. For comparison the inviscid shock jump for a 34° inviscid cone is $\tilde{u}/U_\infty \approx 0.78$. As would be expected viscous effects and flow distortion due to separation will cause the present case to differ from that of the equivalent inviscid case. Close to the reattachment point, there is no such clear shock jump because the shock is close to the wall and embedded in a complex interaction with the boundary layer and separation shock wave emanating from the incipient separation point (these features are more visible in Figure 4.3). The wall-normal velocity indicates that the mean flow direction is away from the wall ($\tilde{v}/U_\infty > 0$) in the recirculating bubble with an increasing maximum up until the corner. Downstream of the corner, the mean flow direction is towards the wall ($\tilde{w}/U_\infty < 0$). At the furthest downstream stations, the flow becomes more parallel to the wall and the wall-normal velocity decreases significantly near the wall relative to the wall-parallel velocity.

The peak temperature near the wall increases through the bubble from ~7 times the freestream value prior to separation to ~13 times the freestream value near reattachment. The contour plot shows that the maximum temperature occurs just before reattachment in the recirculating low speed fluid in the temperature bubble. The large wall normal temperature gradient near the wall is expected to produce significant heat flux to the wall according to Fourier heat conduction law as will be observed later in Figures. Density has a minimum point in the boundary layer close to the wall upstream of separation. The minimum density point increases through the separation bubble where low speed fluid exists, then increases significantly past reattachment reaching ~7 times the freestream value close to the wall at $x = 4.0\delta_0$. Pressure is constant through the upstream undisturbed boundary layer, then increases through the low speed fluid in the separation bubble reaching ~48 times the freestream value close to the wall at $x = 3.0\delta_0$. Note that while the maximum wall temperature occurs near reattachment, the maximum density and pressure occurs further downstream in the range $x = 3\text{-}4\delta_0$. The shock jump at the downstream station at $x = 9.0\delta_0$ incurs $\tilde{T}/T_\infty \approx 7.5$, $\tilde{\rho}/\rho_\infty \approx 5.0$ and $\tilde{p}/P_\infty \approx 40$ at $z_n \approx 1.4\delta_0$, which is comparable to inviscid theory for conical shocks that predicts $\tilde{T}/T_\infty \approx 7.8$, $\tilde{\rho}/\rho_\infty \approx 5.3$ and $\tilde{p}/P_\infty \approx 44$.

4.3 Mean Wall Profiles: Skin Friction, Pressure and Heat Flux

Figure 4.7 (left) shows normalized pressure (p/p_∞), normalized heat flux (Stanton number, St) and normalized shear stress (skin friction, C_f) along the wall. The blue lines are span-averaged instantaneous profiles, and the solid red line is the time-average of the instantaneous profiles. For reference, the LES results of a Mach 10 34° compression ramp [21] and wind tunnel results of a Mach 10 35° cylinder-flare [69] are plotted. Table 4.1 shows the flow conditions of the comparison datasets. Note that the run conditions of the comparison datasets are not exactly the same as the

present test case, so some differences in the results of the comparison datasets are expected. Figure 4.7 (right) shows 3D instantaneous pressure (p), heat flux (q) and x-shear stress (τ_x) on the wall in dimensional SI units as a qualitative reference.

Table 4.1. Mach 10 STBLI Comparison Datasets.

Case*	M_∞	U_∞ (m/s)	ρ_∞ (kg/m^3)	T_∞ (K)	T_w (K)	$\frac{T_w}{T_r}$	δ (mm)	Re_x	Re_δ	Re_{δ^*}	Re_θ	Re_τ	Re^*
34° Flare LES (Present Case)	9.60	1410.8	0.0326	53.8	300	0.32	20.9	1.22e+7	2.54e+5	1.59e+5	7697	431	4830
34° Ramp LES Helm & Martín 2021 [21]	9.19	1410.7	0.0400	58.5	300	0.33	19.7	1.37e+7	2.70e+5	1.55e+5	8276	520	5121
34° Flare WT Coleman 1973 [69]	9.22	1439	0.1482	64.5	295	0.28	4.58	4.70e+7	2.15e+5	1.07e+5	4841	390	3245

The incoming undisturbed turbulent boundary layer shows no large scale unsteadiness in the mean plots of pressure, heat flux and skin friction. The mean wall pressure initially increases gradually following separation, then rises precipitously near reattachment reaching its mean maximum of ~54 times the freestream value at $x \approx 3.5\delta_0$, then gradually relaxes downstream to the inviscid shock solution. At the furthest downstream location, the pressure ratio across the shock is $p_2/p_{_\infty} \approx 43$, which is comparable to $p_2/p_\infty \approx 41.3$ from inviscid shock theory for conical flow. The instantaneous wall pressure profiles reveal the unsteadiness of the separation dynamics. The peak pressure fluctuates by about 15% from the mean peak occurring downstream of the reattachment point. The LES 34° ramp agrees very closely with the flare. The wind tunnel 35° flare shows a more precipitous pressure rise, peaking at the same value as that of the present case, and then relaxing downstream at slightly lower pressure.

The wall heat flux in non-dimensional form, viz, the Stanton number, is defined as $St = q_w/\left[r_e U_e C_p (T_w - T_r)\right]$. The mean Stanton number shows a small decrease below the

upstream value near the separation point, then rises through the separated region and precipitously so after the corner, reaching a mean peak value of ~20 times the upstream value. The small sharp blips at $x/\delta_0 = 0$ are likely due to grid discontinuity at the sharp corner where the wall normal vector, and therefore wall normal temperature gradient, would be undefined and generate a singularity in the calculations. The instantaneous Stanton number profiles show significant fluctuation, ~ 40%, about the mean peak at $x \approx 3.0\delta_0$. The LES 34° ramp agrees closely with the flare, with the largest difference being ~7% at the mean peak. The heat flux of the wind tunnel 35° flare tracks with the present case up to the peak heat flux, but the downstream relaxation is more gradual with higher heat flux in the wind tunnel case.

The separation and reattachments points are indicated by the first and last sign reversals of skin friction, respectively. The mean separation and reattachment points are located at $x_{sep} \approx -3.34\delta_0$ and $x_{rea} \approx 0.83\delta_0$, respectively, as noted in previous Figures. The mean skin friction is negative in the separated region, then increases sharply to ~12 times its upstream value at $x \approx 3.5\delta_0$, followed by a gradual relaxation downstream. At the peak following reattachment, there is a 25% fluctuation from the mean. The instantaneous skin friction profiles highlights the unsteadiness of the separation bubble. Between the mean separation and reattachment locations, the oscillation in skin friction indicates that the separation bubble periodically grows and shrinks. The fact that the skin friction oscillates between positive and negative in this region further indicates that flow reattachment may occur in regions within the bubble thus bifurcating the bubble. The small sharp blips at $x/\delta_0 = 0$ are due to the aforementioned singularity in the calculations generated by the grid corner discontinuity. The LES 34° ramp tracks closely with the present case through separation and reattachment and in the downstream region. However, the mean peak of the flare is ~20% higher than that of the ramp.

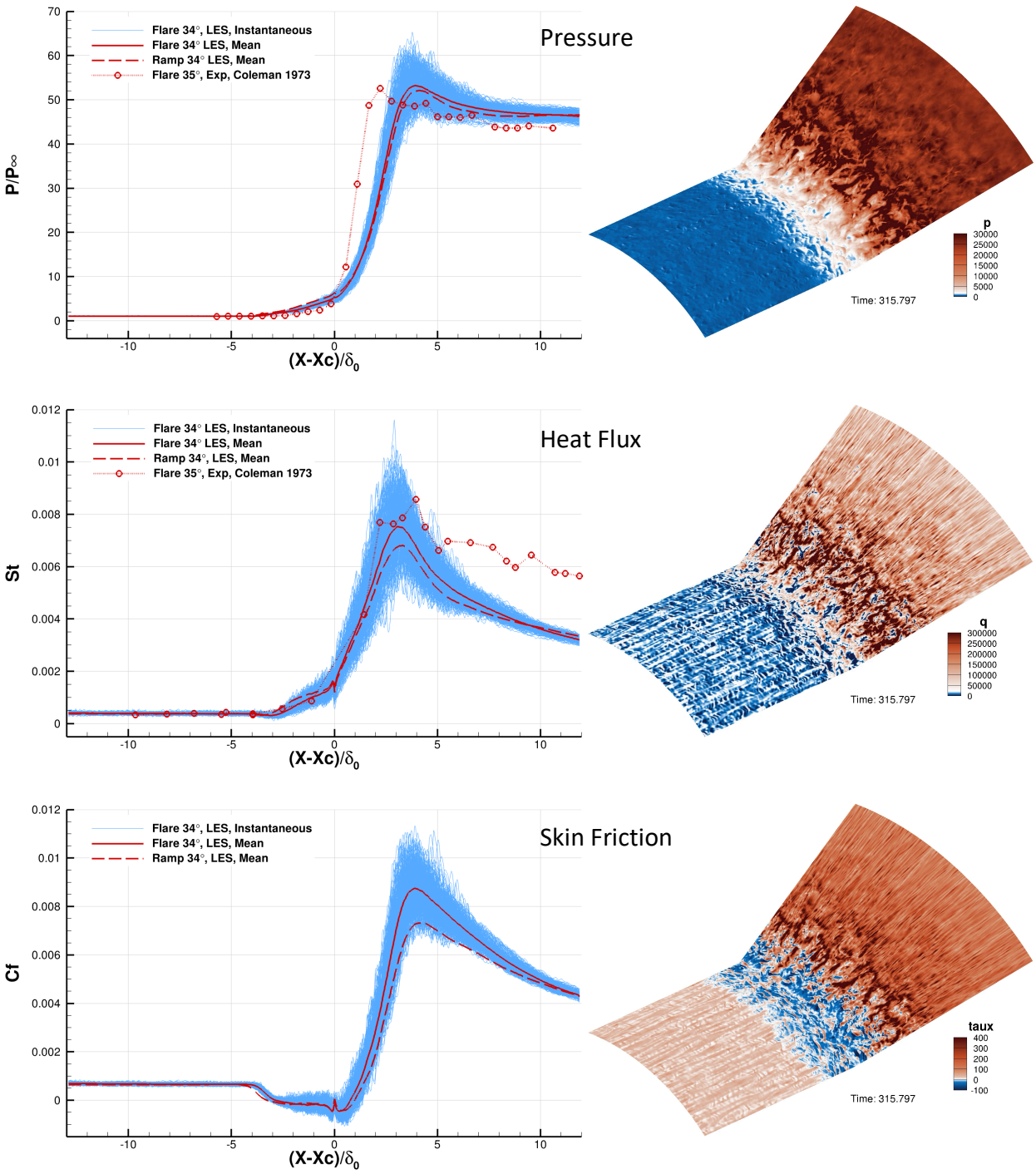


Figure 4.7. Wall pressure, heat flux and shear stress. Left line plots are span-averaged and normalized. Right 3D contour plots are instantaneous snapshots in dimensional SI units.

The large spikes in pressure, heat flux and skin friction are due to the strong boundary layer compression near the foot of the main shock. The shockwave by nature incurs an increase in density and temperature across the shock. Since the mass flux through the boundary layer must be

conserved, the boundary layer is forced to be thinner in this region. From simplified dimensional analysis of hypersonic compressible boundary layers, one finds $q_w \propto dT/dn \sim \mathcal{O}(T_e/\delta)$, where n is the wall-normal vector. Therefore, a thinner boundary layer and higher temperature in the post-shock region will incur higher heat transfer for conserved mass flux. This is the case for compression by both flares and planar ramps.

In the case of the flare, however, versus a planar ramp with the same deflection angle and upstream flow conditions, the spanwise curvature induces azimuthal flow expansion and a shockwave that is conical such that it spreads the compression over a larger area weakening the shock as it moves outward. The result is generally a more gradual increase in pressure and temperature through the corner, as well as lower peak pressure and temperature. Consequently, the heat transfer on the flare is generally lower.

The differences in the datasets in the left of Figure 4.7 however are more likely due to differences in flow conditions. Note that the Coleman wind tunnel flare experiments had lower Reynolds number (for instance 37% lower Re_θ) than the present test case. A lower Reynolds number generally incurs greater energy dissipation due to stronger viscous effects, resulting in higher temperature and heating as observed in the post-shock region in the middle left plot of Figure 4.7. On the hand, the LES 34° ramp had a slightly higher Reynolds number (for instance 7.5% higher Re_θ) than the HCF, implying slightly lower energy dissipation due to viscous effects and therefore slightly lower temperature, heating and skin friction as observed in Figure 4.7. The preceding discussion of course does not take into account computational and experimental errors. While Coleman did not explicitly report measurement errors, typical experiment errors for hypersonic flows with shock-induced separation can range from ~5-20% and ~10-30% for wall pressure and wall heat flux respectively.

4.4 Chapter Summary

The instantaneous and mean LES flowfields were analyzed. Qualitative plots revealed both salient and subtle features of the interaction, such as the incipient separation shock, the separated recirculating flow, the structure and eventual distortion of the turbulence eddies, their ripple effects on the shock sheet, and the compression of the flow through the reattachment point and further downstream. Mean 2D contours and wall-normal 1D profiles describe the flow structure changes through the interaction. The adverse pressure gradient of the shock wave separates the flow, marked by flow reversal in the separation bubble and inflection points in the separation shear layer. Temperature, pressure and density increase significantly through the separated corner and in the downstream post-shock region. The temperature reaches a maximum in vicinity of reattachment, while density and pressure reach a maximum a short distance downstream of reattachment due to strong flow compression. The downstream post-shock flow approaches the inviscid conical shock jump solution as the flow relaxes. Streamwise wall profiles of pressure, heat flux and skin friction show significant spikes near reattachment followed by gradual downstream relaxation to somewhat steady but much higher values than the incoming flow. The instantaneous wall profiles further revealed the unsteadiness of the interaction with significant fluctuations about the mean peaks. The fluctuation of skin friction between positive and negative values in the separation bubble are indicative of the breathing motion (contraction and dilation), and possible bifurcation, of the separation bubble.

Chapter 5: HCF Low Frequency Dynamics and the Centrifugal Instability

5.1 Introduction

Shock-turbulent boundary layer interactions (STBLI) are characteristically unsteady across a broad range of frequencies. Turbulence is associated with the broadband high-frequency end of the spectrum. A range of phenomena associated with the interaction typically occurs in narrow low-frequency ranges that is distinct from the incoming turbulence which has characteristic frequency of $f\delta_0/U_\infty \approx \mathcal{O}(1)$, where f is frequency, δ_0 is the incoming boundary layer thickness and U_∞ is the freestream velocity. In separated compression corner flows, studies have identified a low-frequency event that dominates the energy in the separated corner [34]-[39]. The low-frequency dynamics are characterized by strong adverse pressure gradients, flow separation, shock oscillation, centrifugal instabilities, and high wall pressure, shear stress and heating. This low-frequency event consists of pulsations of the separation bubble that are statistically linked to the separation shear layer flapping and shock oscillation. The characteristic frequency of this event is typically in the range $fL_{sep}/U_\infty \approx 0.02 - 0.1$ (Priebe et al. 2016 [35], Dussauge et al. 2006 [29]), where L_{sep} is the interaction length.

The driving mechanism of the dominant low-frequency event in high-speed separated compression corners has been a topic of research and debate for many decades. Some studies correlated the shock oscillation with the incoming boundary layer turbulence, suggesting that the low-frequency dynamics are driven by upstream influences, e.g., Humble et al. 2009 [30], Ganapathisubramani et al. 2007/2009 [31]-[32] and Beresh et al. 2002 [33]. Other studies have correlated the shock oscillation with the breathing (i.e., contraction and dilation) of the corner

separation bubble, e.g., Priebe & Martín 2012 [34], Wu & Martín 2008 [70], Dupont et al. 2006 [71], Thomas et al. 1994 [72] and Erengil & Dolling 1991 [73]. However, correlation of the shock and separation bubble motions do not explain the driving mechanism. Pirozzoli & Grasso 2006 [27] suggested that for a reflected shock case, the vortical structures generated in the unstable shear layer (between the separation bubble and freestream) interact with the shock wave forming a low-frequency feedback loop. Piponniau et al. 2009 [74] suggested the shear layer entrains fluid from the separation bubble resulting in the breathing motion of the bubble and that the entrainment occurs on a timescale that agrees with the shock oscillation. The latter two studies imply that the low-frequency dynamics are driven by downstream influences intrinsic to the interaction. However, the characteristic frequency of shear layer vortex dynamics is $fL_{sep}/U_\infty \approx 0.5$ (Helm et al. 2021 [75], Dupont et al. 2006 [71]), and is somewhat spectrally distinct from the aforementioned dominant low-frequency event observed in the range $fL_{sep}/U_\infty \approx 0.02 - 0.1$.

Another proposed instability mechanism is that due to large-scale streamwise-oriented vortical structures. Priebe & Martín 2012 [34] used the time-resolved evolution of DNS fields of a Mach 3 24º turbulent compression ramp to show that the unstable shock oscillation is associated with a particular flow structure change in the separated flow and shear layer. The structural change was consistent with the characteristics of an inviscid instability such that the mean velocity profile exhibits inflection points with the associated vorticity maxima. Priebe, Tu, Martín & Rowley 2016 [35] applied dynamic mode decomposition (DMD) to the DNS fields of the same Mach 3 24º compression ramp and identified the most energetic DMD modes in the characteristic range of the low-frequency shock motion. Reconstructing the flow field using a combination of the dominant low-frequency DMD modes, the data showed an inviscid instability, manifested as a pair of counter rotating vortices, generated near separation and developing downstream. Priebe et al. 2016

[35] also showed that low-pass filtering of the flowfield produced the same flow structure as the reconstructed DMD modes. Helm & Martín 2017 [36], and Martín, Helm & Gonzalez-Kosasky 2017 [37] visualized the inviscid instability using filtered streamwise momentum resolved in three-dimensional space and time for a Mach 7 turbulent boundary layer over a 33º compression corner and showed that the instability is an inviscid centrifugal one that may be related to the Görtler instability (Görtler 1941 [40,41]). In addition, the instability was imprinted in the skin-friction and wall-heat-transfer striations across the span. Trichilo, Helm & Martín 2019 [38] visualized vortical structures in the crosstream velocity vector fields with corresponding spanwise variation in turbulent momentum in the interaction region of compression ramps at Mach 3, 7 & 10. While both upstream and downstream forcing may be present, these studies provide reasonable evidence that the dominant low-frequency event may be predominantly driven by a global instability intrinsic to the downstream separated flow (Martín, Priebe & Helm 2016 [39]).

The streamwise centrifugal instability has also been identified in several other compression corner SBLI studies, including the Mach 7.7 laminar DNS of Cao et al. 2019 [76], Mach 7.7 laminar experiment of Roghelia et al. 2017 [77], Mach 3-5 turbulent experiments of Schülein & Trofimov 2011 [78], Mach 11.3 laminar DNS of Brown et al. 2009 [79], Mach 2.95 LES of Loginov et. al 2006 [28], Mach 6.85 laminar DNS of Navarro-Martínez & Tutty 2005 [80] and the Mach 2.85 turbulent experiments of Settles et al. 1979 [81]. Note the 'laminar' characterization of the aforementioned studies refer to the inflow boundary layer, however in some of these studies the flow may have been transitional in the downstream region. Studies of the low-frequency centrifugal instability in hypersonic turbulent compression corners are scarce.

In this work, the low frequency dynamics and particularly the centrifugal instability are investigated in the compression corner of the Mach 10 axisymmetric hollow cylinder-flare (HCF)

using Wall-Resolved Large Eddy Simulations (WRLES). A high-energy low-frequency event that is two orders of magnitude lower than the frequency of the incoming turbulence is identified in the span-averaged separation point and wall pressure signals. The low frequency event is then isolated via lowpass filtering of time-accurate 3D flow solutions. The centrifugal instabilities are visualized and analyzed using a combination of topological and eigenvalue-based vortex ID methods which captures their size, strength, speed direction of rotation and streamwise extent across the separated region. Using temporal correlations, this study is the first the demonstrate a strong statistical link between the strength and speed of the centrifugal instabilities and the periodicity of the breathing motion of the separation bubble.

5.2 Flowfield Processing

Unless otherwise noted, all mean LES data are time-averaged over $\sim 1200\delta_0/U_e$ or 15ms, which approximately represents ~48 flowtimes through the domain. Using scales relevant to the interaction, this corresponds to $\sim 350 L_{sep}/U_e$, where L_{sep} and L_{sep}/U_e are the length scale and timescale, respectively, representative of the low-frequency separation dynamics, U_e is the boundary layer edge velocity and L_{sep} is the distance from the compression corner ($x/\delta_0 = 0$) to the mean upstream separation point.

Several cross-stream planes in the separated corner region were selected for the forthcoming analyses. Their axial locations are shown in Figure 5.1 and Table 5.1. The numbering of the planes, e.g., *i*200, is a custom nomenclature and not necessarily related to the grid index location.

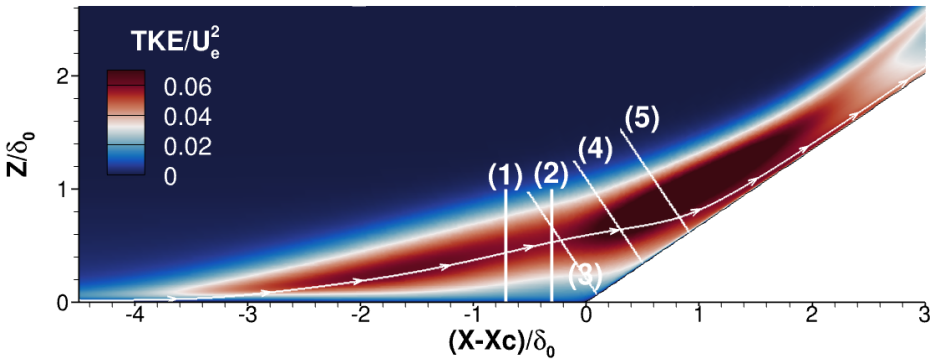


Figure 5.1. Wall normal extraction locations. Contours are mean turbulent kinetic energy.

Table 5.1. Location Data for Selected Cross-Stream Planes.

Label #	(1) *i*200	(2) *i*220	(3) *i*240	(4) *i*260	(5) *i*280
$(\boldsymbol{x - x_c})/\boldsymbol{\delta_0}$	-0.717	-0.309	0.098	0.505	0.915
$(\boldsymbol{x - x_c})/\boldsymbol{L_{sep}}$	-0.215	0.0925	0.0293	0.151	0.274

5.3 Low-Frequency Dynamics

5.3.1 Power Spectra and Lowpass Filtering

Figure 5.2 shows the separation and reattachment point signals (red lines) sampled at a frequency of $f_S = 130U_e/L_{sep}$. Figure 5.3 shows the power spectral density (S) of the signals. The PSD was computed using the Welch method [82] in which the PSD is computed for 8 time segments with 50% segment overlap and averaged together using a Hamming window function. The PSD is normalized such that the integral sum of the spectrum over the normalized frequency range equals one. Additionally, the PSD was smoothed using a bin sampling width of 0.06 on the frequency log scale.

The high frequency end of the spectra for $f > 1.0U_e/L_{sep}$ are broadband in nature and represents the turbulence regime. The low frequency end of the separation point spectrum shows a clear dominant frequency at $f \approx 0.078U_e/L_{sep}$, which corresponds to a characteristic period of

$t = 12.5L_{sep}/U_e$. This dominant low-frequency is associated with the unsteady growing and shrinking of the separation bubble. The time period over which the signals were tracked therefore represents ~17.6 of these low-frequency cycles (LFC).

To isolate the low frequency component, a finite impulse response (FIR) lowpass filter (LPF) was applied to the signals. The FIR filter uses a least-squares approximation to compute filter coefficients and then smooths the impulse response with a Hamming window. The LPF employed a cutoff frequency of $f_{cut} = 0.1U_e/L_{sep}$ at a gain of -6dB and a filter window halfwidth of 100 samples or $0.75L_{sep}/U_e$. The filter coefficients and magnitude response are shown in Figure 5.4. The LPF removes the high frequency turbulence spectrum and isolates the observed dominant low frequency event. In Figure 5.2 the lowpassed filtered signals (blue lines) are superimposed on the high frequency signals. In Figure 5.3, the PSD of the lowpassed filtered signals (blue lines) are plotted to confirm the isolation of the low frequency event.

To strengthen the statistics, data was also collected in spanwise bins of $2\delta_0$ for a total of 5 non-overlapping bins. Figure 5.5 shows the separation point signals in each of the 5 bins along with the lowpass filtered signals. Figure 5.6 shows the PSD of the separation point signals in each bin along with the lowpass filtered PSD. As before, the PSD plots were smoothed using a bin sampling width of 0.06 on the frequency log scale. Each bin shows a dominant low frequency similar to the full-span averaged spectra in Figure 5.3. Bins 1-3 show a single distinct peak, while bins 4-5 show two secondary peaks in the vicinity of the main peak. The mean of the peak frequencies across the 5 bins is $f \approx 0.070U_e/L_{sep}$. The mean of the peak frequencies across the 5 bins and the full-span peak frequency is $f \approx 0.074U_e/L_{sep}$.

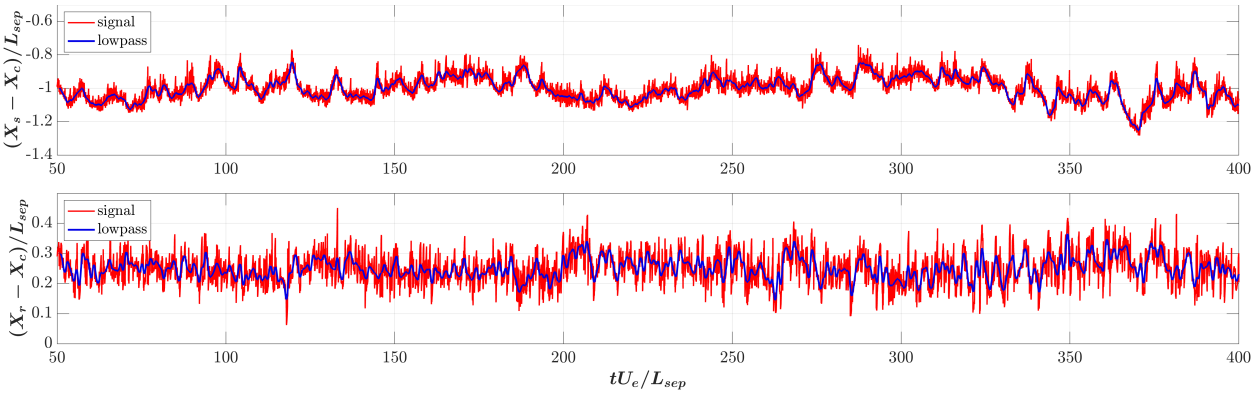


Figure 5.2. Span-averaged separation point (top) and reattachment point (bottom) signals.

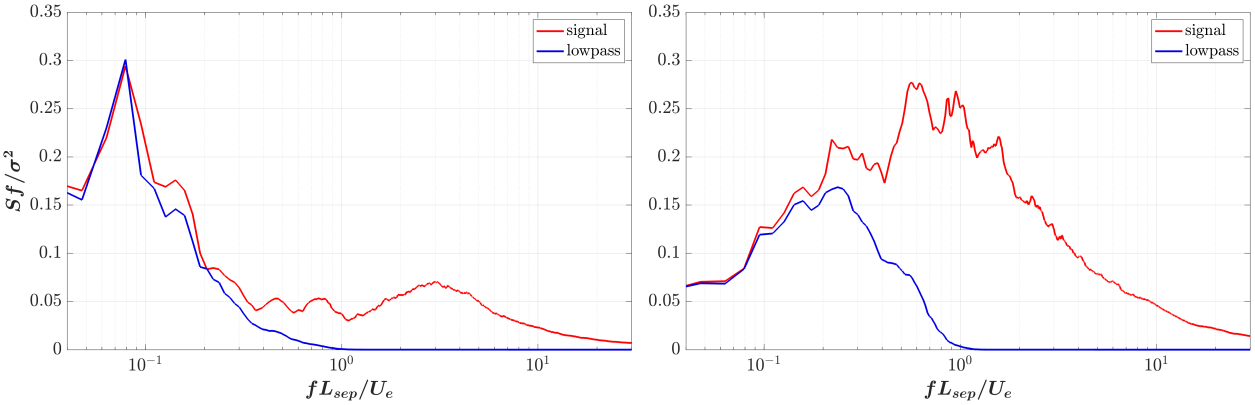


Figure 5.3. PSD of span-averaged separation (left) and reattachment (right) point signals.

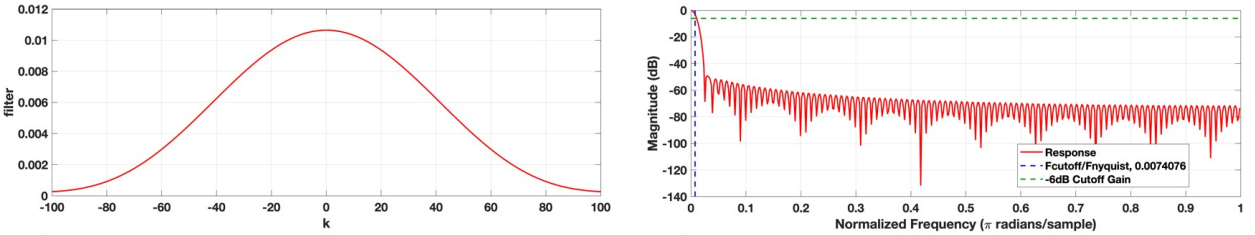


Figure 5.4. Lowpass FIR filter design: filter window (left) and magnitude response (right)

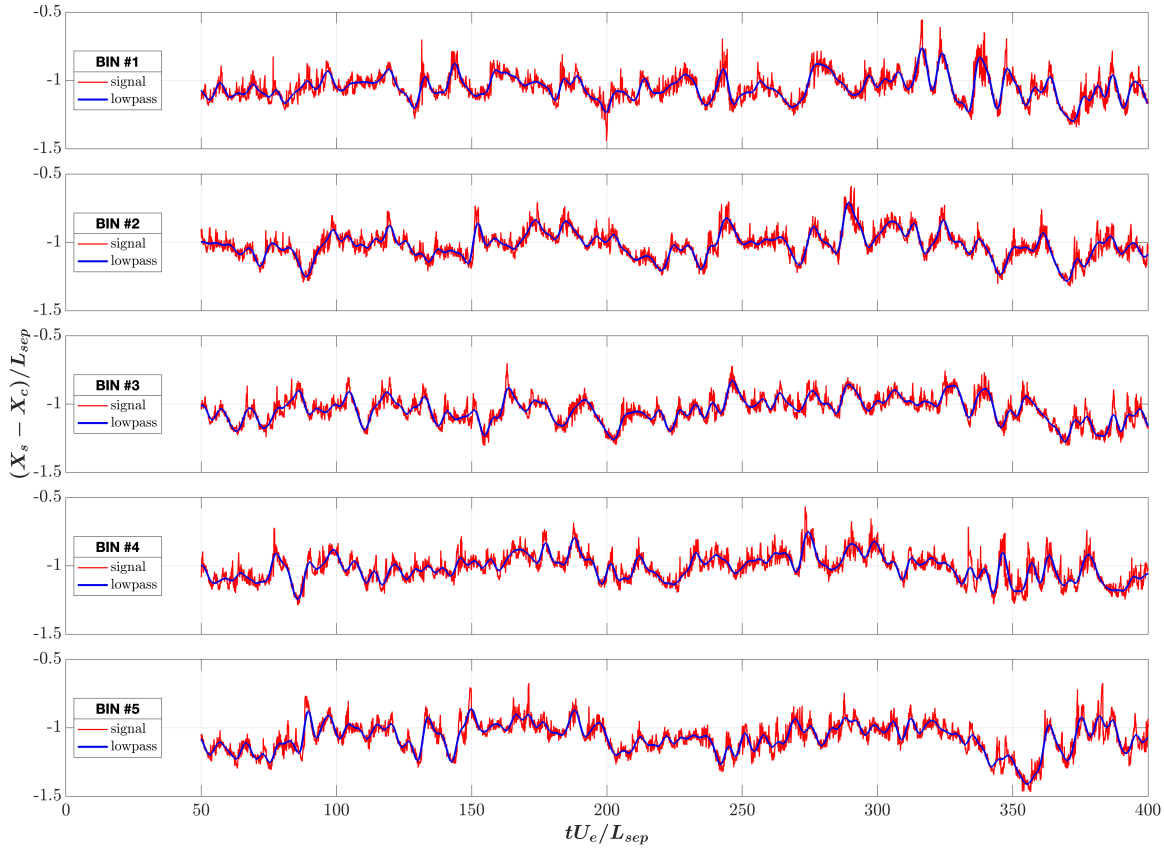


Figure 5.5. Separation point signals in span-averaged bins of $2\delta_0$.

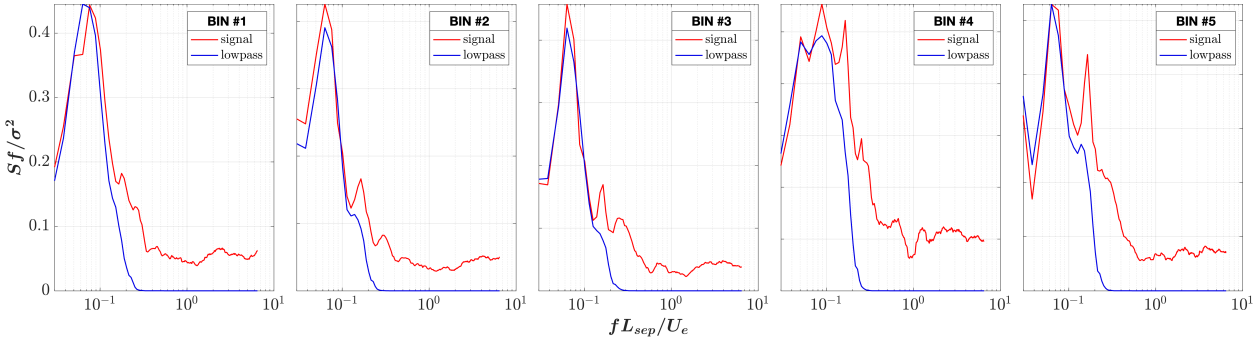


Figure 5.6. PSD of separation point signals in span-averaged bins of $2\delta_0$.

5.3.2 Lowpass Filtered 3D Flowfields

To further investigate the observed low-frequency event, the 3D LES flow solutions are lowpassed filtered to remove the turbulence. The same 1D lowpass filtering technique described in Section 5.3.1 is adapted for the 3D lowpass filtering. Figure 5.7 shows instantaneous lowpass filtered turbulent wall shear stress τ' (Pa) and turbulent wall heat flux $\dot{q}'$ (W/m^2). A clear spanwise

periodicity is observed according to the peaks and valleys in τ' and $\dot{q}'$, particularly following the cylinder-flare junction in the vicinity of reattachment. Noting that the total spanwise wall circumference is $10\delta_0$, a spanwise wavelength of approximately δ_0 can be visually estimated.

Figure 5.8 shows two instantaneous cross-stream planes of lowpass filtered streamwise turbulent momentum $(\rho u)'/(\rho U)_\infty$ with lowpass filtered turbulent shear stress τ' (Pa) on the wall. Plane *i*200 lies just after the separation point and plane *i*280 lies just before the reattachment point. Both planes show an alternating pattern of low (blue contours) and high (red contours) turbulent momentum across the span that correspond to the low and high streaks, respectively, of turbulent wall shear stress. An explanation for this spanwise pattern is seen in the cross-stream $v - w$ velocity vector field in the left plot of Figure 5.8. The vector field shows pairs of counter-rotating vortices across the span with rotation axes oriented in the streamwise direction. Figure 5.9 shows a zoom of one of the pairs of counter-rotating vortices on the plane labeled *i*280. The counter-rotating pairs create alternating downwash and upwash regions across the span. In a downwash region, the transport of high momentum fluid from the outer flow to the wall generates the high shear stress and heat flux observed at the wall. In an upwash region, the opposite occurs, where low momentum fluid from the wall is transported to the outer flow leaving imprint of lower shear stress and heat flux at the wall.

Figure 5.10 shows instantaneous isosurfaces of lowpass filtered streamwise turbulent momentum. Blue and red isosurfaces indicate negative and positive isosurfaces respectively. This image gives a broader view of the low and high turbulent moment streaks extending from just after separation to past reattachment and further downstream. A clear spanwise periodicity is once again evident. A time lapse (not shown) of the turbulent momentum and cross-stream velocity vector fields indicate that these structures appear to form just following the separation point and convect

downstream for some distance before new structures arise and the cycle repeats. Therefore, there is a temporal periodicity that is likely coupled to the unsteady breathing of the separation bubble – to be discussed in later sections. The observations thus far have also been reported in Mach 3 and Mach 7 fully separated compression ramp flows [34-39].

Figure 5.11 shows instantaneous cross-stream variations of turbulent wall shear stress and turbulent momentum at various axial and wall normal locations through the separation zone between planes *i*200 and *i*280 (refer to Figure 5.8 for plane locations). The *x*-axis is normalized spanwise arclength s/δ_0 along the wall. For reference, the normal distances above the wall labeled as [*k*20, *k*30, *k*40, *k*50] are shown in Figure 5.12 on sample plane *i*280. Sinusoidal variations in turbulent wall shear stress are observed that increase in amplitude with downstream distance. Sinusoidal variations in turbulent momentum are also observed at *k*40 (which corresponds roughly to the locus of the vortex cores on plane *i*280) and at *k50*. The sinusoidal variations in turbulent momentum also increase in amplitude with downstream distance. The sinusoidal patterns in the wall shear stress and turbulent momentum corroborate the qualitative observations in the 3D flowfields in Figure 5.7-Figure 5.10.

Figure 5.13 shows autocorrelations of spanwise turbulent moment at various axial locations in the separated zone between planes *i*200 and *i*280 at *k*50 (left plot), and at various wall normal heights on plane *i*280 (right plot). The autocorrelations indicate that the centrifugal instabilities have a spanwise wavelength of approximately δ_0, and therefore confirms the spanwise periodicity that may be qualitatively observed in Figure 5.7-Figure 5.10. Each spanwise wavelength contains approximately a pair of counterrotating streamwise-oriented vortices. Therefore the vortex diameter is approximately $\delta_0/2$. This estimate of spanwise wavelength is in agreement with Trichilo et al. [38] where for a Mach 10 compression ramp, pairs of vortical structures were

observed in the cross-stream velocity vector field in the separation zone which had spanwise wavelength of ~δ. It is worth noting that some lower Mach number ramp studies have observed a ~$2\delta_0$ wavelength. Priebe et. al 2016 [35], using DMD low-frequency reconstruction of a Mach 3 compression ramp flowfield, observed streamwise elongated pairs of structures of spanwise wavelength ~$2\delta_0$. Helm & Martín 2017 [36] observed similar streamwise-oriented structures of spanwise wavelength ~$2\delta_0$ in a Mach 7 compression ramp.

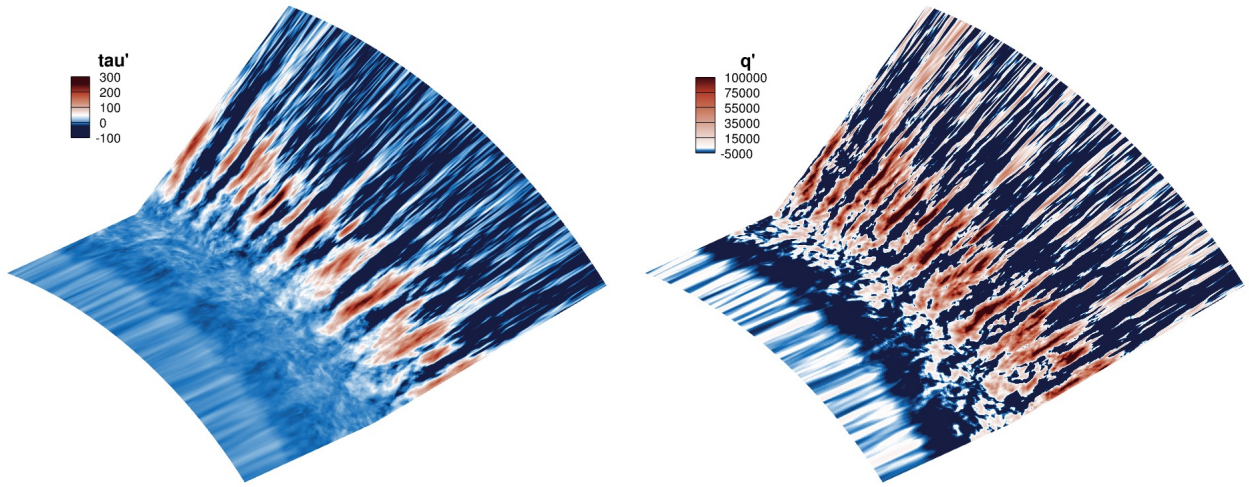


Figure 5.7. Instantaneous lowpassed-filtered turbulent wall shear stress τ' (Pa) and turbulent wall heat flux $\dot{q}'$ (W/m^2).

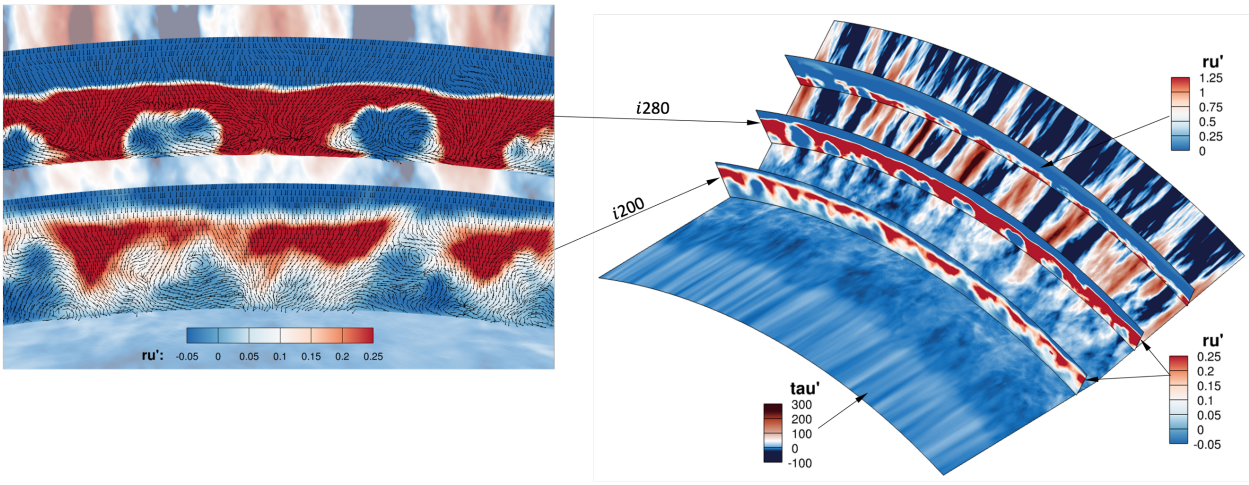


Figure 5.8. Instantaneous cross-stream planes of lowpassed- filtered streamwise turbulent momentum $(\rho u)'/(\rho U)_\infty$ with lowpassed wall shear stress τ' (Pa). Left image also shows cross-stream v-w velocity vector field.

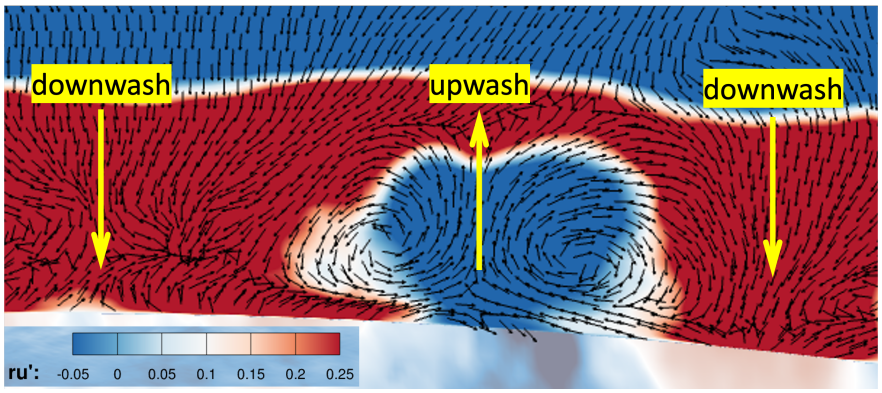


Figure 5.9. Zoom of instantaneous cross-stream plane $i = 280$ showing a pair of counter-rotating vortices. Contours are lowpassed- filtered streamwise turbulent momentum $(\rho u)'/(\rho U)_\infty$ with cross-stream v-w velocity vector field.

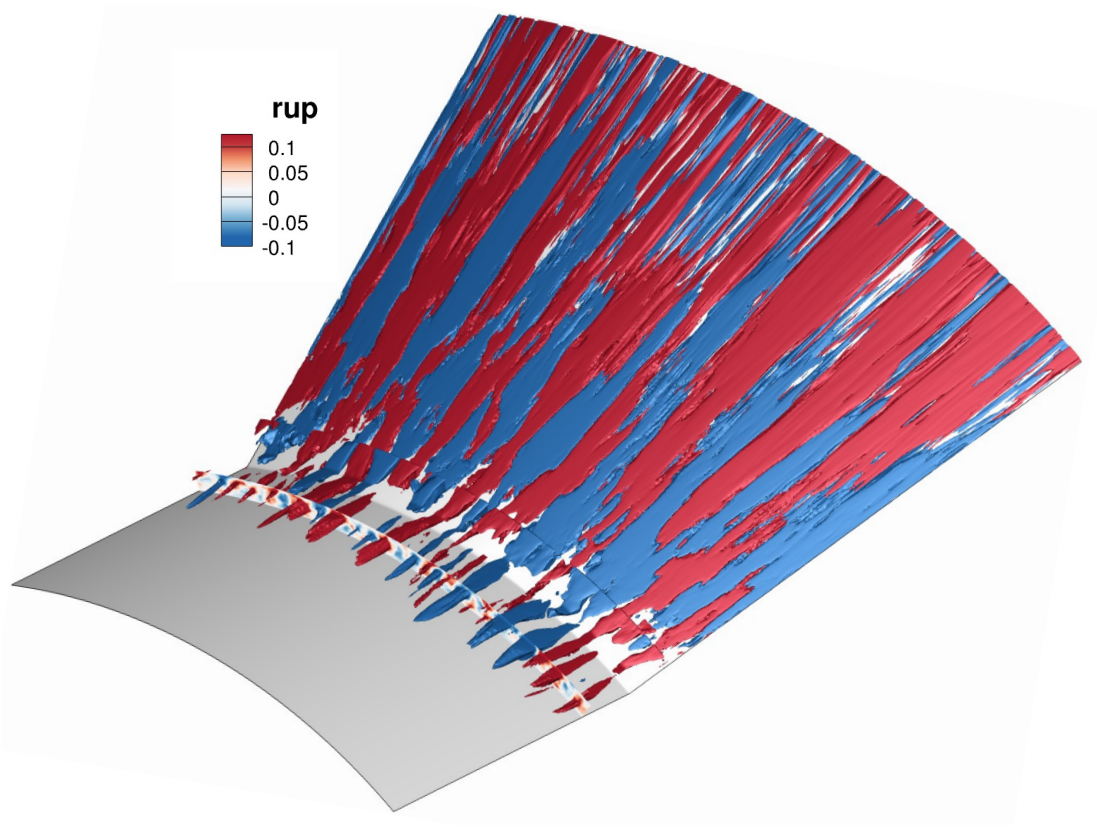


Figure 5.10. Isosurfaces of instantaneous lowpass-filtered streamwise turbulent momentum $(\rho u)'/(\rho U)_\infty$. A positive and a negative isosurface are chosen to highlight the low and high turbulent moment streaks, extending from just after separation to past reattachment.

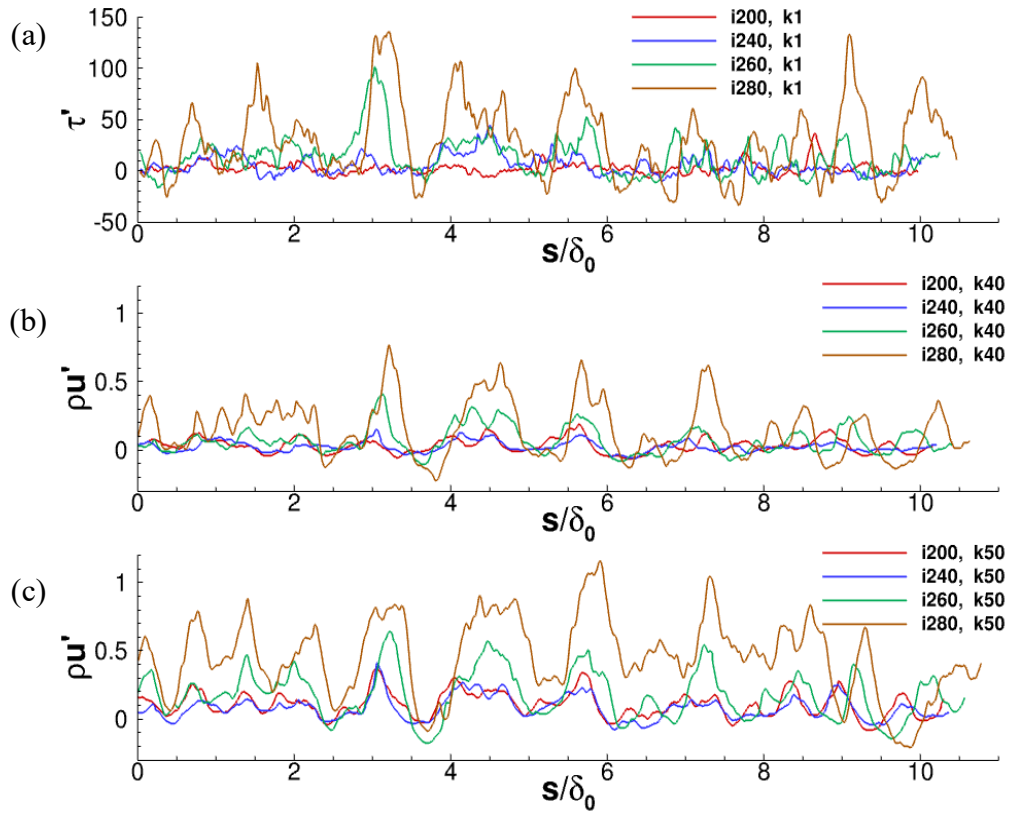


Figure 5.11. Instantaneous cross-stream variations of (a) turbulent wall shear stress τ' (Pa), and (b & c) turbulent momentum $(\rho u)'/(\rho U)_\infty$ at various axial and wall normal locations.

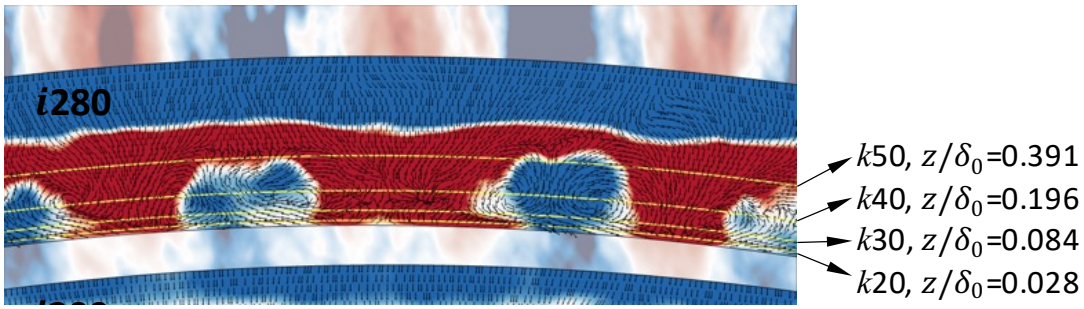


Figure 5.12. Wall normal locations on sample i280 plane for spanwise correlations of turbulent momentum $(\rho u)'/(\rho U)_\infty$.

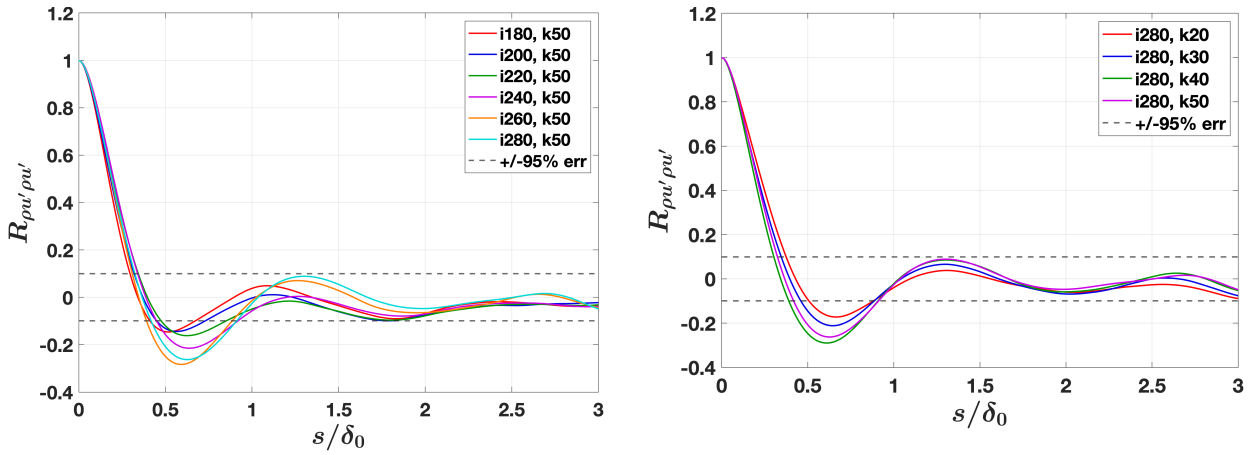


Figure 5.13. Autocorrelation of turbulent momentum $(\boldsymbol{\rho u})'$ at various axial locations across the separated zone (left) and at various boundary layer heights at a single axial location just downstream of the corner.

5.3.3 Görtler-type Centrifugal Instabilities

Görtler (1941) [40,41] first characterized a particular centrifugal instability that arises in incompressible laminar boundary layers on concave walls. Rayleigh 1916 [83] showed that a necessary and sufficient condition for existence of an inviscid centrifugal instability, known as the Rayleigh's circulation criterion, is $d\Gamma^2/dr < 0$, where circulation $\Gamma = rU,\ U = U(r)$ is the streamwise velocity and r is the radius measured from the center of wall curvature. If $|\Gamma|$ increases with increase in r the flow will be stable. If $|\Gamma|$ decreases with increase in R the flow will be unstable as illustrated in Figure 5.14 for a concave and convex wall. Bayly 1987 [84] showed that the criterion holds true for noncircular streamlines, and Floryan 1986 [85] showed that the criterion is applicable to boundary layer flows. Viscosity is expected to have a stabilizing effect within some Reynolds number limit, in which case the criterion becomes only a necessary condition [86].

For boundary layer flow along a concave wall, the circulation is generally nonzero. However, at the wall and at the center of curvature $\Gamma = 0$. Therefore, in between there exists a maximum $|\Gamma|$, and thus a region of instability where $d|rU|/dr < 0$. Under this condition, the local pressure gradient fails "to restrain an excess of angular momentum of a particle undergoing an outward

virtual displacement, leading to the instability" [86]. Görtler showed, through solutions of the linearized disturbance equations, that the instability manifests as streamwise-oriented pairs of counter-rotating vortices, as shown in Figure 5.15 (left) now referred to as Görtler vortices. The vortices distinguish themselves from the closely related Taylor vortices (Taylor 1923 [87], Tag 1992 [88]) and Dean vortices (Dean 1928 [89], Guo & Finlay 1993 [90]).

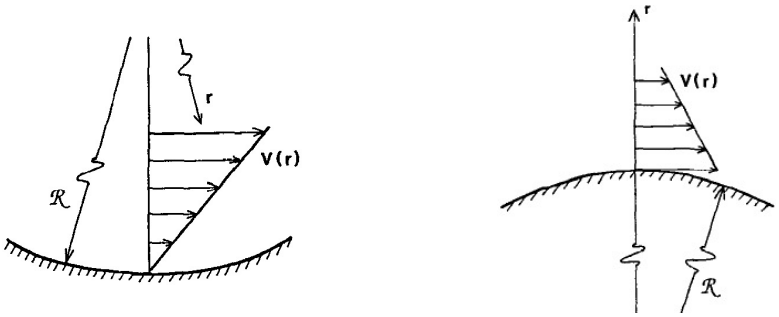


Figure 5.14. Illustrations of unstable Rayleigh circulation condition for a concave (left) and convex (right) wall, reproduced from [86].

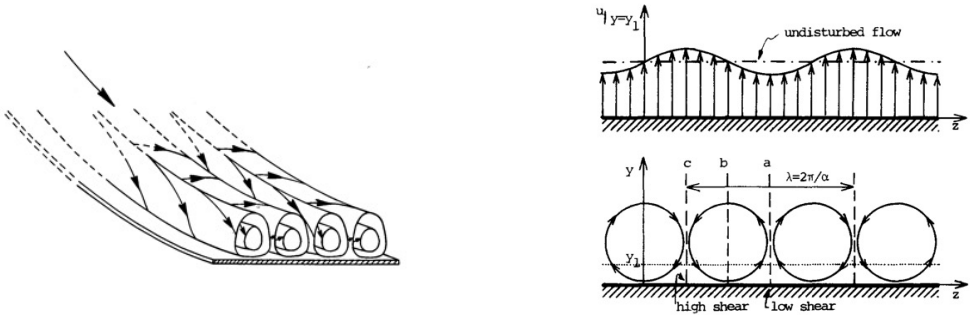


Figure 5.15. Illustrations of Görtler centrifugal instabilities: (left) streamwise vortex pairs on a concave wall, and (right) cross-stream momentum and induced rotation and mixing, reproduced from [41] & [91], respectively.

The Görtler vortices induce sinusoidal fluctuations in momentum in the cross-stream direction (Figure 5.15 right). This incurs mixing of high momentum fluid in the outer boundary layer with low momentum fluid near the wall. At the wall, the result is high shear stress and heating in the downwash region, and low shear stress and heating in the upwash region. Görtler showed that the formation and amplification (or decay) of the vortices is dependent on a parameter now known as the Görtler index, defined as,

$$G_T = Re_\theta \sqrt{\theta/|R|} \quad [32]$$

where Reynolds number $Re_\theta = U_e\theta/\nu$, R is the wall radius of curvature, θ is the boundary layer momentum thickness and ν is the kinematic molecular viscosity.

The spanwise-arranged pairs of streamwise-oriented vortical structures and their induced turbulent momentum and wall shear stress fields across the separated cylinder-flare junction are strongly akin to that of Görtler-type centrifugal instabilities. Like Görtler vortices in incompressible laminar flow on concave walls, the vortices observed herein are hypothesized to be caused by the concavity of the streamlines across the separated region at the corner. To that end, the influence of streamline curvature is investigated next. Figure 5.16 (top) shows the span-averaged and time-averaged separated corner flow on the Mach 10 cylinder-flare. The recirculating streamlines at the corner indicate the separation bubble. The region of high turbulent kinetic energy (red contours) indicates the shear layer above the separation bubble. Streamline S1 is the dividing streamline between the separation bubble and the shear layer. Streamline S2 is the streamline just above S1 and is included for comparison. The streamline radii of curvature, R, of S1 and S2 are calculated via,

$$R = \left(\frac{d^2z}{dx^2}\right)^{-1}\left[1+\left(\frac{dz}{dx}\right)^2\right]^{3/2} = \frac{(u^2+w^2)^{\frac{3}{2}}}{u^2\frac{\partial v}{\partial x} - 2uw\frac{\partial u}{\partial x} - w^2\frac{\partial u}{\partial z}} \rightarrow \begin{Bmatrix} concave\ if\ 1/R > 0 \\ convex\ if\ 1/R < 0 \end{Bmatrix} \quad [33]$$

For turbulent flows, Tani 1962 [92] suggested that the replacing the molecular viscosity with the outer layer eddy viscosity ν_t. Smits & Dussauge 2006 [93] suggested using $\nu_t = 0.018U_e\delta^*$ for the outer layer eddy viscosity as given by Clauser 1956 [94], but this value was found to be an order of magnitude too large for the present test case. Instead, ν_t herein was calculated directly from the mean LES solution using the Boussinesq approximation of eddy viscosity [5], viz,

$$\tilde{b}_{ij} = -\frac{\nu_t}{\tilde{k}} \tilde{S}_{ij}^{dev} \quad [34]$$

where $\tilde{b}_{ij}$ is the mean Reynolds stress anisotropy tensor, $\tilde{k}$ is the mean turbulent kinetic energy and $\tilde{S}_{ij}^{dev}$ is the mean deviatoric strain rate. For calculating the Görtler index, reference values are calculated in the upstream undisturbed boundary layer just prior to separation. At this location, we can simplify the Boussinesq approximation for simple shear to,

$$\widetilde{u''w''} = -\nu_t \frac{\partial \tilde{u}}{\partial z} \quad [35]$$

where $\widetilde{u''w''}$ is the Reynolds shear stress, $\tilde{u}$ is the mean streamwise velocity and z is the wall normal distance. Using this relation, ν_t is then computed as the mean across the outer boundary layer. The Görtler index is then computed as,

$$G_T = \frac{U_e \theta}{\nu_t} \sqrt{\theta / |R|} \quad [36]$$

where U_e, θ and ν_t are measured at a reference location just upstream of separation.

Figure 5.16 (middle) shows that the normalized streamline curvature δ/R for streamline S1 is nearly zero upstream of separation, then increases mildly from $x = -4$ across the initial separation, then becomes negative at $x = -1$ at the thickest part of the bubble where the streamline curvature is convex, then spikes precipitously near reattachment where the curvature is highly concave peaking at $x = 0.9$, then decreasing back to near zero. The Görtler index shown in Figure 5.16 (bottom) approximately tracks with $\sqrt{\delta/|R|}$ with several peaks. Referring to streamline S1, G_T increases modestly where S1 is concave near incipient separation with a local peak of $G_T = 0.87$ at $x = -3.3$, followed by mild fluctuations about a mean of about $G_T = 0.5$, then a drop to near zero at $x = -0.7$. From $x = -0.7$ to $x = 0.3$, G_T has another local peak where the streamline is convex ($R < 0$) at the thickest part of the bubble. Following this convex region, G_T increases

precipitously where the streamline has significant concavity closer to flow reattachment reaching a global peak of $G_T = 1.8$ at $x = 0.85$.

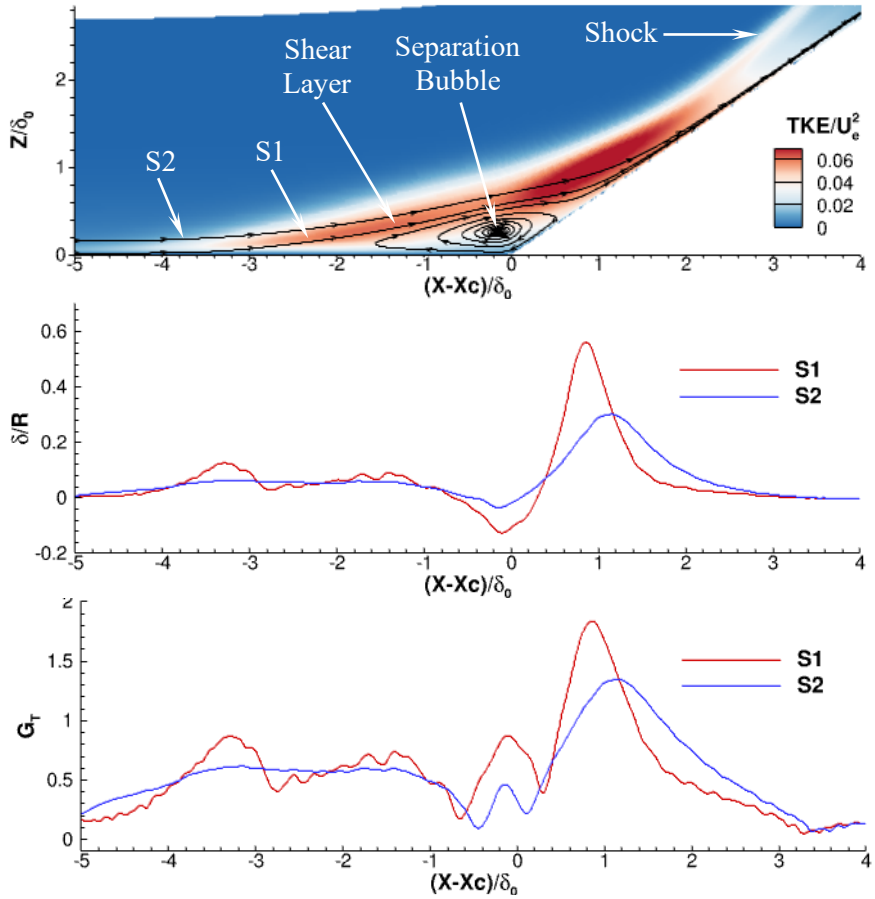


Figure 5.16. Streamlines labeled S1 & S2 across the separation bubble with contours of mean turbulent kinetic energy k/U_e^2 (top), streamline curvatures (middle), and corresponding Görtler indices (bottom).

While Görtler suggested a critical threshold of $G_T = 0.6$ for the appearance of a centrifugal instability in laminar incompressible attached flows, there is no established stability criterion for turbulent, compressible and separated flow. For separated flow, it may be reasoned that an inflection point in the mean velocity profile due to separation makes the flow even more unstable and potentially lower the G_T limit for the onset of the Görtler instability. For the present test case, it is noted that the Görtler index spikes to a maximum of $G_T = 1.8$ along the separation streamline, which is three times the threshold for laminar incompressible attached flows. The spike in

concavity of the separation streamline in the interaction corner and the accompanying spike in the Görtler index supports the hypothesis that the pairs of streamwise vortical instabilities, along with its spanwise sinusoidal imprint of shear stress and heat flux on the wall, as observed in Section 5.3.2 are of a Görtler-type.

5.4 Vortex Dynamics

In order to correlate the dynamics of the observed centrifugal instabilities with the unsteady separation event, vortex identification (ID) methods were investigated that can robustly track certain properties, such as vortex location and strength over time. There are a number of vortex (ID) methods available in the literature [95]. While most methods work well for idealized vortices, they can be challenging to implement for practical flows, especially flows with compressibility, turbulence and shock-induced separation. Two Eulerian vortex ID methods are explored that take two different approaches but together work well for the intended purpose herein. These are discussed below.

5.4.1 Vortex ID Methods: $\Gamma_{1,2}$ Criterion

The $\Gamma_{1,2}$ criterion was first proposed by Michard et al. [96] and further developed by Graftieaux [97] for identifying vortex cores in 2D PIV (particle image velocimetry) measurement planes. The method was successfully used by in Dupont et al. [98] and Helm et al. [75] to identify shear layer vortices in shock-separated flows. The method identifies points within a 2D vortex core by examining the net rotational motion around each point using the topology of the velocity vector field. Unlike many vortex ID methods, this method does not rely on the velocity gradient field and is therefore not subject to errors that can be amplified when taking derivatives. The net rotational motion is quantified by a pseudo-circulation $\Gamma_{1,2}$. Referring to Figure 5.17, for a point P in a 2D

measurement plane with normal vector $\hat{n}$, S is some area surrounding P, and M is an arbitrary point inside S with in-plane velocity U_M, the pseudo-circulation $\Gamma_{1,2}$ function is defined as,

$$\Gamma_{1,2}(P) = \frac{1}{S}\oint_{M\in S} \frac{(PM \times U_M)\cdot \hat{n}}{\|PM\|\|U_M\|} dS = \frac{1}{S}\oint_{M\in S} sin(\theta_M)\, dS, \quad \left|\Gamma_{1,2}\right| \leq 1 \qquad [37]$$

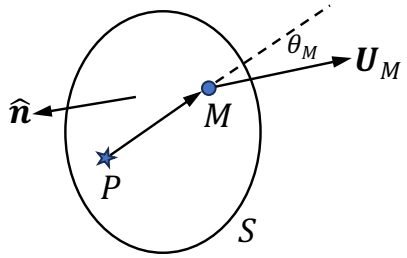


Figure 5.17. Illustration of interrogation window S of point P for computing pseudo-circulation $\Gamma_{1,2}$.

For S containing N number of discrete points M, this becomes,

$$\Gamma_{1,2}(P) = \frac{1}{N}\sum_{N} sin(\theta_M) \qquad [38]$$

If U_M is taken as the absolute velocity of M, then the method is termed the Γ_1 criterion and a vortex center is identified as $|\Gamma_1|_{max} \to 1$. If U_M is taken as the velocity of M relative to a local convection velocity around P defined by $U_P = 1/S \oint_S U\, dS$, then the method is termed the Γ_2 criterion. Graftieaux showed that for an idealized vortex,

$$|\Gamma_2| \to \begin{cases} < 2/\pi, & strain\ dominated \\ = 2/\pi, & pure\ shear \\ > 2/\pi, & rotation\ dominated \end{cases} \qquad [39]$$

Therefore, a vortex core is defined by the region where rotation dominates strain, that is, $|\Gamma_2| > 2/\pi$. In practice the thresholds above will be approximate. Since $\Gamma_{1,2}$ is an integral quantity, it acts as a spatial filter that removes small spatial scales (such as turbulence) but only weakly affects $\left|\Gamma_{1,2}\right|$. Note that Γ_2 is Galilean invariant, while Γ_1 is not.

Herein, $\Gamma_{1,2}$ is calculated on cross-stream planes using a circular interrogation window S of nominal radius $0.08\delta_0$ centered at each grid point. However, the radius is made to decrease for points close to the wall in proportion to distance from the wall with the constraint that $N \geq 8$. By performing the calculations on successive cross-stream planes one can reconstruct the vortex cores in a 3D sense.

5.4.2 Vortex ID Methods: λ_{ci} Criterion

The λ_{ci} criterion, a.k.a. the 'swirl' strength criterion, is a velocity gradient based criterion. The underlying theory was first proposed by Chong et al [99] and later applied to vortex cores in works such as that by Haimes et al [100] and Zhou et al [100]. The basis of the method is rooted in critical point theory. First, we note that an Eigendecomposition of the velocity gradient $\nabla U \equiv G$ as follows,

$$\nabla U \equiv G = V\Lambda V^{-1}, \text{ where } \Lambda = \begin{bmatrix} \lambda_r & 0 & 0 \\ 0 & \lambda_{cr} + i\lambda_{ci} & 0 \\ 0 & 0 & \lambda_{cr} - i\lambda_{ci} \end{bmatrix}, \text{ or } \Lambda = \begin{bmatrix} \lambda_r & 0 & 0 \\ 0 & \lambda_{cr} & \lambda_{ci} \\ 0 & -\lambda_{ci} & \lambda_{cr} \end{bmatrix} [40]$$

where V and Λ are the eigenvectors and eigenmatrix of G respectively. The local velocity at some small distance away y from a point x can be expressed by the linear Taylor approximation $u(x+y) = u(x) + Gy + \mathcal{O}(\|y\|^2)$. Note that the kinematics of a fluid particle is captured in this expression, viz, $u(x)$ represents translation, and $G = S + \Omega$ represents average strain rate/deformation due to symmetric tensor S and average rotation rate due to antisymmetric tensor Ω. The trajectory of a neighboring fluid particle is then determined by the linear first order ODE $\dot{y} = Gy$ with initial condition $y_0 = Vc$, where c is a constant vector. The general solution is then $y = Ve^{\Lambda t}V^{-1}c$. The general solution implies that if eigenvalues of G are all real, then the critical point is a node (source or sink) or saddle (stagnation point). If one eigenvalue is real and the other two are complex conjugates, then the critical point is a focus (spiraling flow) indicating a vortex.

In order words, spiraling flow exists when $\lambda(G) = (\lambda_r, \lambda_{cr} \pm i\lambda_{ci})$ or more succinctly when $\lambda_{ci} > 0$. Moreover, λ_{ci} quantifies the local swirl or vortex strength, a property that is desirable for the forthcoming analyses. One can also show that the local orbit period is $2\pi/\lambda_{ci}$. To determine $\lambda(G)$, we solve $\det(G - \lambda I) = 0$ resulting in the characteristic equation below whose coefficients P, Q and R are the principal invariants of G.

$$\lambda^3 + P\lambda^2 + Q\lambda + R = 0 \qquad [41]$$

$$P = -tr(G), \quad Q = \tfrac{1}{2}[tr(G)^2 - tr(G^2)], \quad R = -det\,(G)$$

5.4.3 $\Gamma_{1,2} + \lambda_{ci}$ Criteria Assessment

In the author's experience, no single method was optimal for tracking vortex cores. However, the combination of $\Gamma_{1,2}$ and λ_{ci} criteria provided a very good method of tracking the vortex cores over time. A vortex core map is generated using the following modified criteria,

$$\Gamma_2 = \begin{cases} \Gamma_2, & |\Gamma_2| > 2/\pi \ \cap \ \lambda_{ci} > 0 \\ 0, & otherwise \end{cases} \qquad [42]$$

Or alternatively,

$$\lambda_{ci} = \begin{cases} \lambda_{ci}, & |\Gamma_2| > 2/\pi \ \cap \ \lambda_{ci} > 0 \\ 0, & otherwise \end{cases} \qquad [43]$$

Note that in practice the Γ_2 thresholds are approximate, and the λ_{ci} threshold may be a small positive number rather than 0. Figure 5.18 demonstrates the application of the modified Γ_2 and λ_{ci} vortex ID methods to a sample instantaneous lowpass filtered cross-stream plane just before reattachment. The location of the plane is shown in the right of Figure 5.18. For ease of viewing, the plane is a central $4\delta_0$ wide section of the full $10\delta_0$ span. The Γ_2 and λ_{ci} maps successfully identify vortical regions very well as confirmed by the swirl of the in-plane streamlines. The two maps appear qualitatively equivalent. In the Γ_2 map, yellow colored vortices indicate clockwise rotation in which $\Gamma_2 > 0$, and red colored vortices indicate anticlockwise rotation in which $\Gamma_2 < 0$.

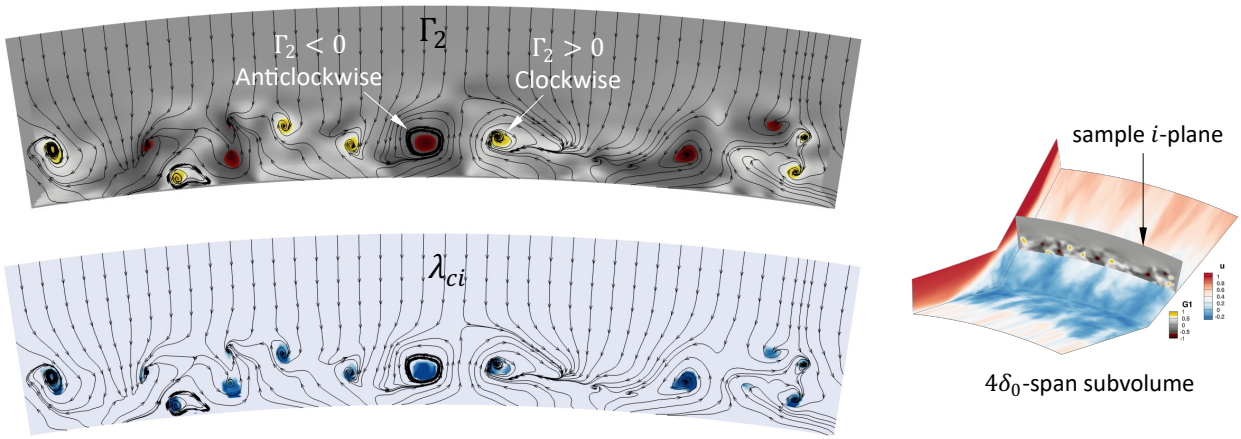


Figure 5.18. Identification of vortex cores using the modified Γ_2 criterion (top left) and the modified λ_{ci} criterion (bottom left) for a sample lowpass filtered cross-stream plane cropped to width $4\delta_0$ (location shown right).

5.4.4 Vortex Center Detection and Strength

The strength of a vortex is classically determined by its circulation $\Gamma = \oint_S \nabla \times U dS$. Note that Γ is somewhat different from the pseudo-circulation $\Gamma_{1,2}$ defined previously. Circulation Γ is an integral quantity and requires defining the boundary of a vortex core. In the author's experience, identifying vortex core boundaries can sometimes be unreliable when using an automated algorithm, especially in a complex flowfield. Instead, we chose to characterize the strength of a vortex by the swirl strength λ_{ci} at the vortex center. The vorticity of a vortex is strongest at its center and λ_{ci} can be shown to be related to the vorticity, so conceptually the approach seems reasonable. In practice, the non-uniformity of λ_{ci} across a vortex core still begs the question: can λ_{ci} at the center reliably track with the circulation Γ over a period of time? This will be addressed in Section 5.5.1 . In order to identify a vortex center, we algorithmically search within a vortex cross-section for stationary points of $\Gamma_{1,2}$. Therefore, a vortex center must satisfy,

$$\begin{cases} \nabla\Gamma_{1,2} = 0 \\ |\Gamma_2| \gtrsim 2/\pi \\ \lambda_{ci} > 0 \end{cases} \quad [44]$$

Figure 5.19 shows the same lowpass filtered plane as in Figure 5.18 with vortex cores identified by contours of Γ_2. The vortex centers resulting from the search algorithm described above are marked with white diamond symbols, and the vortex swirl strength at the center marked with the value of λ_{ci}. The vectors are the cross-stream $v - w$ velocity vectors which converge to a critical point at the vortex centers where the streamline slope is indeterminate. Figure 5.19 demonstrates the accuracy of the methods to robustly identify vortex cores, vortex centers and vortex center strength on a cross-stream plane.

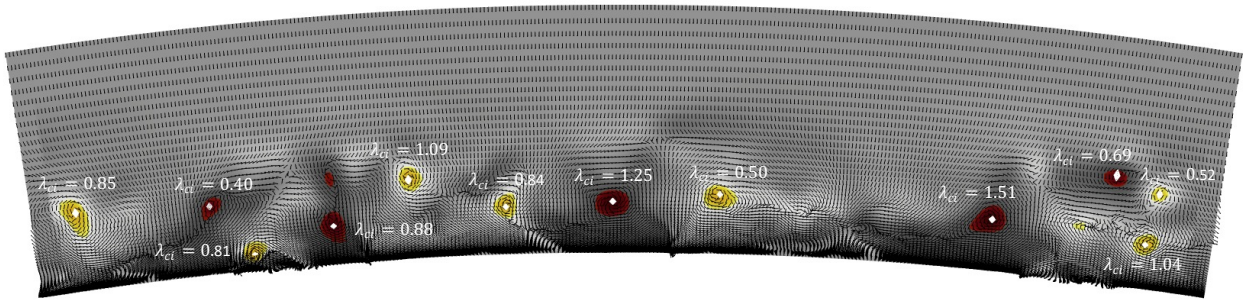


Figure 5.19. Vortex centers and strength on sample lowpass filtered cross-stream plane (cropped to width $4\delta_0$).

5.4.5 3D Vortex Visualization

Finally, a 3D rendering of the centrifugal instabilities at any time instant can be obtained by generating vortex core maps in successive cross-stream planes from upstream to downstream in the lowpass filtered flow. The centrifugal instabilities are then identified by isosurfaces of $|\Gamma_2| \approx 2/\pi$. Figure 5.20 shows an instantaneous snapshot of the streamwise centrifugal instabilities across the full $10\delta_0$ span. The vortices extend across the boundary of the separation bubble from just downstream of separation to just downstream of reattachment. The contours are lowpass filtered streamwise velocity contours u/U_∞ on a plane just above the wall and on a plane on the 'left'

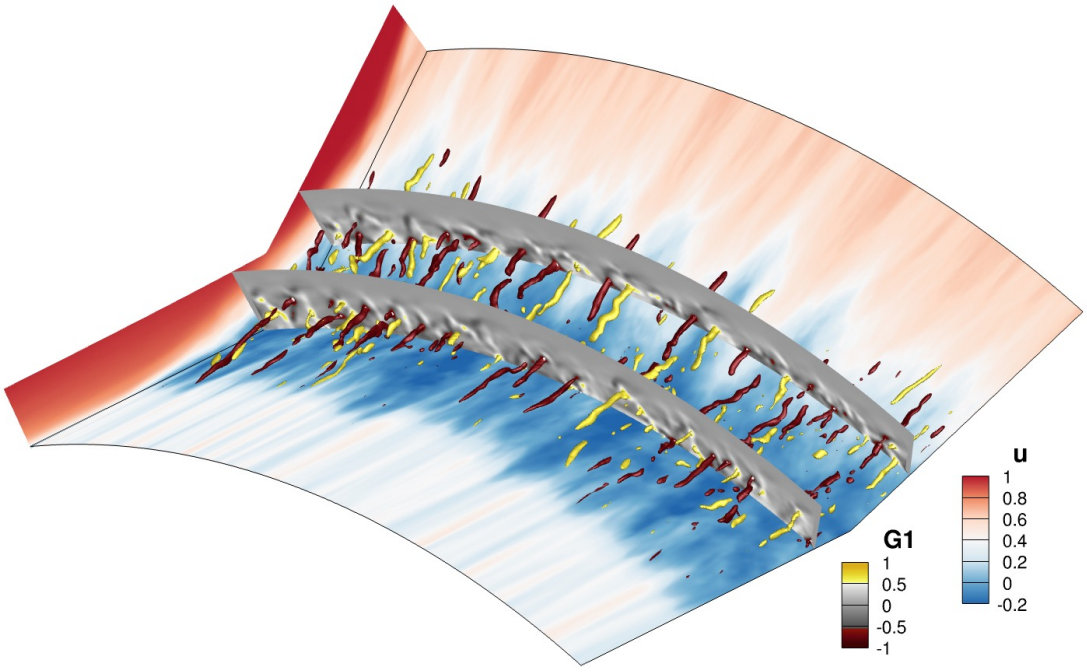


Figure 5.20. Isosurfaces of $|\Gamma_2| \approx 2/\pi$ showing an instantaneous snapshot of the streamwise centrifugal instabilities at the separated corner on the full $10\delta_0$ span. Also shown are lowpass filtered streamwise velocity contours u/U_∞ on a plane just above the wall and on a longitudinal plane on a spanwise boundary.

spanwise boundary. The separation zone is approximately indicated by the blue contoured regions of low speed fluid. Clockwise (yellow) and anticlockwise (red) rotating vortices are approximately alternating producing the periodic pattern of low and high velocity across the span. The vortex cores are also observed to meander short distances in time in both the spanwise and wall normal directions, i.e., they are weakly nonstationary in the cross-stream direction. The vortices also appear to travel a short distance downstream decreasing in strength as they do so. These observations are consistent with that of Priebe et al. 2016 [35] for a Mach 3 compression ramp in which DMD of the flowfield revealed a pair of streamwise elongated vortical structures in the low-frequency range of interest. The most energetic low-frequency DMD modes were associated with movement of the structures in the spanwise and wall normal directions, as well as varying turbulent momentum strength. Floryan 1991 [85], in reviewing various experiments of Görtler vortices in

low-speed turbulent flows, noted that when the vortical instabilities are not predominantly driven by upstream disturbances, they are likely unsteady and may not be detected by time-averaged measurement techniques. When attempting to extract the vortices from the time-averaged lowpassed filtered flowfields for the present case, no reliable detection of vortices could be obtained; this is consistent with Floryan's observation.

5.5 Vortex Signals and Correlations with Separation Event

5.5.1 Tracking Mean Vortex Properties over Time

In order to correlate the centrifugal instabilities with the separation event, the vortex ID techniques discussed above are used to track properties of vortices in time averaged over planar spanwise bins of a chosen width. Figure 5.21 shows a sample tracking of such properties, namely, circulation Γ, swirl strength λ_{ci} and convection velocity U_c, averaged over a single $2\delta_0$ spanwise bin for plane *i*240. The higher frequency noise in the signals (red lines) are mainly due to calculation uncertainties, hence the signals are smoothed (blue lines). The signals appear to be statistically stationary and represent ~10 low frequency cycles (LFCs). The circulation shown here is the actual circulation $\Gamma = \oint_S \nabla \times UdS$ (not the pseudo-circulation $\Gamma_{1,2}$). As stated previously, the tracking of swirl strength λ_{ci} is strongly preferred over circulation Γ as a measure of vortex strength. This is because λ_{ci} is simpler to track via an automated algorithm since it only requires probing the center of a vortex once the center is identified. By contrast, Γ is an integral property that requires bounding a vortex, thus requiring more computational effort and may be subject to larger errors. The sample signals in Figure 5.21 are mainly to demonstrate the correlation between Γ and λ_{ci}. The cross-correlation of Γ and λ_{ci} averaged over δ_0 and $2\delta_0$ spanwise bins are shown in Figure 5.22 and Figure 5.23, respectively, for three sample planes *i*200, *i*240 and *i*280. The *x*-

axis is the normalized time lag. The correlation is shown for each bin and the mean of all bins is the single black line. The mean peak correlations at zero time lag is >0.5 for δ_0 bins and >0.4 for $2\delta_0$ bins. This indicates a moderately strong correlation between Γ and λ_{ci}. The mean correlations reach zero at ~$5U_e/L_{sep}$ (not visible in the current plots). The results confirm that the imaginary eigenvalue component λ_{ci}, the so-called swirl strength, can be reliably used as a means to track mean vortex circulation strength. From here on, vortex strength will refer to λ_{ci} unless otherwise stated.

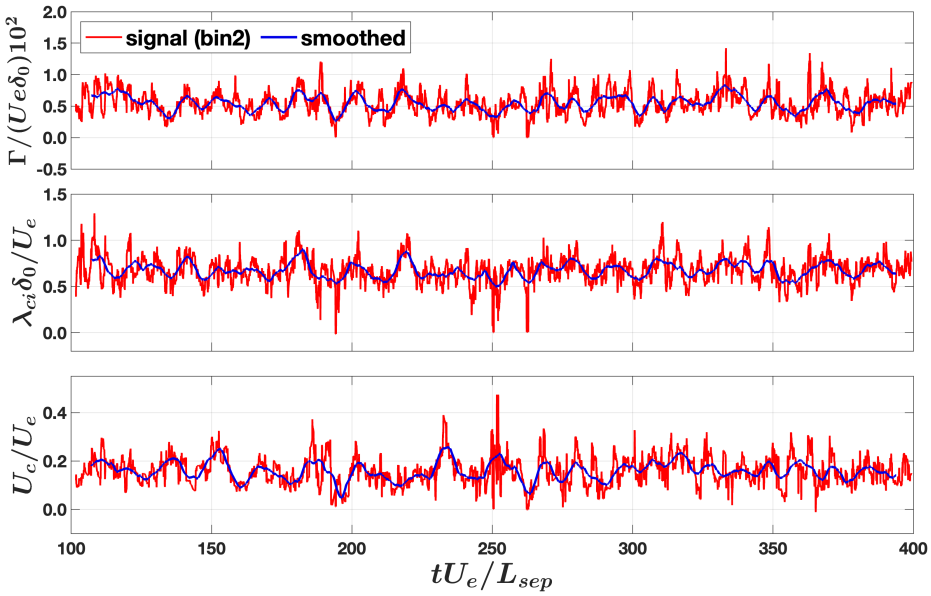


Figure 5.21. Sample vortex signals span-averaged over a $2\delta_0$ bin on plane *i*240: (from top) circulation Γ, swirl strength λ_{ci} and convection velocity U_c.

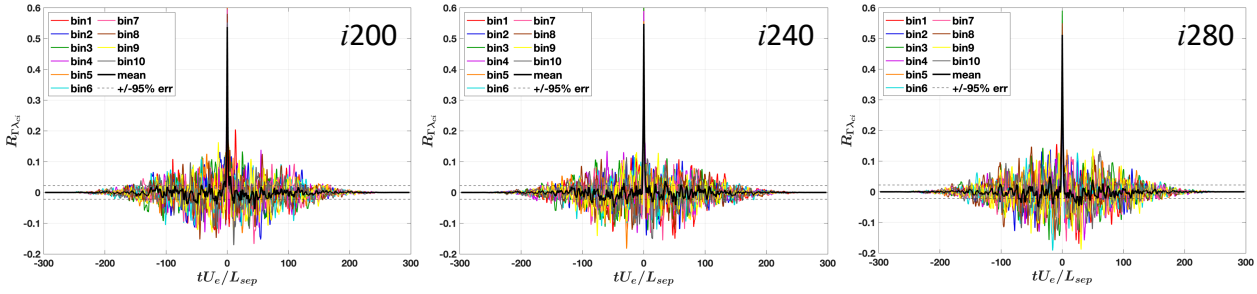


Figure 5.22. Cross-correlation of vortex circulation Γ and vortex swirl strength λ_{ci} in δ_0 spanwise bins.

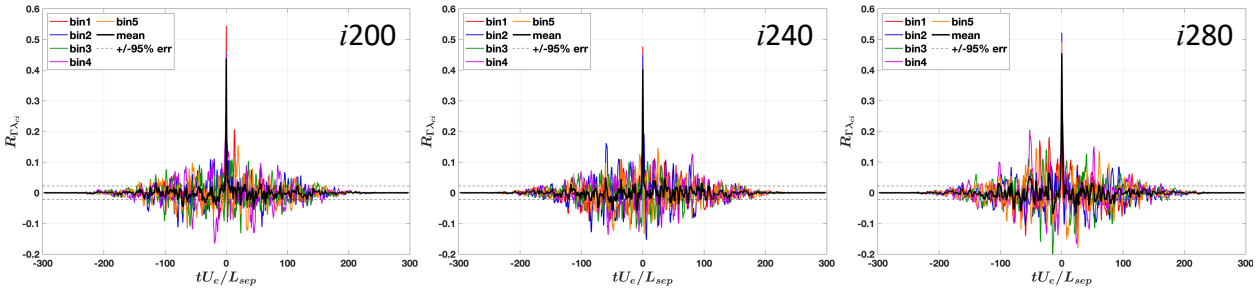


Figure 5.23. Cross-correlation of vortex circulation Γ and vortex swirl strength λ_{ci} in $2\delta_0$ spanwise bins.

5.5.2 Time Correlation of Vortex Strength and Separation Point Motion

Figure 5.24 shows filtered signals of vortex strength fluctuation λ'_{ci} and separation point fluctuation X'_{sep} averaged over $2\delta_0$ bins across the span on a sample cross-stream plane *i*240. The signals are split into two equal consecutive time bins ΔT_1 and ΔT_2. Time correlations of λ'_{ci} and X'_{sep} are performed in each time bin and averaged to strengthen the statistics. The cross-correlations of λ'_{ci} and X'_{sep} averaged in δ_0 and $2\delta_0$ spanwise bins are shown in Figure 5.25 and Figure 5.26, respectively. The binned correlations were shifted to zero lag, smoothed and averaged, resulting in the mean correlation (black line). The mean peaks at zero lag in all cases are in the range 0.45-0.55, indicating a moderately strong correlation between vortex strength and separation point motion. The correlation increases slightly with downstream distance. The mean correlations also indicate a mean periodicity of $\sim 20 L_{Sep}/U_e$, corresponding to a characteristic frequency of $f \approx .05 U_e/L_{sep}$, which is within the range of the characteristic low frequency observed in the spectra in Section 5.3.1 . The mean time delay between the two signals (not shown) was $\sim 4 L_{sep}/U_e \approx 0.3 T_c$, where $T_c \approx 13.5 L_{sep}/U_e$ is the low-frequency characteristic period as observed in the spectra in Section 5.3.1 . This implies that the strength of the vortices and the separation bubble breathing have a phase difference of approximately $-0.6\pi^c$.

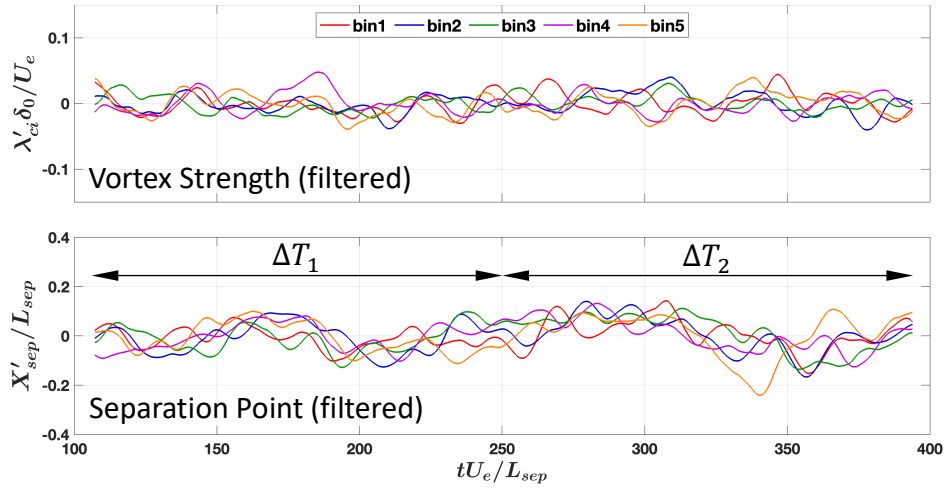


Figure 5.24. Sample signals of vortex strength fluctuation λ'_{ci} and separation point fluctuation X'_{sep} on plane $i240$ span-averaged over $2\delta_0$ bins and filtered to remove high-frequency noise.

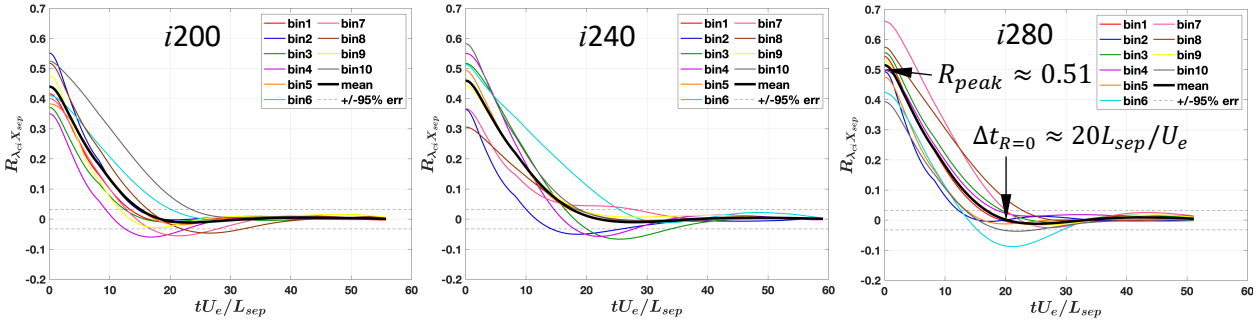


Figure 5.25. Cross-correlation of vortex strength λ'_{ci} and separation point X'_{sep} in δ_0 spanwise bins.

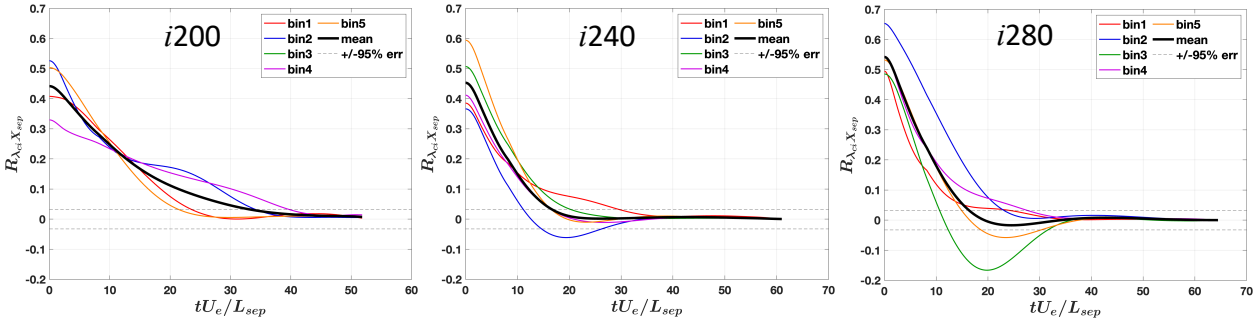


Figure 5.26. Cross-correlation of vortex strength λ'_{ci} and separation point X'_{sep} in $2\delta_0$ spanwise bins.

These findings are significant because it provides strong evidence that the low-frequency separation bubble breathing, which is also correlated with the shock oscillation, is driven by

centrifugal instabilities intrinsic to the separation dynamics itself. The implied mechanism is that the bubble growth due to the shock-induced adverse pressure gradient generates Görtler-type centrifugal instabilities due to concavity of the streamline across the separated zone, which in-turn induces mixing and transports fluid momentum away from the bubble causing it to shrink. When the bubble has shrunk enough, the Görtler-type instabilities weaken. Subsequently the bubble regrows because the adverse pressure gradient still exists due to the compression corner, and the cycle starts again. The mechanism supports the hypothesis suggested by Martín, Priebe & Helm 2016 [39].

5.5.3 Time Correlation of Vortex Convection Velocity and Separation Point Motion

Figure 5.27 shows filtered signals of vortex convection velocity U_c' and separation point fluctuation X_{sep}' averaged over $2\delta_0$ bins across the span on a sample cross-stream plane i240. The signals are split into two equal consecutive time bins ΔT_1 and ΔT_2. Time correlations of U_c' and X_{sep}' are performed in each time bin and averaged to strengthen the statistics. The cross-correlations of U_c' and X_{sep}' averaged in δ_0 and $2\delta_0$ spanwise bins are shown in Figure 5.28 and Figure 5.29, respectively. The binned correlations were shifted to zero lag, smoothed and averaged, resulting in the mean correlation (black line). The mean peaks at zero lag in all cases are in the range 0.45-0.62, indicating a moderately strong correlation between vortex convection velocity and separation point motion. The correlation increases slightly with downstream distance. This suggests that as the bubble grows, the vortices develop, increase in strength and convect faster downstream. Then, as the bubble shrinks, the vortices convect more slowly as they weaken. The mean correlations also indicate a mean periodicity of $\sim 20 L_{Sep}/U_e$, corresponding to a characteristic frequency of $f \approx .05 U_e/L_{sep}$, which is in line with the periodicity observed in

Section 5.5.2 and is within the range of the characteristic low frequency observed in the spectra in Section 5.3.1 .

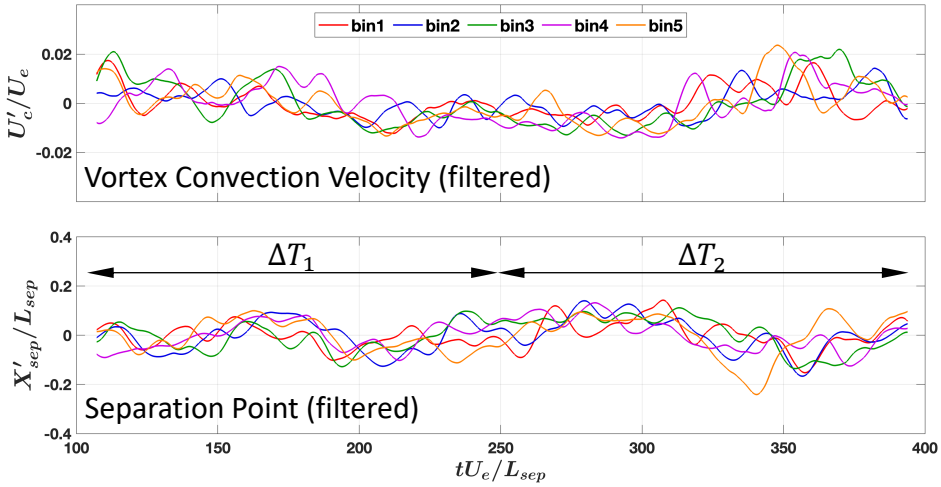


Figure 5.27. Sample signals of convection velocity fluctuation U_c' and separation point fluctuation X_{sep}' on plane $i240$ span-averaged over $2\delta_0$ bins and filtered to remove high-frequency noise.

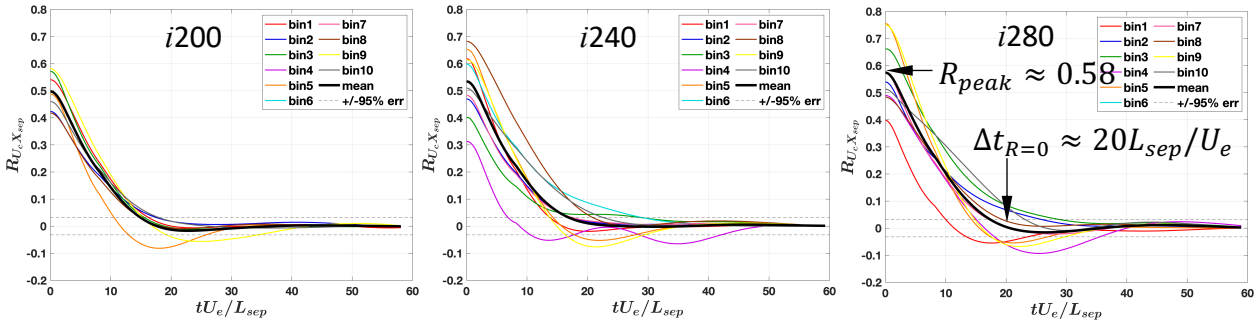


Figure 5.28. Cross-correlation of convection velocity U_c' and separation point X_{sep}' in δ_0 spanwise bins.

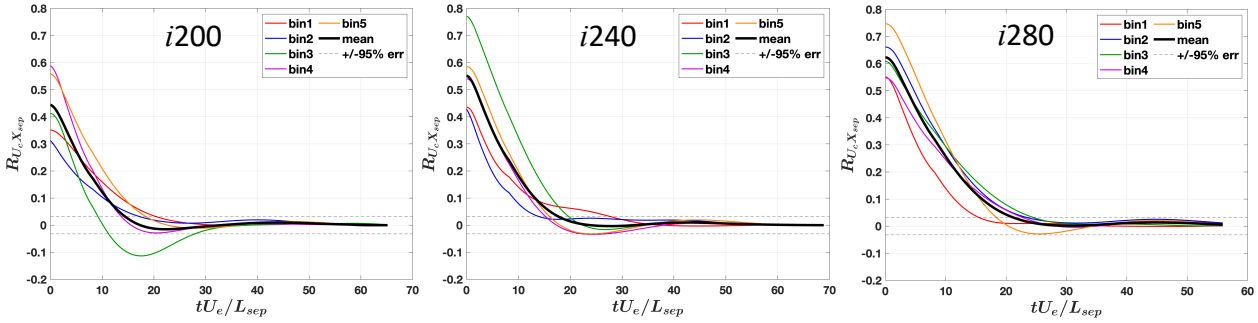


Figure 5.29. Cross-correlation of convection velocity U_c' and separation point X_{sep}' in $2\delta_0$ spanwise bins.

5.5.4 Estimate of Vortex Pitch

One can also obtain a crude estimate of the vortex pitch. The term "vortex pitch", as coined herein, is defined as the distance a vortex travels downstream in one rotation (analogous to the geometrical pitch of a helix or the manufacturing term for pitch of a screw). The cross-sectional area of the vortices can be estimated from the $\Gamma_{1,2}$ algorithm. For the pitch estimate, we assume that the cross-section of a vortex can be approximated by a circle of area equal to the mean area estimated from the algorithm. Then the vortex pitch can be estimated via,

$$L_p \approx \frac{4\pi^2 r^2 \overline{U}_c}{\overline{\Gamma}} = \frac{4\pi \bar{A} \overline{U}_c}{\overline{\Gamma}} \qquad [45]$$

Using the values for mean cross-sectional area $\bar{A} \approx 0.00362\delta_0^2$, mean convection velocity $\overline{U}_c \approx 0.135U_\infty$ and mean circulation $\overline{\Gamma} \approx 0.00434U_\infty\delta_0$, one obtains that the vortex pitch is $L_p \approx 1.4\delta_0 \approx 0.4L_{sep}$. This estimate implies that the vortices convect a distance of $L_p \approx 0.4L_{sep}$ (roughly half a separation length) in one full rotation. Recall that separation length L_{sep} is measured from the corner of the cylinder-flare to the upstream separation point. The pitch estimate is plausible because at least one rotation, or some significant fraction of a rotation, is needed to induce the necessary mixing and fluid entrainment from the separation bubble to sustain the low-frequency contraction and dilation of the bubble.

5.6 Chapter Summary

The low frequency dynamics of the shock-turbulent boundary layer interaction on the Mach 10 cylinder-flare configuration was investigated using solutions obtained via wall-resolved large eddy simulations. Wall measurements of pressure, heat flux and skin friction displayed spikes through the corner interaction and a large degree of unsteadiness about the mean. Instantaneous skin

friction profiles revealed the cyclic breathing of the separation bubble. Power spectra identified a high-energy low-frequency event in the separation point signals that is two orders of magnitude lower than the frequency of the incoming turbulence. This characteristic low frequency event is statistically linked to the periodic growing and shrinking of the separation bubble and shock oscillation. Lowpass filtered flowfields removed the small-scale turbulence and isolated the low-frequency event. Lowpass filtered velocity vector fields showed large scale vortices approximately arranged in counter-rotating pairs across the span with axes oriented in the streamwise direction. The vortices induce a sinusoidal pattern of turbulent momentum across the span, which induces low wall shear stress and wall heat flux in the upwash regions between counter-rotating vortex pairs and high wall shear stress and wall heat flux in the downwash regions between co-rotating vortex pairs. These findings are consistent with that observed in the literature for a supersonic Mach 3 [35] and a hypersonic Mach 7 [36] compression ramps with shock-induced separation. Autocorrelations of spanwise turbulent momentum indicated that the spanwise wavelength of the vortical structures was $\sim\delta_0$, and the mean vortex diameter was $\sim\delta_0/2$, where δ_0 is the incoming boundary layer thickness. This is in contrast to the $\sim 2\delta_0$ wavelength reported for the aforementioned Mach 3 and Mach 7 compression ramps.

The origin of the large-scale vortices appears to be that of Görtler-type instabilities in which the concavity of the dividing streamline between the separation bubble and the shear layer just above incurs a centrifugal force on the fluid that onsets the instability. The dividing streamline computed from the mean flowfield indeed showed a modest concave curvature near separation associated with a modest increase in the Görtler index, and a large concave curvature near reattachment associated with a large spike in the Görtler index. The Görtler index marks the onset of the centrifugal instability if its value exceeds a certain threshold. The Görtler index has been

mainly studied in the context of incompressible laminar flows, so thresholds for turbulent, compressible and separated flows are not established. Nevertheless, the index spiked to more than twice the threshold for incompressible laminar flows.

To investigate the centrifugal instabilities, topological and eigenvalue-based vortex ID methods were used to extract and visualize the large-scale vortical instabilities that extended across the separated region. Two Eulerian vortex ID methods were applied to the lowpass filtered solutions. The first is a pseudo-circulation criterion ($\Gamma_{1,2}$) that identifies a vortex core at a given point on a 2D plane if the net rotational flow, computed using only the topology of the velocity vector field, exceeds a certain threshold. The second method is an eigenvalue value criterion (λ_{ci}) that is an indication of rotation strength and identifies a vortex core if the imaginary component of the complex eigenvalue of the velocity gradient tensor is nonzero. The combination of these criteria applied to the lowpass filtered flowfields was key to accurately capturing the streamwise centrifugal instabilities, including their size, strength, speed, direction of rotation, 3D orientation and transient motion. A time lapse of the centrifugal instabilities showed that the vortical structures extend from just downstream of separation to just downstream of reattachment across the boundary of separation bubble. They are observed to meander short distances in time in both the spanwise and wall normal directions, i.e., they are weakly nonstationary in the cross-stream direction. The vortices also appear to travel a short distance downstream while weakening.

The strength and convection velocity of the vortices were tracked over time and cross-correlated with the separation point fluctuation. The moderately strong time correlations of vortex strength and vortex convection velocity with the separation point motion revealed important insights into the separation dynamics. The results showed that the periodic growth and contraction of the separation bubble is concurrent with the strengthening and weakening, respectively, of the Görtler-

type centrifugal instabilities. The mean period of the cycle deduced from the correlations was consistent with that of the dominant low-frequency peak in the spectra of the separation point fluctuation. This study provided strong evidence that the low frequency pulsations of the separation bubble and shock wave are driven by Görtler-type centrifugal instabilities which are in turn generated by streamline distortion caused by the separation bubble, thus creating a low-frequency feedback loop that is intrinsic to the corner interaction.

Chapter 6: HCF Turbulence Nonequilibrium

6.1 Introduction

Numerical computation of turbulent flow fields has typically utilized Direct Numerical Simulation (DNS), Large Eddy Simulation (LES) and Reynold-Averaged Navier Stokes (RANS) methods. For the last few decades, the most common approach by far, particularly in the commercial sector, is RANS which models all scales of turbulence and therefore incurs significantly less computational cost than higher fidelity LES or DNS. In the RANS equations, the turbulent stresses or Reynolds stresses, $\overline{\rho u_i'' u_j''} = \bar{\rho}\widetilde{u_i'' u_j''}$, need to be modeled in order to close the time-averaged Navier-Stokes system of equations. This forms the basis of RANS turbulence modeling or just simply stated as RANS modeling. RANS models are classed by the number of additional differential (transport) equations required to close the time-averaged Navier-Stokes equations, viz, zero-equation (algebraic), one-equation, two-equation, three-equation and Reynolds stress transport (RST) (also referred to as second-order or second-moment closure) models.

Boussinesq 1877 [5] postulated that the anisotropic turbulent stress tensor is linearly related to the mean strain rate tensor, which when modified for compressible flows is written as,

$$\widetilde{u_i'' u_j''} - \frac{2}{3} k \delta_{ij} = -2\,\mu_t/\bar{\rho}\left(\tilde{S}_{ij} - \frac{1}{3}\tilde{S}_{kk}\delta_{ij}\right) \qquad [46]$$

Equivalently,

$$b_{ij} = -\frac{\mu_t}{\bar{\rho} k}\tilde{S}_{ij}^{dev} \qquad [47]$$

Here μ_t is the turbulent eddy viscosity, k is the turbulent kinetic energy, S_{ij} is the strain rate, S_{ij}^{dev} is the deviatoric mean strain rate and b_{ij} is the Reynolds stress anisotropy tensor. Typically,

0,1,2,3-equation RANS models compute the Reynolds stresses using the Boussinesq hypothesis and are thus known as linear eddy viscosity models (EVM). The Boussinesq hypothesis is based on the assumed similarity between momentum transfer caused by molecular stresses and momentum transfer caused by turbulent stresses. However, the physics of the two processes are fundamentally different and the hypothesis is not accurate for many types of flows. Nevertheless, EVMs have demonstrated significant practical value. The spectrum of EVMs that have evolved is mainly based on the modeling of the turbulent eddy viscosity μ_t.

At the lowest fidelity are algebraic zero-equation models that compute the Reynolds stresses using the Boussinesq eddy-viscosity relation which in turn is computed based on the mixing-length hypothesis (e.g., Prandtl 1925 [102], Cebeci-Smith 1974 [103], Baldwin-Lomax 1978 [104], Johnson-King-Coakley 1985/1987/1990 [105],[106],[107]). One- and two-equation transport models are most popular for their balance of fidelity and computational expense. One-equation models compute the Reynolds stresses using the Boussinesq eddy-viscosity relation which in turn is computed from the transport of turbulent kinetic energy k (e.g., Prandtl 1945 [108], Emmons-Glushko 1965 [109],[110], Wolfshtein 1967 [111], Bradshaw-Ferris-Atwell 1967 [112], Goldberg 1991 [113]), or from the transport of eddy viscosity μ_t itself or related variable (e.g., Baldwin-Barth 1990 [114], Spalart-Allmaras 1992 [115], Wray-Agarwal 2018 [116]). Two-equation models also compute the Reynolds stresses using the Boussinesq eddy-viscosity relation which in turn is computed from the transport of turbulent kinetic energy k and the transport of a turbulence scale of which several choices exist, e.g., the turbulence dissipation rate ϵ, the specific turbulence dissipation rate ω, the turbulent length scale l or turbulent timescale τ. Some popular two-equation models include Jones-Launder 1972 k-ϵ [117], Launder-Sharma 1974 k-ϵ [118], Chien 1982 k-ϵ [119], Shih et al. 1995 Realizable k-ϵ [120], Yakhot et al 1992 RNG k-ϵ [121], Menter SST 1994

k-ω [122], Menter BSL 1994 k-ω [122], Wilcox 2006 k-ω [123]. Three-equation models additionally solve a third transport equation, e.g., Goldberg et al. 2009 k-ϵ-R_t [124] where R_t is a pseudo-eddy viscosity, Durbin 1995 k-ϵ-$\overline{v^2}$ elliptic relaxation model [125] where $\overline{v^2}$ is a turbulence velocity scale, and Hanjalić et al. 2004 k-ϵ-ζ elliptic relaxation model [126] where $\zeta = \overline{v^2}/k$.

While the linear Boussinesq relation has seen widespread use in engineering applications, the relation fares poorly in flows with rapid changes in strain rate, high surface curvature, rotating flows, secondary motions and many three-dimensional flows. The linear Boussinesq relation is inherently an equilibrium expression that implies that the Reynolds anisotropy tensor is a linear function of the local instantaneous mean strain rate. In the presence of strong-enough nonequilibrium effects, there is a phase lag between the turbulence anisotropy and mean strain rate that cannot be accounted for by Eq. [47] (Hamlington & Dahm 2008 [127]). To address one or more of these deficiencies, nonlinear extensions of the Boussinesq relation, referred to as nonlinear EVMs, have been developed, e.g., Lien et al. 1996 cubic k-ϵ [128], Olsen & Coakley 2001 lag model [129], Hamlington & Dahm 2008 [127], and the wider class of Algebraic Stress Models (ASMs) such as Hellsten 2005 ASM [130] and Abdol-Hamid 2018 k-kL ASM [131], among others.

At a higher fidelity of modeling is the transport of the Reynolds stress tensor itself, requiring six transport equations, one for each component of the tensor. Typically, an additional seventh transport equation for a turbulence scale is required, such as ϵ or ω. RST models obviate the need for the Boussinesq relation. The conceptual advantage of RST models is the natural incorporation of non-local effects, history effects and sudden changes in strain rate, streamline curvature, rotation and body forces. Linear EVMs on the other hand require empirical terms to model these effects.

The RST equations involve higher-order correlations that require modeling and is an active area of research. Chou 1945 [132] and Rotta 1951 [133] established the earliest known full closure modeling of the RST equation. Many notable researchers have since contributed to modeling of the RST equation. Several such models will be discussed later.

All RANS models contain multiple terms that require modeling. Models are semi-empirical in nature and have been calibrated and validated over the years with varying levels of success using theory, experiment, DNS and LES solutions of canonical flows such as wall-bounded flows (flat plates, channel flows, pipe flows) and free shear flows (wakes, mixing layers, jets), among others (Wilcox 2006 [134], Pope 2000 [135]). Many such early canonical studies were incompressible and have served as a guide for developing models for supersonic compressible flows. Extension of the models to hypersonic compressible flows is less studied, and even more so for nonequilibrium flows such as those with shock wave interactions. Part of the difficulty lies in the ability to obtain detailed turbulence statistics for model development with reliable accuracy from both experiment and numerical simulation. While experiments are key tools for system design and model validation, high-fidelity LES and DNS numerical solutions can be mined to obtain more detailed turbulence physics that complement experimental measurements, e.g., velocity and thermodynamic correlations and related higher-order moments.

Shock wave interactions with solid boundaries have been study extensively for decades via experiment and simulation with progress reviews at various times, e.g., Zuo & Pirozzoli 2024 [6], Gaitonde & Adler 2023 [7], Sabnis & Zabinsky 2023 [8], Gaitonde 2015 [9], Gnoffo et al. 2013 [10], Roy & Blottner 2006 [11], Knight et al. 2003 [12], Andreopoulos et al. 2000 [13], Settles & Dolling 1992 [14], Settles & Dodson 1991/1994 [15]-[16], Fernholz et al. 1989 [17] and Fernholz & Finley 1981 [18]. Many studies provide mean data (such as velocity, pressure, wall heat flux

and skin friction) but often limited turbulence data. Studies that use RANS methods rely on modeling of the full turbulence spectrum and can only provide time-averaged data. Unsteady RANS (URANS) can provide low-frequency unsteady data but cannot be relied on for high-frequency turbulence statistics. Even for mean flow prediction, as discussed above, RANS models are known to be less reliable for flows with shock-boundary layer interactions in which nonequilibrium effects persist (Georgiadis et al. 2015 [19] and Debonis et al. 2012 [20]). Few studies provide the richer set of turbulence dynamics in the nonequilibrium separated and post-shock flow regions desired for turbulence model development and a priori model validation. Even fewer such studies exist for the hypersonic regime ($M \gtrsim 5$) in which compressibility and nonequilibrium effects become more important and need to be accounted for by models to capture the flow physics. Some studies that have reported SBLI turbulence statistics in some detail using LES or DNS include Helm & Martín 2022 [21], Priebe & Martín 2021 [22], Fang 2020 [23], Vyas et al. 2019 [24], Morgan et al. 2013 [25], Wu & Martín 2007 [26], Pirozzoli & Grasso 2006 [27], and Loginov et al. 2006 [28].

In this work, the turbulence dynamics are analyzed in the Mach 10 axisymmetric hollow cylinder-flare (HCF) compression corner with shock-induced flow separation. The Reynolds stresses, their properties and their transport mechanisms (often referred to as budgets) as described by the RST equation are analyzed. The a priori performance of closures used to model the RST budgets are evaluated using the LES flowfield solutions. The thermodynamic fluctuations and turbulent heat flux that appears in the time-averaged energy equation are also analyzed. Note that since turbulent kinetic energy (TKE) is the trace of the Reynolds stress tensor, similar modeling approaches are also used in the transport of TKE, i.e., the k-equation. Note that an extensive list of models exists in the literature. Here, a suite of classical single-point closure models and

assumptions that are commonly used in industrial-level codes were selected to be evaluated. The objective is to provide detailed insight into the turbulence dynamics to inform model development for EVMs and RSTs.

6.2 The Reynolds Stress Transport and Turbulent Kinetic Energy Transport Equations

6.2.1 The Reynolds Stress Transport Equation

The Reynolds stress tensor is given by,

$$\bar{\rho}\tau_{ij} = \overline{\rho u_i'' u_j''} = \bar{\rho}\widetilde{u_i'' u_j''} \quad [48]$$

Here Einstein summation notation is used where subscripts $i, j = 1, 2, 3$ represent the three spatial directions. The RST equation is obtained by taking the second-moment of the Navier-Stokes momentum equation as follows. Let

$$\mathcal{N}(u_i) = 0 \quad [49]$$

be the symbolic representation of the Navier-Stokes equation. Then the second-moment is formed by multiplying by u_i'' and time-averaging, viz,

$$\overline{u_i'' \mathcal{N}(u_j) + u_j'' \mathcal{N}(u_i)} = 0 \quad [50]$$

After some derivation, one obtains the exact compressible RST equation in Eq. [51], the terms of which are described by Eqs. [52-60]. The left hand side is the material derivative of the Reynolds stresses consisting of the unsteady term and the convection term. The transport of Reynolds stresses is controlled by the balance of processes on the right hand side. Except for production and viscous diffusion, all other terms on the right hand side require modeling. In many approaches some terms are assumed negligibly small. The transport processes will be discussed in more detail in later sections.

$$\frac{D}{Dt}\left(\bar{\rho}\tau_{ij}\right) = \frac{\partial}{\partial t}\left(\bar{\rho}\tau_{ij}\right) + \mathcal{C}_{ij} = \mathcal{P}_{ij} + \mathcal{D}_{ij} + \Pi_{ij} - \epsilon_{ij} + \mathcal{M}_{ij} \quad [51]$$

Convection: $$\mathcal{C}_{ij} = \frac{\partial}{\partial x_k}\left(\widetilde{u_k}\bar{\rho}\tau_{ij}\right) \quad [52]$$

Production: $$\mathcal{P}_{ij} = -\bar{\rho}\tau_{ik}\frac{\partial \widetilde{u_j}}{\partial x_k} - \bar{\rho}\tau_{kj}\frac{\partial \widetilde{u_\iota}}{\partial x_k} = -\bar{\rho}\tau_{ik}\left(\tilde{S}_{kj} - \widetilde{W}_{kj}\right) - \bar{\rho}\tau_{jk}\left(\tilde{S}_{ik} + \widetilde{W}_{ik}\right) \quad [53]$$

Diffusion: $$\mathcal{D}_{ij} = \mathcal{D}_{ij}^{V} + \mathcal{D}_{ij}^{T} + \mathcal{D}_{ij}^{P} \quad [54]$$

Viscous Diffusion: $$\mathcal{D}_{ij}^{V} = \frac{\partial}{\partial x_k}\left[\overline{u_\iota'' t_{jk}''} + \overline{u_j'' t_{\iota k}''}\right] \quad [55]$$

Turbulent Diffusion: $$\mathcal{D}_{ij}^{T} = -\frac{\partial}{\partial x_k}\left[\overline{\rho u_\iota'' u_j'' u_k''}\right] \quad [56]$$

Pressure Diffusion: $$\mathcal{D}_{ij}^{P} = -\frac{\partial}{\partial x_k}\left[\overline{p' u_\iota''}\delta_{jk} + \overline{p' u_j''}\delta_{ik}\right] \quad [57]$$

Viscous Dissipation: $$\epsilon_{ij} = \overline{t_{jk}''\frac{\partial u_\iota''}{\partial x_k} + t_{\iota k}''\frac{\partial u_j''}{\partial x_k}} = \overline{t_{\iota k}'' s_{kj}''} + \overline{t_{kj}'' s_{\iota k}''} - \left(\overline{t_{\iota k}'' \omega_{kj}''} - \overline{t_{kj}'' \omega_{\iota k}''}\right) \quad [58]$$

Pressure Strain: $$\Pi_{ij} = \overline{p'\left(\frac{\partial u_\iota''}{\partial x_j} + \frac{\partial u_j''}{\partial x_\iota}\right)} = \overline{p' s_{\iota j}''} \quad [59]$$

Turbulent Mass Flux: $$\mathcal{M}_{ij} = \overline{u_\iota''}\left(\frac{\partial \bar{t}_{jk}}{\partial x_k} - \frac{\partial \bar{p}}{\partial x_j}\right) + \overline{u_j''}\left(\frac{\partial \bar{t}_{ik}}{\partial x_k} - \frac{\partial \bar{p}}{\partial x_i}\right) \quad [60]$$

In the equations above the following are defined,

Viscous Stress Tensor: $$t_{ij} = 2\mu\left(S_{ij} - \frac{1}{3}S_{kk}\delta_{ij}\right), \quad t_{ij}'' = t_{ij} - \tilde{t}_{ij} \quad [61]$$

Strain Rate Tensor: $$S_{ij} = \frac{1}{2}\left(\frac{\partial u_i}{\partial x_j} + \frac{\partial u_j}{\partial x_i}\right), \quad s_{ij}'' = S_{ij} - \tilde{S}_{ij} \quad [62]$$

Rotation Rate Tensor: $$W_{ij} = \frac{1}{2}\left(\frac{\partial u_i}{\partial x_j} - \frac{\partial u_j}{\partial x_i}\right), \quad \omega_{ij}'' = W_{ij} - \widetilde{W}_{ij} \quad [63]$$

6.2.2 The Turbulent Kinetic Energy Transport Equation

The turbulent kinetic energy (TKE) is one-half the trace of the Reynolds stress tensor given by,

$$\bar{\rho}k = \frac{1}{2}\bar{\rho}\tau_{ii} = \frac{1}{2}\overline{\rho u_\iota'' u_\iota''} = \frac{1}{2}\bar{\rho}\widetilde{u_\iota'' u_\iota''} \quad [64]$$

where k is the specific TKE. The TKE transport equation is therefore one-half the trace of the RST equation, for example $\mathcal{P} = \mathcal{P}_{ii}/2$. The exact compressible TKE transport equation is given by Eq [65]. Except for viscous diffusion, all right hand side terms require modeling, including production (unlike the RST equation).

$$\bar{\rho}\frac{Dk}{Dt} = \bar{\rho}\frac{\partial k}{\partial t} + \mathcal{C} = \mathcal{P} + \mathcal{D}^V + \mathcal{D}^T + \mathcal{D}^P + \Pi - \epsilon + \mathcal{M} \quad [65]$$

Convection: $$\mathcal{C} = \frac{\partial}{\partial x_k}\left(\widetilde{u_k}\bar{\rho}\tau_{ij}\right) \quad [66]$$

Production: $$\mathcal{P} = -\bar{\rho}\tau_{ik}\frac{\partial \widetilde{u_\iota}}{\partial x_k} = -\bar{\rho}\tau_{ik}\tilde{S}_{ki} \quad [67]$$

Diffusion: $$\mathcal{D} = \mathcal{D}_{ij}^V + \mathcal{D}_{ij}^T + \mathcal{D}_{ij}^P \quad [68]$$

Viscous Diffusion: $$\mathcal{D}^V = \frac{\partial}{\partial x_k}\left[\overline{u_\iota'' t_{\iota k}''}\right] \quad [69]$$

Turbulent Diffusion: $$\mathcal{D}^T = -\frac{\partial}{\partial x_k}\left[\overline{\rho u_\iota'' u_\iota'' u_k''}\right] \quad [70]$$

Pressure Diffusion: $$\mathcal{D}^P = -\frac{\partial}{\partial x_k}\left[\overline{p' u_\iota''}\delta_{ik}\right] \quad [71]$$

Viscous Dissipation: $$\epsilon = \overline{t_{\iota k}''\frac{\partial u_\iota''}{\partial x_k}} = \overline{t_{\iota k}'' s_{k\iota}''} \quad [72]$$

Pressure Dilatation: $$\Pi = \overline{p'\frac{\partial u_\iota''}{\partial x_\iota}} = \overline{p' s_{kk}''} \quad [73]$$

Turbulent Mass Flux: $$\mathcal{M} = \overline{u_\iota''}\left(\frac{\partial \bar{t}_{ik}}{\partial x_k} - \frac{\partial \bar{p}}{\partial x_i}\right) \quad [74]$$

6.3 Flowfield Processing

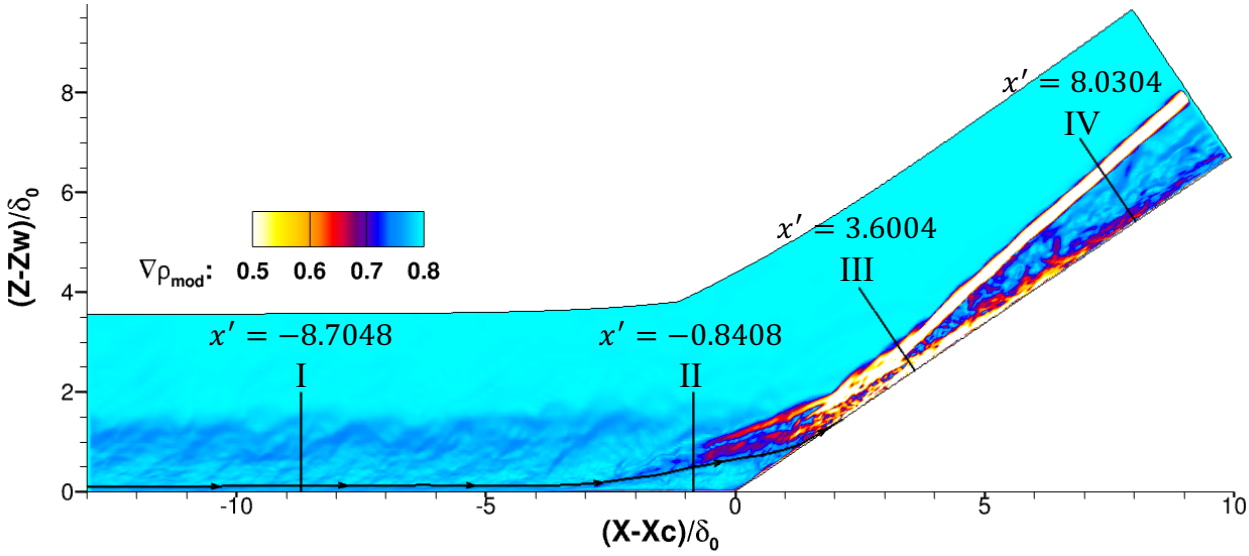


Figure 6.1. Wall normal extraction locations annotated by streamwise location $x' = (x - x_c)/\delta_0$. Contours are instantaneous modified density gradient.

Wall normal boundary profiles were extracted from 3D LES solutions of the HCF flowfield. The profiles were extracted at four axial locations on the streamwise centerplane as displayed in Figure 6.1. The profiles were time-averaged over 942 δ_0/U_∞ or 12ms, which approximately represents 37 flowtimes through the domain. The profiles were not span-averaged or spatially averaged. Unless otherwise stated, 2D flow contours are time-averaged over the same time period and then span-averaged. During postprocessing, derivatives were computed using a 4th-order central stencil for first derivatives and a 2nd-order central stencil for second derivatives. At boundaries, such as at the wall, a 2nd-order one-sided stencil was used. Where possible, classical turbulence theory and RANS models are evaluated using the LES solutions. Unless otherwise stated wall normal distance will be in units z/δ_0 and/or $z^* = z/z_\tau^*$. The latter is the semilocal scaling of Huang et al. 1995 [68] that uses local density instead of wall density such that $z_\tau^* = \tilde{\mu}(z)/(\tilde{\rho}(z)u_\tau^*)$ and $u_\tau^* = \sqrt{\tau_w/\tilde{\rho}(z)}$. This scaling produces better collapse of data for

compressible wall bounded flows as demonstrated by Coleman 1995 [136], Maeder 2000 [137], Morinishi et al. 2004 [138] and Duan et al. 2010/2011 [49],[50].

6.4 Reynolds Stresses and Turbulent Kinetic Energy

Figure 6.2 shows the Favre-averaged Reynolds stresses and TKE normalized by the upstream friction velocity squared at location I, $u_{\tau,ref}^2$, on time-averaged and span-averaged streamwise planes. All Reynolds stresses have maximum amplification at the corner interaction. Strong amplification occurs immediately following separation and persists through the shear layer above the separation bubble and towards the reattachment region and shock impingement location at $x/\delta \approx [-3,3]$. All stresses appear to attain their maximum values close to the wall near the reattachment region and/or near the shock line following reattachment. Stress $\widetilde{u''^2}$ is the largest stress reaching values over three times the other stresses, with high values throughout the separation shear layer and peaking slightly off the wall near reattachment. Stress $\widetilde{v''^2}$ peaks very near the wall in the reattachment region. Stress $\widetilde{w''w''}$ peaks in the near wall region of reattachment as well as along the shock line more so near the foot of the shock. The latter is likely due to the shock oscillation which causes the w-velocity component to oscillate between the almost zero freestream value and the larger positive value in the post-shock deflection region, driving the observed strong fluctuation in w''. Stress $\widetilde{u''w''}$ shows a smaller positive peak in the near-wall reattachment region, and a larger negative peak region along the shock line near the foot of the shock. The latter is likely due to the shock jump which causes a decrease in u-velocity and an increase in w-velocity and shock oscillations which cause the out-of-phase (negatively correlated) fluctuations of u'' and w''. Stresses $\widetilde{u''v''}$ and $\widetilde{v''w''}$ show peaks in a small region near the wall near reattachment, although their magnitudes are much smaller than the other stresses.

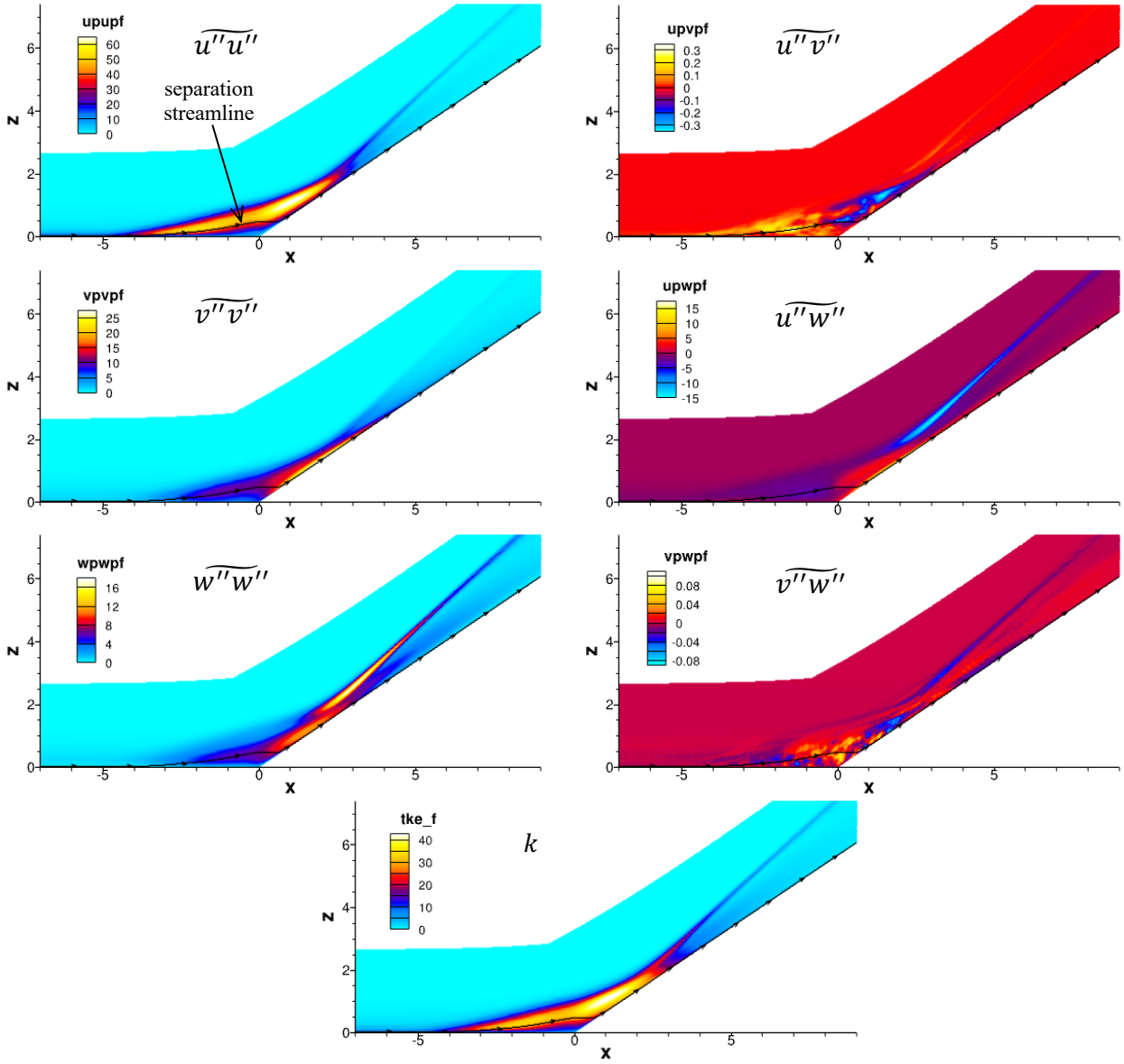


Figure 6.2. Reynolds stresses and TKE, scaled by upstream $u^2_{\tau,ref}$.

To obtain more insight into the turbulence amplification, the Favre-averaged Reynolds stresses and TKE along the wall-normal lines at each of the axial locations I-IV are plotted in Figure 6.3 scaled by the upstream wall friction velocity squared at location I, $u^2_{\tau,ref}$. Figure A.1 and Figure A.2 (Appendix) also show the Reynolds stresses scaled by the semi-local Morkovin factor $(\bar{\rho}/\bar{\rho}_w)^{.5}u_\tau^{-2}$ and by the local TKE, respectively. The former scaling has been shown to provide

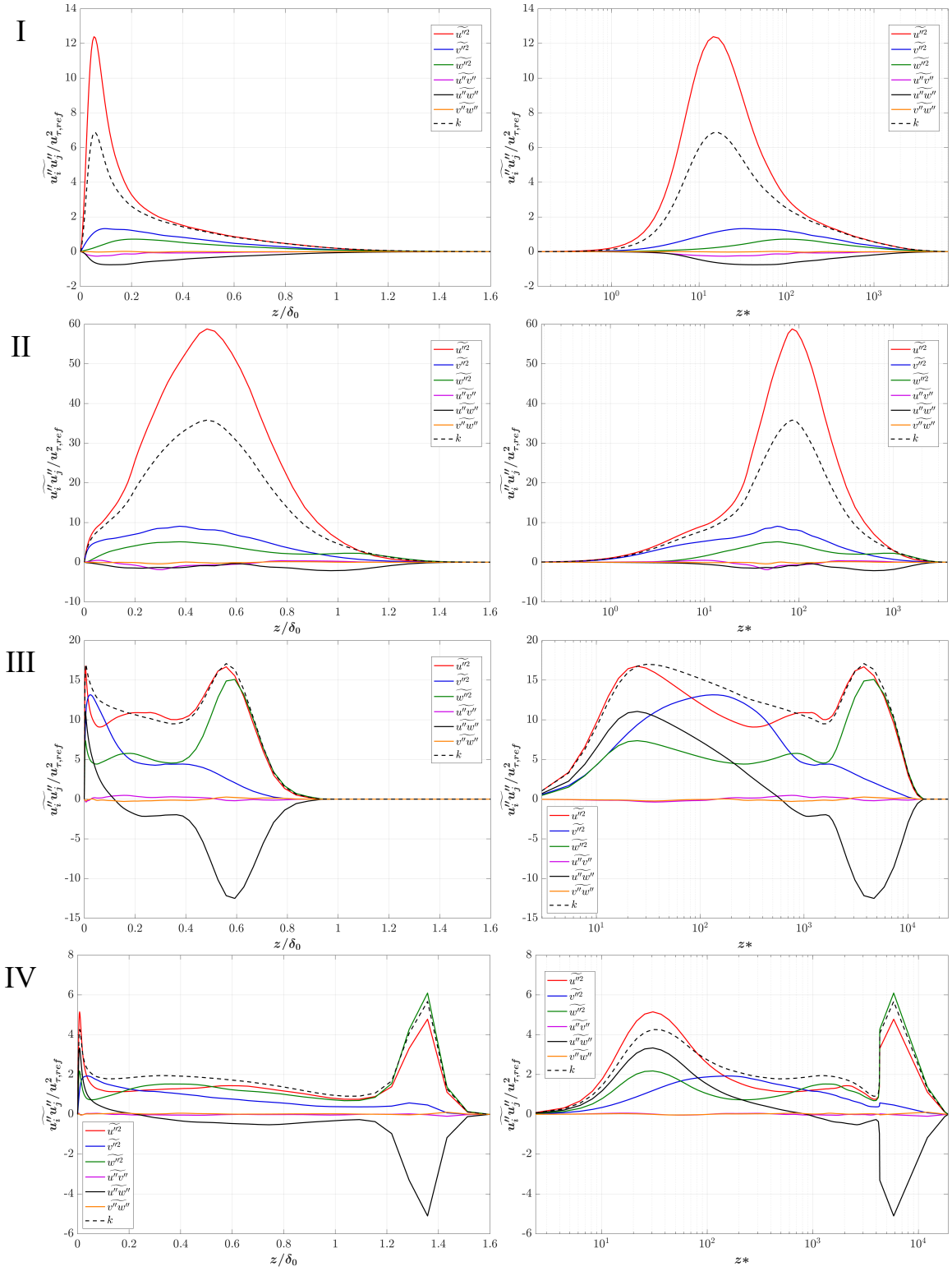


Figure 6.3. Reynolds stresses and TKE vs. z/δ_0 (left) and z^* (right), scaled by $u_{\tau,ref}^2$.

better collapse of data across Mach numbers. For all Reynolds stress 1D plots at the four locations, the u, v, w-velocity components have been rotated so that u is parallel to the wall, v is azimuthally tangential to the wall and w normal to the wall. The stresses are plotted from the wall to the freestream in all cases, including through the shock line for the downstream locations. Referring to Figure 6.3-I, the profile at upstream location I is representative of a canonical equilibrium turbulent boundary layer. There is a large peak in the normal stress $\widetilde{u''^2}$ close to the wall at $z^* \approx 17$, which approximately coincides with peak turbulence production (see Figure 6.6-I) and the strongest fluid ejection and sweep events. Following the peak, $\widetilde{u''^2}$ decreases monotonically to zero at the boundary layer edge. Normal stresses $\widetilde{v''^2}$, $\widetilde{w''^2}$ and shear stress $\widetilde{u''w''}$ are smaller in magnitude with peaks in the near wall region. Shear stresses $\widetilde{u''v''}$ and $\widetilde{v''w''}$, i.e., cross-correlations with $\widetilde{v''}$, are almost negligible. The growth in $\widetilde{u''^2}$ and $\widetilde{v''^2}$ from the wall is larger in magnitude than that of $\widetilde{w''^2}$ and $\widetilde{u''w''}$. This is consistent with a Taylor series analysis of the boundary condition for a canonical wall bounded flow where it can be shown that k, $\widetilde{u''^2}$ and $\widetilde{v''^2}$ increase as z^2, while $\widetilde{w''^2}$ and $\widetilde{u''w''}$ increase as z^4 and z^3, respectively, where z is normalized by boundary layer thickness. The shear stress $\widetilde{u''w''}$ is negative, as expected, due to momentum transfer of faster moving fluid away from the wall towards slower moving fluid near the wall.

Through the corner interaction and following reattachment, Figure 6.3 shows significant amplification of the Reynolds stresses. The maximum amplification, A_{ij}, at a given axial location (not necessarily the global maximum in the flowfield) can be quantified by the ratio of maximum stress along the wall normal profile at that axial location to the maximum stress upstream in the undisturbed boundary layer (location I herein), as given by Eq [75]. The amplification factors for the downstream locations II-IV are given in Table 6.1. Also shown are the wall normal locations where the maximum amplification occurs in units z/δ_0, where δ_0 is the reference upstream

boundary layer thickness. The maximum amplifications across the three locations are marked by an asterisk. Note that while $\widetilde{u''v''}$ and $\widetilde{v''w''}$ show seemingly non-negligible amplification (greyed out values in Table 6.1), their magnitudes as noted in Figure 6.3 at all locations are relatively small. Therefore, the focus of the discussion will be on the four remaining stresses.

$$A_{ij} = \max\left|\widetilde{u_i''u_j''}\right|_x / \max\left|\widetilde{u_i''u_j''}\right|_{ref} \quad [75]$$

Table 6.1. Downstream Amplification of Reynolds Stresses

Location	Amplification and Location	$\widetilde{u''^2}$	$\widetilde{v''^2}$	$\widetilde{w''^2}$	$\widetilde{u''w''}$	$\widetilde{u''v''}$	$\widetilde{v''w''}$
II	A_{ij}	4.75*	6.82	7.13	2.84	7.25*	13.2*
	z/δ_0	0.48	0.38	0.38	0.97	0.31	0.29
III	A_{ij}	1.35	9.90*	10.2*	14.7*	1.62	7.07
	z/δ_0	.005	.023	.005	.005	.122	.007
IV	A_{ij}	0.42	1.45	3.02	4.44	0.23	1.97
	z/δ_0	.008	.038	.008	.008	.004	.168

At location II, all stresses are significantly amplified in the corner interaction. The maximum amplification of the normal stresses $\widetilde{u''^2}$, $\widetilde{v''^2}$ and $\widetilde{w''^2}$ shift from the near-wall region to the core of the free shear layer just above the separation bubble, moving further away from the wall, and approximately coinciding with the location of the inflection points in the mean $\tilde{u}$, $\tilde{v}$, and $\tilde{w}$ profiles in Figure 4.5, similar observations have been reported by Helm & Martín 2021 [75], Helm & Martín 2022 [21], Fang et al. 2020 [23] and Dupont 2008 [98]. While the maximum amplification of shear stress $\widetilde{u''w''}$ appears to occur at the edge of the shear layer towards the freestream, its magnitude is small relative to the other components at this location.

At locations III & IV following reattachment, multiple peaks in the stresses are observed. All stresses peak near wall. Following the near-wall peak, the normal stresses $\widetilde{u''^2}$, $\widetilde{v''^2}$ and $\widetilde{w''^2}$ remain elevated (unlike at I & II) through the diffusing free shear layer between the wall and the shock, and they remain positively elevated all the way to near the shock line. While shear stress $\widetilde{u''w''}$ is negative in the upstream region at I (as expected) and in the separated corner at II, it is strongly positively amplified in the near-wall region downstream of reattachment at III & IV, after which it decreases to a steady negative value through the shear layer and all the way to near the shock line. The second large peak in the stresses occurs across the shock wave at $z/\delta_0 \approx 0.6$ and 1.35 for locations III & IV, respectively. The exception is $\widetilde{v''^2}$ which decreases monotonically through the shock wave at III and shows a very small peak at the shock location at IV. The normal stresses remain positive through the shock wave, while shear stress $\widetilde{u''w''}$ is negative. Note that at the furthest downstream location IV, more grid resolution through the shock wave would result in smoother peaks, but this does not detract from the analysis herein.

Across the three locations, maximum amplification of $\widetilde{u''^2}$ occurs at location II reaching $A_{11} \approx 5$, and of $\widetilde{v''^2}$, $\widetilde{w''^2}$ and $\widetilde{u''w''}$ at location III with values of $A_{22} \approx A_{33} \approx 10$ and $A_{13} \approx 15$, respectively. Of the three locations, stress $\widetilde{u''w''}$ is therefore the strongest amplified component, followed by normal stresses $\widetilde{v''^2}$ and $\widetilde{w''^2}$, and then normal stress $\widetilde{u''^2}$. In general, the magnitudes of the stresses decrease when marching downstream through the recovering boundary layer on the flared section. At IV, $\widetilde{u''^2}$ appears to be 'damped' rather than amplified relative to location I.

6.5 Reynolds Stress Anisotropy

Classical modeling of the Reynolds stresses and transport processes have been constructed, in part, by examining the anisotropic nature of turbulence. Isotropic turbulence is the state whereby

turbulence fluctuations are independent of direction. Any deviation from the isotropic state, such as shear flows in boundary layers and mixing layers, is characterized by the anisotropy tensor. The normalized anisotropy tensor can be written as,

$$b_{ij} = \widetilde{u_i'' u_j''}/(2k) - \delta_{ij}/3 \qquad [76]$$

One can further characterize the anisotropic state via the invariants of the anisotropic tensor. Since b_{ij} is deviatoric, its first invariant, the trace, is zero ($I = b_{ii} = 0$). Consequently, b_{ij} can be characterized by its two independent second and third invariants given by,

$$II = -b_{ij}b_{ji}/2\,, \qquad III = b_{ij}b_{jk}b_{ki}/3 \qquad [77]$$

A modified form of the invariants convenient for plotting can be written as,

$$\zeta = (III/2)^{1/3}, \qquad \eta = (-II/3)^{1/2} \qquad [78]$$

Figure 6.4 plots the anisotropy tensor as a function of wall normal distance at locations I-IV. Figure 6.5 plots the locus of the invariants in the (ζ, η) plane at the four locations. In Figure 6.4 and Figure 6.5, the maximum wall normal distance was limited to the freestream-boundary layer edge at I & II, and just before the shock wave at the downstream locations III & IV. The physically realizable limits of the invariant pair mapping in Figure 6.5 is marked by a somewhat triangular shape, also known as a Lumley triangle (Lumley 1977 [139]). The vertices of the triangle (0,0), (1/3,1/3) and (-1/6,1/6) correspond to isotropic (iso), one-component (1C) and two-component axisymmetric (2C, axi) turbulence, respectively. The top, right and left sides of the triangle correspond to two-component (2C), axisymmetric prolate (elongated) and axisymmetric oblate (compressed) turbulence, respectively. This is depicted in the top plot of Figure 6.6. Axisymmetric prolate turbulence implies one dominant normal stress and two smaller normal stresses. Axisymmetric oblate turbulence implies two dominant normal stresses and one smaller normal stress.

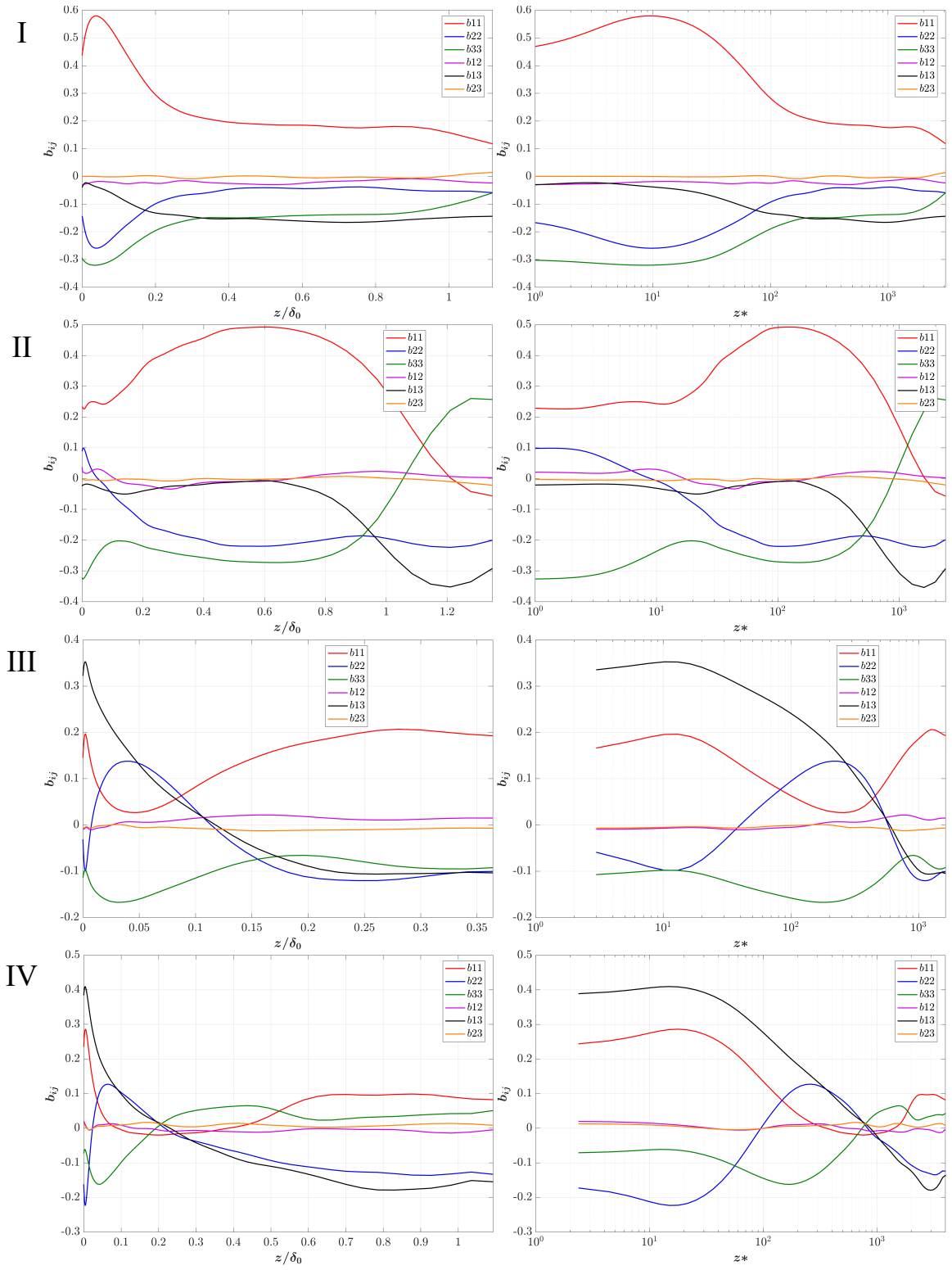


Figure 6.4. Reynolds stress anisotropy tensor vs. z/δ_0 (left) and z^* (right).

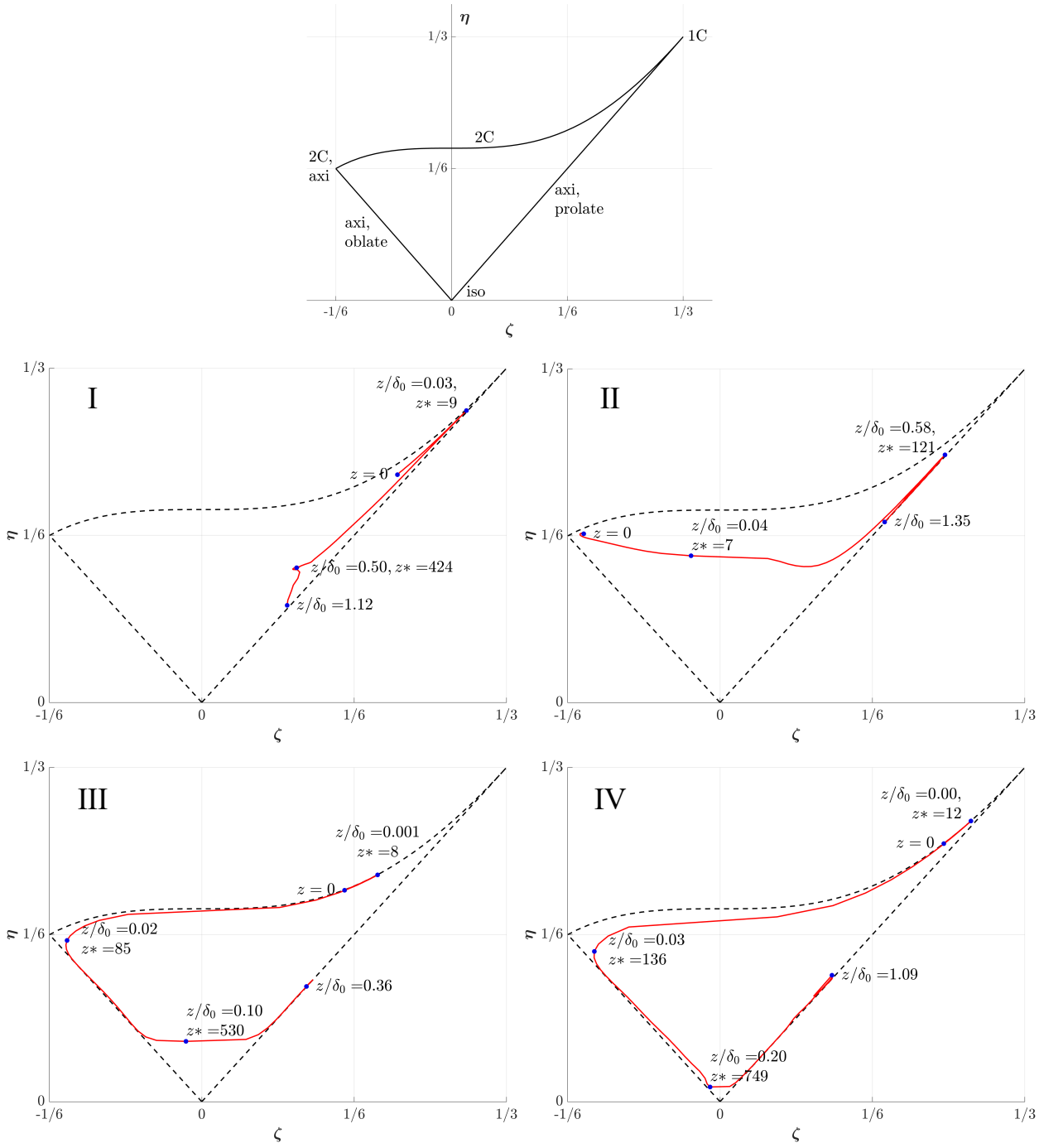


Figure 6.5. Reynolds stress anisotropy invariant map (Lumley triangles).

The Reynolds stresses at any point in a turbulent flow must fall within the Lumley triangle. The Lumley triangle therefore defines 'realizability' constraints on the Reynolds stress tensor. It follows that any turbulence modeling of Reynolds stress transport phenomena should obey this

realizability constraint. A convenient way to quantify this realizability is to look at the behavior of dF/dt, where F is the normalized determinant of the Reynolds stress tensor as given by Eq [79]. Within the triangle $F > 0$, on the 2C line $F = 0$, and above the 2C line $F < 0$. A model that then satisfies Eq [80] is said to satisfy strong realizability. A model that satisfies Eq [80] or Eq [81] is said to satisfy weak realizability.

$$F \equiv \det\left[\frac{\widetilde{u_i''u_j''}}{\frac{1}{3}\widetilde{u_k''u_k''}}\right] \quad [79]$$

$$dF/dt|_{F=0} = 0, \qquad d^2F/dt^2|_{F=0} > 0 \quad [80]$$

$$dF/dt|_{F=0} > 0 \quad [81]$$

At the upstream equilibrium boundary layer at location I, two-component turbulence is realized very near the wall where the invariant map tracks near the top of the Lumley triangle for $z/\delta_0 \lesssim 0.03$ and where $\widetilde{u''^2}, \widetilde{v''^2} \gg \widetilde{w''^2}$. This is due to the damping effect of the wall on $\widetilde{w''}$. Anisotropy reaches a peak at $z/\delta_0 \approx 0.03$ near the right vertex of the triangle where the turbulence is essentially one-component dominated by $\widetilde{u''}$. Marching away from the wall, the invariant map tracks along the right side of the triangle representing axisymmetric prolate turbulence which is characteristic of the log-layer and where $\widetilde{u''^2}$ is larger than $\widetilde{v''^2}$ & $\widetilde{w''^2}$. Approaching the boundary layer edge, the turbulence becomes more isotropic as the invariant trace approaches the bottom vertex of the triangle.

In the separated region at location II, there is a significant distortion of the invariant curve from the upstream location I. At II, the turbulence is two-component axisymmetric very near the wall with $\widetilde{u''^2}$ & $\widetilde{v''^2}$ larger than $\widetilde{w''^2}$. The curve tracks through the middle of the triangle but closer to the two-component state until it reaches the one-component state dominated by $\widetilde{u''^2}$. The

turbulence becomes axisymmetric prolate as it approaches the freestream with $\widetilde{u''^2}$ being larger but decreasing at a faster rate than $\widetilde{v''^2}$ & $\widetilde{w''^2}$.

At locations III & IV in the post-reattachment zone, the invariant curves are similar but differ significantly from that at I & II. At III & IV, the turbulence is two-component dominated by $\widetilde{u''^2}$ & $\widetilde{v''^2}$ in the viscous near-wall region. The turbulence then becomes two-component oblate as it approaches the left side of the triangle where $\widetilde{u''^2}$ & $\widetilde{v''^2}$ is larger than $\widetilde{w''^2}$. This is characteristic of the core of a mixing layer which is present between the boundary layer and the shock line. Away from the core, the turbulence tends more to isotropy (proximity to lower vertex), then approaches an axisymmetric prolate state as the invariant curve hugs the right side of the triangle where $\widetilde{u''^2}$ is larger than $\widetilde{v''^2}$ & $\widetilde{w''^2}$.

6.6 Turbulent Kinetic Energy Transport Budgets

The compressible Favre-averaged transport equations for TKE and Reynolds stresses are given in Eq [65] and Eq [51], respectively. The right hand side terms are the so-called budgets that serve as sources or sinks. Typically, the budgets through a wall normal boundary layer profile are scaled by the local viscous wall units. Here the viscous wall units at the upstream station I are used instead to scale all downstream locations in order to compare the change in budgets across the stations, and also because in the separated region the friction velocity becomes small thereby skewing the analysis. Figure 6.6 shows the budgets (labeled as $\mathcal{B}$ on the y-axis) of the TKE transport equation along wall-normal lines at locations I-IV. The plots are normalized by the reference viscous wall units $\bar{\rho}_w \bar{u}_\tau^3/\bar{z}_\tau = \bar{\rho}_w \bar{u}_\tau^4/\bar{\nu}_w$ computed at upstream location I. The maximum wall normal distance

was limited to the freestream edge at I & II, and just before the shock wave at the downstream locations III & IV.

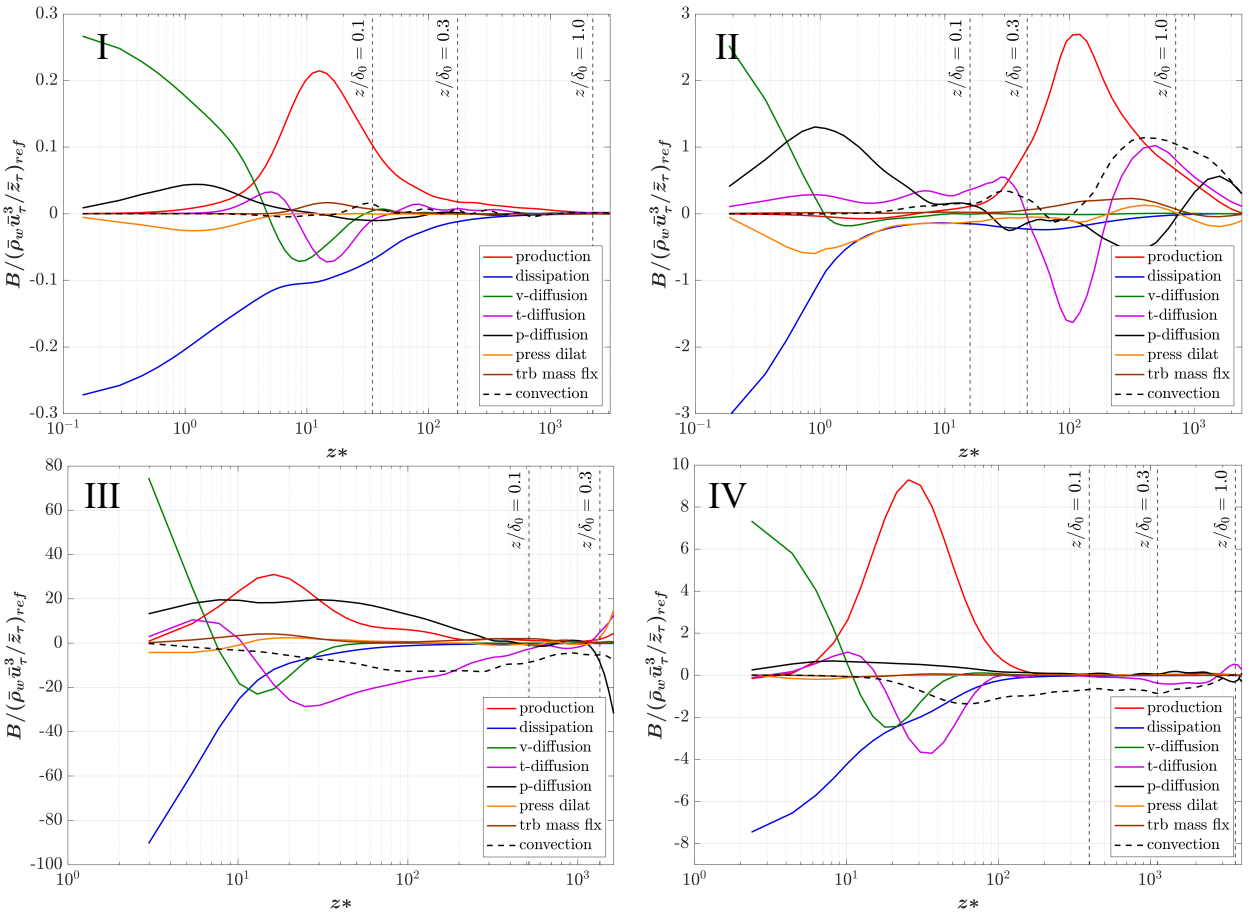


Figure 6.6. Turbulent kinetic energy transport budgets, normalized by viscous wall units.

Production is generally a source term and represents the rate of transfer of energy from the mean flow to the turbulent kinetic energy. Noting that $\mathcal{P} = -\bar{\rho}\widetilde{u_i''u_k''}\partial\tilde{u}_i/\partial x_k = -\bar{\rho}\widetilde{u_i''u_k''}\tilde{S}_{ki}$, the term is also seen as the rate at which work is done by the mean strain rate against the turbulent stresses. Dissipation is generally a sink term and represents the rate of transfer of TKE to thermal internal energy. Noting that $\epsilon = \overline{t_{ik}'' \, \partial u_i''/\partial x_k} = \overline{t_{ik}'' S_{ki}''}$, it is seen as the rate at which work is done by the fluctuating strain rate against the fluctuating viscous stresses. Viscous diffusion is the rate at which TKE is transported by the action of molecular viscosity. Turbulent diffusion is the rate at which TKE is transported by velocity fluctuations. Pressure diffusion is the rate at which TKE is

transported by fluctuating pressure-velocity correlations. Pressure dilatation (the isotropic component of pressure strain in RST equation) and turbulent mass flux arise due to compressible effects. Both terms vanish in the incompressible limit as density fluctuations go to zero because $\widetilde{u_i''}$ and $\nabla \cdot \widetilde{u_i''}$ (divergence) go to zero. All other terms in the compressible TKE and RST transport equations have analogs in the incompressible TKE and RST transport equations. Pressure dilatation represents the conversion between TKE and turbulent potential energy due to pressure fluctuations, particularly in rapidly compressed turbulence. Turbulent mass flux represents the rate at which TKE is transported due to fluctuating velocity-viscous stress gradient and fluctuating velocity-pressure gradient fields.

The profiles at station I in Figure 6.6-I are representative of a canonical equilibrium boundary layer. At the wall ($z^* \lesssim 2$), viscous diffusion and to a lesser extent pressure diffusion transports TKE to the wall, while viscous dissipation and to a lesser extent pressure dilatation converts TKE to internal energy. Typically, pressure diffusion and pressure dilatation are assumed to be negligible in an equilibrium wall bounded flow. In the present study, they appear to be small but non-negligible at the wall. They appear to be almost in balance with pressure diffusion acting as a source and pressure dilatation acting as sink. All other budgets, including convection, are negligible at the wall. Like $\widetilde{u''w''}$, production increases as z^3 from the wall, peaking in the in the buffer layer in the near-wall region at $z^* \approx 13$. Peak production approximately coincides with positive peaks in TKE and the normal turbulent stresses and the negative peak in the shear stress $\widetilde{u''w''}$. At this peak, production exceeds dissipation by a factor of ~2.1 ($\mathcal{P}/\epsilon \approx 2.1$). The excess energy not converted to thermal energy at this peak is transported away by diffusion processes, mainly viscous and turbulent diffusion. In the log layer ($0.1 \lesssim z/\delta_0 \lesssim 0.3$), production and dissipation dominate with production being slightly larger than dissipation ($\mathcal{P}/\epsilon \approx 1.25$) through

the log layer. Pressure diffusion, viscous diffusion, turbulent mass flux and convection also show small increases or decreases in the buffer and log layers. Finally, all wall-normalized budgets decline to near zero outside of the log-layer for $z/\delta_0 \gtrsim 0.3$, concurrent with the decline in Reynolds stresses.

At separation, the profiles at Figure 6.6-II show notable amplification of the budgets relative to the upstream location. Close to the wall in the separation bubble, pressure diffusion and turbulent diffusion significantly increase, balanced mainly by dissipation and pressure dilatation. Away from the wall, at $z/\delta_0 \approx 0.6$, production is significantly amplified balanced mainly by viscous diffusion. The peak production is further away from the wall than at the upstream location coinciding with the peaks in TKE and the normal turbulent stresses that occur in the separation shear layer. Further away from the wall, production decreases to zero, while turbulent diffusion switches from a sink to a source. Pressure diffusion also shows a negative peak followed by a positive peak. Convection, while negligible in the low-speed separated flow near the wall, increases in the separation shear layer away from the wall.

Shortly following reattachment, the profiles at Figure 6.6-III show significantly more amplification exceeding that at the other stations by about an order of magnitude. At the wall, viscous diffusion is significantly amplified mainly balanced by the significant dissipation. Other budgets also show amplification at the wall, most notably pressure diffusion and pressure dilatation, albeit smaller than the viscous diffusion and dissipation budgets. Away from the wall but still within the thin viscous boundary layer, production peaks at $z^* \approx 16$, coinciding with the peaks in TKE and the turbulent stresses. In this region, production and pressure diffusion are balanced by dissipation, viscous diffusion, turbulent diffusion and convection. Further away from the wall, following the peak, production and pressure diffusion sources remain elevated through

the mixing layer balanced by turbulent diffusion and convection. Except for convection, the budgets eventually decay to near zero before the shock line between $0.1 \lesssim z/\delta_0 \lesssim 0.3$. The increase in budgets in Figure 6.6-III for $z/\delta_0 \gtrsim 0.3$ is due to the amplification through the unsteady shock wave (not directly discussed here). Turbulent mass flux shows a small increase in the peak production region, and is otherwise negligible. Pressure dilatation is also negligible outside of the near-wall viscous sublayer.

At the far downstream station, the recovering boundary layer in Figure 6.6-IV shows yet still amplified budgets relative to the upstream equilibrium station I, but less so that at station III just following reattachment. As the boundary layer attempts to relax back to equilibrium, the profiles resemble the trends in the upstream station I, but with larger magnitudes. At the wall viscous diffusion is once again balanced by dissipation. Away from the wall, but still within the thin viscous boundary layer, production peaks at $z^* \approx 25$, approximately coinciding with the peaks in TKE and the turbulent stresses. Production is mainly balanced by dissipation, viscous diffusion, turbulent diffusion and to a lesser extent convection. Pressure diffusion acts as a small source term for most of the viscous boundary layer. Pressure dilatation and turbulent diffusion are negligible throughout. Further away from the wall all budgets, except for convection, decay to zero for $z^* \gtrsim 200$ or $z/\delta_0 \gtrsim 0.05$.

Overall, throughout the flowfield, the dominant turbulence mechanisms at the wall are the viscous diffusion source and the viscous dissipation sink. Away from the wall but still in the viscous wall layer, production is the primary source balanced primarily by viscous dissipation, turbulent diffusion and viscous diffusion. Pressure diffusion plays a secondary role as a source at the wall and as a source or sink in other parts of the profile. Pressure dilatation plays only a secondary role as a sink at the wall, and is otherwise negligible. Turbulent mass flux shows up as

a small source term in the region of peak production, but is other negligible. The profiles follow almost similar trends in the pre-separation and post-reattachment regions. In the post-reattachment region, other than generally significantly amplified budgets, only pressure diffusion and convection appear to take on a stronger role away from the wall, while all other budgets follow similar trends to the pre-separated equilibrium flow. The exception is in the separated corner, where trends and amplifications may differ depending on where in the separated corner the wall normal profiles are extracted.

6.7 Reynolds Stress Transport Budgets

The RST budgets are further examined in Figure 6.7a-d at locations I-IV, respectively. The y-axis is labeled $\mathcal{B}_{ij}$ which corresponds to the transport budgets of stress $\tau_{ij} = \widetilde{u_i''u_j''}$. Transport budgets of the normal stresses are shown on the left side of the plots and transport budgets of the shear stresses are shown on the right side of the plots.

Station I – Upstream Equilibrium Boundary Layer

At station I, Figure 6.7a shows that the turbulent stresses are driven primarily by the transport of normal stress $\widetilde{u''^2}$, and to a lesser extent the normal stresses $\widetilde{v''^2}$ and $\widetilde{w''^2}$ and the shear stress $\widetilde{u''w''}$. The budgets of shear stresses $\widetilde{u''v''}$ and $\widetilde{v''w''}$ are at least an order of magnitude smaller (see y-axis scales). For $\widetilde{u''^2}$, production $\mathcal{P}_{11}$ is mainly driven by the mean streamwise velocity gradient and is the dominant source of $\widetilde{u''^2}$ (and TKE) in the boundary layer where it peaks in buffer region. Turbulent mass flux $\mathcal{M}_{11}$ also acts as a small source of $\widetilde{u''^2}$ in the buffer layer. The sources of $\widetilde{u''^2}$ are balanced by the sinks viscous dissipation ϵ_{11}, viscous diffusion $\mathcal{D}_{11}^{V}$, turbulent diffusion $\mathcal{D}_{11}^{T}$ and to a lesser extent pressure strain Π_{11} in the buffer layer. At the wall, viscous

diffusion acts as a source of $\widetilde{u''^2}$ while viscous dissipation acts as a sink. Pressure diffusion $\mathcal{D}_{11}^P$ for $\widetilde{u''^2}$ is negligible throughout.

For $\widetilde{v''^2}$, at the wall pressure strain Π_{22} and viscous diffusion $\mathcal{D}_{22}^V$ are sources balanced by dissipation ϵ_{22}, while away from the wall in the buffer and log layers pressure strain is mainly balanced by dissipation and pressure diffusion $\mathcal{D}_{22}^P$. For $\widetilde{w''^2}$, at the wall for $z^* \lesssim 10$, pressure diffusion $\mathcal{D}_{33}^P$ acts as a source, while pressure strain Π_{33} acts as a sink. Away from the wall, the budgets of $\widetilde{w''^2}$ are smaller with pressure strain Π_{33} being a source term and viscous dissipation ϵ_{33}, pressure diffusion $\mathcal{D}_{33}^P$ and turbulent diffusion $\mathcal{D}_{33}^T$ beings sinks. For $z^* \gtrsim 10$, most of the production source is in $\widetilde{u''^2}$, while $\widetilde{v''^2}$ and $\widetilde{w''^2}$ have little production. By contrast, pressure strain acts as a sink for $\widetilde{u''^2}$ and as a dominant source for $\widetilde{v''^2}$ and $\widetilde{w''^2}$, thereby redistributing the energy from the streamwise to the wall-normal and spanwise components.

For $\widetilde{u''w''}$, at the wall pressure diffusion $\mathcal{D}_{13}^P$ now acts as a sink and pressure strain Π_{13} now acts as source. Away from the wall, pressure diffusion switches to being a source in the buffer and early log layers balanced by the production sink $\mathcal{P}_{13}$. Recall that $\widetilde{u''w''} < 0$ at station I, and is generally so for an equilibrium wall bounded flow, then one can consider these sources to be sinks and vice versa for transport of $-\widetilde{u''w''}$ (as is sometimes the case in the literature). In contrast to the normal stresses, dissipation ϵ_{13} is relatively small throughout.

Station II – Separated Region

All budgets are significantly amplified by an order of magnitude compared to the upstream station I. Relative to this station, budgets of $\widetilde{u''v''}$ and $\widetilde{v''w''}$ are again an order of magnitude smaller than the budgets of the other components. For $\widetilde{u''^2}$, at the wall for $z^* \lesssim 10$ the primary balance is between pressure strain Π_{11} and dissipation ϵ_{11}. Away from the wall, production $\mathcal{P}_{11}$ of

$\widetilde{u''^2}$ peaks in the shear layer balanced by turbulent diffusion $\mathcal{D}_{11}^T$ and pressure strain Π_{11}. For $\widetilde{v''^2}$, the main balance at the wall is again between pressure strain Π_{22} and dissipation ϵ_{22}. Away from the wall pressure strain shows a relatively large peak for $\widetilde{v''^2}$ in the shear layer compared to the other budgets. For $\widetilde{w''^2}$, at the wall pressure diffusion $\mathcal{D}_{33}^P$ acts as a source and pressure strain Π_{33} acts as a sink, while away from the wall their roles invert in the shear layer along with a small decrease then increase in production. Like station I, for $z^* \gtrsim 10$, most of the production source is in $\widetilde{u''^2}$, while $\widetilde{v''^2}$ and $\widetilde{w''^2}$ have little production. By contrast, pressure strain acts as a sink for $\widetilde{u''^2}$ and as a dominant source for $\widetilde{v''^2}$ and $\widetilde{w''^2}$, thereby redistributing the energy from the streamwise to the wall-normal and spanwise components.

For $\widetilde{u''w''}$, at the wall for $z^* \lesssim 7$ pressure diffusion $\mathcal{D}_{13}^P$ now acts as a sink and pressure strain Π_{13} now acts as source. Away from the wall, the budgets of $\widetilde{w''^2}$ appear relatively small, but a zoom on the plot (not shown, but can be deduced from Figure 6.8b) shows that some budget magnitudes are on the order of that of B_{11} where sources pressure strain, pressure diffusion and turbulent diffusion are balanced by the production sink. In contrast to the normal stresses, dissipation ϵ_{13} is relatively small throughout.

Station III & IV – Downstream Post-Shock Nonequilibrium Region

All budgets are amplified relative to the upstream station I. Pressure strain and pressure diffusion play a dominant role in the near-wall turbulence for $z^* \lesssim 11$ approximately balancing each other. At the wall for $z^* \lesssim 11$, pressure strain acts as a sink for $\widetilde{u''^2}$ and as a source for $\widetilde{v''^2}$ and $\widetilde{w''^2}$, thereby redistributing the energy from the streamwise to the longitudinal and spanwise components. Except for $\widetilde{v''^2}$, away from the wall the roles of pressure strain and pressure diffusion invert, albeit smaller in magnitudes than at the wall. The other budgets are obscured by the

inordinately large magnitudes of the pressure strain and pressure diffusion at the wall; these will be discussed more in the section below. Between stations III and IV, the amplification of the budgets reduces (relative to the upstream station I), consistent with the amplification of the stresses themselves. At IV the profiles appear to resume the trends observed at station I as the flow attempts to relax back to the equilibrium.

Combining Pressure Strain and Pressure Diffusion

In general, it is observed that pressure strain plays the role of redistributing the energy from the streamwise to the longitudinal and spanwise components. For this reason, it is often referred to as the 'redistribution' term. In contrast to the transport of TKE in which pressure diffusion and pressure dilatation (the trace of the pressure strain tensor) play a secondary role, in RST pressure diffusion and pressure strain play a central role. They appear to approximately balance in many instances especially in the near-wall turbulence for $z^* \lesssim 10$. Some modeling and analyses, particularly in incompressible flows, consider the sum of these terms instead, which combines the effect of pressure fluctuations into a single term referred to as the velocity-pressure gradient correlation (Lumley 1975 [140]), viz,

$$\Pi_{ij}^{tot} = \Pi_{ij} + \mathcal{D}_{ij}^{P} = \overline{-u_\iota'' \frac{\partial p'}{\partial x_j} - u_\jmath'' \frac{\partial p'}{\partial x_\iota}} \qquad [82]$$

Figure 6.8a-d shows the budgets at stations I-IV, but with pressure strain and pressure diffusion combined into the velocity-pressure gradient budget Π_{ij}^{tot}. The large magnitudes of the pressure strain and pressure diffusion budgets at the wall, particularly at the downstream stations III-IV, no longer obscures the plots of other budgets which may play a significant role away from the wall. At stations I & II, away from the wall for $z^* \gtrsim 10$, the velocity-pressure gradient term is a sink of $\widetilde{u''^2}$ and a dominant source of $\widetilde{v''^2}$ and $\widetilde{w''^2}$ where production is much smaller. Hence the action

of the velocity-pressure gradient term is similar to the pressure strain term in that p' correlation terms redistribute energy from streamwise to wall-normal and spanwise components. For shear stress $\widetilde{u''w''}$, it is a dominant source term balanced by production.

At stations III & IV, the prevailing trend at the wall for $z^* \lesssim 10$ is a balance between the dissipation sink and viscous diffusion source and in the case of $\widetilde{v''^2}$ the velocity-pressure gradient source. One exception at III & IV is for shear stress $\widetilde{v''w''}$, where the viscous diffusion budget is the only significant budget acting as a source at the wall and as a sink a little away from the wall, while the other budgets are much smaller. Away from the wall for $z^* \gtrsim 10$, the velocity-pressure gradient term has a similar redistributive effect of energy transfer from $\widetilde{u''^2}$ to $\widetilde{v''^2}$ and $\widetilde{w''^2}$ at station III and from $\widetilde{u''^2}$ to $\widetilde{v''^2}$ at station IV. One observation at station IV is that production of $\widetilde{w''^2}$ is the dominant source unlike the stations I-II and to some extent III. Another observation is that unlike stations I & II, dissipation is a significant sink in the $\widetilde{u''w''}$ budgets. It is also observed that the turbulent mass flux is particularly amplified in the transport of $\widetilde{u''^2}$, $\widetilde{w''^2}$ and $\widetilde{u''w''}$ following reattachment at station II than in the upstream and downstream stations.

Summary

In modeling of RST transport budgets, much attention has been given to viscous dissipation and pressure strain terms. Turbulent diffusion is either modeled using the gradient diffusion hypothesis or is ignored. Pressure diffusion may be lumped with turbulent diffusion using a constant empirical coefficient or is ignored. Turbulent mass flux is often simply ignored. Modeling choices have typically been based on the budgets of canonical equilibrium flows, and to a lesser extent simple nonequilibrium flows. Few shock-separated supersonic flows have computed the budgets in the post-shock region where nonequilibrium prevails. There is certainly a dearth of evidence for the behavior of the budgets in hypersonic nonequilibrium flows, especially at Mach

numbers as high as Mach 10. This study provides insight into the RST budgets of the equilibrium and nonequilibrium regions of the Mach 10 shock-separated axisymmetric flowfield with compression. Several observations in this flow regime warrant consideration for modeling of the budgets.

Firstly, all budgets are significantly amplified through the interaction and in the post-shock nonequilibrium region. The amplification is greatest just following reattachment where flow compression is high due to the impinging shock and the flow is highly strained. Amplification of the budgets relative to the upstream undisturbed boundary layer far exceeds that of supersonic and lower speed shock-boundary layer interaction flows. At the wall pressure strain and pressure diffusion are prominent with inordinately large amplifications just following reattachment. Both budgets are also important away from the wall. If pressure strain and pressure diffusion are to be modeled separately instead of combining into the velocity-pressure gradient term, then more modeling consideration should be given to pressure diffusion. The same can be said for turbulent diffusion since it plays a key role in many parts of the flowfield. The turbulent mass flux is generally small, but is particularly amplified relative to the other budgets just following reattachment in the transport of $\widetilde{u''^2}$, $\widetilde{w''^2}$ and $\widetilde{u''w''}$ and may warrant modeling consideration.

In the separated corner, production, pressure strain and turbulent diffusion play primary roles where they peak in the separation shear layer. Pressure strain plays the role as a redistributor of energy from streamwise to wall-normal and spanwise components, as it does in the equilibrium undisturbed boundary layer. Dissipation in not as significant in contrast to the equilibrium undisturbed flow.

In the post-shock nonequilibrium region following reattachment, the general trends of streamwise stress $\widetilde{u''^2}$ budgets remains unchanged, albeit significantly amplified. For spanwise

stress $\widetilde{v''^2}$ budgets, besides being amplified, the energy balance is between pressure strain, viscous diffusion and dissipation as it was in the equilibrium undisturbed boundary layer, except that turbulent diffusion becomes prominent just following reattachment before relaxing back to being negligible further downstream. For wall-normal stress $\widetilde{w''^2}$ budgets, besides being amplified, their trends now resemble the trends of the streamwise stress $\widetilde{u''^2}$ budgets with production becoming a dominant source, except that the velocity-pressure gradient and turbulent mass flux are prominent just following reattachment before relaxing back to being negligible further downstream. In general, pressure strain (or velocity-pressure gradient) retains its role as a redistributor of energy from streamwise to wall-normal and spanwise components.

In the post-shock nonequilibrium region following reattachment, the shear stress $\widetilde{u''w''}$ switches sign from being negative in the equilibrium undisturbed boundary layer to being positive. The behavior of the shear stress budgets change significantly, appearing to follow the trends of the streamwise stress $\widetilde{u''^2}$ budgets, where dissipation, viscous diffusion and turbulent diffusion now play key roles in addition to production and pressure diffusion. For smaller shear stresses $\widetilde{u''v''}$ and $\widetilde{v''w''}$, some budgets become noticeably amplified, particularly the viscous diffusion budget of $\widetilde{v''w''}$.

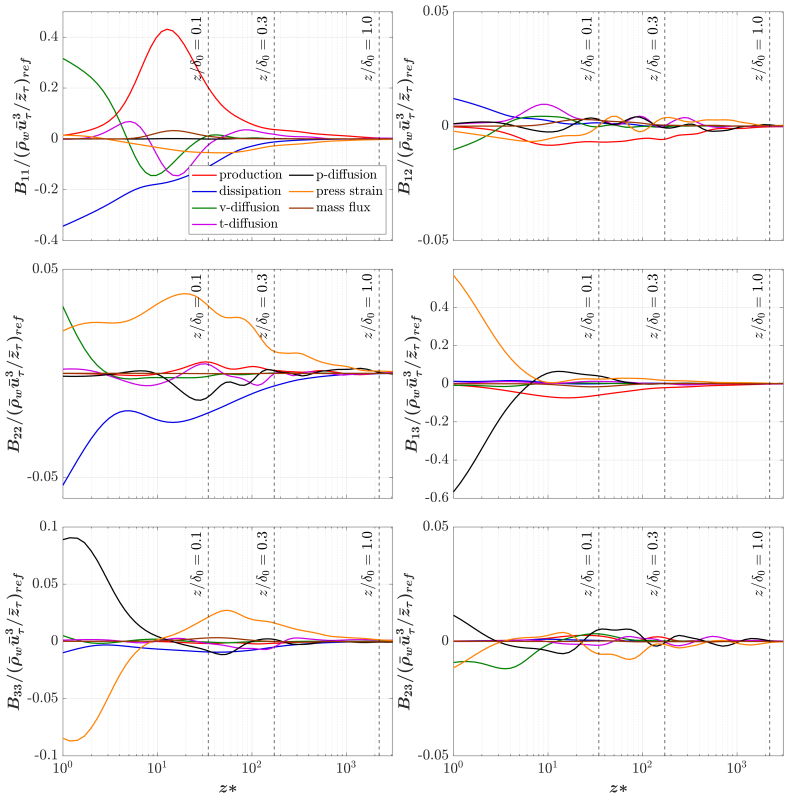


Figure 6.7a. Reynolds stress transport budgets, location I.

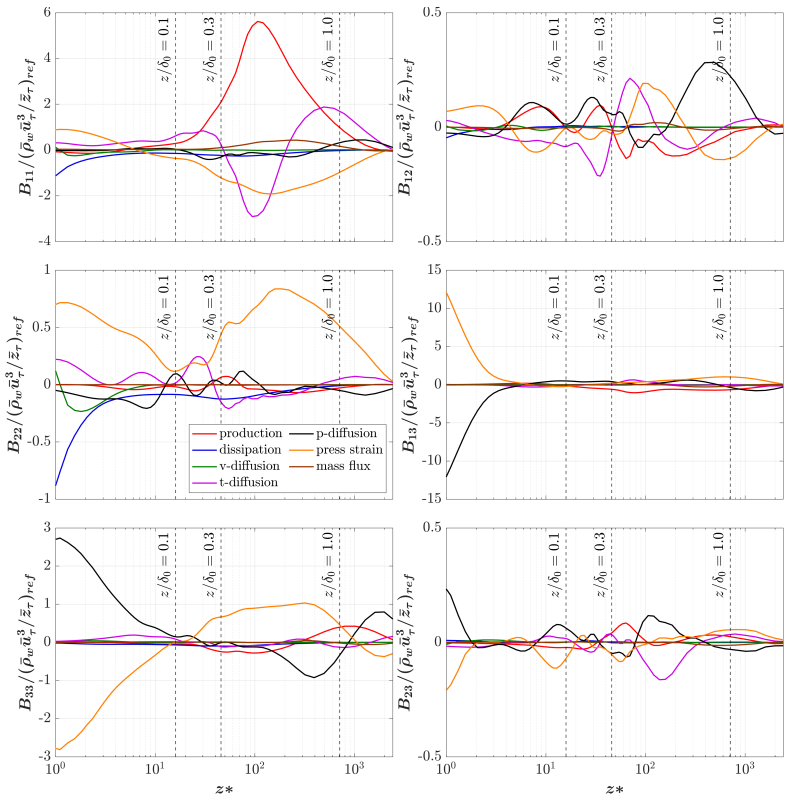


Figure 6.7b. Reynolds stress transport budgets, location II.

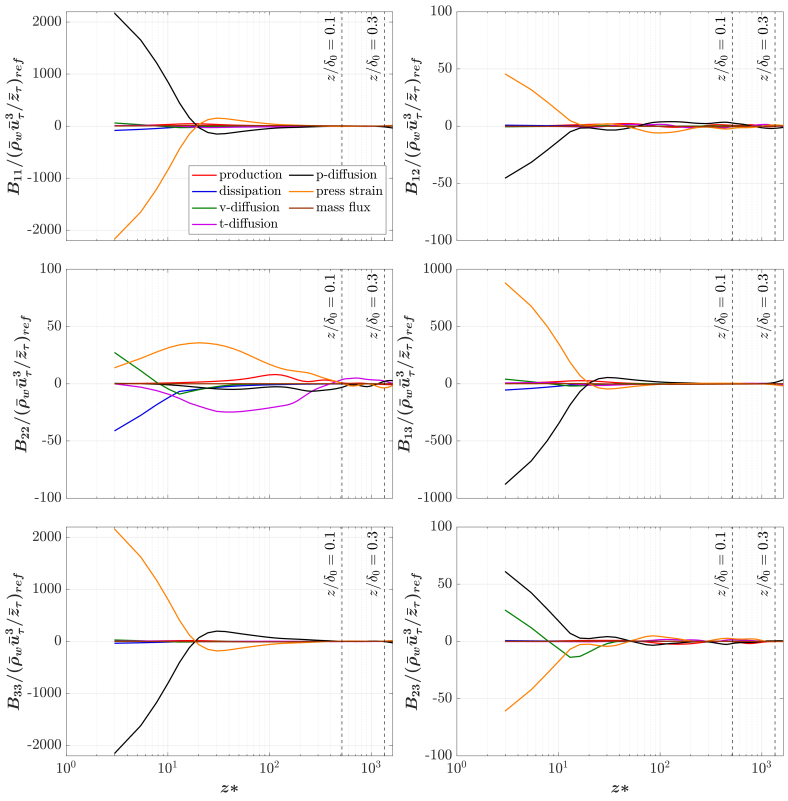


Figure 6.7c. Reynolds stress transport budgets, location III.

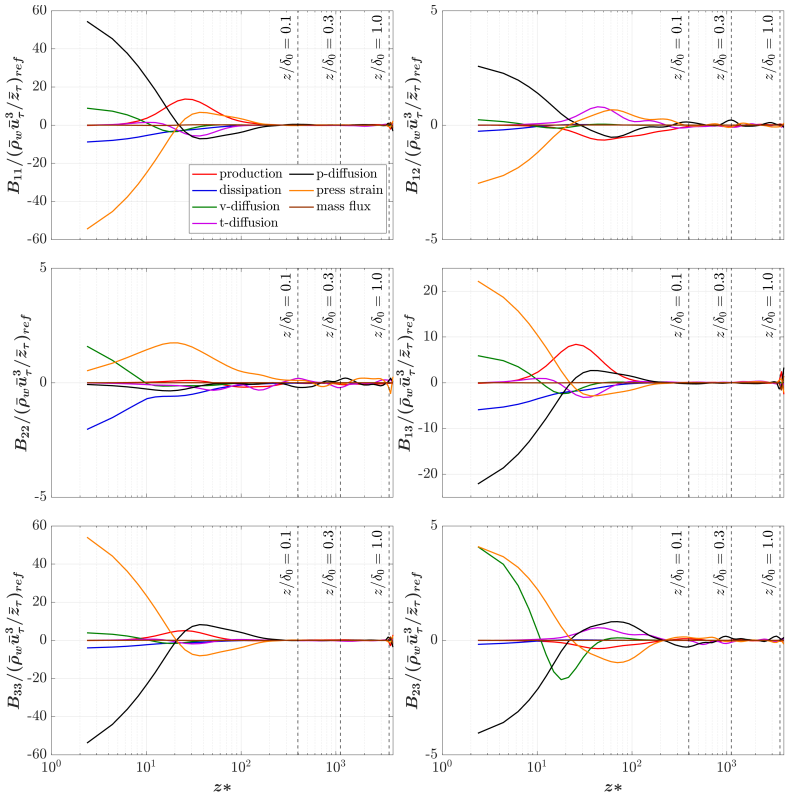


Figure 6.7d. Reynolds stress transport budgets, location IV.

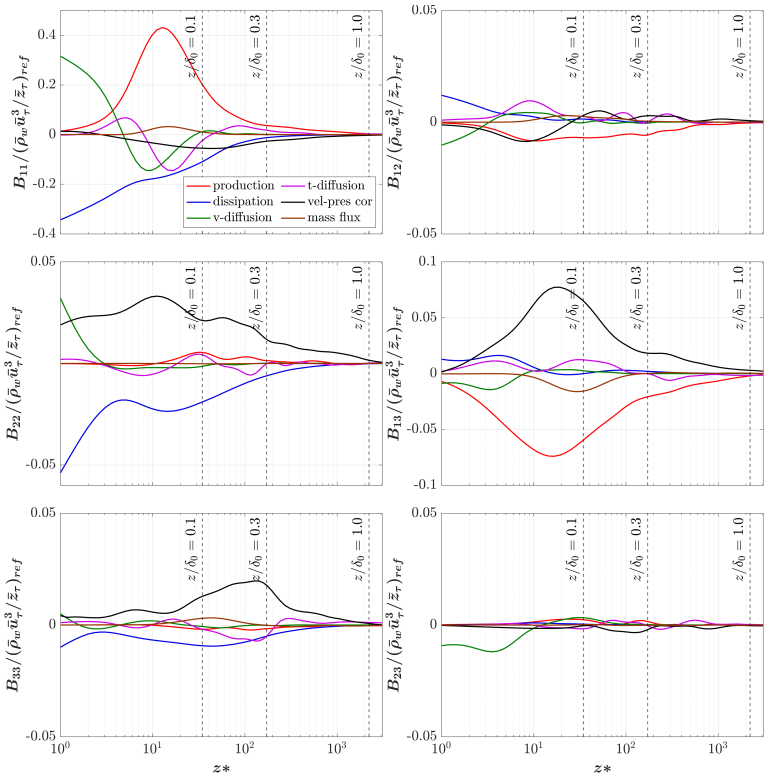


Figure 6.8a. Reynolds stress transport budgets, location I, $\Pi_{ij}^{tot} = \Pi_{ij} + \mathcal{D}_{ij}^{P}$.

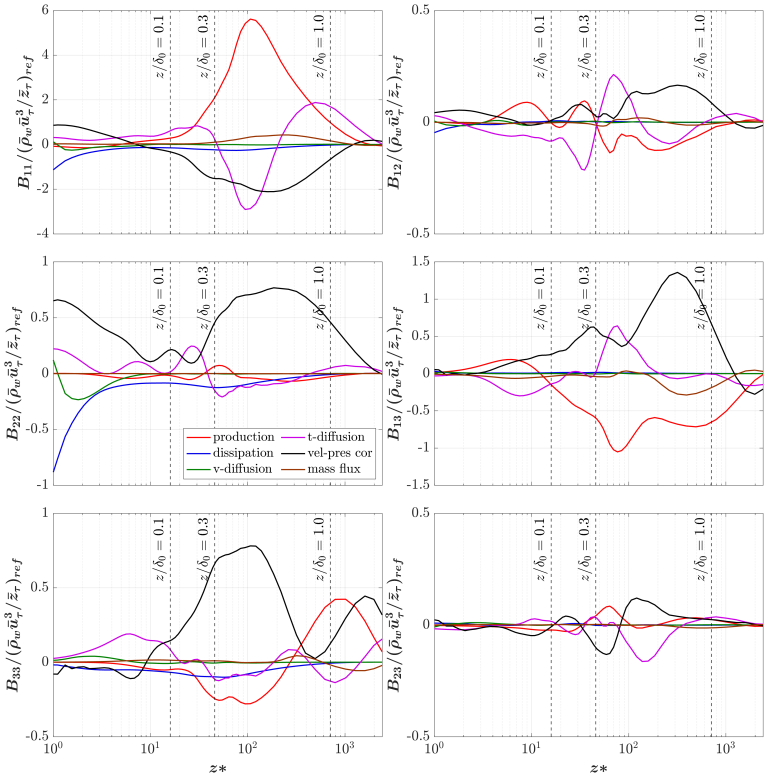


Figure 6.8b. Reynolds stress transport budgets, location II, $\Pi_{ij}^{tot} = \Pi_{ij} + \mathcal{D}_{ij}^{P}$.

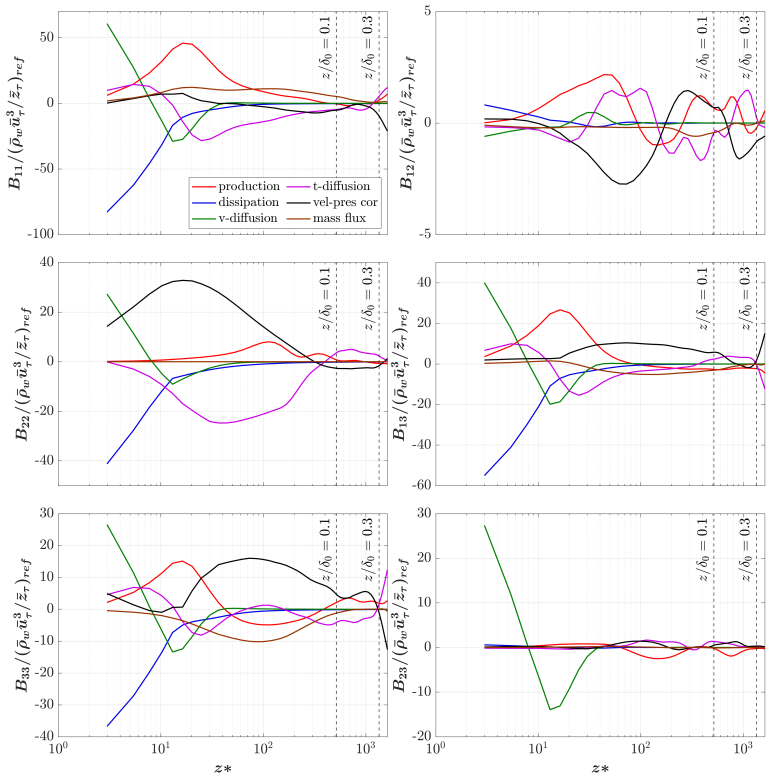


Figure 6.8c. Reynolds stress transport budgets, location III, $\Pi_{ij}^{tot} = \Pi_{ij} + \mathcal{D}_{ij}^{P}$.

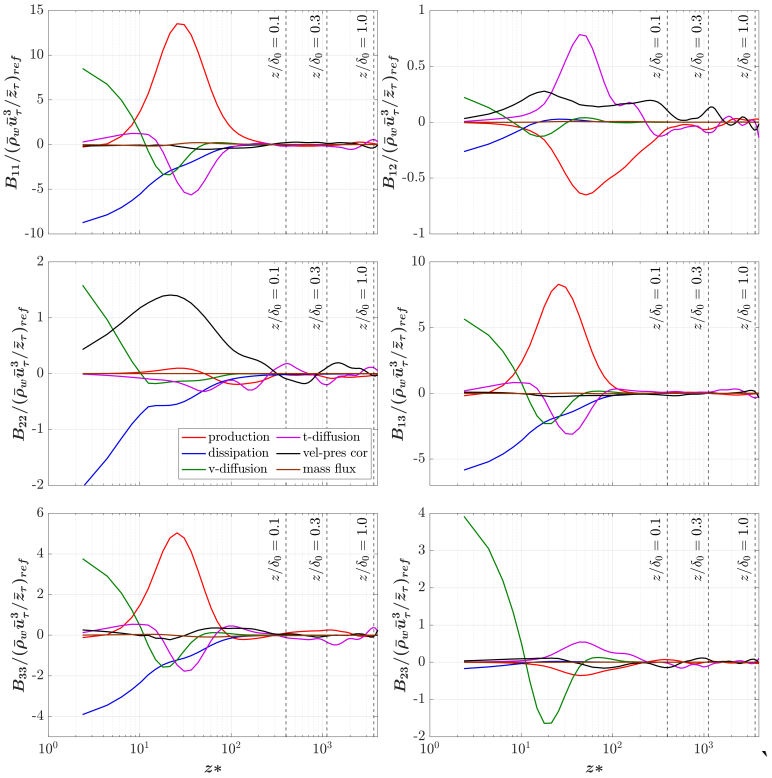


Figure 6.8d. Reynolds stress transport budgets, location IV, $\Pi_{ij}^{tot} = \Pi_{ij} + \mathcal{D}_{ij}^{P}$.

6.8 Viscous Dissipation

The TKE viscous dissipation rate plays a crucial role in the balance of the TKE and RST transport equations. This is especially true in the near-wall turbulence where it represents the conversion of kinetic energy into thermal internal energy. The region near the wall is very thin and the transport processes are complex. It is very challenging to obtain experimental measurements so close to the wall. DNS and LES data has proven indispensable in understanding this region of the flow. Even so, there is a sparsity of simulation data, especially flows with high Mach number and strong nonequilibrium, as is the case study herein.

In RANS $k-\epsilon$ EVMs, a transport equation is solved for the scalar TKE dissipation rate $\epsilon = \epsilon_{ii}/2$. For $k-\omega$ EVMs, a transport equation is solved for the specific dissipation rate ω, from which ϵ is easily calculated. For the RST equation, one approach to computing the TKE dissipation rate tensor, ϵ_{ij}, may be to derive a transport equation for ϵ_{ij}. Such an equation is very complex with higher-order correlations whose modeling is subject much uncertainty. Instead, typically a transport equation is solved for ϵ (or ω) and the dissipation rate tensor is then assumed to be (Sarkar 1991 [141]),

$$\epsilon_{ij} = 2/3\epsilon\delta_{ij} \qquad [83]$$

This model assumes that the dissipation is isotropic, i.e., that the anisotropic component is zero. This approach has validity for high Reynolds number flows and remote from walls, but is not entirely accurate, for example in the near-wall viscous region of boundary layer flows. Additional modeling complexities are typically introduced to account for departures from isotropy. These will be discussed later.

6.8.1 Dissipation Components

Recall from the TKE transport equation that the scalar dissipation is given by,

$$\epsilon = \frac{\epsilon_{ii}}{2} = \overline{t''_{\iota k} \frac{\partial u''_{\iota}}{\partial x_k}} = \overline{t''_{\iota k} s''_{k\iota}} \quad [84]$$

Model development for ϵ usually then assumes the following partition of scalar dissipation. Following Gatski & Bonnet 2013 [142], rewriting the fluctuating viscous stress tensor t''_{ik} and fluctuating strain rate tensor s''_{ki} as the difference between the instantaneous and mean fields, one obtains,

$$\epsilon = 2\bar{\mu}\widetilde{s''_{\iota k} s''_{k\iota}} - {}^{2}/_{3}\,\bar{\mu}\widetilde{s''_{kk} s''_{ll}} + 2\widetilde{\mu'' s''_{ij}}\tilde{S}_{ij} - {}^{2}/_{3}\,\widetilde{\mu'' s''_{kk}}\tilde{S}_{ll} + 2\mu''\widetilde{s''_{\iota k} s''_{k\iota}} - {}^{2}/_{3}\;\mu''\widetilde{s''_{kk} s''_{ll}} \quad [85]$$

The first two terms can be further partitioned into the sum of a solenoidal dissipation ϵ_s, a dilatational dissipation ϵ_d and an inhomogeneous contribution ϵ_{ih}. The last four terms containing double and triple correlations of fluctuating viscosity will be assigned as $\epsilon_{\mu''}$. Thus,

$$\epsilon = \epsilon_s + \epsilon_d + \epsilon_{ih} + \epsilon_{\mu''} \quad [86]$$

$$\epsilon_s = \bar{\mu}\widetilde{\omega''_{\iota}\omega''_{\iota}} \quad [87]$$

$$\epsilon_d = {}^{4}/_{3}\,\bar{\mu}\widetilde{s''_{kk} s''_{ll}} \quad [88]$$

$$\epsilon_{ih} = 2\bar{\mu}\frac{\partial}{\partial x_k}\left[\widetilde{\frac{\partial u''_k u''_l}{\partial x_l}} - 2\widetilde{u''_k s''_{ll}}\right] \quad [89]$$

$$\epsilon_{\mu''} = 2\widetilde{\mu'' s''_{ij}}\tilde{S}_{ij} - {}^{2}/_{3}\,\widetilde{\mu'' s''_{kk}}\tilde{S}_{ll} + 2\mu''\widetilde{s''_{\iota k} s''_{k\iota}} - {}^{2}/_{3}\;\mu''\widetilde{s''_{kk} s''_{ll}} \quad [90]$$

In modeling, the inhomogeneous contribution and all fluctuating viscosity correlation terms are assumed negligible, i.e., $\epsilon_{ih} = \epsilon_{\mu''} \approx 0$. The solenoidal dissipation ϵ_s is associated with the fluctuating vorticity component ω''_i of the velocity-gradient field and is postulated to be unaffected by compressibility. The dilatational dissipation is associated with the dilatational characteristic of the fluctuating velocity-gradient field and arises only in variable density flows. The dilatational

dissipation is therefore considered to be the compressible contribution, and its modeling has received much attention in past decades. Thus modeling assumes,

$$\epsilon \approx \epsilon_s + \epsilon_d \qquad [91]$$

For high Reynolds number turbulence, Sarkar 1991 [141] indicated that the decomposition of ϵ into $\epsilon_s + \epsilon_d$ is asymptotically valid and is exact for constant-viscosity homogeneous turbulence.

To this end, the relative contributions of the scalar dissipation components are evaluated in Figure 6.9 at stations I-IV. The left plots show the components normalized by the viscous wall units at that station. The right plots show the components as a fraction of the local total scalar dissipation. The dashed black line is $(\epsilon_{ih} + \epsilon_{\mu''})/\epsilon$, and the dash-dot black line is $(\epsilon_d + \epsilon_{ih} + \epsilon_{\mu''})/\epsilon$. At all locations it is observed that the ϵ_s generally accounts for the majority of the total dissipation. In the undisturbed equilibrium boundary layer at station I, $\epsilon_{\mu''}$ fraction accounts for up to 10% in the near wall region and almost 30% for $z^* > 10^3$, however, note that the left plot indicates that the total dissipation and its components are much smaller for $z^* > 10^3$ (the outer boundary layer) and the division of small decreasing numbers skews the interpretation. In the separated region at station II, the left plot shows that normalized $\epsilon_{\mu''}$ is small but non-negligible while normalized ϵ_d and ϵ_{ih} are small. The right plot at station II shows that ϵ_d, ϵ_{ih}, and $\epsilon_{\mu''}$ fractions can individually or in combination account for up to 50% of the total local dissipation in the separation bubble and shear layer above it for $z/\delta_0 < 10^3$. This may be significant considering that ϵ_{ih}, $\epsilon_{\mu''}$ and sometimes ϵ_d are ignored in modeling approaches. In the post-reattachment nonequilibrium station III, ϵ_s dominates, with some local exceptions: (i) at the wall $\epsilon_{\mu''}$ accounts for up to 15% of the local dissipation, (ii) slightly away from the wall $\epsilon_{\mu''}$ can account for up to 40% of the local dissipation at $z^* \approx 25$, and (iii) ϵ_d increase for $z^* \sim 10^3$ reaching 40% of the total dissipation, however note once again that the total dissipation and it components are much smaller

away from the wall as indicated by the left plot. At the far downstream nonequilibrium station IV, ϵ_s continues to dominate, with one local exception, that is, $\epsilon_{\mu''}$ accounts for up to 17% of the local dissipation near the wall, while away from the wall ϵ_s dominates.

In summary, the dominance of solenoidal dissipation component ϵ_s is ascertained. Close to the wall for $z^* \lesssim 11$ (the viscous sublayer), only the $\epsilon_{\mu''}$ component accounts for up to 17% of the total dissipation. The ϵ_{ih} and ϵ_d components are generally small. The only exception is in the separated low speed separation bubble and shear layer above it, where ϵ_{ih}, $\epsilon_{\mu''}$ and ϵ_d can individually or in combination account for up to 50% of the total dissipation at a given location between the wall and freestream; this may warrant modeling considerations.

Besides at the separated corner, the results imply that the compressible contribution ϵ_d is very small even in the highly compressed and highly strained post-reattachment non-equilibrium region. This is in contrast to DNS results of Sarkar et al. 1992 [143] and Blaisdell et al. 1993 [144] for homogeneous shear flows, which show that ϵ_d accounted for up to 20% of the total dissipation. The findings herein are in line with that of Huang et al 1995 [68] for a compressible turbulent channel flow at $M = 3$, where it was shown that $\epsilon_{\mu''}$ contributed up to 16% of the total dissipation very near the wall and was otherwise small, while ϵ_{ih} accounted for $\pm 3\%$ of the total dissipation, and ϵ_d accounted for up to 0.1% at the wall and up to 0.03% otherwise. Zhang et al. 2018 [145] showed that for turbulent flat plate DNS, $\epsilon_d/\epsilon_s \lesssim 6\%$ for Mach 8 and $\epsilon_d/\epsilon_s \lesssim 13\%$ for Mach 14 occurring in the near-wall viscous regions. Vreman et al. 1996 [146] also showed that for a compressible mixing layer at $M = 1.2$ that ϵ_d is negligible.

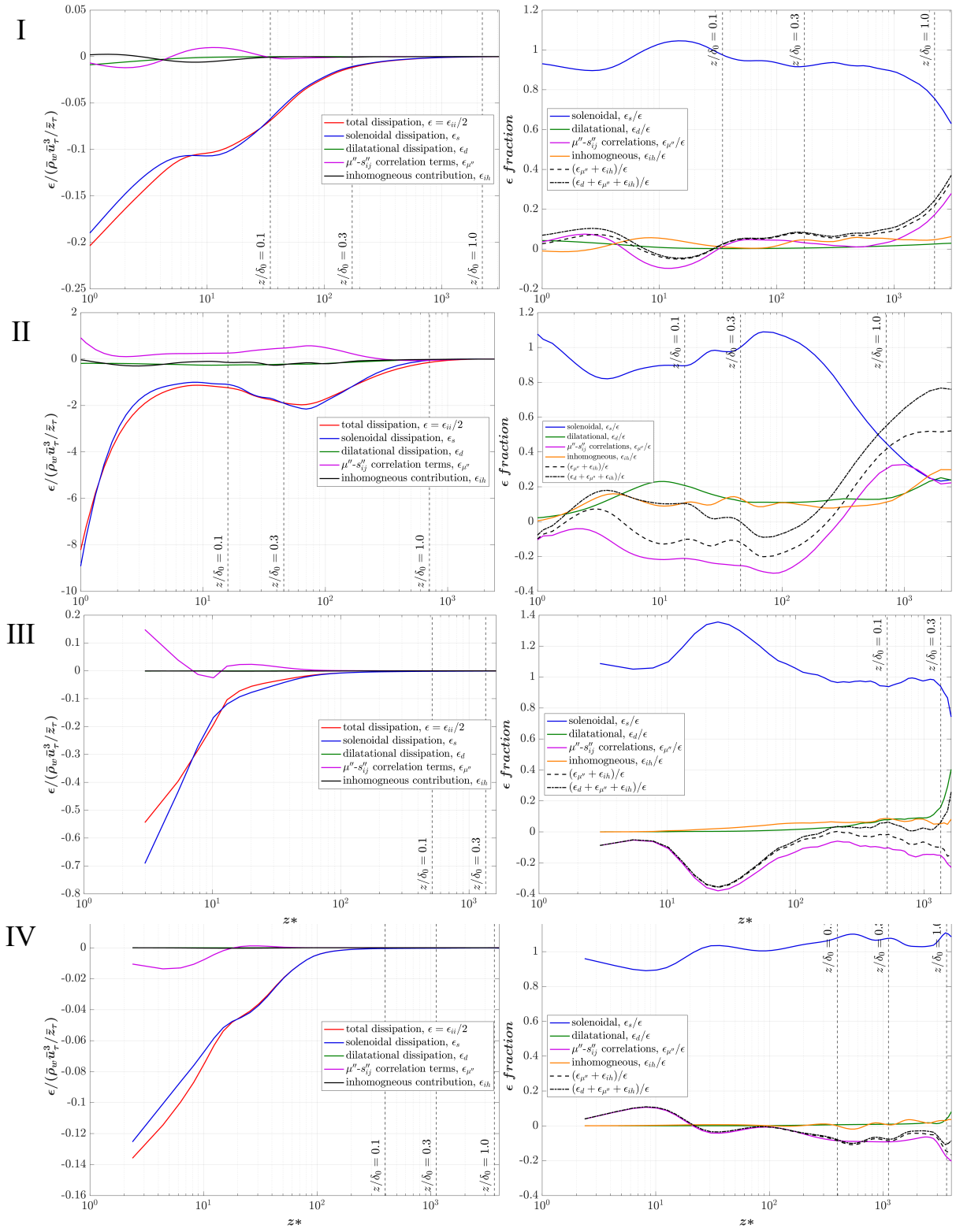


Figure 6.9. Dissipation components, in local wall units (left) and as a fraction of total dissipation (right).

6.8.2 Dilatational Dissipation

Given the historical modeling interest in ϵ_d and the persistence of ϵ_d-model choices in commercial RANS codes, the modeling assumptions of ϵ_d are investigated next. The most common modeling approach is to solve a transport equation for $\epsilon = \epsilon_s$ as is equivalently done in the incompressible case, then add the dilatational dissipation as a 'compressibility correction'. Furthermore, the dilatational dissipation is assumed to be proportional to the product of the solenoidal dissipation and a function of the turbulent Mach number, $M_t = \sqrt{2k}/\tilde{a}$, where $\tilde{a}$ is the speed of sound. So for scalar dissipation in $k-\epsilon$ type EVMs and the dissipation tensor in RST,

$$\epsilon = \epsilon_s + \epsilon_d = \epsilon_s[1 + \alpha F(M_t)] \quad [92]$$

$$\epsilon_{ij} = {}^{2}/_{3}\,\epsilon_s[1 + \alpha F(M_t)]\delta_{ij} \quad [93]$$

Zeman 1990 [147] used phenomenological arguments based on DNS data to show that the presence of eddy shocklets can augment the (incompressible) dissipation with a compressible dilatational component and thus derived an expression for ϵ_d. Sarkar et al. 1991 [148] used a fundamentally different approach based on DNS data and asymptotic analysis to obtain an expression for ϵ_d. An alternative form of ϵ_d was proposed by Wilcox 1992 [149] which used the same functional form as Sarkar et al. 1991 but with Zeman's 1990 turbulent Mach number threshold. The three models are summarized below.

Sarkar et al. 1991 [148]: $F(M_t) = M_t^2, \;\; \alpha = 1$ [94]

Zeman 1990 [147]: $F(M_t) = \left[1 - e^{-1/2(\gamma+1)(M_t - M_{t0})^2)/\Lambda^2}\right]\mathcal{H}(M_t - M_{t0})$ [95]

$$\alpha = 0.75, \quad M_{t0} = c\sqrt{2/(\gamma+1)}$$

Free Shear: $\Lambda = 0.60, \;\; c = 0.10$

Boundary Layer: $\Lambda = 0.66, \;\; c = 0.25$

Wilcox 1992 [149]: $F(M_t) = [M_t^2 - M_{t0}^2]\mathcal{H}(M_t - M_{t0}), \quad \alpha = 1.5, \quad M_{t0} = 0.25$ [96]

Here $\mathcal{H}$ is the Heaviside step function and γ is the specific heat ratio. Blaisdell et al. 1993 [144] and Pirozzoli & Grasso 2004 [150] evaluated the models and found that dilatation dissipation had a behavior consistent with M_t^2.

Ristorcelli 1997 [151] argued that for high-R_t, low-M_t^2, nonequilibrium flows, the dilatational dissipation can be split into slow and rapid components, ϵ_d^s and ϵ_d^r respectively, which scale as,

$$\epsilon_d^s/\epsilon_s \propto M_t^4 R_t^{-1}, \qquad \epsilon_d^r/\epsilon_s \propto M_t^4 (Sk/\epsilon_s)^4 R_t^{-1} \sim M_s^4 R_t^{-1} \tag{97}$$

Here Ristorcelli defined turbulent Mach number $M_t^2 = 2/3\, k/\tilde{a}^2$, the strain rate magnitude $S^2 = \tilde{S}_{ij}^{dev}\tilde{S}_{ij}^{dev}$, turbulent Reynolds number $R_t = 4k^2/(9\tilde{\nu}\epsilon)$, and the strain rate Mach number $M_s \sim M_t\, Sk/\epsilon_s$ (note the definitions may vary slightly from the standard literature). Ristorcelli's scalings show a stronger M_t^4 dependence as opposed to the M_t^2 dependence of the previous models. Another implication is, given that $M_t^4 R_t^{-1} \sim \nu\epsilon_s\tilde{a}^{-4}$, then the dependence of ϵ_d on M_t is through its dependence on temperature and not kinetic energy. The scaling of the rapid component implies a sensitivity to the normalized strain rate magnitude Sk/ϵ_s. For $Sk/\epsilon_s > 1$, it follows that $\epsilon_d^r \gg \epsilon_d^s$. A noteworthy feature is the dependence on viscosity through R_t and the implied vanishing of both components and therefore total ϵ_d as $R_t \to \infty$ for fixed M_t.

Figure 6.10 evaluates the aforementioned models and scalings for dilatational dissipation. The left side plots show the ϵ_d/ϵ_s fraction through the boundary layer. For all stations, all models severely overpredict the fraction of ϵ_d compared to the LES solution which shows very small ϵ_d fraction, <5% in the near-wall turbulence. The only exception is in the near-wall turbulence of the separation bubble at station II, which appears to show that the models track with the LES solution up to $z^* \approx 10$ where ϵ_d/ϵ_s reaches ~20%. Note that at stations II & III, the ϵ_d/ϵ_s fraction increases, but bear in mind that both ϵ_d and ϵ_s become very small towards the outer edge (see Figure 6.9) and the division of ϵ_d by ϵ_s skews the interpretation in this region. The middle plots

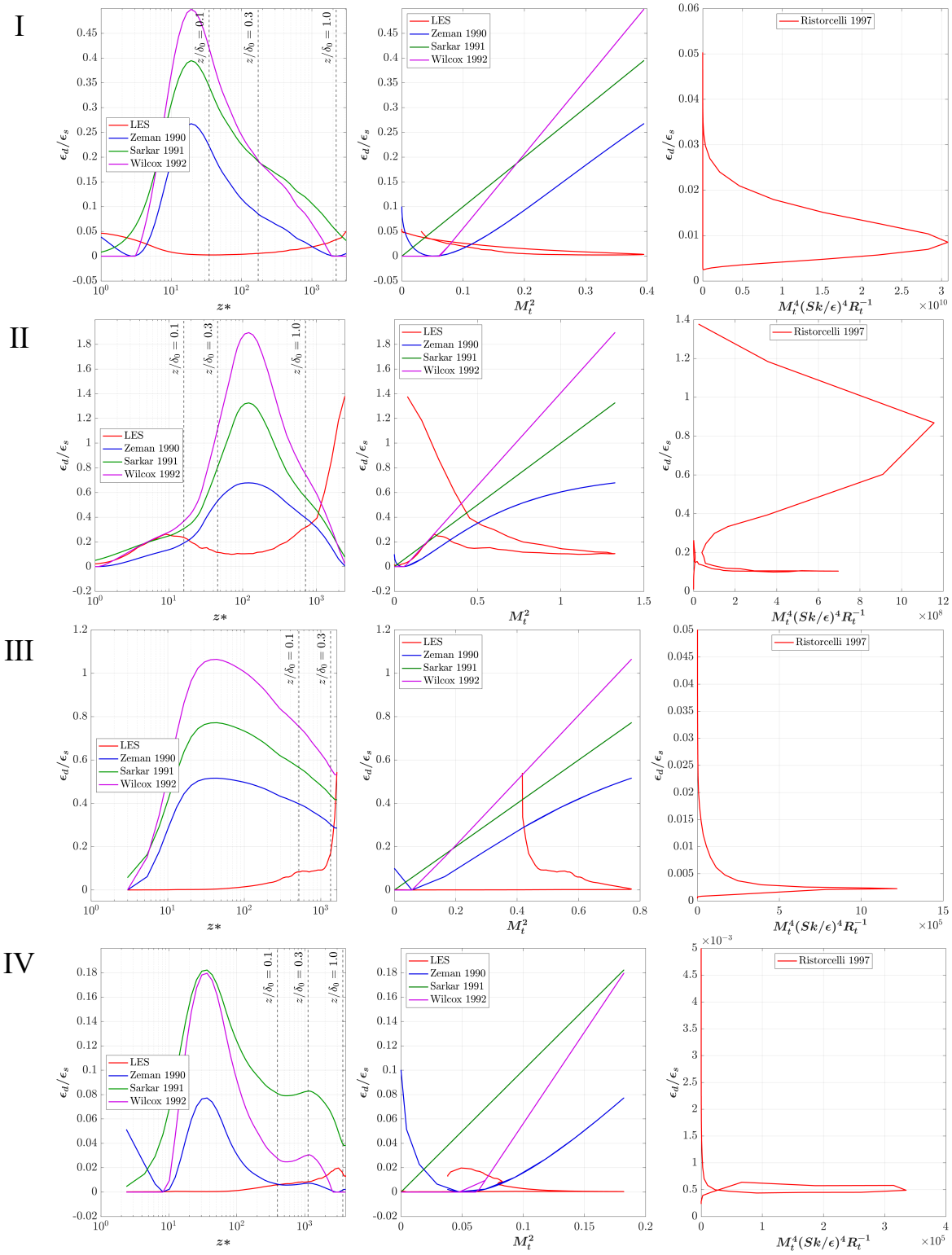


Figure 6.10. Dilatational dissipation model assessment, versus z^* (left), M_t^2 (middle) and $M_t^4(Sk/\epsilon_s)^4 R_t^{-1}$ (right).

of Figure 6.10 shows the functional dependence of ϵ_d/ϵ_s on M_t^2. As expected, the Sarkar model assumes a linear form, while Wilcox's model is linear above a certain M_t^2 threshhold. Zeman's model is nearly linear away from the wall. When compared to the LES solution, it is clear that there is no correlation between ϵ_d/ϵ_s and M_t^2 as the models would suggest. Again, the one exception is at station II in the separation bubble for $z^* \lesssim 10$. The right side plots show Ristorcelli's scaling for the so-called rapid component of ϵ_d/ϵ_s, assuming $\epsilon_d^r/\epsilon_s \gg \epsilon_d^s/\epsilon_s$. Ristorcelli's scaling imply a monotone variation of ϵ_d/ϵ_s. The plots indicate that this may be true in a piecewise sense for parts of the profiles, but no conclusions can be obtained without further investigation.

Besides the near-wall separated region at station II, the results herein are in line with Duan et al. 2010/2011 [49],[50], where for turbulent flat plate DNS at Mach 3-12, it was shown that ϵ_d/ϵ_s was no more than 5% occurring in the outer boundary layer (note that total dissipation is very small in this region) and that the functional dependence of ϵ_d/ϵ_s on M_t^2 and M_t^4 failed. Huang et al 1995 [68] also showed that ϵ_d/ϵ_s is small and that ϵ_d/ϵ_s and M_t are uncorrelated for a compressible turbulent channel flow. The results herein show that compressibility corrections for dilatational dissipation may generally not be needed for the present test case given the low to negligible levels of dilatational dissipation observed. Additionally, existing models do not reflect the low levels of dilatational dissipation or confirm their functional dependencies. However, note that the models of Zeman, Sarkar and Wilcox have been shown to improve predictions of mixing layer growth rates as a function of convective Mach number (Sarkar & Lakshmanan 1991 [141], Barone et al. 2006 [152], Wilcox 2006 [134]). The strain rate Mach number, $M_s \sim M_t\, Sk/\epsilon_s$ (also proportional to the gradient Mach number M_g), is one parameter used to characterize the compressibility effect in mixing layers and wall boundary layers. Sarkar 1995 [153] argued that

dilatational compressibility effects are far more significant in mixing layers than in wall boundary layers. Sarkar compared a mixing layer where $M_s \sim 6$ to a wall boundary layer where $M_s \sim 1$ and showed that dilatational dissipation was $\sim 6^2$ more important in the mixing layer than in the wall boundary layer (Ristorcelli 1997 [151]).

6.8.3 Dissipation Tensor

The most common approach to modeling the dissipation tensor in the RST equation, based on Kolmogorov's hypothesis of local isotropy of fine scale motions, is to initially assume $\epsilon_{ij} = 2/3\epsilon\delta_{ij}$, where scalar dissipation ϵ is obtained via a transport equation (such transport equations are not addressed in this study). This assumption has validity for high Reynolds number flows and remote from walls, but is not entirely accurate. An obvious consequence of this assumption is that there is no sink for Reynolds shear stresses via the dissipation budget. Models in use today account for departures from isotropy in various ways. One approach is to assume that the anisotropic dissipation tensor has the same mathematical form as the pressure strain tensor and thus absorb the anisotropic dissipation into the model for the pressure strain tensor (Lumley 1979 [154]).

For wall bounded flows, dissipation is strongly affected by the presence of the wall through viscosity of the fluid and by the inviscid wall blocking effect. Archival DNS results have shown that as the wall is approached the dissipation becomes anisotropic, e.g., Spalart 1988 [155]. In this case a different modeling approach is needed. Near-wall corrections (NWC), also referred to as low-Reynolds number corrections (LRC), are often used in wall-bounded flows. Several models exist in the literature. Three such popular anisotropic LRCs are investigated herein, viz,

Rotta 1951 [133]: $$\epsilon_{ij}^{w} = \frac{\widetilde{u_i'' u_j''}}{k}\epsilon \qquad [98]$$

Launder & Reynolds 1983 [156], Kebede, Launder & Younis 1985 [157] (LRKY):

$$\epsilon_{ij}^{w} = \epsilon \frac{\widetilde{u_i'' u_j''} + n_j n_k \widetilde{u_i'' u_k''} + n_i n_k \widetilde{u_j'' u_k''} + n_k n_l \widetilde{u_k'' u_l''} \delta_{ij}}{k + {}^{5}/_{2}\, n_p n_q \widetilde{u_p'' u_q''}} \quad [99]$$

Hanjalić & Jakirlić 1993 [158] (HJ):

$$\epsilon_{ij}^{w} = \epsilon \frac{\widetilde{u_i'' u_j''} + \left(n_j n_k \widetilde{u_i'' u_k''} + n_i n_k \widetilde{u_j'' u_k''} + n_i n_j n_k n_l \widetilde{u_k'' u_l''}\right) f_d}{k + {}^{3}/_{2}\, n_p n_q \widetilde{u_p'' u_q''} f_d} \quad [100]$$

$$f_d = (1 + 0.1 Re_t)^{-1}$$

The models aim to satisfy the low Reynolds number near-wall limit of the dissipative fine-scale eddies, and the high Reynolds number outer-wall limit of the large scale energy-bearing eddies. This is achieved by blending the LRC correction, ϵ_{ij}^{w}, with the isotropic assumption, ϵ_{ij}^{iso}, away from the wall as follows,

$$\epsilon_{ij} = f_\epsilon \epsilon_{ij}^{w} + (1 - f_\epsilon)\epsilon_{ij}^{iso}, \qquad \epsilon_{ij}^{iso} = 2/3 \epsilon \delta_{ij} \quad [101]$$

Here f_ϵ is a smooth blending function. Rotta's 1951 [133] model assumes direct proportionality between the deviatoric dissipation tensor and the deviatoric Reynolds stress tensor. Rotta's simple formulation satisfies some limiting values of ϵ_{ij}, but not for all of its components. The model of Launder & Reynolds 1983 [156] and Kebede, Launder & Younis 1985 [157] (denoted as LRKY herein) uses an invariant way of satisfying the limits by using the unit wall normal vector n_i. Some models circumvent the use of the wall topology dependent parameter n_i by using local flow quantities instead, namely $\nabla k^{1/2}$which is a vector in the direction of n_i (Pope 2000 [135]), viz,

$$n_i n_j = \frac{2\nu}{\epsilon} \frac{\partial k^{\frac{1}{2}}}{\partial x_i} \frac{\partial k^{\frac{1}{2}}}{\partial x_j} \quad [102]$$

This relation is exact at the wall and a good approximation through the viscous sublayer (Craft & Launder 1996 [159]). The model of Hanjalić & Jakirlić 1993 [158] (denoted as HJ herein) modified the LRKY expression by introducing the function f_d which limits how far the LRKY near-wall correction extends into the region where dissipation isotropy is assumed.

Several blending functions f_ϵ exist in the literature. A few were tested in this study. Figure B.1 (Appendix) shows the three LRC models evaluated using various blending functions at the upstream equilibrium station I. Based on these tests, the blending function used by Hanjalić & Jakirlić 1993 [158] was chosen for all three dissipation tensor models, viz,

$$f_\epsilon = 1 - A_f^{1/2} E_f^2 \qquad [103]$$

$$A_f = 1 + 9II + 27III, \qquad E_f = 1 + 9II_\epsilon + 27III_\epsilon$$

Here, A_f is Lumley's flatness parameter, E_f is flatness parameter of the small scale dissipative motion, II and III are the second and third invariants of the anisotropic Reynolds stress tensor defined in Section 6.5 , and II_ϵ and III_ϵ are the second and third invariants of the anisotropic dissipation tensor. An interesting feature, unlike other blending functions, is the lack of an empirical tuning constant. It was noted that the blending function used by Gerolymos et al. 2012 [160], $f_{5\epsilon}$ in Figure B.1, yielded almost identical results.

Figure 6.11 and Figure 6.12 demonstrate the a priori performance of the three dissipation tensor models at stations I-IV, where the dissipation components are normalized by viscous wall units and by isotropic dissipation $2/3\epsilon$, respectively. The normalization in Figure 6.12 highlights the near-wall performance as well as the return to isotropy, or lack thereof, away from the wall. At the upstream equilibrium station I, the models show very good comparison with the LES solution. Figure 6.11-I shows that the dissipation is greatest at the wall, with the streamwise component ϵ_{11} being significantly larger and crosstream component ϵ_{22} being second largest. The Rotta model best captures the wall limit of ϵ_{11} versus LRKY and HJ. The dissipation decreases to negligible values by $z^* \approx 100$ in the log layer. Figure 6.12-I shows the anisotropic nature of the dissipation at the wall. Away from the wall by $z^* \approx 100$ the diagonal components tend rapidly towards unity while the off-diagonal components remain small indicating near isotropy. Surprisingly the simple

Rotta model compares better overall at station I, followed by HJ and then LRKY. For the other components, Rotta and HJ perform equally well and better then LRKY. The Rotta and HJ models capture the small degree of anisotropy observed for $z^* \gtrsim 100$, while the LRKY model forces ϵ_{11} and ϵ_{33} to unity by $z^* \approx 100$. Component ϵ_{13} is small near the wall but increases modestly in magnitude for $z^* \gtrsim 100$. All three models predict ϵ_{13} to be moderately larger than the LES solution for $z^* \gtrsim 30$. All models also reflect the negligible values of components ϵ_{12} and ϵ_{23}.

In the separated region at station II, Figure 6.11-II shows that excellent comparison of the models with the LES solution in the near-wall region. The dissipation components are clearly amplified with the ϵ_{11} and ϵ_{22} components being significantly larger than the other components at the wall. The components decrease rapidly a short distance away from the wall, but then show a prominent peak at $z/\delta_0 \approx 0.4$ presumably in the separation shear layer, before decreasing to negligible levels at $z/\delta_0 > 1.2$ near the freestream edge. Figure 6.12-II shows that the models almost precisely capture the wall values. All models track with the LES solution very well up to $z/\delta_0 \approx 0.1$, after which there is some discrepancy more so in components ϵ_{11}, ϵ_{33} and ϵ_{13}. Generally the turbulence is anisotropic throughout.

In the region of strong nonequilibrium following reattachment at station III, Figure 6.11-III shows an excellent comparison between the models and the LES solution. Of the four stations the components are most amplified at station III. Of note is the significant amplification of component ϵ_{13}, where before at stations I & II this component was fairly negligible. Away from the wall, the dissipation decreases rapidly becoming negligible by $z^* \approx 100$. Figure 6.12-III shows that the models compare very well, except for some discrepancy in ϵ_{11} and ϵ_{33} at $z^* \approx 100$ and generally for all components for $z/\delta_0 > 0.1$. Note that the profile at extends all the way to just before the shock line where viscous dissipation is much less apparent according to Figure 6.11-III. Once

again, the significant amplification of ϵ_{13} is evident in the near wall region, but then it decreases towards the shock becoming negative at $z/\delta_0 \approx 0.3$.

At the furthest downstream station IV, Figure 6.11-IV shows that the comparison of the models with the LES solution is excellent, except for some small discrepancy in ϵ_{22}. The components are less amplified than at station II as the boundary layer attempts to relax. The ϵ_{13} component remains significantly amplified relative to the upstream station I where it was negligible. All components again become negligible by $z^* \approx 100$. Figure 6.12-IV shows very good near- wall performance of the models up to $z^* \approx 50$, after which there are some discrepancies. There is a small region of approximate isotropy for $z/\delta_0 \approx [0.1, 0.3]$ where the diagonal components tend to unity and the ϵ_{13} component crosses the zero line. Note that, like station III, the profile at IV extends all the way to just before the shock line where viscous dissipation is much less apparent according to Figure 6.11-IV.

It should be noted that for the a priori comparison herein, the tensor models utilized the scalar dissipation ϵ calculated directly from the LES flowfield. In RANS models, whether EVMs or RSTs, scalar ϵ is typically calculated via a transport equation whose source terms are modeled, likely introducing larger uncertainties in the calculation of scalar ϵ and therefore in the tensor models. Nevertheless, the results herein show that the dissipation tensor models compare remarkably well with the LES solution considering the extent of flow compression and nonequilibrium following the shock wave. Overall the Rotta and HJ models compare better than LRKY, with the Rotta model being marginally better than HJ in some instances. The sophistication of the HJ and LRKY models did not offer the expected improvements over the simple Rotta model for this test case. Considering the ease of calculation and accuracy, Rotta's 1951 model with an appropriate blending function is sufficient for this type of SBLI problem.

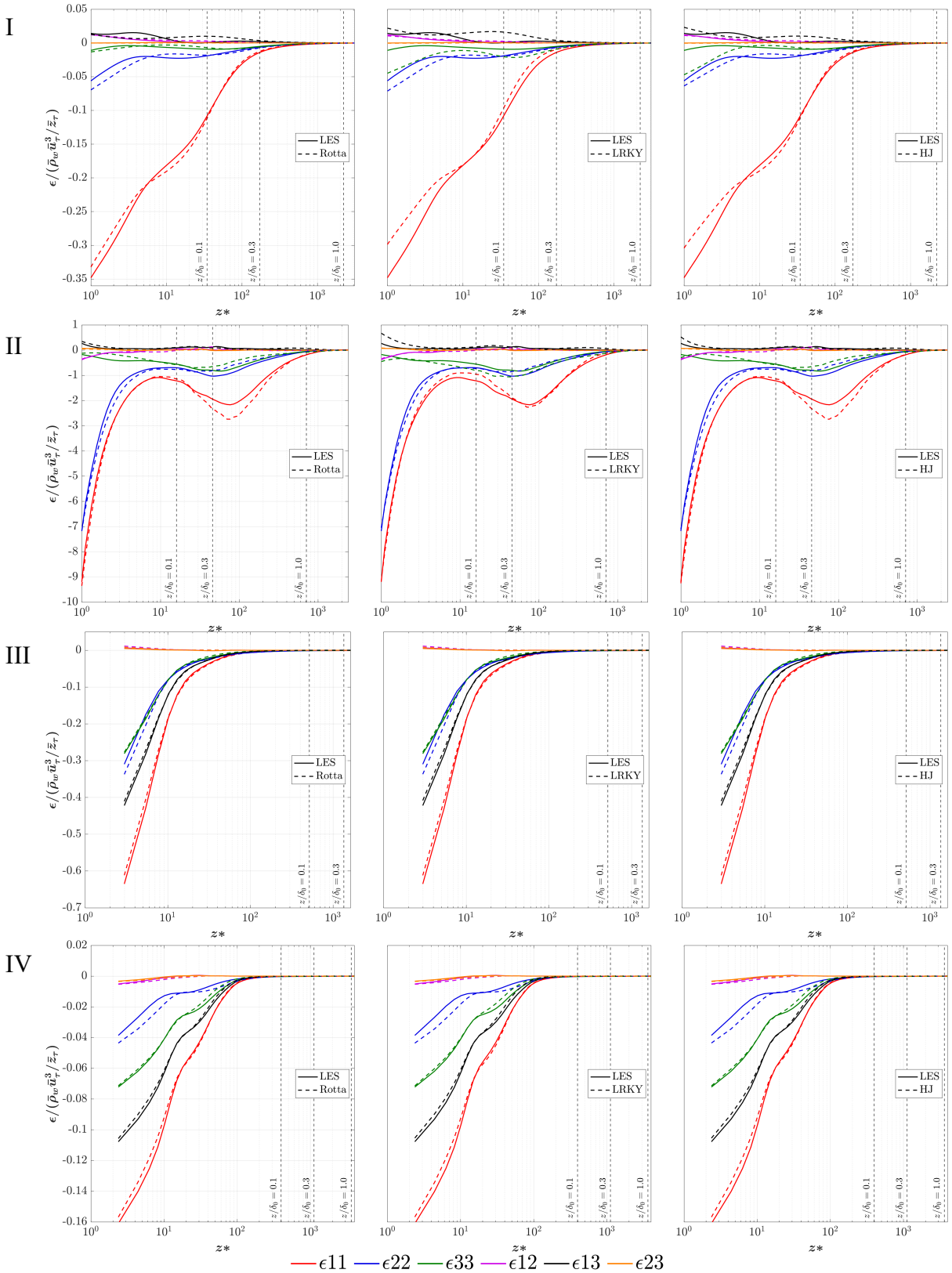


Figure 6.11. Dissipation tensor models, normalized by viscous wall units: Rotta (left), LRKY (middle), HJ (right).

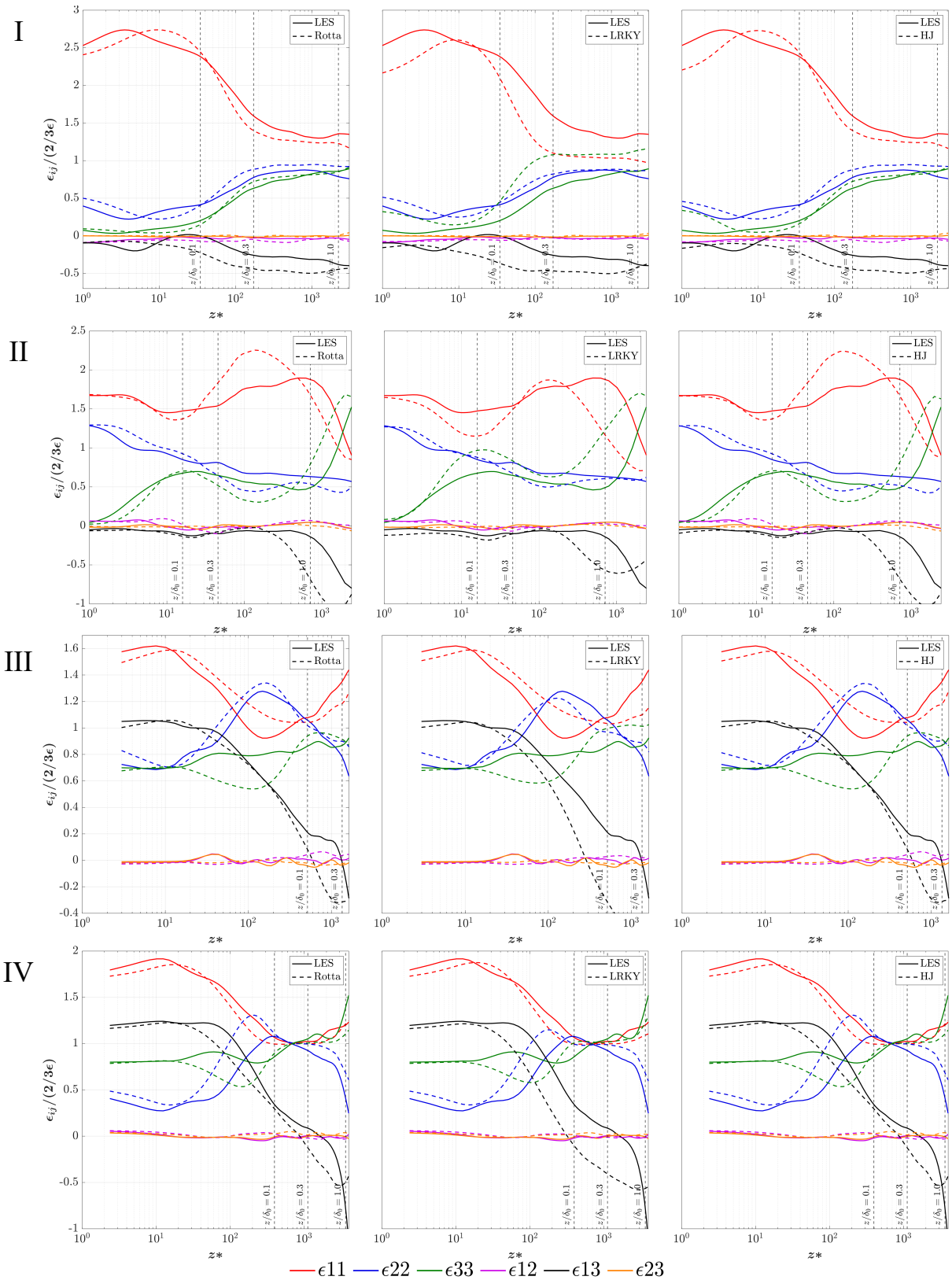


Figure 6.12. Dissipation tensor models, normalized by $2/3\,\epsilon$: Rotta (left), LRKY (middle), HJ (right).

6.9 Pressure Strain and Pressure Dilatation

In the RST balance, the pressure strain Π_{ij}, that is, correlations of pressure fluctuations with velocity gradient, is of the same order of magnitude as production and plays a central role in redistributing energy between the streamwise, wall normal and spanwise stress components. Correlations of this nature are also difficult to measure experimentally. The modeling of the pressure strain term is therefore crucial and has been the subject of extensive research. The most common modeling approach is to split the pressure strain tensor into its isotropic and deviatoric parts and then model the parts separately, viz,

$$\Pi_{ij} = \Pi_{ij}^{dev} + {}^{2}/_{3}\,\Pi\delta_{ij} \qquad [104]$$

Here, $\Pi = \Pi_{ii}/2$, the trace of Π_{ij}, is called the pressure dilatation and appears in the compressible TKE transport equation. The deviatoric component Π_{ij}^{dev} does not appear in the TKE transport equation in either the compressible or incompressible case. The pressure dilatation and pressure strain tensor are investigated below for the present test case.

6.9.1 Pressure Dilatation

Pressure dilatation represents the exchange between TKE and turbulent potential energy due to pressure fluctuations, particularly in rapidly compressed turbulence. The pressure dilatation vanishes in the incompressible limit as density fluctuations go to zero because $\widetilde{u_i''}$ and $\nabla \cdot \widetilde{u_i''}$ (divergence) go to zero. It is therefore considered a compressible effect. The pressure dilatation is given by,

$$\Pi = \frac{1}{2}\Pi_{ii} = \overline{p' \frac{\partial u_i''}{\partial x_i}} = \overline{p' s_{kk}''} \qquad [105]$$

Two popular models are evaluated in this study, viz,

Zeman 1991 [161]:

$$\Pi = \Pi^s + \Pi^{r1} + \Pi^{r2} + \Pi^\rho \quad [106]$$

$$\Pi^s = (\bar{p}\gamma)^{-1}\left(\overline{p'^2} - p_e^2\right)/\tau_a, \quad \tau_a \approx 0.13\tau_t M_t, \quad \tau_t = \frac{2k}{\epsilon}, \quad p_e^2 \propto \bar{p}^2 M_t^4$$

$$\Pi^{r1} = C_{r1}(\gamma\bar{p})^{-1}\overline{p'^2}\tilde{S}_{kk}, \qquad C_{r1} = (5 - 3\gamma)/12$$

$$\Pi^{r2} = C_{r2}\gamma\bar{p}p'_{rms}\tau_t\tilde{S}_{ij}^{dev\,2}, \quad C_{r2} = 0.0004, \quad \tau_t = k/\epsilon$$

$$\Pi^\rho = f_\rho(M_t)\bar{\rho}^{-2}\gamma\bar{p}\tau_t\widetilde{u_i''u_j''}\frac{\partial\bar{\rho}}{\partial x_i}\frac{\partial\bar{\rho}}{\partial x_j}, \quad f_\rho(M_t) = C_\rho\left(1 - e^{-50M_t^2}\right), \quad C_\rho = 0.002$$

Sarkar 1992 [143]:

$$\Pi = \Pi^{\mathrm{s}} + \Pi^{\mathrm{r}} \quad [107]$$

$$\Pi^{\mathrm{s}} = \alpha_3\bar{\rho}\epsilon M_t^2, \qquad \alpha_3 = 0.2$$

$$\Pi^{\mathrm{r}} = \alpha_2\mathcal{P}M_t + {}^4\!/_3\,\alpha_4\gamma\bar{p}\tilde{S}_{kk}M_t^4, \qquad \alpha_2 = 0.15, \qquad \alpha_4 = N/A$$

Zeman 1991 [161] simplified the pressure variance transport equation ($D\overline{p'^2}/Dt = \cdots$) to show that the pressure dilatation is proportional to the rate of change of turbulent potential energy ($\propto \overline{p'^2}$) due to compression work in temporally evolving flows. Supported by DNS of decaying and shear-driven homogenous turbulence, Zeman then proposed a phenomenological model for the rate of change of turbulent potential energy, obtaining an expression for the so-called 'slow' component of the pressure dilatation Π^{s}. The model implies that pressure fluctuations relax to an equilibrium (rms) value $\bar{p}_e$ on a time scale τ_a associated with acoustic wave propagation. Durbin & Zeman 1991 [162] applied rapid distortion theory to show that there is a rapid compression contribution Π^{r1} that is proportional to the pressure-velocity gradient correlation term in the pressure variance transport equation. Zeman & Coleman 1991 [163] showed that the latter rapid contribution can represent only spherical (3D) compression but not anisotropic (1D) compression and therefore added a model for the rapid directional compression component Π^{r2}. This component is negative and therefore acts as a sink converting TKE to turbulent potential energy. For turbulent boundary layer flows, Zeman 1991/1993 [161],[164] suggested that the term

representing interactions between mean density gradient and fluctuating pressure in the pressure variance transport equation may be important and derived an expression for pressure dilatation due to the mean density gradient term Π^{ρ}. This term is positive and therefore acts as a source term converting turbulent potential energy to TKE. In deriving Π^{ρ}, Zeman assumed that the advection of pressure variance $D\overline{p'^2}/Dt$ is negligible such that the slow component Π^{s} is effectively zero. Therefore, Π^{s} will not be considered for the wall-bounded flow herein. Since the rapid component $\Pi^{r} = \Pi^{r1} + \Pi^{r2}$ is deemed important in shock-turbulence interactions, this component is retained herein.

Sarkar 1992 [143] used a Poisson equation for fluctuating pressure, derived by taking the divergence of the Navier-Stokes momentum equation, to decompose the pressure dilatation into slow and rapid components, Π^{s} and Π^{r}, respectively. Supported by DNS of decaying isotropic turbulence and homogenous shear turbulence, Sarkar derives algebraic expressions to model the slow and rapid pressure dilatation terms. The rapid component reacts instantaneously to changes in mean velocity gradient. In the rapid distortion limit (characterized by $Sk/\epsilon \to \infty$, where S strain rate magnitude) Π^{r} has a leading-order effect. Furthermore, for $M_t < 1$, the linear term in M_t has the leading order effect in Π^{r}. Note that α_4 remains uncalibrated. The slow component can be expected to be non-negligible in most cases except in the limit of rapid distortion.

Ristorcelli 1997 [151] describes pressure dilatation as a nonequilibrium phenomenon. Restricted to low-M_t flows, Ristorcelli suggests that the pressure dilatation scales as $\Pi \propto M_t^2 (Sk/\epsilon)^2 [\mathcal{P}/\epsilon - 1]$. Several features are worth noting. The scaling implies that pressure dilatation scales with the magnitude of the departure from equilibrium, that is, departure of $\mathcal{P}/\epsilon$ from unity. Thus for statistically stationary flows the pressure dilatation is expected to be small. Depending on the ratio $\mathcal{P}/\epsilon$, pressure dilatation can be positive (TKE source) or negative (TKE

sink), which has a destabilizing or stabilizing effect, respectively, consistent with observations of Sarkar 1995 [153] and Simone et al. 1997 [165]. Also the strain rate Mach number $M_S \sim M_t\, Sk/\epsilon_s$ must be non-negligible for pressure dilatation to be important.

Figure 6.13 and Figure 6.14 investigates the aforementioned pressure dilatation models and scalings. Figure 6.13 compares the Sarkar and Zeman models with the LES solution, normalized by viscous wall units. The LES solution shows that pressure dilatation is negative in the near-wall region acting as a TKE sink. Away from the wall pressure dilatation become negligible at stations I & IV, while at stations II & III the pressure dilatation shows one or more sign changes but remain smaller than the wall value. At station III, pressure dilatation increases for $z/\delta_0 > 0.3$, which is likely due to the shock compression. Recall that at stations III & IV that the wall normal profiles extend all the way to just before the shock line.

The Sarkar and Zeman models generally do not capture the pressure dilatation. Sarkar's model predicts positive pressure dilatation (a TKE source) in all cases with the rapid component being greater than the slow component ($\Pi^r > \Pi^s$). Since $M_t \leq 1$ for most of the flowfield, the linear term in M_t of the rapid component dominates, i.e., $\Pi \approx \Pi^{\mathrm{r}} = \alpha_2 \mathcal{P} M_t$. This explains why the peaks in the modeled pressure dilatation approximately coincides with the production budget as seen in Figure 6.6. This also justifies ignoring the M_t^4 term in the rapid component (which was the case here) in which empirical coefficient a_4 was not available. Also note that Sakar's model forces the pressure dilatation to be zero at the wall, which is not the case in the LES solution. The one exception to the poor model performance is at station III, where Sarkar's model tracks with the LES for $z^* \approx [10{,}110]$, but this may or may not be fortuitous.

Zeman's model shows that the rapid component Π^r is dominant. The density gradient component Π^ρ, purported to be important in boundary layer flows, is negligible at all stations.

Zhang et al 2018 [145] also showed negligible Π^{ρ} using DNS of a turbulent flat plate at M=2-14. Zeman's model for total pressure dilatation captures the correct sign of the pressure dilatation in the near-wall region and predicts the pressure dilatation to be negligible away from the wall at stations I & IV as did the LES. However, the comparisons are still generally poor, with gross overpredictions of the pressure dilatation magnitude at stations III & IV in the post-shock nonequilibrium region. As previously discussed, the Zeman's slow pressure dilatation term is not plotted.

Figure 6.14 tests the scalings of pressure dilatation implied by the models at the upstream equilibrium station I. The plots show no correlation between pressure dilatation and turbulent Mach number or strain rate Mach number. Although not shown, the conclusion is the same at stations II-IV. The rightmost plot shows that the scaling of Ristorcelli does not hold. Ristorcelli's scaling suggests that the flow must be in a state of nonequilibrium ($\mathcal{P}/\epsilon \neq 1$) and M_S must be non-negligible. This is certainly true of the downstream stations. However, Ristorcelli's scalings do not hold for the downstream stations II-IV (plots not shown).

In summary, the a priori performance of the models for pressure dilatation evaluated herein is poor when compared to LES solution. As shown in Figure 6.6, pressure dilatation budget in the TKE transport balance is generally small relative to other budgets, acting as a small (but not necessarily negligible) sink in viscous near-wall region and negligible otherwise (except at the separated corner). For RANS modeling of this and similar SBLI cases, it would be preferrable to ignore the pressure dilatation than to inherit the inaccuracies of these models. This does not necessarily imply that the theoretical analyses that led to the development of these models are without merit.

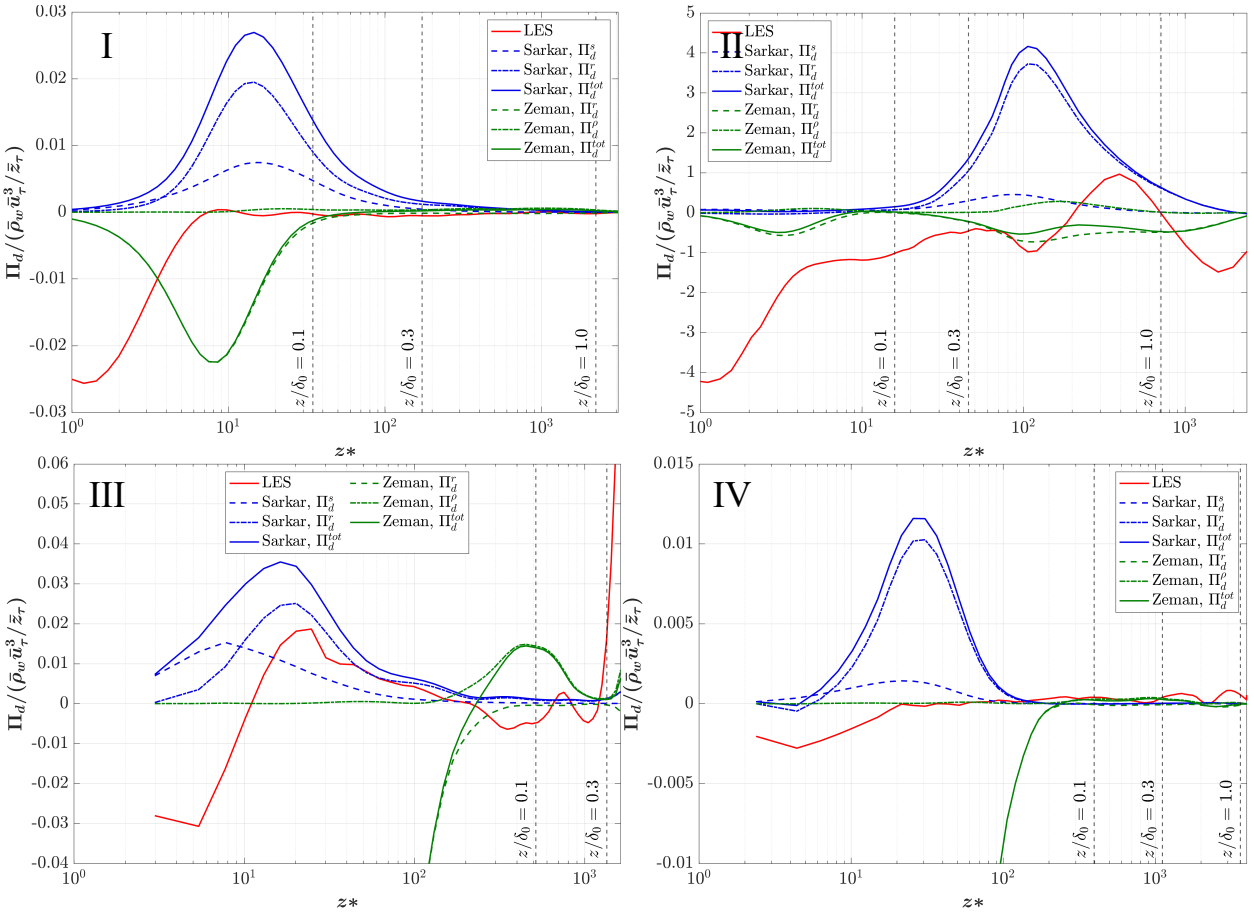


Figure 6.13. Pressure dilatation models.

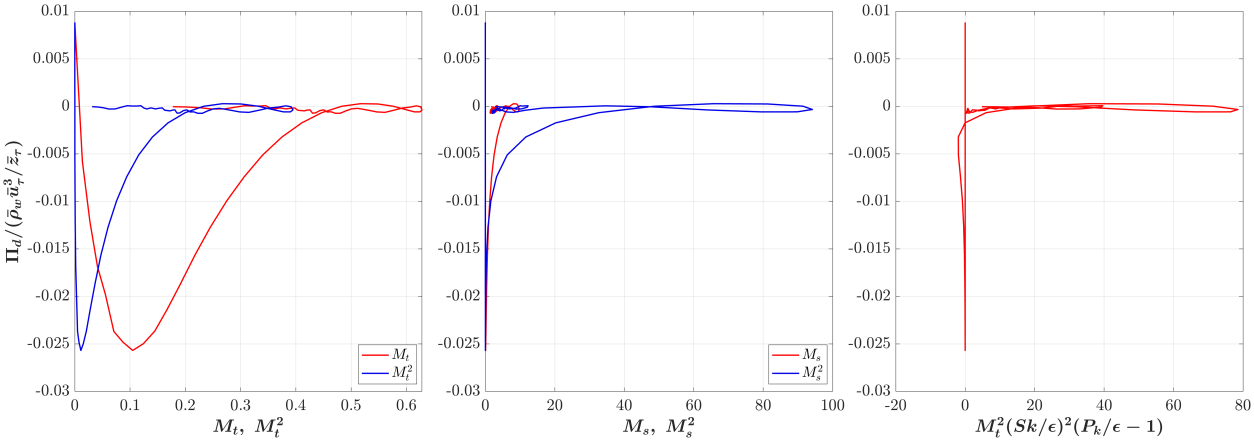


Figure 6.14. Pressure dilatation model scalings at upstream equilibrium station I.

6.9.2 Pressure Strain Tensor

The most common approach to modeling the pressure strain tensor is to decompose the pressure strain into slow, rapid and harmonic components, Π^s, Π^r and Π^h, respectively, viz,

$$\Pi_{ij} = \overline{p'\left(\frac{\partial u_i''}{\partial x_j} + \frac{\partial u_j''}{\partial x_i}\right)} = \overline{p' s_{ij}''} = \Pi^s + \Pi^r + \Pi^h \qquad [108]$$

The rapid component of pressure strain is directly proportional to the mean strain rate, and in the limit of rapid distortion ($Sk/\epsilon \to \infty$, S is normalized strain rate) has a leading-order effect. The slow component of pressure strain involves nonlinear turbulence-turbulence interactions, and in the limit of zero mean velocity gradients ($Sk/\epsilon \to 0$) is the leading order term. This decomposition of pressure strain is obtained from the Poisson equation for fluctuating pressure p', derived by taking the divergence of the Navier-Stokes momentum equation. Chou 1945 [132] used the Green-function solution to the p' Poisson equation to show that the slow and rapid components of pressure strain are integral functions of two-point spatial correlations over some volume of the flowfield. Therefore pressure strain is not a localized process. Nevertheless, current modeling approaches assume a locally-homogenous approximation where modeling assumes singe-point correlations.

By examining decaying homogenous anisotropic turbulence in which the rapid and harmonic components are zero, and based on the notion that turbulence has a tendency towards isotropy as it decays, Rotta 1951 [133] proposed the 'linear return to isotropy' model for slow pressure strain:

$$\Pi_R^s = -2C_R \epsilon b_{ij}, \qquad 1.4 \leq C_R \leq 1.8 \qquad [109]$$

Several models for pressure strain exist in the literature. Three popular single-point closures that model the slow and rapid components of the pressure strain tensor are evaluated herein. Following Pope 2000 [135], the following nondimensional, symmetric, deviatoric tensors $\mathcal{T}_{ij}^{(n)}$ are first

defined in terms of stress anisotropy tensor b_{ij}, normalized mean strain rate $\hat{S}_{ij}$ and normalized mean rotation rate $\widehat{W}_{ij}$, viz,

$$\hat{S}_{ij} = {}^{k}/_{e}\, \tilde{S}_{ij}^{dev}$$
$$\widehat{W}_{ij} = {}^{k}/_{e}\, \widetilde{W}_{ij}$$
$$\mathcal{T}_{ij}^{(1)} = b_{ij}$$
$$\mathcal{T}_{ij}^{(2)} = b_{ij}^{2} - {}^{1}/_{3}\, b_{kk}^{2}\delta_{ij}$$
$$\mathcal{T}_{ij}^{(3)} = \hat{S}_{ij}$$
$$\mathcal{T}_{ij}^{(4)} = \hat{S}_{ik}b_{kj} + \hat{S}_{kj}b_{ik} - {}^{2}/_{3}\, \hat{S}_{kl}b_{lk}\delta_{ij}$$
$$\mathcal{T}_{ij}^{(5)} = \widehat{\mathrm{W}}_{ik}b_{kj} + \widehat{\mathrm{W}}_{kj}b_{ik}$$

The three models evaluated herein are then constructed as follows:

$$\Pi_{ij} = \epsilon \sum_{n=1}^{5} f^{(n)}\, \mathcal{T}_{ij}^{(n)} \qquad [110]$$

	LRR 1975 [166]	LRR-QI 1975 [166]	SSG 1991 [167]
$f^{(1)}$	$-2C_1$	$-2C_1$	$-C_1 - C_{1s}\mathcal{P}/\epsilon$
$f^{(2)}$	0	0	C_2
$f^{(3)}$	${}^{4}/_{3}\, C_2$	${}^{4}/_{5}$	$C_3 - \sqrt{6}C_{3s}\eta,$ $\eta = \sqrt{-II/3}$
$f^{(4)}$	$2C_2$	${}^{6}/_{11}\,(2 + 3C_2)$	C_4
$f^{(5)}$	$2C_2$	${}^{2}/_{11}\,(10 - 7C_2)$	C_5
Constants	$C_1 = 1.8$ $C_2 = 0.6$	$C_1 = 1.5$ $C_2 = 0.4$	$C_1 = 3.4,\ C_{1s} = 1.8$ $C_2 = 4.2$ $C_3 = 0.8,\ C_{3s} = 1.3$ $C_4 = 1.25$ $C_5 = 0.4$

The Launder-Reece-Rodi 1975 [166] (LRR) model is the most common model for pressure strain. The LRR model adds a rapid pressure strain model to Rotta's 1951 slow pressure strain model. The theoretically enhanced quasi-isotropic Launder-Reece-Rodi 1975 [166] (LRR-QI) model was developed so that pressure strain would be linear in mean strain rate in the limit of rapid distortion ($Sk/\epsilon \to \infty$). The first term of LRR and LRR-QI is Rotta's linear return to isotropy model for slow pressure strain Π_R^s. The Speziale-Sarkar-Gatski 1991 [167] (SSG) model is a classic quadratic model where the slow pressure strain (the first term) also includes Rotta's model as well as a dependence on $\mathcal{P}/\epsilon$. SSG has a nonzero $f^{(2)}$ value which also accounts for nonlinear return to isotropy of the slow pressure strain component. Contributions from tensors $\mathcal{T}_{ij}^{(3-5)}$ model the rapid pressure strain in all three models.

The harmonic component Π^h, also referred to as the pressure echo effect or more popularly the wall reflection effect in wall bounded flows, satisfies boundary conditions on p'. It is sometimes ignored, and yet it is sometimes qualitatively important near walls and free-flow surfaces. It is responsible for the redistribution of normal stresses, where near a wall it tends to damp the stress normal to the wall while enhancing stresses parallel to the wall. Some models attempt to automatically account for the harmonic component in the slow and rapid pressure strain terms. One example is to modify the standard LRR model by recomputing $\hat{S}_{ij}$ and $\widehat{W}_{ij}$ using an effective velocity gradient per Launder & Tselepidakis 1991 [168]. Another approach is to explicitly add a wall reflection term to the standard LRR model. The latter approach is evaluated herein using the wall reflection model of Gibson & Launder 1978 [169] (GL) for use with the standard LRR model, detailed below. For this model, the wall reflection term is further split into slow and rapid components, viz,

$$\Pi_{ij}^h \equiv \Pi_{ij}^w = \Pi_{ij}^{s,w} + \Pi_{ij}^{r,w} \qquad [111]$$

Gibson & Launder 1978 [169] (GL):

$$\Pi_{ij}^{s,w} = C_1^w \frac{\epsilon}{k}\left(n_k n_l \widetilde{u_k'' u_l''}\delta_{ij} - {}^3/_2\, n_j n_k \widetilde{u_i'' u_k''} - {}^3/_2\, n_i n_k \widetilde{u_j'' u_k''}\right) \qquad [112]$$

$$\Pi_{ij}^{r,w} = C_2^w\left(n_k n_l \Pi_{kl}^r \delta_{ij} - {}^3/_2\, n_j n_k \Pi_{ik}^r - {}^3/_2\, n_i n_k \Pi_{jk}^r\right)$$

$$C_1^w = 0.5 C_l \ell_t d^{-1}, \quad C_2^w = 0.3 C_l \ell_t d^{-1}, \quad C_l = C_\mu^{3/4}/\kappa$$

$$C_\mu = 0.06, \quad \kappa = 0.41, \quad \ell_t = k^{3/2}/\epsilon$$

Here, n_i is the unit wall normal vector, d is the normal distance to the wall, ℓ_t is the turbulence length scale and κ is the Von Karman constant. Note that the GL model is dependent on wall topology through n_i and d. As a result, they may pose issues for complex geometries, such as those with highly curved surfaces or multiple distinct adjacent faces. The GL model uses $C_\mu = 0.09$ as default, but here $C_\mu = 0.06$ is used instead.

The above pressure strain models were generally developed for high Reynolds number flows remote from no-slip walls. Close to a no-slip wall, low Reynolds number corrections (LRC) are often employed to correct for viscous effects. Two such modifications for the LRR model, without and with the GL wall reflection term, are investigated, viz, the Launder-Shima (LS) 1989 LRC [170] and the Gerolymos & Vallet (GV) 2001 LRC [171]. Essentially the coefficients become semi-empirical functions of Reynolds stress invariants and turbulence Reynolds number, viz,

Launder- Shima 1989 LRC [170] (LS):

$$C_1 = 1 + 2.58 A_f A_2^{0.25}\left[1 - e^{-\left(\frac{Re_t}{150}\right)^2}\right], \qquad A_f = 1 + 9II + 27III, \qquad A_2 = -8II$$

$$C_2 = 0.75 A_f^{1/2}$$

$$C_1^w = C_l \ell_t d^{-1}\left(1.67 - \tfrac{2}{3}C_1\right)$$

$$C_2^w = C_l \ell_t d^{-1} \max\left[\tfrac{2}{3} - \tfrac{1}{6C_2}, 0\right]$$

$$C_l = C_\mu^{1/4}/\kappa, \quad C_\mu = 0.06, \quad \kappa = 0.42, \quad \ell_t = k^{3/2}/\epsilon$$

Gerolymos & Vallet LRC 2001 [171] (GV):

$$C_1 = 1 + 2.58A_f A_2^{0.25}\left[1 - e^{-\left(\frac{Re_t}{150}\right)^2}\right], \qquad A_f = 1 + 9II + 27III, \qquad A_2 = -8II$$

$$C_2 = \min\left[1, 0.75 + 1.3\max\left(0, A_f - 0.55\right)\right] A_f^{\max\left[0.25, 0.5 - 1.3\, max\left(0, A_f - 0.55\right)\right]}\left[1 - \max\left(0, 1 - \frac{Re_t}{50}\right)\right]$$

$$C_1^w = 0.83\left[2 - \frac{2}{3}C_1\right]\|\nabla \ell_1^w\|, \qquad \ell_1^w = \ell_t\left(1 - e^{-Re_t/30}\right)\left(1 + 2A_2^{0.8}\right)^{-1}, \qquad \ell_t = k^{3/2}/\epsilon$$

$$C_2^w = \max\left[\frac{2}{3} - \frac{1}{6C_2}, 0\right]\|\nabla \ell_2^w\|, \qquad \ell_2^w = \ell_t\left(1 - e^{-Re_t/30}\right)\left(1 + 1.8A_2^{\max\left(0.6, A_f\right)}\right)^{-1}$$

For the slow and rapid components, the GV LRC uses the LS LRC in the near-wall region, but calibrates the model for improved results in the outer boundary layer and in separated regions.

Typically, the quadratic SSG model is applied without LRCs or wall reflection terms because in principle it accounts for wall-proximity effects to a larger extent than the standard LRR model. So, Aksoy, Yuan & Sommer (SAYS) 1996 [172] however applied a near-wall correction to attempt to improve the wall asymptotic values of the SSG model. The SAYS model adds the following wall correction component to the SSG pressure strain tensor:

So, Aksoy, Yuan & Sommer 1996 [172] (SAYS):

$$\Pi_{ij}^w = f_w[(C_1\epsilon + C_1^*\mathcal{P})b_{ij} - C_2\epsilon\left(b_{ik}b_{kj} - 1/3b_{ij}^2\delta_{ij}\right) + C_3\left(P_{ij} - 2/3\mathcal{P}\delta_{ij}\right) + 2C_4 k\tilde{S}_{ij}^{dev} \quad [113]$$

$$C_1 = 3.4, \quad C_1^* = 1.8, \quad C_2 = 4.2, \quad C_3 = -0.29, \quad C_4 = 0.065, \quad f_w = e^{-\left(\frac{A_f Re_t}{60}\right)^3}$$

Figure 6.15a-d compare the a priori performance of the models with the LES solutions at stations I-IV. Lumley 1979 [154] suggested that, since the deviatoric pressure strain Π_{ij}^{dev} and the deviatoric dissipation ϵ_{ij}^{dev} tensors have similar mathematical form, the two can be modelled as a whole, that is, $\Pi_{ij}^{\Delta} = \Pi_{ij}^{dev} - \epsilon_{ij}^{dev}$. All models tested herein actually compute Π_{ij}^{Δ}. Thus, for the LES solution both Π_{ij} (solid red lines) and Π_{ij}^{Δ} (dashed red lines) are plotted. The Rotta linear return to isotropy model for slow pressure strain is also plotted (solid brown line), as well as Rotta's model with the LRC of Launder & Shima (dashed brown line). Since all models considered include Rotta's model as their first term, the latter two plots then represent the contribution of Rotta's slow pressure strain term, and the quantitative difference between Rotta's model and other models

represent the contribution of the rapid, wall reflection and/or nonlinear terms. For the LRR model, several versions are plotted. The blue lines (solid, dashed and dotted) are the standard LRR model and LRR model with LRCs of Launder-Shima (LS) and Gerolymos & Vallet (GV). The green lines (solid, dashed and dotted) are LRR with wall reflection (WR) term included and their corresponding LRC. Finally, the last three plots are LRR-QI (purple line), SSG (black line) and SSG with wall correction of So, Aksoy, Yuan & Sommer (SAYS) (dashed black line).

Normal Stress Pressure Strain Budgets

Figure 6.15a at the upstream equilibrium station I shows that the standard LRR model (solid blue line) does not capture the pressure strain budgets of the normal stresses, showing a large erroneous peak at $z^* \approx 12$. When LRCs are applied, the LRR+LRC models show excellent comparison with the LES Π_{ij}^{Δ} solution for the streamwise Π_{11} budget. For the spanwise and wall normal budgets Π_{22} and Π_{33} the LRR+LRC models show excellent comparison for $z^* \gtrsim 8$, while for $z^* \lesssim 8$ in the viscous near-wall region the LRR+LRC models deviate up to ~47% at $z^* \approx 1.4$, but head closer towards the LES wall value where the difference is ~15%. The LRC models of LS and GV yield equally good results for the normal stress budgets. When the GL wall reflection is added to LRR (LRR+WR_{GL}, solid green line) the result is mainly a reduction in the streamwise Π_{11} and wall normal Π_{33} budgets and an increase in the spanwise Π_{22} budgets in the region of $5 \lesssim z^* \lesssim 30$. However adding wall reflection does not considerably improve the comparison to the LES solution. When LRCs are again added, that is, LRR+WR_{GL}+LRC, the models show similar performance to the LRR+LRC models. The difference between the LRR+LRCs and the LRR+WR+LRCs is no more than ~3% for $z^* \lesssim 5$ and no more than ~12% for $5 \lesssim z^* \lesssim 100$. This indicates that the LRCs have a significant impact and is required to produce good results in the viscous near-wall region. The LRR-QI, SSG and SSG-SAYS show similarly poor performance to

the standard LRR model. The SAYS near-wall correction for SSG forces the pressure strain to be zero at the wall and somewhat tracks with the LES Π_{ij}^{dev} and not the LES Π_{ij}^{Δ} (even though SSG is meant to model Π_{ij}^{Δ}). For $z^* \gtrsim 75$, all models show a good match with the LES solution where the pressure strain asymptotically approaches zero. Finally, the Rotta *slow* pressure strain model without LRC (solid brown line) shows a significantly closer match to the LES in the region $5 \lesssim z^* \lesssim 60$ over the standard LRR, LRR+WR, LRR-QI, SSG and SSG+SAYS for all the normal stress budgets. It is inferred that the rapid pressure strain is a significant fraction of the total pressure strain only in the buffer and log layers as predicted by the standard LRR model, LRR-QI and SSG models. For the standard LRR the rapid pressure strain adds up to ~50% near the peak at $z^* \approx 12$ for all three normal stress budgets, deviating further from the LES solution. When LRC is added to the Rotta model (dashed brown line), the comparison to the LES Π_{ij}^{Δ} is quite good, tracking close to the LRR+LRC models.

Figure 6.15b compares the models with the LES solution at station II in the separated corner. The region $z^* \gtrsim 10$ is first analyzed. The LRR+LRC models generally compare best to the LES solution in this region. Towards the end of the profile, the GV LRC shows some improvement over LS LRC (dotted and dashed blue lines respectively). The GV LRC model was infact calibrated to yield improved results in separated flows. The standard LRR model also compares well to the LES solution particularly for Π_{22} and Π_{33}. Adding the GL wall reflection to the standard LRR (LRR+WR_{GL}, solid green line) worsens the results for Π_{22} and Π_{33}. Adding LRCs with wall reflection, that is, LRR+WR+LRCs (dashed and dotted green lines) somewhat improves the results over LRR+WR. Once again, it is the LRCs that have a significant impact on accuracy of the results. The LRR-QI, SSG and SSG-SAYS capture the trend of the LES in this region but overpredict the pressure strain budget for Π_{11} and Π_{22}. The Rotta slow pressure strain term (brown lines) is small

is this region, indicating that rapid pressure strain and/or wall reflection comprises a majority of the pressure strain in this region according to the models. For $z^* \lesssim 10$, none of the models capture the pressure strain budgets. Where pressure strain acts as a source, the models generally predict the pressure strain to be a sink and vice versa. It is only right at the wall that the LRR+LRC and LRR+WR+LRC models start to converge to the LES Π_{ij}^{Δ} solution.

In the post-reattachment nonequilibrium stations III & IV, Figure 6.15c and Figure 6.15d show that LES pressure strain budgets Π_{11} and Π_{33} are large sink and source terms respectively, while Π_{22} is a very small source. The models generally show poor comparison to the LES solution in the near wall region. For $z^* \gtrsim 60$, all models except those with wall reflection (green lines) track with the LES solution where pressure strain asymptotes to near zero. The models with wall reflection show erroneous fluctuations for $z^* \gtrsim 100$.

Shear Stress Pressure Strain Budgets

The only significant shear stress pressure strain budget is the Π_{13} component. The Π_{12} and Π_{23} components are an order of magnitude or more smaller than the Π_{13} and normal stress budget components. Therefore the discussion is limited to the Π_{13} component. The LES solution shows that Π_{13} is a significant source in the near-wall region at all stations. Infact it is an order of magnitude larger than the other components in the separated region at station II. For $z^* \lesssim 5$ at stations I-II and for $z^* \lesssim 12$ at stations III-IV none of the models capture this component of pressure strain. The LRR, LRR+WR, LRR-QI, SSG and SSG-SAYS (all models without LRC) predict some rise in the pressure strain magnitude but not necessarily trending with the LES. The LRR+LRC models predict a negligible amount of pressure strain relative to the LES. For $z^* \gtrsim 5$ at stations I-II and for $z^* \gtrsim 12$ at stations III-IV, the LRR+LRC models trend with the LES as pressure strain asymptotes towards relatively negligible values. It is also noted that the GL wall

reflection model generates erroneous fluctuations in the outer profile at stations III-IV; the effect is far more pronounced in the smaller shear stress components Π_{12} and Π_{23}.

Summary

For the undisturbed equilibrium turbulent boundary layer (station I), the standard LRR slow plus rapid pressure strain model with either the Launder & Shima 1989 LRC or the Gerolymos & Vallet 2001 LRC compares reasonably well with the LES Π_{ij}^{Δ} solution for the normal stress budgets, especially for the streamwise normal stress budget. It is difficult to assess the accuracy of the Gibson & Launder 1978 wall reflection model for this test case, but when LRC was paired with GL wall reflection, the results for the normal stress budgets were similar to the models with LRC without the wall reflection model. Clearly, the LRCs make a significant impact on accuracy in the near-wall viscous region. The models that should better account for wall proximity effects, viz, LRR-QI, SSG and SSG with SAYS wall correction, performed worse than the LRR model with LRC for the normal stress budgets. The simple classic Rotta slow pressure strain model with Launder & Shima 1989 LRC performed surprisingly well for the normal stress budgets with only a small difference from the best performing models in the buffer layer. For the shear stress pressure strain budget, all models failed to capture the significant pressure strain rise in the viscous near-wall region.

The model trends at the equilibrium station I were consistent the results of Gerolymos et al. 2012 [160] where similar trends were observed using DNS of fully developed compressible channel flow for the standard LRR, LRR with GL wall reflection, LRR with GV LRC and SSG models. Three other models were tested in Gerolymos et al. 2012 [160] that were not tested in this study, viz, Suga 2004 [173], Jakirlić-Eisfeld-Jester-Zürker-Kroll (JEJK) 2007 [174] and Gerolymos-Lo-Vallet-Younis (GLVY) 2012 [160]. In that study, the best performing models

appeared to be GLVY 2012 for modeling Π_{ij}^{dev} and LRR with GV LRC for modeling Π_{ij}^{Δ}. Observation of results in that study and the study herein shows that the GLVY 2012 model and the LRR model with the LRC of either GV or LS yielded reasonable results for the normal stress budgets with no model being better or worse than the other. For the shear stress budget, no model between either of the two studies captured the rise in the shear stress pressure strain budget in the viscous near-wall region, indicating a severe shortcoming of popular pressure strain closures.

In the separated region (station II) the LRR model with LRC of GV or LS compared well for the normal stress budgets in the outer flow that includes the separation shear layer above the separation bubble, while in the separation bubble near the wall none of the models capture the LES trend. In the strongly nonequilibrium regions downstream of reattachment (stations III-IV), the a priori comparison of the models with the LES solution was worse for the normal stress budgets in the near wall region where pressure strain was most significant. The reasonable results obtained for the normal stress budgets when using the LRR model in the equilibrium turbulent boundary layer (station I) are in large part due to the semi-empirical LRCs that were calibrated for such flows. Regarding the shear stress pressure strain budget, all models failed to capture the significant pressure strain in near-wall region at stations II-IV, as was the case at the upstream equilibrium station I. An a priori model-to-model comparison that also includes the JEJK 2007 model (an extension of the Durbin 1993 elliptic relaxation model [175]) and the GLVY 2012 model (which further splits the slow and rapid components into homogeneous and inhomogeneous components) applied to the nonequilibrium regions of the SBLI test case herein (or similar test case) may be worthwhile in the future to determine if these more advanced models can better capture pressure strain components.

Current viscous wall semi-empirical calibrations work well for predicting normal stress pressure strain budgets in equilibrium wall-bounded turbulent boundary layers, but not for predicting the shear stress pressure strain budget. For these types of flows, LRR with an appropriate LRC suffices. Even the simple Rotta model with an appropriate LRC may very well be acceptable. However, the results suggest that for the present SBLI configuration, the popular single-point algebraic closures tested herein lack the necessary modeling of physics to capture all non-negligible pressure strain tensor components simultaneously in equilibrium and nonequilibrium post-shock regions of the flow, particularly in the near-wall viscous region.

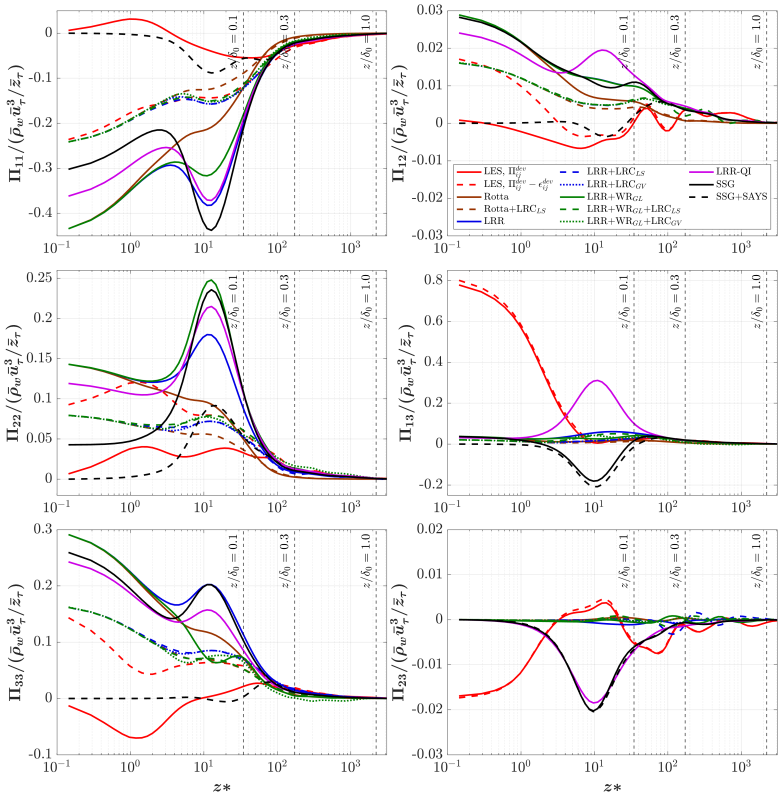


Figure 6.15a. Pressure strain tensor models at station I.

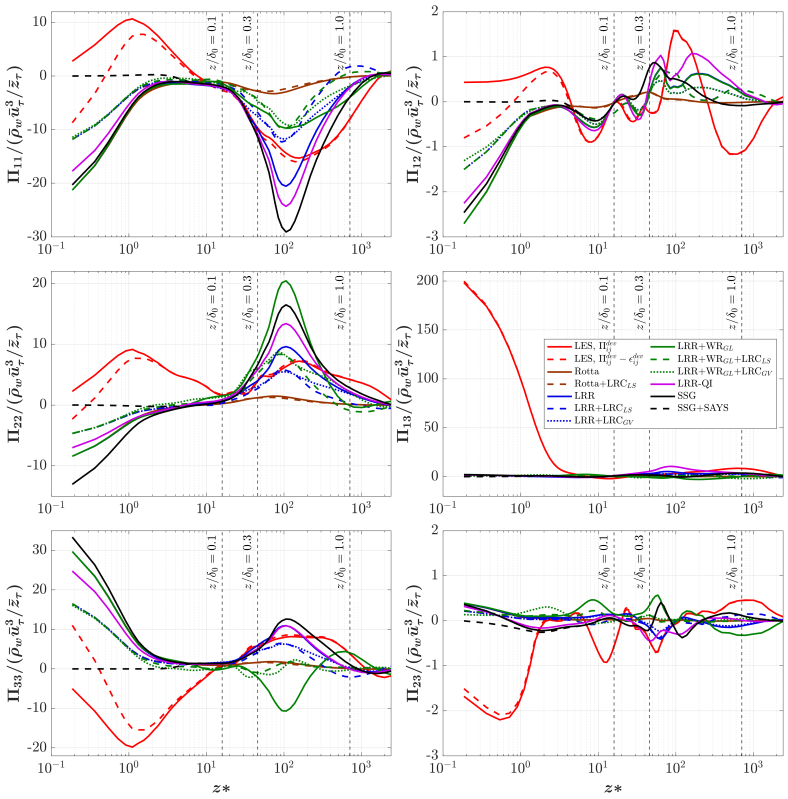


Figure 6.15b. Pressure strain tensor models at station II.

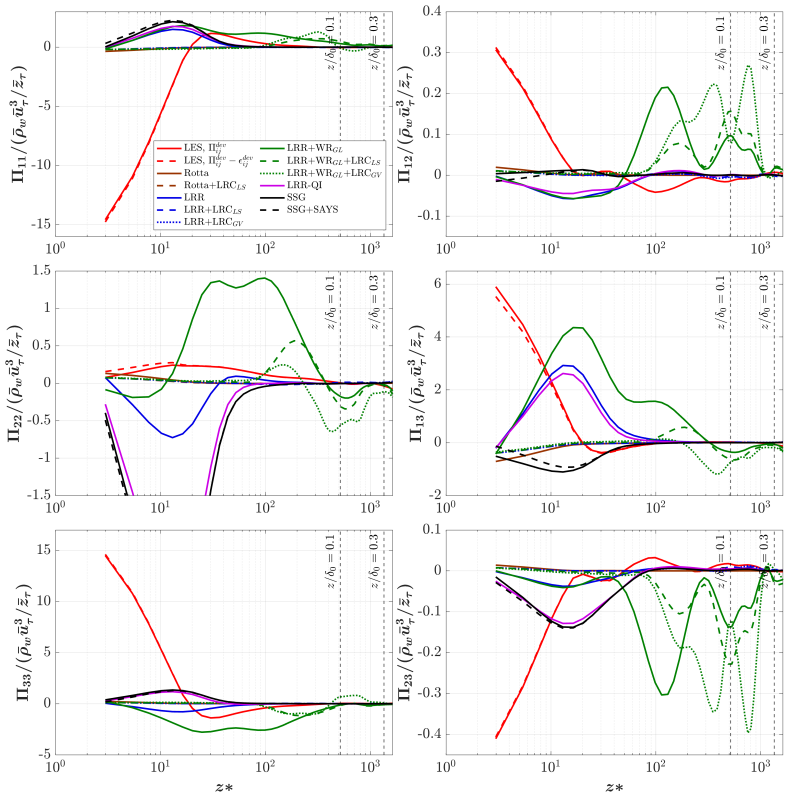


Figure 6.15c. Pressure strain tensor models at station III.

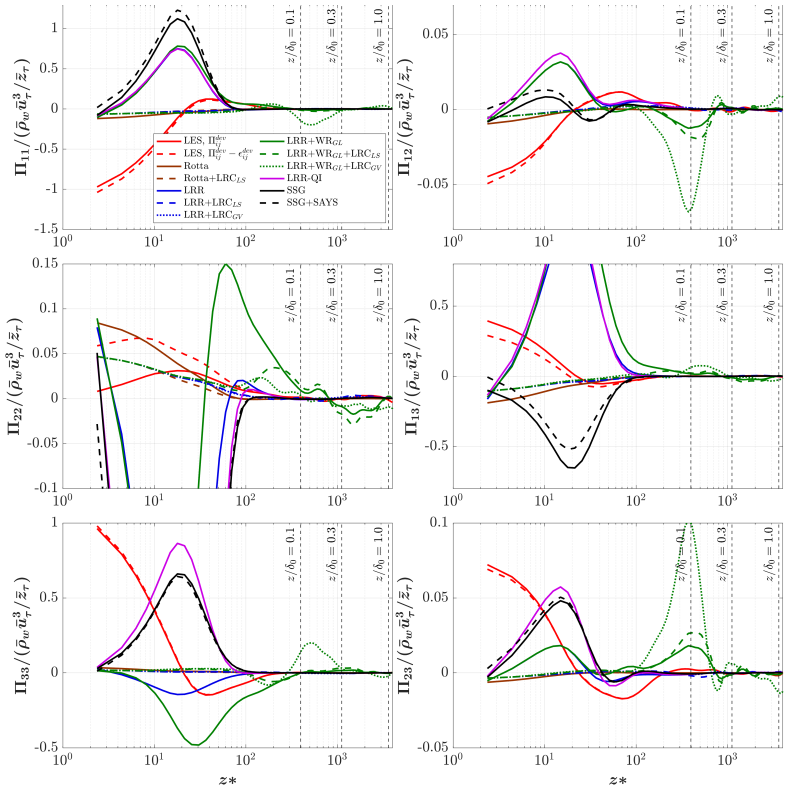


Figure 6.15d. Pressure strain tensor models at station IV.

6.10 Thermodynamic Fluctuations and Correlations

6.10.1 Density, Pressure and Temperature Fluctuations

Figure 6.16-Figure 6.18 show root mean square (rms) of density, pressure and temperature fluctuations at stations I-IV. For all plots the wall normal distance upper limit was $z/\delta_0 \approx 1.1$ at all stations. For stations I-II, this upper limit is near the boundary layer edge. For station III, the profile extends across the shock wave which is located at $z/\delta_0 \approx 0.6$. For station IV, the profile extends to just before the shock wave. In Figure 6.16, density fluctuations are normalized by local and wall values. Unlike incompressible flows, density fluctuations are nonzero in compressible flows and plays a role in turbulent mass transport. At the upstream equilibrium station I, the density fluctuations when normalized by local density is fairly constant throughout the boundary layer except in the viscous wall region below $z/\delta_0 \approx 0.1$. When normalized by mean wall density, the

density fluctuations grow significantly away from the wall. At station II there is some mild fluctuation in the density fluctuations through the separation bubble and shear layer. At stations III-IV, except in the near-wall viscous region, density fluctuations are fairly constant through profile up until the shock wave. At station III, the large rise in $\rho'_{rms}/\bar{\rho}$ at $z/\delta_0 \approx 0.7$ is due to the shock jump. This effect is much milder for $\rho'_{rms}/\bar{\rho}_w$.

The fluctuating pressure field has a strong dynamic influence on the transport of TKE and the Reynolds stresses, for example, through the pressure dilatation, pressure strain and pressure diffusion correlation terms in the transport equations. The impact is significant in the near-wall viscous region of wall bounded flows and in compressible free shear layers such as mixing layers. In Figure 6.17 pressure fluctuations are normalized by local and wall values. At the upstream equilibrium station I, the pressure fluctuations are larger in the viscous near-wall region and decreases away from the wall. At stations II-III, the pressure fluctuation fraction is much higher than at station I. The large rise in $p'_{rms}/\bar{p}$ at $z/\delta_0 \approx 0.7$ at station III is due to the shock jump. This effect is much milder for $p'_{rms}/\bar{p}_w$. At station IV, the pressure fluctuation fraction is generally less than at stations I-III. Morkovin 1962 [67] assumed that normalized pressure fluctuations are negligible relative to normalized density fluctuations in an adiabatic-wall compressible boundary layer, leading to the assumption that for a perfect gas $\rho'/\bar{\rho} \approx -T'/\bar{T}$. This may be a good approximation in supersonic flows, but not necessarily in hypersonic flows. Pressure fluctuations in the present test case are generally on the same order of magnitude as density fluctuations.

Temperature fluctuations appear in the energy transport equation and play a significant role in the transport of turbulent heat flux and associated modeling assumptions such as the Reynolds analogies. Figure 6.18 shows both static and total temperature fluctuations normalized by the local mean static and total temperatures respectively. Both the Reynolds- and Favre-averaged forms are

plotted. At all stations, static temperature (or just temperature herein) fluctuations rise precipitously through the near-wall viscous region then remain fairly constant through the boundary layer. The total temperature fluctuations are often assumed negligible in modeling formulations such as Morkovin's 1962 strong Reynolds analogy [67] (discussed in the next section). Here it is observed that total temperature fluctuations are of the same order of magnitude as that of static temperature fluctuations. There is some difference in Reynolds- and Favre-averaged forms for static temperature fluctuations, but the difference is generally negligible for total temperature fluctuations.

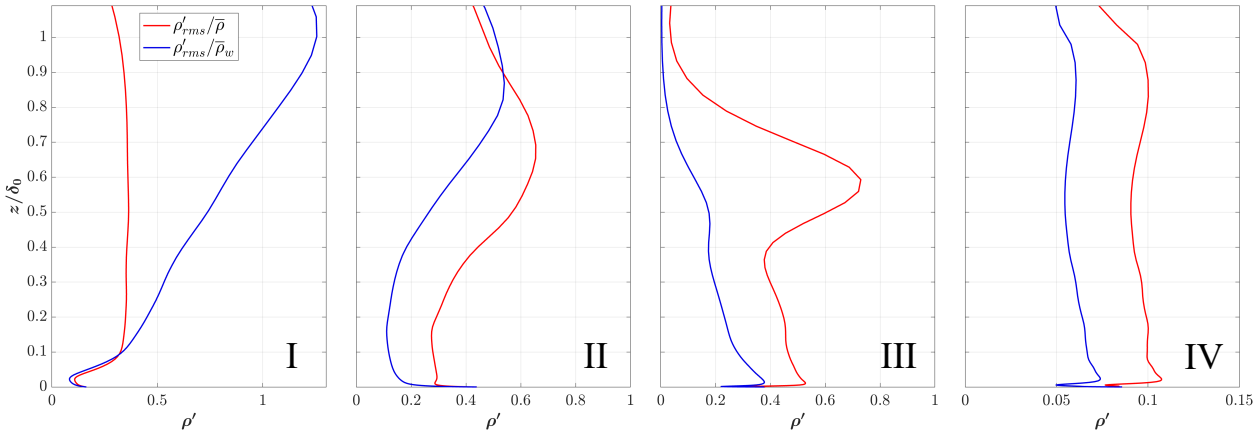


Figure 6.16. Density fluctuations.

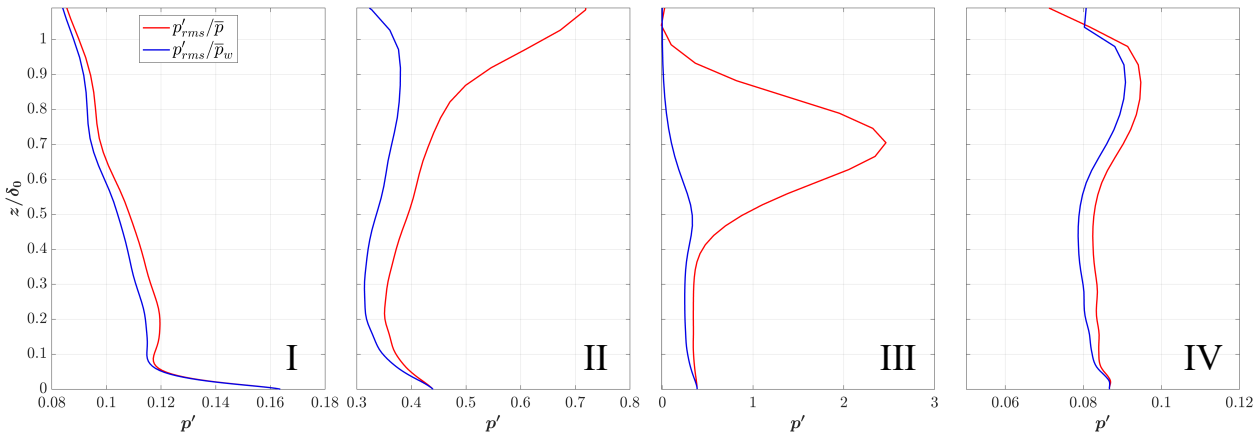


Figure 6.17. Pressure fluctuations.

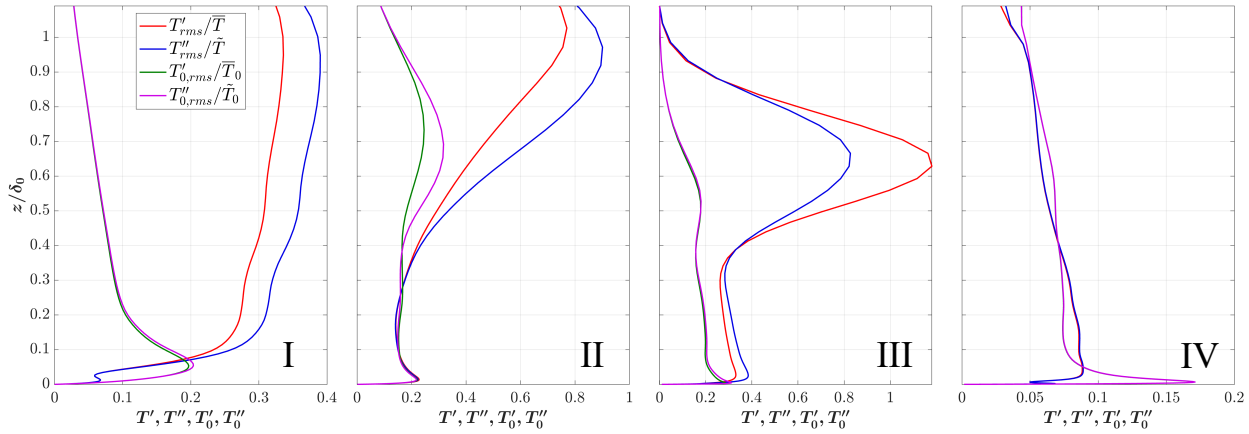


Figure 6.18. Temperature fluctuations.

6.10.2 The Strong Reynolds Analogies

Morkovin 1962 [67] derived several relations, known as the strong Reynolds analogies (SRA), between velocity fluctuations and temperature fluctuations from the Reynolds-averaged conservation equations for mass, momentum and energy for boundary layer flows. For a 2D boundary layer in which it is assumed that $\tilde{u}u'' \gg \tilde{w}w''$, wall heat flux is zero ($q_w = 0$, i.e., adiabatic wall) and mean total temperature is constant and equal to the total temperature at the wall ($\tilde{T}_0 = \tilde{T}_{0,w} = \tilde{T}_w$) which implies that total temperature fluctuations are zero ($T_0'' = 0$), the original Morkovin SRAs rewritten using Favre variables are as follows:

Turbulent Prandtl Number:
$$Pr_t = \frac{\widetilde{u''w''}}{\widetilde{w''T''}} \frac{\partial \tilde{T}/\partial z}{\partial \tilde{u}/\partial z} \approx 1 \qquad [114]$$

Phase Relations:
$$-R_{u''T''} \equiv -\frac{\widetilde{u''T''}}{u''_{rms} T''_{rms}} \approx 1 \qquad [115]$$

$$-R_{w''T''} \equiv -\frac{\widetilde{w''T''}}{w''_{rms} T''_{rms}} \approx R_{u''w''} \qquad [116]$$

Magnitude Relation:
$$SRA_{III} = \frac{T''_{rms}/\tilde{T}}{(\gamma - 1)\tilde{M}^2 u''_{rms}/\tilde{u}} \approx 1. \qquad [117]$$

If total temperature fluctuations are non-negligible, one can obtain the following for turbulent Prandtl number (Pirozzoli et al. 2004 [176]), viz,

$$Pr_t = \left[1 - \frac{\widetilde{w''T_0''}}{\widetilde{w''T''}}\right]\left[1 - \frac{\partial \widetilde{T}_0}{\partial \widetilde{T}}\right]^{-1} \quad [118]$$

Cebeci & Smith 1974 [103] formulated an extended magnitude relation ($eSRA_{III}$) assuming non-zero wall heat flux and non-zero total temperature fluctuations, viz,

$$eSRA_{III} = \frac{T''_{rms}/\tilde{T}}{(\gamma-1)\widetilde{M}^2 u''_{rms}/\tilde{u}}\left[1 + C_p \frac{\left(\tilde{T}_w - \tilde{T}_{0,e}\right)}{\tilde{u}\tilde{u}_e}\right]^{-1} \approx 1 \quad [119]$$

Several other modified SRA_{III} relations have been proposed that also assume non-zero wall heat flux and non-zero total temperature fluctuations. Three of these are summarized as follows,

$$SRA_{III} = -\frac{T''_{rms}/\tilde{T}}{(\gamma-1)\widetilde{M}^2 u''_{rms}/\tilde{u}}\left[1 - \frac{\partial \widetilde{T}_0}{\partial \widetilde{T}}\right] C \approx 1 \quad [120]$$

Gaviglio 1987, gSRA [177]: $C = 1.0$

Rubensin 1990, rSRA [178]: $C = 0.75$

Huang et al. 1995, hSRA [68]: $C = Pr_t =$ Eq. [118]

Total temperature comprises both the mean and turbulent kinetic energies, viz,

$$\tilde{T}_0 = \tilde{T} + \frac{1}{2c_p}\left(\tilde{u}_i{}^2 + \widetilde{u_i'' u_i''}\right) \quad [121]$$

However, to be consistent with the assumptions of the SRA relations above, the total temperature and fluctuating total temperature are computed via (Gatski & Bonnet 2013 [142]),

$$\tilde{T}_0 \simeq \tilde{T} + \frac{\tilde{u}^2}{2c_p} \quad [122]$$

$$T_0'' \simeq T'' + \frac{\tilde{u}}{c_p}u'' \quad [123]$$

Figure 6.19-Figure 6.21 investigate the SRAs at stations I-IV. Stations I-II are plotted through the boundary layer up to the freestream edge. Stations III-IV are plotted through the boundary

layer and up to just before the shock wave. Figure 6.19 shows the turbulent Prandtl number. Turbulent Prandtl number represents the ratio of turbulent heat transport to turbulent momentum transport. Many RANS modeling approaches assume Pr_t is close to 1 based Morkovin's analysis; then the turbulent thermal diffusivity for turbulent heat flux calculations can be computed as $\kappa_t = \mu_t c_p / Pr_t$. At the upstream equilibrium station I, Pr_t is approximately unity across most of the layer as predicted by Morkovin assuming $T_0'' = 0$, dropping towards the boundary layer edge to $Pr_t \approx 0.75$. This profile is typical of equilibrium turbulent boundary layers. When $T_0'' \neq 0$, Pr_t only drops slightly across the layer and is actually closer to unity than when $T_0'' = 0$ for $0.1 \lesssim z/\delta_0 \lesssim 0.5$. Close to wall on the outer edge of the viscous sublayer at $z/\delta_0 \approx 0.03$ or $z^* \approx 7.5$ there is a singularity that causes $|Pr_t|$ to have extremely large absolute values. This is due to the maximum turning point in the mean wall normal temperature profile where $\partial \tilde{T}/\partial z = 0$ (as observed in Figure 6.24) coinciding with the $\widetilde{w''T''}$ correlation switching signs when crossing zero (as observed in Figure 6.20); note that $\widetilde{u''w''} < 0$ and $\partial \tilde{u}/\partial z > 0$ throughout the profile. The maximum in static temperature at this location is the result of competing effects of wall cooling (recall that the wall is isothermal at 300K) and viscous heating. Below the singularity in the viscous sublayer for $z^* \lesssim 5$, Pr_t is approximately constant at 0.4 for the case that assumes $T_0'' = 0$, and drops continuously to -1 at the wall for the case that assumes $T_0'' \neq 0$ (see the inlaid plot in Figure 6.19 at station I). It is only in this region that the $T_0'' = 0$ and $T_0'' \neq 0$ assumptions significantly depart from each other.

The Pr_t profile in the separated corner at station II has two singularities that cause $|Pr_t|$ to have inordinately large values. The first singularity at $z/\delta_0 \approx 0.08$ or $z^* \approx 12$ where Pr_t goes from negative to positive is due to a minimum turning point in $\tilde{u}$ such that $\partial \tilde{u}/\partial z$ goes from negative at the wall (giving rise to negative shear stress/skin friction in the separation bubble) to positive

above $z/\delta_0 \approx 0.08$. Above the first singularity, Pr_t drops from 1 to -1 through the separation bubble, crossing 0 where $\tilde{T}$ has a maximum turning point such that $\partial\tilde{T}/\partial z = 0$ at $z/\delta_0 \approx 0.2$ (see Figure 6.24). A second singularity is encountered at $z/\delta_0 \approx 0.67$ where $\widetilde{w''T''}$ correlation switches signs and crosses zero (as observed in Figure 6.20). Above the second singularity which extends through the shear layer towards the freestream, Pr_t is approximately unity. The profiles that assume $T_0'' = 0$ and $T_0'' \neq 0$ are very similar.

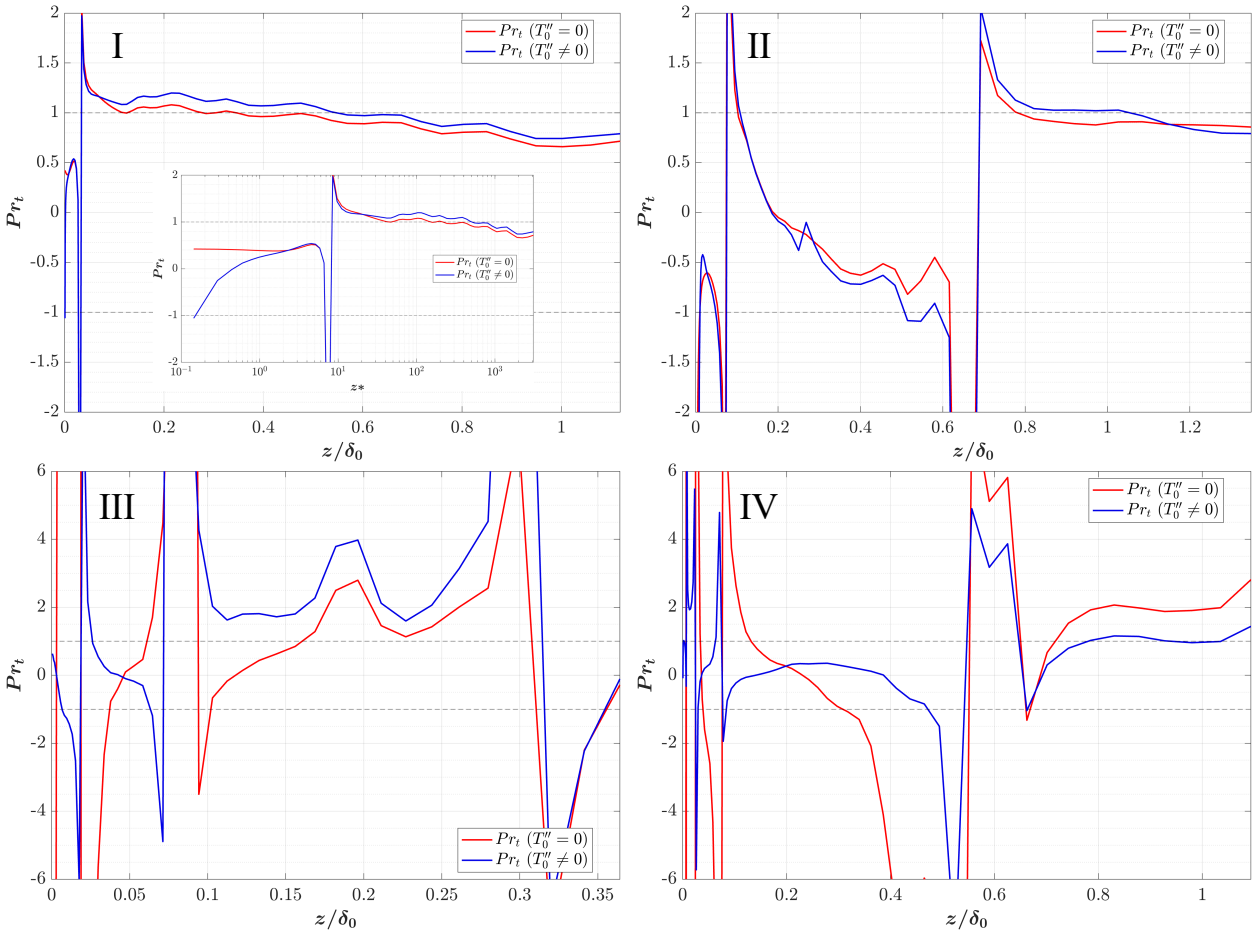


Figure 6.19. SRA: Turbulent Prandtl number.

The Pr_t profiles at stations III-IV in the downstream post-reattachment regions show multiple singularities occur and there is a larger discrepancy between the $T_0'' = 0$ and $T_0'' \neq 0$ assumptions. The boundary layer is much thinner in the post-shock region than in the upstream region. For

reference, the 99% velocity boundary layer thicknesses at stations III and IV are $z/\delta_0 \approx 0.12$ and $z/\delta_0 \approx 0.21$, respectively. There is a large heating effect due the shock jump and compression of the boundary layer which causes $|Pr_t|$ to have large values exceeding 1 (apart from the singularities). The effect is far more significant near reattachment at station III. There are some regions where $|Pr_t|$ is roughly of order unity, but no straightforward conclusions can be made.

Figure 6.20 plots velocity-temperature fluctuation correlation ('phase' relation) $-R_{u_j''T''}$ for all three components. The correlations are directly related to the turbulent heat flux in the Favre-averaged energy conservation equation defined as $q_{T_j} = c_p\bar{\rho}\widetilde{u_j''T''}$. In the upstream equilibrium boundary layer at station I, the streamwise correlation $-R_{u''T''}$ shows that u'' and T'' are strongly correlated in the viscous sublayer where $-R_{u''T''} \approx -0.95$ at the wall, then change precipitously through the buffer layer to become strongly anticorrelated at $z/\delta_0 \approx 0.05$ or $z^* \approx 15$ where $-R_{u''T''} \approx 0.93$. Through the log layer and outer layer u'' and T'' remain anticorrelated decreasing to $-R_{u''T''} \approx 0.64$ at $z/\delta_0 \approx 0.3$ or $z^* \approx 180$. Note that Morkovin's analysis predicts $-R_{u''T''} \approx 1$. The wall normal correlation at station I goes from $-R_{w''T''} \approx 0.44$ in the viscous sublayer (anticorrelated) to $-R_{w''T''} \approx -0.37$ in the buffer layer (correlated), and remains approximately steady at $-R_{w''T''} \approx -0.4$ through the log and outer layers. The trend of $-R_{w''T''}$ is generally opposite to that of $-R_{u''T''}$, except that $-R_{w''T''}$ is about half the magnitude of $-R_{u''T''}$. The match between $-R_{w''T''}$ and $-R_{u''w''}$ is excellent outside of the viscous sublayer, indicating that $-R_{w''T''}$ and $-R_{u''w''}$ are strongly anticorrelated, and verifying the SRA phase relation in Eq. [116] at this station. The magnitude of the spanwise correlation at station I is $|-R_{v''T''}| < 0.012$ throughout indicating little to no correlation between v'' and T''. Note that all three correlation components cross zero at $z/\delta_0 \approx 0.03$ or $z^* \approx 7.5$ which coincides with the maximum point in the mean temperature gradient (as observed in Figure 6.24).

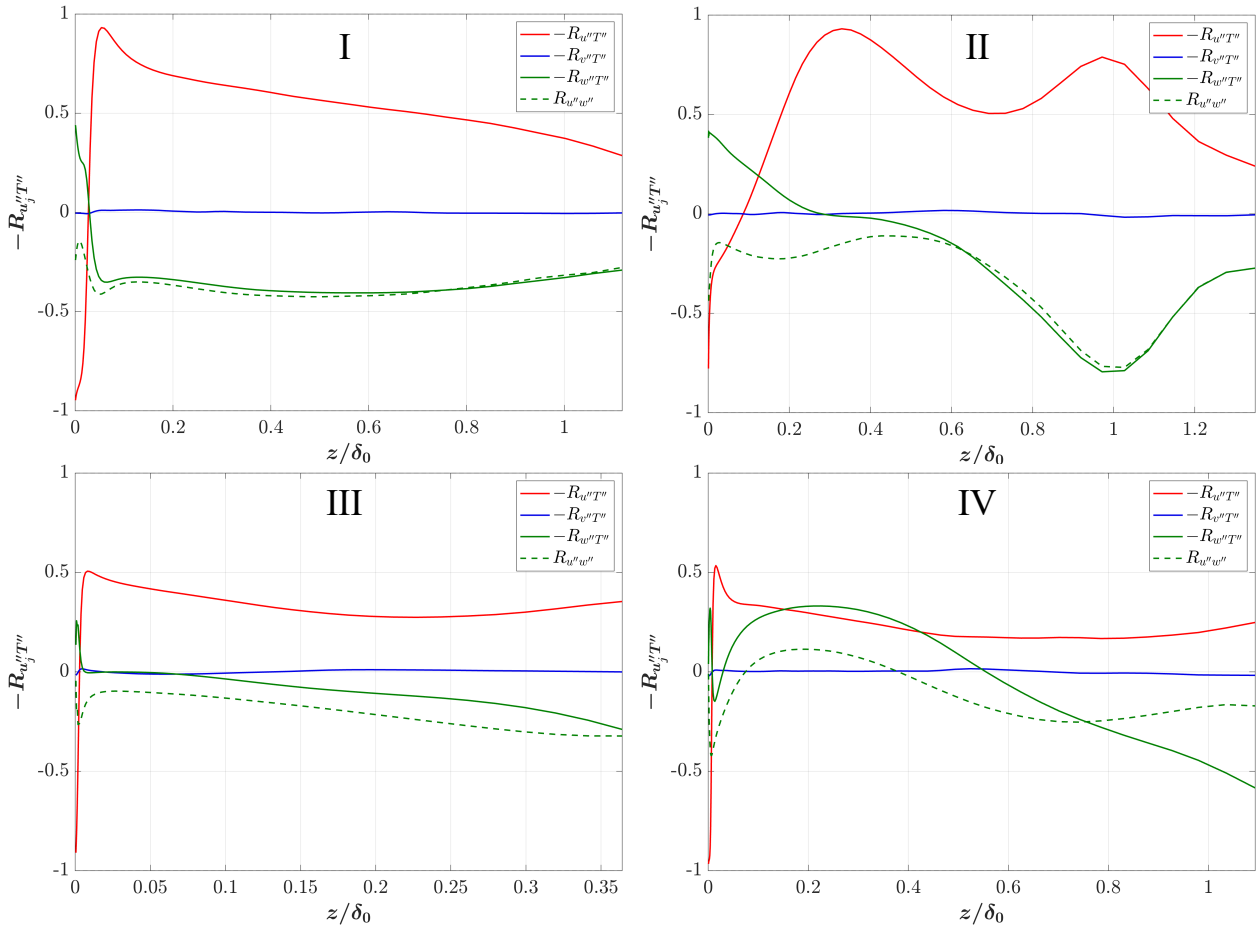


Figure 6.20. SRA: Phase relations.

At the separated corner station II, u'' and T'' are strongly correlated at the wall where the streamwise correlation $-R_{u''T''} \approx 0.8$, switching to being anticorrelated away from the wall where $-R_{u''T''}$ varies in the range [0.5,1]. The wall normal correlation $-R_{w''T''}$ goes from ~0.4 in the viscous sublayer (anticorrelated) and steadily decreases becoming negative for $z/\delta_0 > 0.3$. The magnitude of the spanwise correlation $|-R_{v''T''}|$ is once again near zero.

At the downstream nonequilibrium stations III-IV, the streamwise correlation $-R_{u''T''}$ follows the trend of the upstream station I in that u'' and T'' are strongly correlated at the wall reaching $-R_{u''T''} \approx 0.94$ and then become moderately anticorrelated away from the wall reaching $-R_{u''T''} \approx 0.5$ before leveling off to somewhat smaller values. Like stations I-II, the spanwise

correlation $-R_{v''T''}$ is near zero. The wall normal correlation $-R_{w''T''}$ at stations III-IV however has more variation in the trends. Just past reattachment at station III, w'' and T'' are mildly anticorrelated at the wall where $-R_{w''T''} \approx [0.1,0.2]$, then $-R_{w''T''}$ precipitously decreases to near zero. Further away from the wall the correlation becomes negative with $-R_{w''T''} > -0.25$. At station IV, $-R_{w''T''}$ switches signs multiple times. $-R_{w''T''} \approx [0.1,0.3]$ at the wall (mildly anticorrelated), then decreases to a local minimum where $-R_{w''T''} \approx -0.15$ at $z/\delta_0 \approx 0.01$, then rises to a maximum of $-R_{w''T''} \approx 0.3$ (mildly anticorrelated) at $z/\delta_0 \approx 0.2$, and finally decreases to a negative values with stronger correlation in the outer flow reaching $-R_{w''T''} \approx -0.5$.

Figure 6.21 plots the relation termed SRA_{III} ('magnitude' relation). Morkovin's original form, as well as the modified forms, are plotted (Eqs. [117], [119], [120]). At the upstream equilibrium station I, away from the wall, Morkovin's original SRA_{III} has a mean value of ~0.55. Of the modified forms, Cebeci & Smith's $eSRA_{III}$ tracks closest to unity. The remaining three modified forms ($gSRA_{III}$, $rSRA_{III}$, $hSRA_{III}$) depend on the value of C. With the values of C suggested by the original models, they track close to unity but not as well as $eSRA_{III}$. Close to wall in the viscous sublayer for $z/\delta_0 \lesssim 0.03$ or $z^* \lesssim 7.5$, the inlaid plot in Figure 6.21 at station I shows that Morkovin's original form increases, $hSRA_{III}$ varies between positive and negative, while the remaining three modified forms are negative and fairly constant with values $eSRA_{III} \approx$-1, $gSRA_{III} \approx$-1.3 and $rSRA_{III} \approx$-1. The singularity at $z/\delta_0 \approx 0.03$ in the modified forms is due to division by zero related to the term containing $\tilde{T}_0$.

At station II in the separation bubble, the SRA models generally vary between -1 and 1 except at some singular points. Above the separation bubble the models generally vary between 0.5 and 1, with the $eSRA_{III}$, $gSRA_{III}$ and $hSRA_{III}$ tracking close to unity. At stations III and IV, close to wall in the viscous sublayer (not shown) the SRA forms track close to -1, except for Morkovin's

original form, trending similar to the upstream station I. Away from the wall, besides the singularities where the relations have inordinately large absolute values, the SRA_{III} forms generally track between 0.2 and 1.3. At stations III and IV, the $eSRA_{III}$ tracks closest to unity.

To summarize the SRA_{III} results, Morkovin's original form consistently tracks between 0.3 and 0.5 away from the wall at all stations, rather than 1.0 as predicted. The extended SRA_{III} form by Cebeci & Smith that accounts for wall heat transfer and nonzero total temperature fluctuations consistently tracks closer to unity than all other forms away from the wall at all stations. Close the wall in the viscous sublayer, except for Morkovin's original SRA_{III} form, the relations track closer to -1. The exception to these general observations is in the separation bubble (station II) where the SRA_{III} relations are most inconsistent.

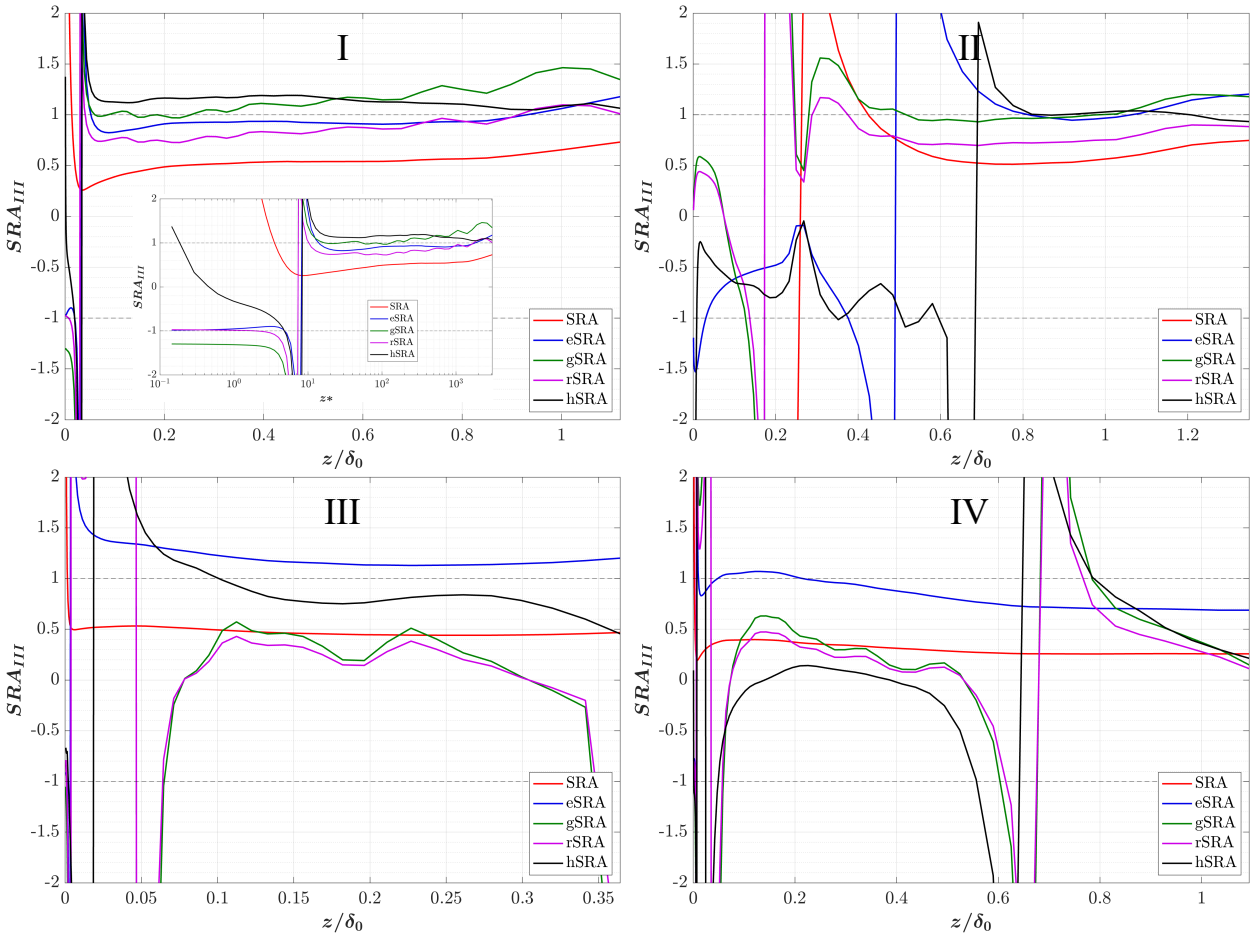


Figure 6.21. SRA: Magnitude Relation.

6.10.3 Turbulent Heat Flux

The turbulent heat flux that appears in the energy equation is written as (for an ideal gas with constant-pressure heat capacity c_p),

$$q_{T_j} = \overline{\rho u_j'' h''} = c_p \overline{\rho u_j'' T''} = c_p \bar{\rho} \widetilde{u_j'' T''} \quad [124]$$

The most common algebraic modeling approach for the turbulent heat flux is based on the gradient diffusion hypothesis (GDH). According to the basic GDH, transport of a turbulent scalar ϕ'' given by the turbulent scalar flux vector $\widetilde{u''\phi''}$ is the direction the mean scalar gradient $-\nabla\tilde{\phi}$. Thus,

$$\widetilde{u''\phi''} = -D_T \nabla\tilde{\phi} \quad [125]$$

Here $D_T = D_T(x_i, t)$ is the turbulent diffusivity. The GDH is analogous to Fourier's law of heat conduction and Fick's law of molecular diffusion.

In RANS EVM models, a simple GDH model (abbreviated SGDH herein) is often used for turbulent heat flux (Eq. [130]). This model assumes that the turbulent diffusivity D_T, or more commonly referred to as the turbulent thermal diffusivity κ_t, is given by,

$$D_T = \kappa_t = \frac{\mu_t}{\bar{\rho} Pr_t} \quad [126]$$

Here μ_t is the turbulent eddy viscosity as defined by the Boussinesq hypothesis (Eq. [46]). The Prandtl number Pr_t is most often assumed constant, or is sometimes assumed a field variable. From Figure 6.19 it is clear the assumption of constant Pr_t is not applicable to the entire SBLI flowfield. Nevertheless, in accordance with most engineering applications for turbulent wall-bounded flows, a constant value of $Pr_t = 0.9$ is used herein for comparison of the SGDH model.

Many models for μ_t exist in the literature. The objective herein is not to investigate the 'best' μ_t model, but to choose a commonly used μ_t model for general flows so that the SGDH heat flux model can be qualitatively compared to other heat flux models. Perhaps the most widely used

algebraic model for turbulent eddy viscosity is $\mu_t = f_\mu C_\mu \bar{\rho} \tau_T k$, where f_μ is an empirical wall correction function, C_μ is an empirical constant, τ_T is a turbulence timescale and k is the turbulent kinetic energy. The timescale is commonly assumed to be that of the large scale turbulent motions, that is, $\tau_T = k/\epsilon$, justified by the assumption that turbulent transport is dominated by inviscid dynamics of large eddies. In the viscous wall region, this timescale vanishes and instead the timescale $\tau_T = C_t(\tilde{\nu}/\epsilon)^{0.5}$ (Kolmogorov 1941 [179]) of the finescale eddy dynamics may be used as suggested by Durbin 1991/1995 [180],[125], where $\tilde{\nu} = \tilde{\mu}/\bar{\rho}$ and C_t is an empirical constant. Then, as computed in this study, μ_t and τ_T can be formulated as,

$$\mu_t = f_\mu \bar{\rho} \tau_T k \qquad [127]$$

$$f_\mu = 1 - e^{-f_{\mu 1} z^* - f_{\mu 2} z^{*2}} \qquad [128]$$

$$\tau_T = \max[C_{\tau 1}(\tilde{\nu}/\epsilon)^{0.5},\ C_{\tau 2} k/\epsilon] \qquad [129]$$

Here, the empirical wall correction function f_μ of Rodi & Mansour 1993 [181] was used with empirical constants $f_{\mu 1}$ and $f_{\mu 2}$ adjusted from their original proposed values for best qualitative match at the upstream boundary layer at station I.

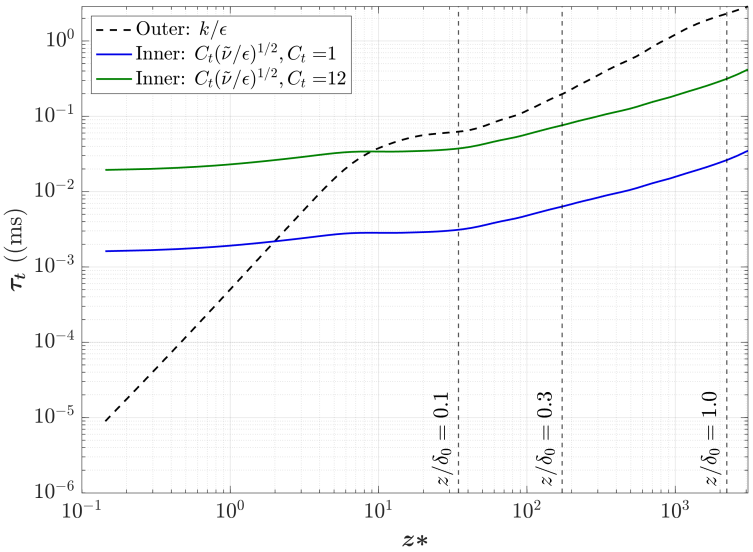


Figure 6.22. Inner and outer turbulence timescales.

Figure 6.22 demonstrates the variation of the inner viscous and outer large-eddy timescales through the boundary layer at the upstream station I. For DNS of turbulent channel flows, Durbin 1995 [125] used $C_{\tau 1} = 6$, while Figueiredo 2018 [182] suggested that $C_{\tau 1}$ can vary by a factor of 2. For the present SBLI test case, $C_{\tau 1}$ and $C_{\tau 2}$ have been adjusted for the upstream boundary layer at station I.

The most widely used algebraic model for turbulent heat flux that obviates the need for specifying a turbulent eddy viscosity is the Daly & Harlow 1970 [183] generalized gradient diffusion hypothesis (GGDH) model. The model is intended to better cope with turbulence anisotropy by relating D_T to turbulence statistics that is the product of a timescale and a velocity scale squared. Specifically $D_T \sim \tau_T \widetilde{u_i'' u_j''}$ resulting in the model in Eq. [131]. Typically, the timescale used in Daly & Harlow's model is $\tau_T = k/\epsilon$, but herein the timescale given by Eq. [129] is used instead. Note that the GGDH model is not rotationally invariant (Galilean invariance is a requirement for RST models) leading to development of more sophisticated rotationally invariant models such as that of Hanjalić and Launder 1972 [184]. However, studies, such as Younis et al. 2000 [185], show that such models have not produced any consistent improvements in accuracy, and are therefore not considered herein.

Abe & Suga 2000 [186] modified Daly & Harlow's model to better capture both streamwise and wall normal $\widetilde{u_j'' T''}$ correlations. The Daly & Harlow model is multiplied by a nondimensional turbulence tensor, in this case the nondimensional Reynolds stress tensor, resulting in the quadratic form in Eq. [132]. The timescale used by Abe & Suga was also $\tau_T = k/\epsilon$, but herein the timescale given by Eq. [129] is once again used instead.

SGDH:
$$\widetilde{u_j''T''} = -\frac{\mu_t}{\bar{\rho} Pr_t}\frac{\partial \tilde{T}}{\partial x_j}, \qquad C_{\tau 1} = 5, \qquad C_{\tau 2} = 0.01 \qquad [130]$$
$$Pr_t = 0.9, \qquad f_{\mu 1} = 1e^{-4}, \qquad f_{\mu 2} = 2e^{-4}$$

GGDH: Daly & Harlow 1970 [183]
$$\widetilde{u_j''T''} = -\tau_T \widetilde{u_i''u_j''}\frac{\partial \tilde{T}}{\partial x_i}, \qquad C_{\tau 1} = 5, \qquad C_{\tau 2} = 0.01 \qquad [131]$$

QGDH: Abe & Suga 2000 [186]
$$\widetilde{u_j''T''} = -\tau_T \frac{\widetilde{u_i''u_k''}\widetilde{u_k''u_j''}}{k}\frac{\partial \tilde{T}}{\partial x_i}, \qquad C_{\tau 1} = 8, \qquad C_{\tau 2} = 0.01 \qquad [132]$$

Figure 6.23 plots the LES turbulent heat flux vector and compares the a priori performance of the models discussed above. To compliment to the discussion, the temperature gradient is plotted in Figure 6.24. First the results at the upstream equilibrium station I are analyzed. As shown in Figure 6.24, at station I the wall normal mean temperature gradient $\partial\tilde{T}/\partial z$ is the only significant component. Heat is transferred away from the wall in the viscous sublayer due to wall cooling ($\partial\tilde{T}/\partial z > 0$), which competes with the heat transfer towards the wall by turbulence dissipation resulting in the sign reversal of $\partial\tilde{T}/\partial z$ away from the wall and the negative peak ($\partial\tilde{T}/\partial z < 0$) in the buffer layer. The SGDH model inherently assumes alignment of the correlation vector $\widetilde{u_j''T''}$ and mean temperature gradient $\partial\tilde{T}/\partial x_j$. This implies that SGDH will only model the dominant wall normal correlation $\widetilde{w''T''}$ and assume that the streamwise $\widetilde{u''T''}$ and spanwise $\widetilde{v''T''}$ components are comparatively negligible. From Figure 6.23 (or Figure 6.20), at station I, it is clear that both $\widetilde{u''T''}$ and $\widetilde{w''T''}$ are non-negligible, and infact $\widetilde{u''T''}$ is much larger than $\widetilde{w''T''}$. This is a significant shortcoming of the SGDH. For the $\widetilde{w''T''}$ component, the SGDH model works reasonably well at station I, but is strongly dependent on the empirical corrections f_μ, $C_{\tau 1}$ and $C_{\tau 2}$. The GGDH model captures the $\widetilde{w''T''}$ component very well. Unlike the SGDH model, the GGDH model also predicts the 'existence' and correct direction of the $\widetilde{u''T''}$ component, but not its correct

magnitude. The QGDH model on the other hand captures the magnitude and direction of both $\widetilde{u''T''}$ and $\widetilde{w''T''}$ components very well. Note that the spanwise $\widetilde{v''T''}$ component is comparatively small.

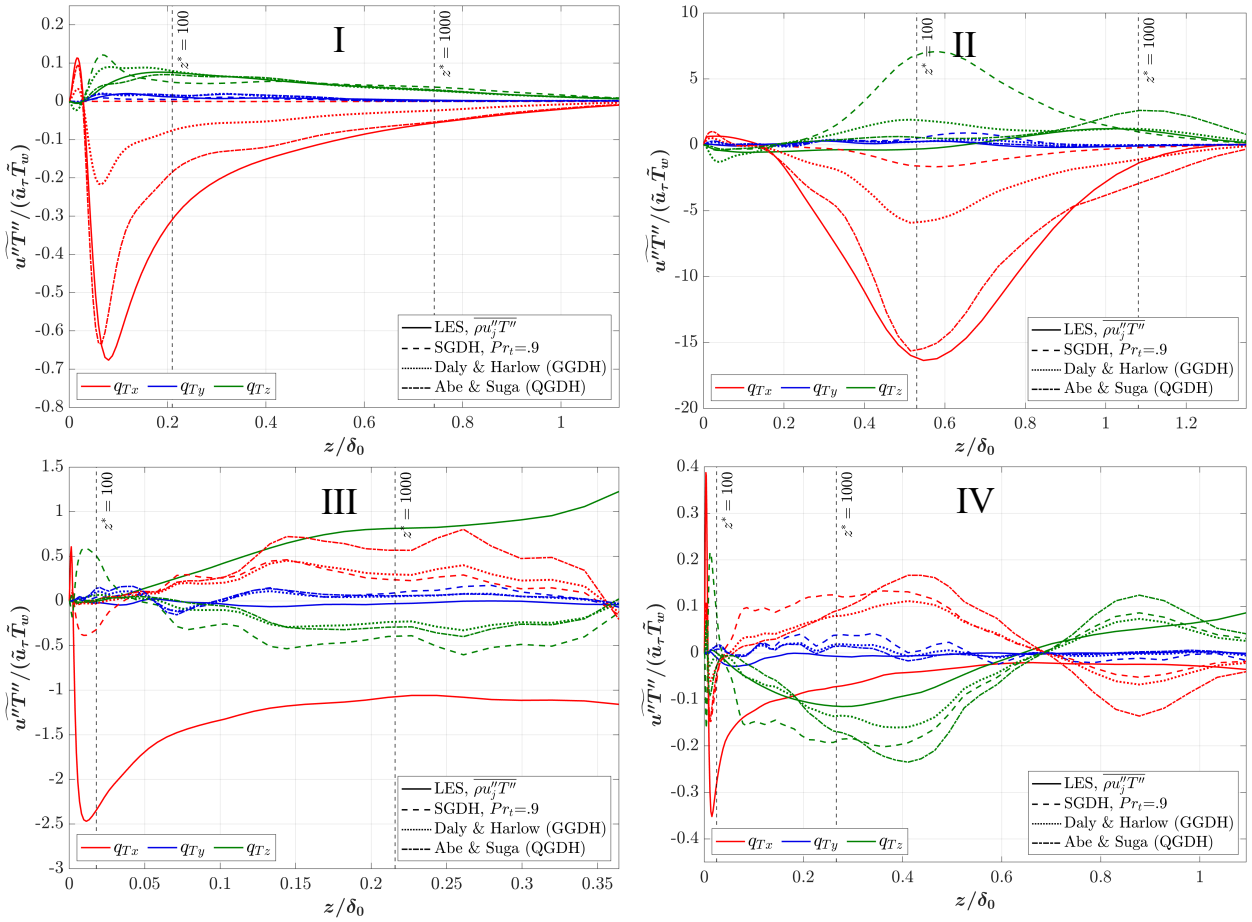


Figure 6.23. Turbulent Heat Flux.

Similar observations are made at the separation corner at station II. Figure 6.24 shows that $\partial\tilde{T}/\partial z$ is the only non-negligible temperature gradient component. Heat is transferred away from the wall in the separation bubble ($\partial\tilde{T}/\partial z > 0$). In the separation shear layer there is a small transfer of heat towards the wall where $\partial\tilde{T}/\partial z < 0$. Referring to Figure 6.23, the $\widetilde{w''T''}$ component is negative but small in the separation bubble, then becomes positive above the bubble. All three models however predict $\widetilde{w''T''}$ to be positive in the bubble, with the SGDH prediction significantly

larger. Above the bubble, all three models capture the positive rise and fall of q_{T_z} in the outer flow, however QGDH shows a some overprediction. The $\widetilde{u''T''}$ component is significantly larger than the other components, except close to the wall. The SGDH model severely underpredicts the $\widetilde{u''T''}$, unsurprisingly. The GGDH model, captures the direction of $\widetilde{u''T''}$, but not its correct magnitude. The QGDH model captures the direction and magnitude of $\widetilde{u''T''}$. The $\widetilde{v''T''}$ is mostly negligible, but shows a small positive increase in the vicinity of $z/\delta_0 \approx 0.6$, which all three models approximately predict.

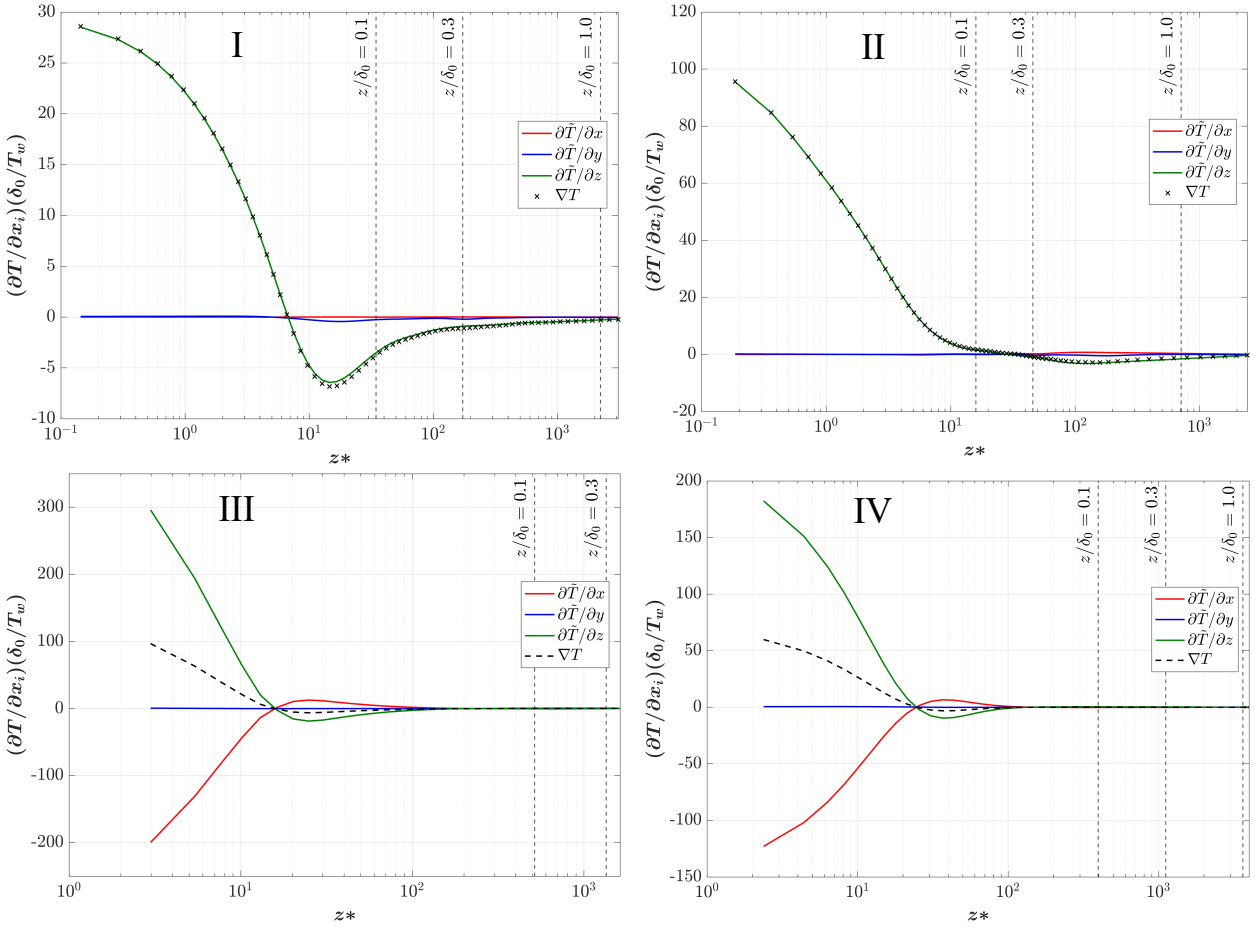


Figure 6.24. Temperature gradients.

In the post-shock nonequilibrium region at stations III and IV, none of the models perform well within the thin boundary layer and between the boundary layer and shock line. The one exception

is the prediction of the $\widetilde{w''T''}$ component at station IV, where the models capture the trend and roughly the magnitude of $\widetilde{w''T''}$. For $\widetilde{u''T''}$ and $\widetilde{w''T''}$ at station III and $\widetilde{u''T''}$ at station IV, the models generally predict these components to have opposite sign to the LES solution. Once again $\widetilde{v''T''}$ is small, but the models predict a slightly larger value of $\widetilde{v''T''}$ than the LES solution. Figure 6.24 shows that at stations III and IV, both the streamwise $\partial\tilde{T}/\partial x$ and wall normal $\partial\tilde{T}/\partial z$ temperature gradients are significant, and as a result all models generally predicted both $\widetilde{u''T''}$ and $\widetilde{w''T''}$ to be significant. Component $\partial\tilde{T}/\partial z$ follows a similar trend to the upstream station I, while $\partial\tilde{T}/\partial x$ follows the opposite trend.

In summary, the assumption that the turbulent heat flux vector is aligned with the temperature gradient as described by the simple GDH is flawed. Furthermore, the use of the turbulent eddy viscosity in SGDH requires additional modeling assumptions that introduce more uncertainty and a larger dependence on empirical corrections. The GGDH model of Daly & Harlow and the QGDH of Abe & Suga obviate the need for the turbulent eddy viscosity. In the equilibrium and separated regions of the flow, the GGDH model captures the wall normal component of the turbulent heat flux reasonably well, but captures only the direction and not the magnitude of the streamwise turbulent heat flux. In contrast, the QGDH model generally captures both the wall normal and streamwise turbulent heat flux components reasonably well, proving to be the best performing model of the three. In the post-shock nonequilibrium regions however, the models are clearly inadequate. Finally, the choice of turbulence timescale is an important consideration. If the typical timescale $\tau_T = k/\epsilon$ of large eddy transport is used, the turbulent heat flux may be overpredicted, sometimes severely so. Instead the timescale should by adjusted by the Kolmogorov timescale $\tau_T = C_t(\tilde{\nu}/\epsilon)^{0.5}$ of the finescale dynamics in the near-wall viscous region in order to achieve reasonable results.

6.11 Chapter Summary

The turbulence fields in the Mach 10 cylinder-flare SBLI configuration have been investigated using wall-resolved LES. The velocity and thermodynamic fluctuation correlations have been analyzed as they pertain to Reynolds Stress Transport, Turbulent Kinetic Energy Transport and Turbulent Heat Flux in lower-order RANS modeling. Where possible, the a priori performance of classical single-point RANS closures were investigated by comparing to the LES solution. Results show that the Reynolds stresses are strongly amplified through the separation zone and in the region just following reattachment where the flow experiences the significant compression and mean strain. The Reynolds stresses generally peak in the viscous near-wall region and in the separation bubble coinciding with the peak in turbulence production. Anisotropy of the stresses increase in these regions also, where the near-wall turbulence goes from one-component at the upstream equilibrium station to two-component in the separation bubble and post-shock nonequilibrium stations. In the post-shock region following reattachment, the Reynolds shear stress ($\widetilde{u''w''}$) switches sign from being negative in the undisturbed equilibrium boundary layer to being positive, with a synchronous and significant change in the Reynolds shear stress transport budgets.

For RANS eddy viscosity models that solve the TKE transport equation, modeling of the transport budgets must consider the nonequilibrium effects in the post-shock region that amplifies certain components, some of which were thought to be negligible in canonical equilibrium flows. Throughout the flowfield, the dominant turbulent kinetic energy transport mechanisms at the wall are the viscous diffusion source and the viscous dissipation sink. Away from the wall but still in the viscous wall layer, production is the primary source balanced primarily by viscous dissipation, turbulent diffusion and viscous diffusion. Pressure diffusion and convection play a secondary but

non-negligible role, particularly so in the post-shock region. The pressure dilatation and turbulent mass flux were generally small throughout, consistent with typical modeling assumptions.

For Reynolds stress transport, modeling of the transport budgets has typically been based on the budgets of canonical equilibrium flows, and to a lesser extent simple nonequilibrium flows. As a result much effort has been focused on modeling of the pressure strain and viscous dissipation terms, and to a lesser extent turbulent diffusion. Little attention has been given to modeling of the pressure diffusion, which is often ignored or lumped with turbulent diffusion via a single constant empirical coefficient. Turbulent mass flux is often simply ignored. The strong shock interaction in the configuration herein amplifies all budgets significantly in the separation zone and post-shock region, far exceeding that of supersonic and lower speed shock-boundary layer interaction flows. Pressure strain and pressure diffusion are prominent throughout the near-wall region, with inordinately large amplifications just following reattachment. Away from the wall these budgets are also important transport mechanisms. This indicates that accurate modeling of these terms are crucial to accurately capturing their effects on the Reynolds stresses, particularly in the post-shock region. The same conclusion is true for turbulent diffusion which plays a key role in many parts of the flowfield. The turbulent mass flux is generally small, but is particularly amplified just following reattachment and may warrant modeling consideration.

Viscous dissipation represents the conversion of turbulent kinetic energy into thermal internal energy, and pressure strain and dilatation represent the exchange between turbulent kinetic energy and turbulent potential energy due to pressure fluctuations. Both transport mechanisms are on the order of turbulence production and play crucial roles in the Reynolds stress transport balance, particularly in the thin near-wall region. Experimental turbulence data is very challenging to obtain in this region, and there is sparsity of detailed simulation data for high Mach number shock-

separated flows. In this study, the viscous dissipation and pressure strain and pressure dilatation transport processes have been investigated in some detail, along with an a priori comparison of popular classical models. The common assumptions that the solenoidal component of scalar viscous dissipation is the only significant component, and that the dilatational compressible contribution is negligible, are ascertained throughout the flowfield, with one exception. In the separation bubble and separation shear layer, the dilatation, inhomogeneous and viscosity-strain rate fluctuation correlation components can individually or in combination account for up to 50% of the total dissipation, therefore warranting modeling consideration. The so-called compressibility corrections as suggested by Zeman 1990, Sarkar et al. 1991 and Wilcox 1992 that purport a functional dependence of the ratio of dilatational dissipation to solenoidal dissipation on turbulent Mach number, as well as the functional dependence suggested by Ristorcelli 1997, all failed for this test case (although such corrections have been shown to improve mixing layer predictions in which dilatational dissipation was deemed to be more important than in wall-bounded flows). The classical closures of Rotta 1951, Hanjalić & Jakirlić 1993 and Launder-Reynolds-Kebede-Younis 1983/85 for modeling the full dissipation tensor compared remarkably well with the LES solution considering the extent of nonequilibrium following the shock wave. Considering the ease of calculation and accuracy, the Rotta dissipation tensor model for near-wall anisotropy with appropriate blending to isotropy in the outer flow is adequate, obviating the need for the costly sophistication of the newer dissipation tensor models for the present and similar SBLI flows.

The pressure dilatation budget in the turbulent kinetic energy transport balance is generally small relative to other budgets, acting as a small but not necessarily negligible sink in viscous near-wall region, and negligible otherwise except at the separated corner. The so-called compressibility corrections as suggested by Zeman 1991 and Sarkar 1992 that purport a functional dependence on

turbulent Mach number, as well as the functional dependence suggested by Ristorcelli 1997, all failed for this test case. Many models have been proposed for the closure of the pressure strain tensor, several of which were evaluated herein. The models generally assume that the pressure strain can be split into slow, rapid and wall-reflection components. In the upstream equilibrium boundary layer, the standard Launder-Reece-Rodi 1975 slow and rapid pressure strain model, with either the low Reynolds number viscous near-wall correction of Launder & Shima 1989 or Gerolymos & Vallet 2001, compared reasonably well with the LES solution of the normal stress budgets, especially for the streamwise normal stress budget. The efficacy of the Gibson & Launder 1978 wall- reflection model was inconclusive for this test case. It was observed that the semi-empirical low Reynolds number corrections, originally calibrated for equilibrium wall-bounded flows, had a significant impact on accuracy in the near-wall viscous region, with and without the wall-reflection model. The models that should better account for wall proximity effects, viz, the quasi-isotropic Launder-Reece-Rodi 1975 and the Speziale-Sarkar-Gatski 1991 models performed worse. In another study of turbulent channel flow, the newer model of Gerolymos-Lo-Vallet-Younis 2012 performed no better or no worse than the best performing model tested herein. For the shear stress pressure strain budget at the upstream equilibrium boundary layer, no model captured the significant rise in the shear stress pressure strain budget in the viscous near-wall region, indicating a severe shortcoming of popular pressure strain closures. In the separation zone and post-shock nonequilibrium region where the near-wall pressure strain was particularly amplified, none of the models in general compared well for any of the stress components. It was generally concluded that for the present SBLI configuration, the popular single-point algebraic closures tested herein lack the necessary modeling of physics to capture all non-negligible pressure

strain tensor components simultaneously in equilibrium and nonequilibrium post-shock regions of the flow, particularly in the near-wall viscous region.

The fluctuating density and pressure fields have a strong dynamic influence on the transport of turbulent kinetic energy and Reynolds stresses. Temperature fluctuations appear in the energy transport equation and play a significant role in the transport of turbulent heat flux. The density, pressure and temperature fields were demonstrated to be significant in the present test case. Total temperature fluctuations, which are typically assumed negligible, were on the same order of magnitude as the static temperature fluctuations. The strong Reynolds analogies of Morkovin 1962 that relate velocity and temperature fluctuations were evaluated. The turbulent Prandtl number was near unity as predicted by Morkovin's analysis in the upstream equilibrium boundary layer and in the separation shear layer. Elsewhere in the flowfield the turbulent Prandtl number varied significantly but was mostly of order ± 1. The typical assumption of turbulent Prandtl number equal to 0.9 is flawed in nonequilibrium regions of the SBLI flowfield. The streamwise correlation coefficient of velocity and temperature fluctuations at all sampled axial locations showed negative correlation in the wall viscous sublayer, which then precipitously switched to positive correlation for the remainder of the wall normal profiles varying between 0 and 1, but not quite unity as predicted by Morkovin's analysis. The wall normal correlation coefficient of velocity and temperature fluctuations showed the opposite trend, that is, positive in the viscous sublayer and negative otherwise, but was smaller in magnitude than the streamwise correlation. Morkovin's original magnitude relation (termed SRA_{III} herein) tracked between 0.3 and 0.5 at all sampled axial locations rather than unity as predicted. The extended SRA_{III} by Cebeci & Smith 1974 that accounts for wall heat transfer and nonzero total temperature fluctuations consistently tracked closer to unity, except in the viscous near-wall region, than all other modified SRA_{III} forms. Close

the wall in the viscous sublayer, modified SRA_{III} forms tracked closer to -1. The exception was in the separation bubble where the SRA_{III} relations are most inconsistent.

The turbulent heat flux that appears in the energy equation involves the correlation of velocity and temperature fluctuations and requires modeling. Many algebraic modeling approaches are based on the gradient diffusion hypothesis. The basic (simple) gradient diffusion hypothesis model incorrectly assumes that the turbulent heat flux vector is aligned with the temperature gradient, and as a result was only able to predict the wall normal turbulent heat flux. Furthermore, the use of the turbulent eddy viscosity concept in the simple gradient diffusion hypothesis model required additional assumptions that introduced more uncertainty and a larger dependence on empirical corrections. The gradient diffusion hypothesis model of Daly & Harlow 1970 incorporates a dependence on the Reynolds stresses that improved the wall normal turbulent heat flux prediction, but only predicted the direction and not the magnitude of the streamwise turbulent heat flux. The quadratic gradient diffusion hypothesis formulation of Abe & Suga 2000 generally captured both the wall normal and streamwise turbulent heat flux components reasonably well, proving to be the best performing model of the three tested herein. All models required specification of a turbulence timescale. If the typical timescale $\tau_T = k/\epsilon$ of large eddy transport is used, the turbulent heat flux may be overpredicted, sometimes severely so. Instead the timescale should by adjusted by the Kolmogorov timescale $\tau_T = C_t(\tilde{\nu}/\epsilon)^{0.5}$ of the finescale dynamics in the near-wall viscous region in order to achieve reasonable results.

Chapter 7: BoLT-II Hypersonic Vehicle

7.1 Introduction

BoLT is a hypersonic research vehicle [190,191] aimed at studying boundary layer instabilities, laminar-turbulence transition, turbulence, aerothermal loads, aeroelasticity and various other hypersonic phenomena. The geometry presents several challenging features, such as highly swept leading edges, surfaces with spanwise concavity, significant bow-shock curvature, highly three-dimensional flow, multiple vortical instabilities and competing transition mechanisms. The first flight test was aimed at transition experiments and occurred in June 2021 at Esrange Space Center, Sweden. Several preflight ground tests and postflight analyses have been conducted [192-200]. Direct Numerical Simulation (DNS) calculations have been performed to study the response of boundary layer stability to broadband acoustic disturbances, surface roughness and wall temperature [201-207]. Linear and Nonlinear Parabolized Stability Equation (PSE) computations have been used to study relevant flow stability mechanisms, such as second mode, stationary crossflow and traveling crossflow, on both full-scale and wind tunnel-scale models [208-213].

BoLT-II is the second iteration of the vehicle in which the geometry has been extended to achieve natural laminar-turbulence transition on the smooth side of the vehicle (‘Side A’) and forced transition using roughness elements on the other side (‘Side B’). The vehicle was heavily instrumented to measure surface temperatures, heat flux, skin friction, wall pressure fluctuations and spectra. The flight test was conducted in May 2022 at NASA Wallops Flight Facility [214-216]. Simulations in support of BoLT-II have included inviscid calculations to assess aerodynamic stability, and RANS (Reynolds-Averaged Navier Stokes) calculations to predict thermal loading and optimal sensor array layout [214-215]. Instability modes and transition behavior has been

studied experimentally [217] and computationally using BiGlobal/Planar-Marching PSE predictions [218] and Spectral Proper Orthogonal Decomposition (SPOD) using a DNS base flow with stochastic perturbations [219]. Postflight analyses of sensor measurements in the laminar, transitional and turbulence regimes with thermal and mechanical loading comparisons to RANS coupled with Conjugate Heat Transfer (CHT) were performed [220]-[223].

In this work, high-fidelity simulations of a condition along the flight trajectory were conducted in support of the BoLT-II flight test campaign. It is important to note that the flight-tested vehicle was 1.0 m long, whereas the model herein was extended to 1.48 m long, referred to as "Long BoLT-II", in order to allow further turbulent development of the flow following transition. In this work, BoLT-II will refer to "Long BoLT-II". Two types of simulations are conducted, viz, (i) an adiabatic wall with no heat transfer and no freestream disturbances, and (ii) an isothermal wall with heat transfer and artificially generated freestream disturbances based on acoustic wave theory intended to simulate the inflight freestream environment. This study investigates the wall pressure, shear stress and heat flux distributions, and compares to flight experiment where available. For the adiabatic wall case, the time-averaged profiles and spectral characteristics of the downstream three-dimensionally strained turbulent boundary layer are investigated.

7.2 Geometry and Flight Conditions

The BoLT-II vehicle is shown on the left in Figure 7.1. The vehicle has a highly swept leading edge and two pairs of symmetric sides all having spanwise concave curvature. One pair consists of the top (Side A) and bottom (Side B) experimental surfaces (referring to the orientation in Figure 7.1). The other pair consists of the gutter side regions that separate the top and bottom flowfields designed such that there is no flow leakage between them. The nose radius is 5 mm. As mentioned

in the previous section, the total length of the flight-tested vehicle was 1.0 m long, but the simulated model herein is $L = 1.4756$ m.

Flight conditions were obtained from flight tests conducted in May 2022. A point in the descent phase of the trajectory at flight time 404.50 sec and altitude 19.43 km was selected for simulation. Table 3.4 details the simulated flight conditions. Figure 7.2 shows the point in the Mach and Reynolds number trajectory that corresponds to the simulated flight condition. The simulated vehicle is assumed to have zero angle of attack and zero yaw.

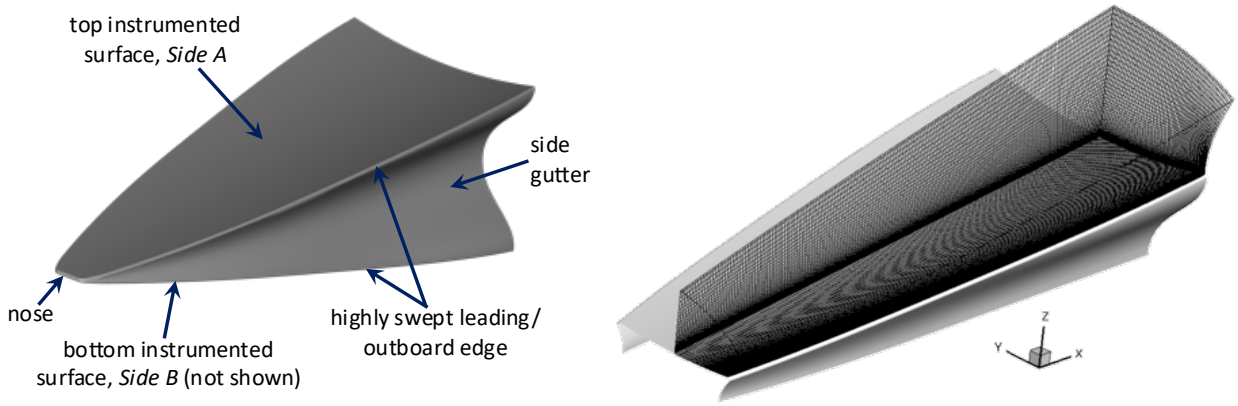


Figure 7.1. Full BoLT-II vehicle (left) and simulated top (Side A) half of the vehicle (right) with partial slices of the computational grid (coarsened for viewing). Note the grid encompasses the full upper half minus the nose.

Table 7.1. Simulated Flight Conditions.

Altitude (km)	M_∞	Re_∞ (m^{-1})	U_∞ (ms^{-1})	T_∞ (K)	ρ_∞ (kgm^{-3})	p_∞ (Pa)	T_w/T_a	L (m)
19.43 (descent)	6.11	1.29E+7	1774.12	209.84	0.1004	6048.59	1.0 0.215	1.4756

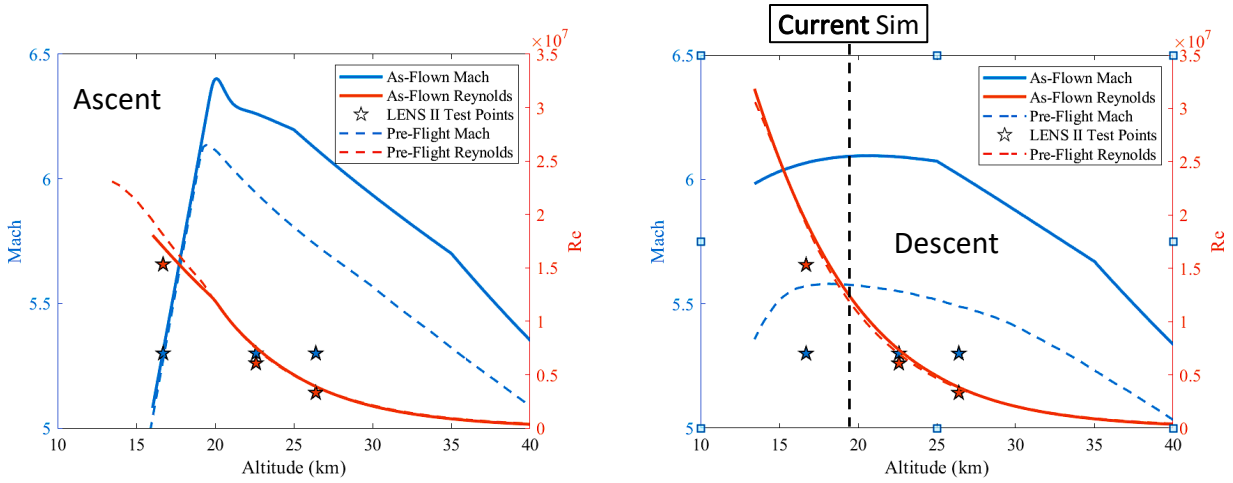


Figure 7.2. Mach number and Reynolds number during BoLT-II ascent phase (left) and descent phase (right). Simulated flight condition denoted on right. Figure reproduced from Portoni & Dufrene 2023 [216].

7.3 Methodology

7.3.1 Computational Domain and Grid Generation

In this study only Side A (the top) was of interest (refer to Figure 7.1). Here, x, y and z are the streamwise, spanwise and wall-normal oriented cartesian axes, respectively. Since the geometry was symmetrical in the xy symmetry plane, then the computational domain only consisted of the top half of the geometry. However the nose was excluded from the LES simulations such that the inlet was located at $x/L = 0.203$ – this will be discussed later. Despite geometrical symmetry of the top experimental surface in the xz symmetry plane, the full spanwise extent of the top surface was simulated to capture any asymmetric unsteady flow effects. Figure 7.1 (right) shows coarsened slices of the grid displayed on the top experimental surface. The grid slices are only partial slices chosen to illustrate the grid topology and do not necessarily indicate the extent of the computational domain.

The computational grid was generated using Pointwise V18 [224]. Referring to Figure 7.1 (right), the volume atop the experimental surface (not including the gutters) consisted of

920x649x180 nodes (streamwise x spanwise x wall normal). With the side gutters included, the total spanwise nodes were 929 and the total cell count was 154M. All grid cells were structured hexahedrons. The downstream boundary layer properties at $x/L \approx 1.0$ on the centerline $y/L = 0$ and on the outboard region $y/L = -0.17$ are shown in Table 7.2 for the adiabatic wall case. Here, δ/L is the local boundary layer thickness, and $\Delta x_w^+, \Delta y_w^+, \Delta z_w^+$ are the local grid spacings in 'law of the wall' coordinates in which the spacings are normalized by the local wall turbulence length scale $z_\tau = \nu_w/u_\tau$ obtained from the LES simulation, where $u_\tau = \sqrt{\tau_w/\rho_w}$ is the wall friction velocity, ν_w is the wall kinematic viscosity, ρ_w is the wall density and τ_w is the wall shear stress. Figure 7.2 shows the normalized wall-normal spacing Δz_w^+ on the experimental surface for the adiabatic wall case. It is observed that while the maximum is $\Delta z_w^+ \approx 0.2$, most of the surface has $\Delta z_w^+ < 0.15$. The grid resolution is conservatively consistent with WRLES specifications for the CRoCCo code in this flight regime. Cubic spline smoothing was applied to the vehicle surface to smooth out unwanted discontinuities generated by the vehicle CAD model. Iterative elliptic smoothing was applied to the bounding surface and interior volume meshes to enhance grid cell orthogonality and grid Jacobian continuity in order to minimize numerical noise. These factors can be important for high-bandwidth-resolving numerical methods such as the WENO method used herein (see Section 2.2).

Table 7.2. Downstream Boundary Layer (BL) Properties (Adiabatic Wall)

	x/L	y/L	δ/L	Nodes in BL	Δx_w^+	Δy_w^+	Δz_w^+	Δx_w	Δy_w	Δz_w
Centerline	.9894	0	.0310	101	10	6	<0.1	0.5 mm	0.3 mm	.005 mm
Outboard	.9894	-.1674	.0032	63	20	10	<0.2			

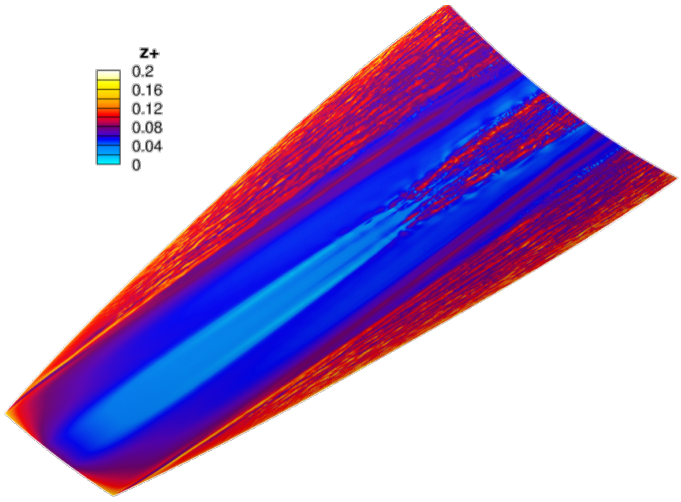


Figure 7.3. Normalized wall-normal spacing on experimental surface, Δz_w^+ (adiabatic wall).

7.3.2 Numerical Method

Wall-Resolved Large eddy simulations (LES) were conducted using the CRoCCo code. The WRLES method, including the SGS modeling, WENO flux discretization and Runge-Kutta time integration, was described in Sections 2.1 -2.3 . In this simulation the working fluid is air for which the ideal gas equation of state is assumed. The timestep, Δt, at each iteration was computed based on a Courant number stability condition, viz, $C_n = (|u_i| + a)\Delta t/|\Delta x_i| < 1$, where u_i is the local flow velocity, Δx_i is the local grid spacing and a is the speed of sound. For this case, this resulted in a mean stable timestep of 0.7 ns. If, for example, one assumes 100 timesteps per wave period, one can resolve a characteristic wave up to 14 MHz. Temporal data presented herein was sampled every 0.5 μs or at a sampling frequency of 2 MHz.

7.3.3 Initial Conditions

The flowfield for the LES run was initialized using a steady laminar solution from FUN3D V13.7 [225]. In this case, the full streamwise extent of the vehicle was simulated. The grid for this case was the same was that used for the LES run, but also included the nose portion. The total cell

count for this grid, which encompasses the flow environment over the top half of the vehicle, was 222M cells. The FUN3D inviscid flux construction was a 2nd-order 'dissipative low diffusion flux splitting scheme', which switches to Van Leer flux vector splitting near shocks. A Van Leer stencil-based flux gradient limiter was also applied. Residuals of density, momentum and energy terms decreased at least 17 orders of magnitude before converging to a steady-state. Sample field plots of the initial condition are shown below for the adiabatic wall case. Figure 7.4 shows the steady-state pressure on the xz symmetry plane and the steady-state pressure and skin friction on the top experimental surface.

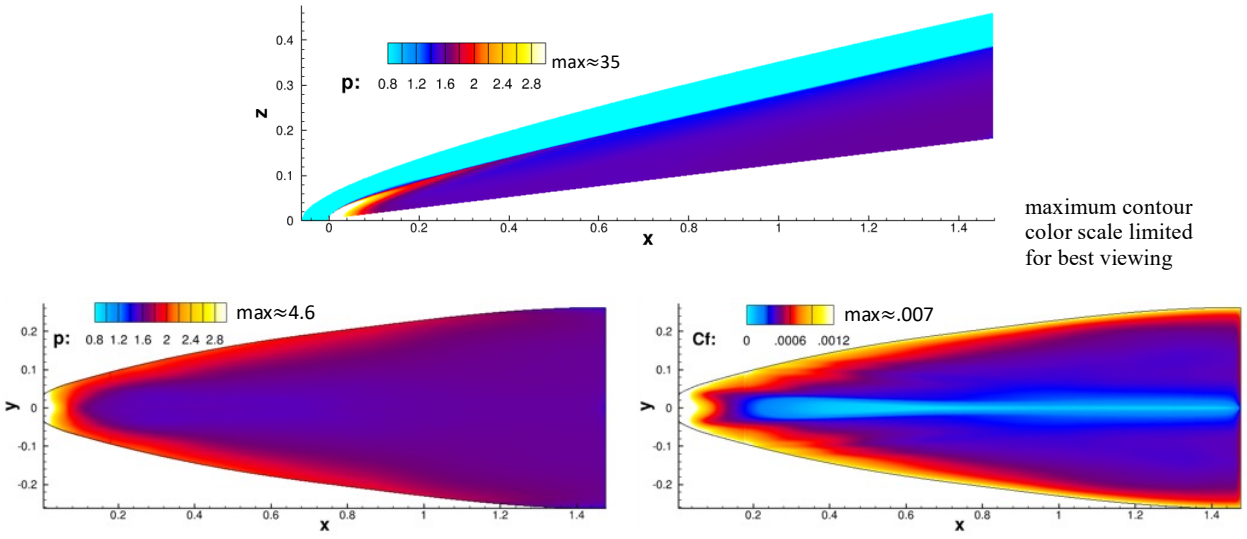


Figure 7.4. FUN3D laminar adiabatic wall solution: pressure $p/(\rho_\infty a_\infty^2)$ on xz symmetry plane (top) and experimental surface (bottom left), and skin friction $\tau_w/(0.5\rho_\infty U_\infty^2)$ on experimental surface (bottom right).

7.3.4 Boundary Conditions

The vehicle surface was modeled as a smooth, viscous, no-slip surface. Two wall temperature boundary conditions were simulated, viz, (i) an adiabatic wall with no heat transfer, and (ii) an isothermal wall with heat transfer. The theoretical adiabatic wall temperature based on recovery factor 0.9 was estimated to be 1627 K. The assigned wall temperature for the isothermal condition was based on RANS simulations coupled with conjugate heat transfer performed by Wirth et al.

2023 [220]. Based on the latter study, an isothermal wall temperature of 390 K was applied. The top boundary (w.r.t. the orientation in Figure 7.1-right) upstream of the primary shockwave was assigned as a supersonic freestream inlet. The outflow at the downstream end of the geometry was assigned as a supersonic extrapolation boundary. The xy plane through the side gutters was assigned an inviscid symmetry condition.

The inlet was prescribed as a Dirichlet boundary and was supplied by the FUN3D time-averaged laminar solution. For the adiabatic wall case, the downstream flow was allowed to develop naturally without any artificial forcing. For the isothermal wall case, the steady inlet was perturbed using stochastic broadband forcing. The stochastic broadband forcing was intended to model the freestream disturbance environment in flight so that the vehicle may naturally select one or more laminar-to-turbulent transition paths thereby removing bias towards exciting a particular instability mechanism (Hader & Fasel 2018 [226], Goparaju & Gaitonde 2021 [227], Johnston, Hemati & Candler 2022 [207]). In hypersonic boundary layers, acoustic disturbances generally dominate transition over vorticity and entropy disturbances (Balakumar 2011 [228]). The procedure was to generate white nose pressure fluctuations across four consecutive axial planes near the inlet in order to force planar acoustic waves (Kovasznay 1953 [229]) that vary with (x, y, z, t). The perturbed planes were just downstream of the inlet and extended from the first grid point off the wall to a few grid points just below the freestream (top) boundary. Fluctuations of density, temperature and streamwise velocity were then applied through the linearized isentropic relations consistent with acoustic wave propagation. Fluctuations of streamwise velocity satisfied the slow acoustic mode, which has shown to result in higher boundary layer receptivity compared to the fast acoustic mode (Balakumar 2011 [228], Fedorov 2003 [230]). Specifically, the disturbances at the inlet were computed as,

$$p' = A(2r - 1) \quad [133]$$

$$\begin{bmatrix} \rho' \\ T' \\ u' \\ v' \\ w' \end{bmatrix} = \begin{bmatrix} \frac{1}{\bar{a}^2} \\ \frac{(\gamma - 1)\bar{T}}{\bar{\rho}\bar{a}^2} \\ -\frac{1}{\bar{\rho}\bar{a}} \\ 0 \\ 0 \end{bmatrix} p' \quad [134]$$

where $A = \max(p'/\bar{p})$ is the maximum amplitude of the pressure fluctuations, $r = r(x, y, z, t) \in [0,1]$ is a random number and a is the speed of sound.

7.4 Adiabatic Wall Case

7.4.1 General Flowfield

The following presents LES solutions of the BoLT-II experimental surface. Figure 7.5 shows surface contours of pressure, temperature and shear stress in SI units. Pressure generally reaches a maximum at the nose stagnation point (not simulated here, but can be observed in Figure 7.4 in the FUN3D solution) and along the upstream outboard edge (seen in Figure 7.4 and Figure 7.5) which lies close to the main shockwave. In the upstream central region, the pressure, as well as temperature and skin friction, shows little to no breakdown. Further downstream, the central region becomes very nonuniform. In this region the temperature and more so skin friction increases drastically reaching a maximum on the surface, indicating increased mixing and breakdown to turbulence. Figure 7.6 also shows pressure waves appearing to emanate in a circular manner from the downstream central instabilities. The wall temperature varies from about 1400-1800 K reaching a maximum in the downstream central region. The wall temperature is in the vicinity of the theoretical adiabatic wall temperature of 1627 K based on recovery factor 0.9. In the outboard region of the surface, Figure 7.5 shows instabilities arising from the upstream outboard edge where

temperature and skin friction rises and continues to develop in the streamwise direction indicating increased mixing and similar breakdown behavior as the central region.

Figure 7.7 shows streamwise velocity contours on a plane just above the surface within the boundary layer and on slices across the span. The central region shows two distinct streamwise counterrotating vortices developing downstream. These vortices grow in diameter and become more unstable developing into eddy-like structures at the downstream end, where the increasing mixing leaves an imprint of increased skin friction and wall temperature as observed in Figure 7.5. Instabilities arising from the upstream outboard edge show streamwise streaks in the velocity contours that continue downstream, consistent with the behavior observed in Figure 7.5. There also appears to be two distinct streamwise vortical streaks in between the central region and outboard instabilities.

Figure 7.8 shows an isosurface of Q-criterion colored by normalized vorticity magnitude. Q-criterion is the second invariant of the velocity gradient tensor and is defined as $Q = 0.5(\|\Omega\|^2 - \|\mathrm{S}\|^2)$, where Ω is the vorticity tensor and S is the strain rate tensor. Thresholding Q to positive values therefore identifies vorticity-dominated regions of the flow. The unusual BoLT-II geometry lends itself to multiple instabilities and complex inviscid-viscous interactions. From Figure 7.8 one may be able to decipher four types of coherent flow structures in general regions labeled (1)-(4). Some previous observations also become clearer. Firstly, down the centerline labeled (1), the two separate vortical structures grow in diameter and coalesce further downstream resulting in a larger downstream region of vorticity and flow mixing, which would result in the higher temperature and skin friction. Secondly, the plot clearly shows crossflow vortical instabilities emanating from along the outboard edge, labeled (2), developing into a region of larger spanwise vorticity and mixing at the outboard downstream region. Thirdly, in between the central

and outboard flow structures, labeled (3), the two (possibly more) streamwise-running vortical tubes can be observed. Finally, there appears to be secondary crossflow vortical structures in between the central and outboard region, labeled (4), that seem to have a crisscross pattern. This work is primarily concerned with the downstream breakdown/turbulent flow. To analyze the downstream development of these structures, specific locations across the span are further interrogated in the next section.

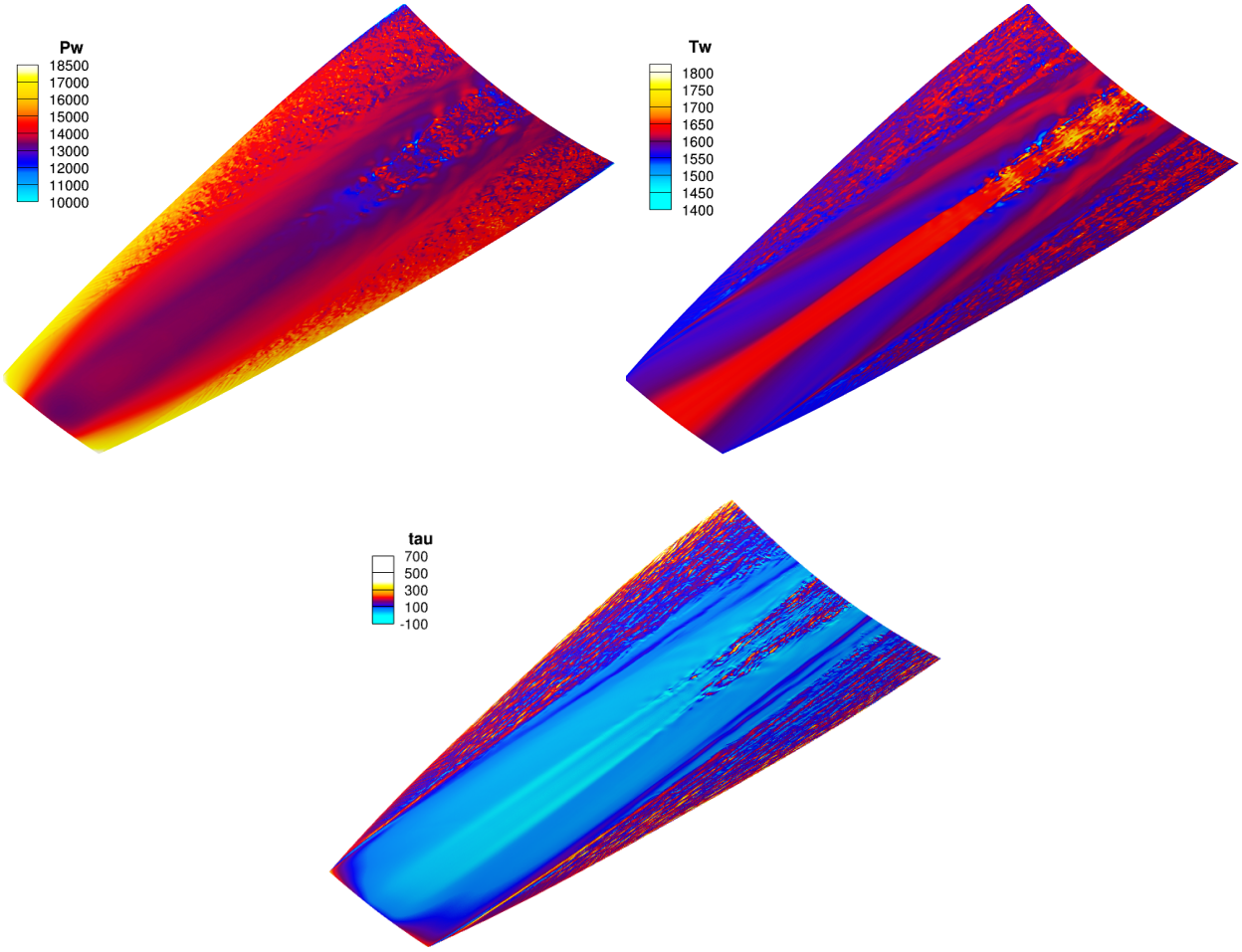


Figure 7.5. Instantaneous surface contours: pressure P_w (Pa), temperature T_w (K) and shear stress τ_w (Pa).

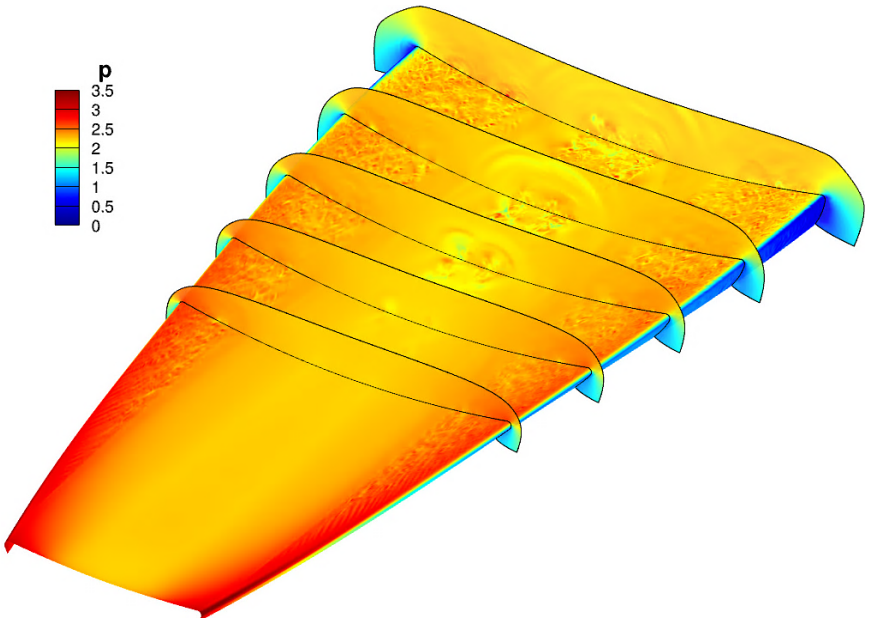


Figure 7.6. Pressure contours P/P_∞ on a plane just above the surface and on slices across the span.

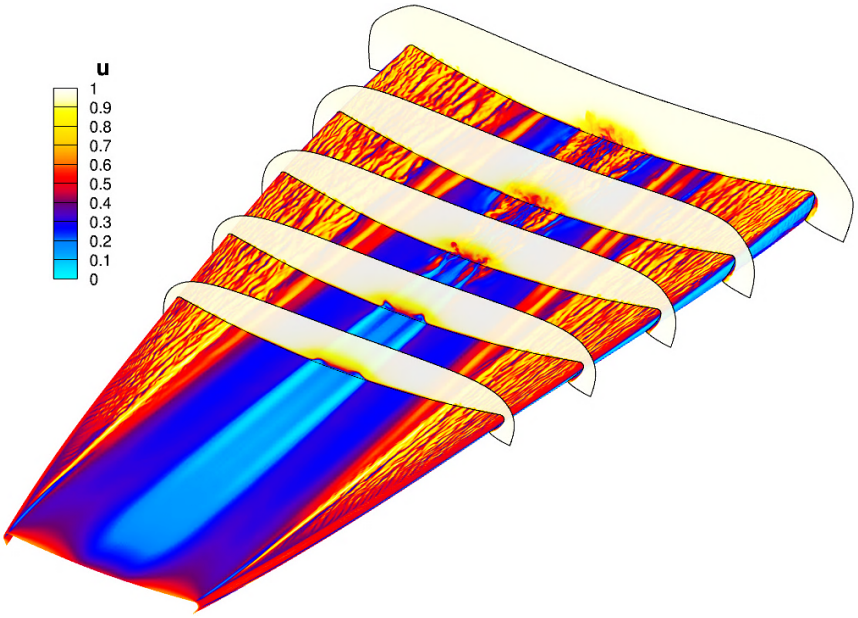


Figure 7.7. Streamwise velocity u/U_∞ on a plane just above the surface and on spanwise slices showing downstream development of flow.

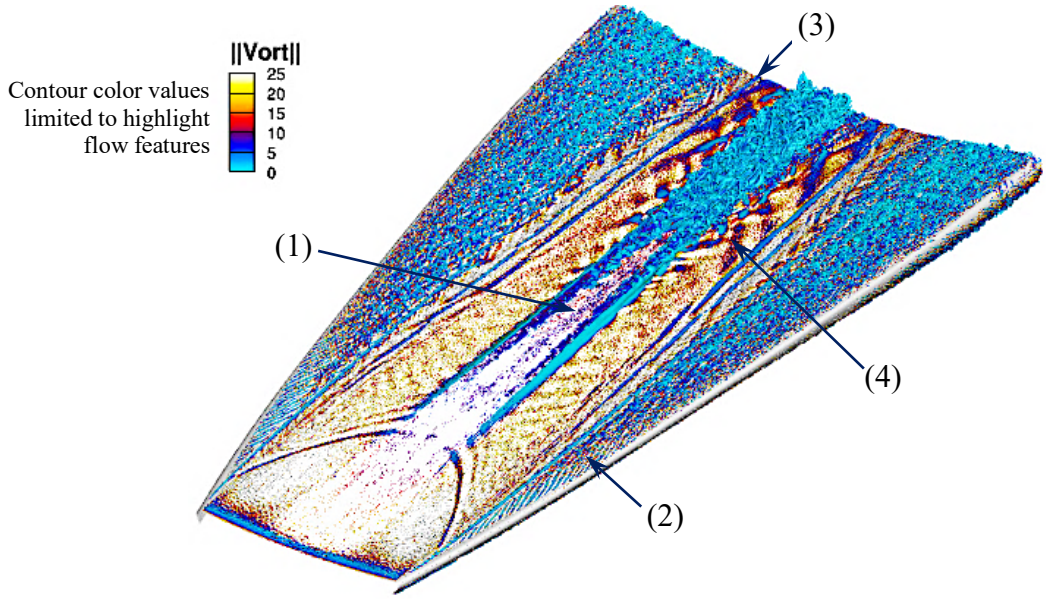


Figure 7.8. Isosurface of Q-criterion colored by normalized vorticity magnitude $\omega\delta_0/U_\infty$.

7.4.2 Boundary Layer Profiles: Mean Profiles

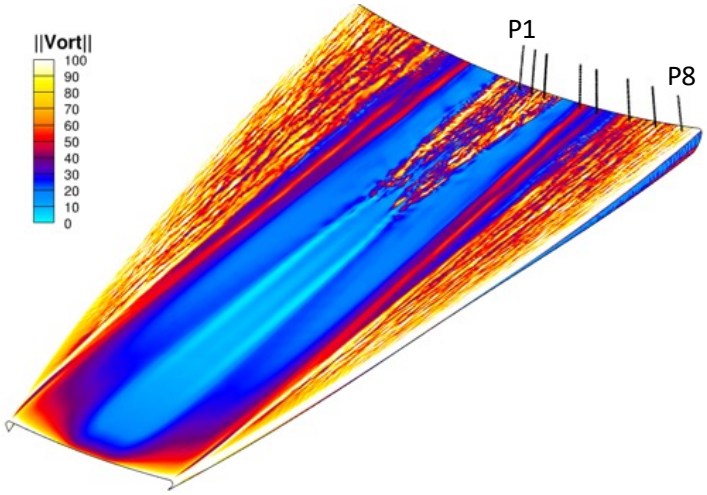


Figure 7.9. Vorticity magnitude $\omega\delta_0/U_\infty$ with wall normal line extractions labeled P1-P8.

To analyze the far downstream behavior of the flow, boundary layer profiles, also referred to as probes herein, are extracted at 8 key locations across the span at $x/L = 0.9894$ as shown in Figure 7.9. The first 3 locations P1-P3 lie within the central region of high vorticity. The second 2 locations P4-P5 each lie on the two streamwise vortical structures. The final 3 locations P6-P8 lie in the outboard region of instabilities. The wall normal profiles were computed at each time instant

using wall-normal vector projection into the boundary layer and trilinear interpolation in computational space to obtain the data along the lines.

Figure 7.10 shows the mean velocity parallel to the wall under the Van Driest II [66] similarity transformation (red lines). For a 2D equilibrium boundary layer, the theoretical viscous sublayer defined by $u^* = z^*$ (blue lines), and the theoretical log layer defined by $u^* = 1/\kappa \log(z^*) + C$, where $\kappa = 0.41, C = 5.2$ (green lines) are also shown. The * superscript indicates semi-local 'law of the wall' coordinates, where $u^* = u/u_\tau^*$, $z^* = z/z_\tau^*$, and u_τ^* and z_τ^* are velocity and length scales respectively relevant to the viscous wall layer. The viscous sublayers in the profiles remain nearly universal, except for some small deviation for the central probe P1. The central probe has a log layer that is offset from the theoretical but has a similar slope. Interestingly all the profiles have some form of a log layer, but they all significantly depart from the classical 2D turbulent boundary layer similarity scaling. They exhibit nonequilibrium in this region, energized likely by low frequency dynamics inferred from the spectral analysis (shown later).

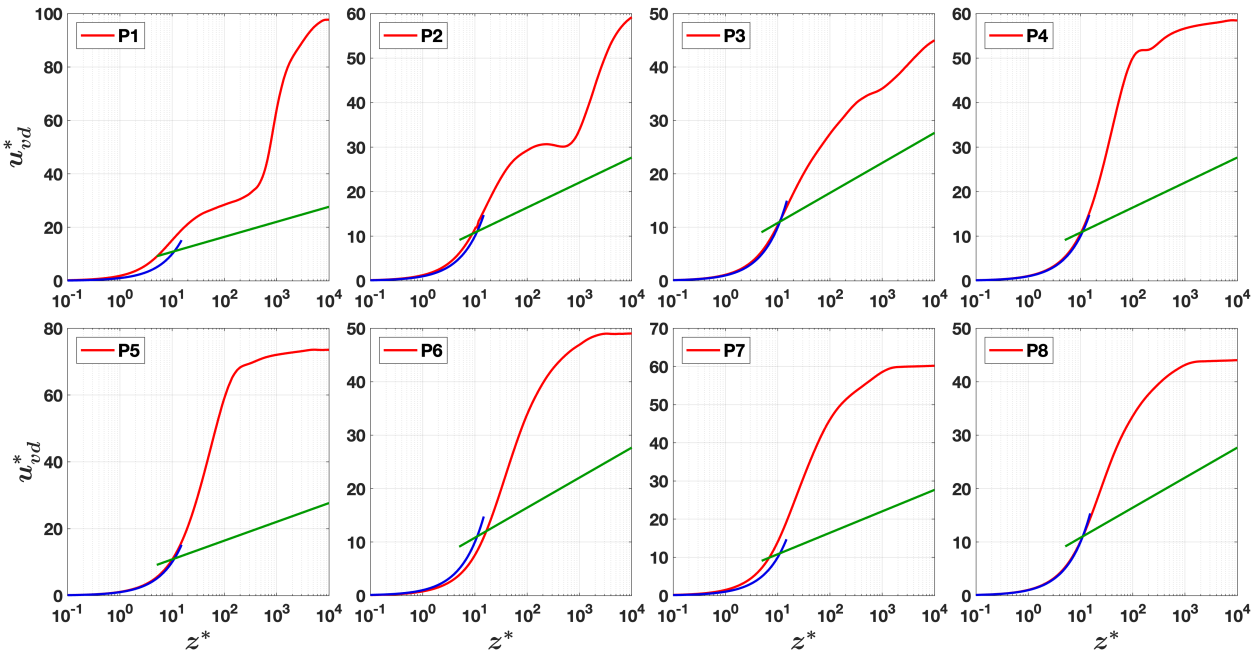


Figure 7.10. Van Driest transformed mean u-velocity u^*_{vd}, (red line), with theoretical viscous sublayer (blue line) and theoretical log-law layer (green line).

Figure 7.11 shows the mean profiles of u, v, w, T, ρ, p normalized by local boundary layer edge values. The streamwise u-velocity at the central probes P1-P3 show inflection points in the region $z/\delta < 0.7$ indicative of an adverse pressure gradient that is strongest at the centerline and diminishes away from the centerline. The boundary layers at the middle probes P4-P5 are much thinner with mild inflection points. The boundary layers at the outboard region, probes P6-P8, monotonically increase from the wall to boundary layer edge. The spanwise v-velocity at the central probes show that at the centerline, P1, there is negligible spanwise flow. Slightly away from the center at P2 and P3, v goes from positive maxima near the wall to negative maxima further away from the wall, which would be consistent with a vortex whose spin direction is in the positive streamwise direction as given by the right-hand rule. The probes at P4 and P5 at the middle vortex tubes show similar v profiles in the near-wall region, indicating vortices that also rotate in the same direction. For the outboard probes, P6 shows a small positive peak in v near the wall that goes negative away from the wall, while $|v|$ at P7 and P8 monotonically increase from wall to boundary layer edge. The v profiles in general show increasing spanwise velocity from center to outboard region. Interestingly, the wall normal w-velocity profiles show similar trends to the streamwise u-velocity profiles, albeit an order of magnitude smaller.

The mean temperature profiles in Figure 7.11 show that the temperature at the wall reaches a maximum of ~5.5 times the boundary layer edge value (adiabatic wall condition). Probes P1-P5 show inflection points for $z/\delta < 0.7$. The strongest inflections are at the central probes where the temperature rise away from the wall is due to increased mixing. Probes P6-P8 show a monotonic decrease in temperature from wall to boundary layer edge. The mean density at the wall is ~0.2 times the boundary layer edge for all profiles, and essentially shows reverse trends to mean temperature from wall to boundary layer edge. The mean pressure shows a decrease in pressure in

the near-wall region for the central probes P1-P3. The pressure variation is milder away from the central region.

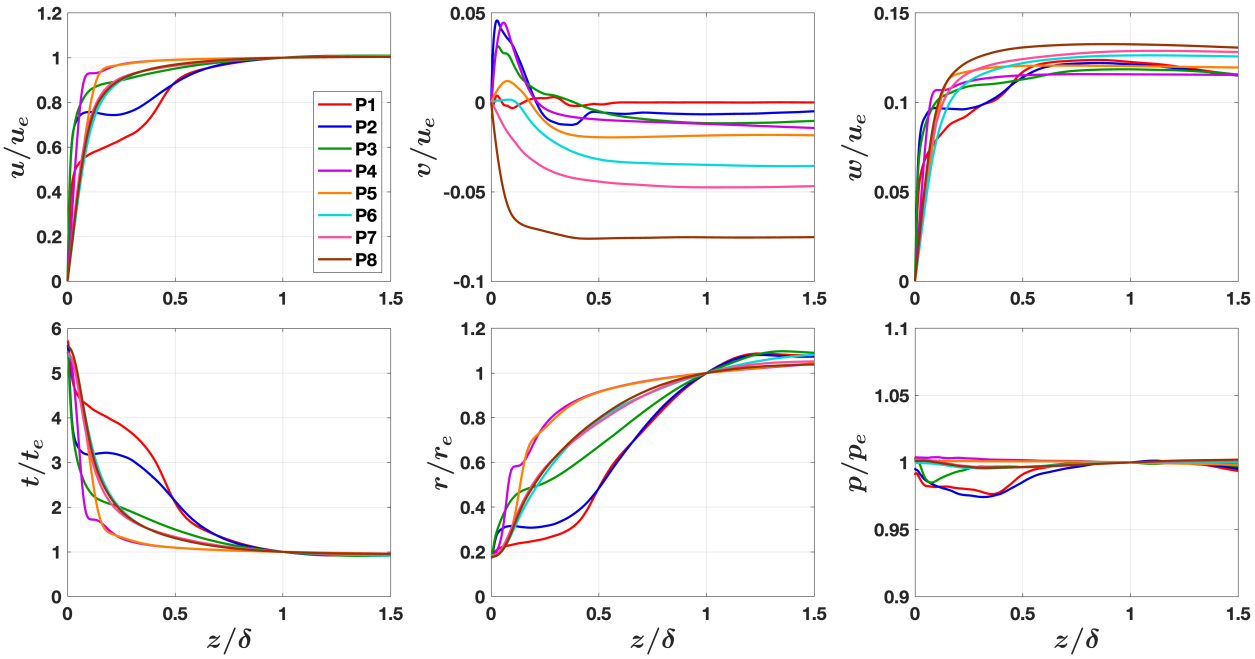


Figure 7.11. Mean profiles of u, v, w, T, ρ, p normalized by boundary layer edge values.

7.4.3 Boundary Layer Profiles: Signals and Spectra

Figure 7.12 shows the time history of u-velocity u/u_e at a sample location $z/\delta = 0.1$ in the boundary layer for each of P1-P8, where z is the wall normal distance, δ is the local boundary layer velocity thickness and u_e is the local boundary layer edge velocity. Since local normalizing quantities were used, the time axis is different for each probe, but the physical flow time is exactly the same for each.

Figure 7.13 and Figure 7.14 plot the power spectral density (PSD) of u-velocity signals through the boundary layer profiles. The PSD is computed via the Welch method [82] which uses a Hamming window function with prescribed 4 total windows and 50% window overlap. The PSD is normalized such that the integral sum of the spectrum over the normalized frequency range should equal 1. Figure 7.13 plots the PSD against frequency, f, and z/δ. Figure 7.14 plots the

PSD against frequency and semi-local similarity coordinate z^*, where $z^* = z/z_\tau^*, z^* = \nu/u_\tau^*, u_\tau^* = \sqrt{\tau_w/\rho}$ is the semi-local friction velocity, ν is the local kinematic viscosity, ρ is the local density and τ_w is the wall shear stress. The contour extrema values have been adjusted to emphasize maximal values in the spectra. All probes show a 'streaks' of peak energy throughout the boundary layer. For the central probes P1-P3, the frequencies span ~3-100 kHz, within distinct peaks in the vicinity of 20 kHz for $z/\delta > 0.6$. For middle vortex structure, probe P4, there appear to be distinct peaks at 6, 8 and 15 kHz in the vicinities of $z/\delta = 0.01, 0.2, 0.9$, respectively. For middle vortex structure, probe P5, there appears to be peaks at 8 and 15 kHz in the vicinities of $z/\delta = 0.1, 0.9$, respectively. For the final three probes P6-P8, peaks are more difficult to identify but generally frequencies span the range ~3-200 kHz. Figure 7.14 visually allows an expanded view of the viscous sublayer where in each probe there exists a 'streak' of peak energy at roughly 10 kHz for $z^* < 30$.

Figure 7.15 shows the energy spectra at a sample location of $z/\delta = 0.9$. All center probes P1-P3 show a main low frequency peak at 20 kHz, while center probes P2-P3 show an additional main peak at 30 kHz. There are also several secondary peaks. At this z/δ, the center probes show no higher frequency content. The middle probes P4-P5 both show a primary 15 kHz peak and a secondary 8 kHz peak. The middle probes also show no higher frequency content at this z/δ. The outboard probes P6-P8 at this z/δ all show higher frequency content that is broadband and indicative of turbulence. These probes have multiple low frequency peaks. The observations in the spectra at this z/δ location are consistent with that observed in the 2D spectral maps in Figure 7.13.

Figure 7.16 shows the spectra of wall pressure signals at locations P1-P8. The center probes P1-P3 in this case show high frequency content that is broadband and indicative of turbulence.

These probes have several low frequency peaks in the range 15-100 kHz and at 135 kHz for P3. The middle probes P4-P5 have little to no high frequency content and distinct low frequency peaks at 15 kHz. The outboard probes once again have a broadband nature with some low frequency peaks.

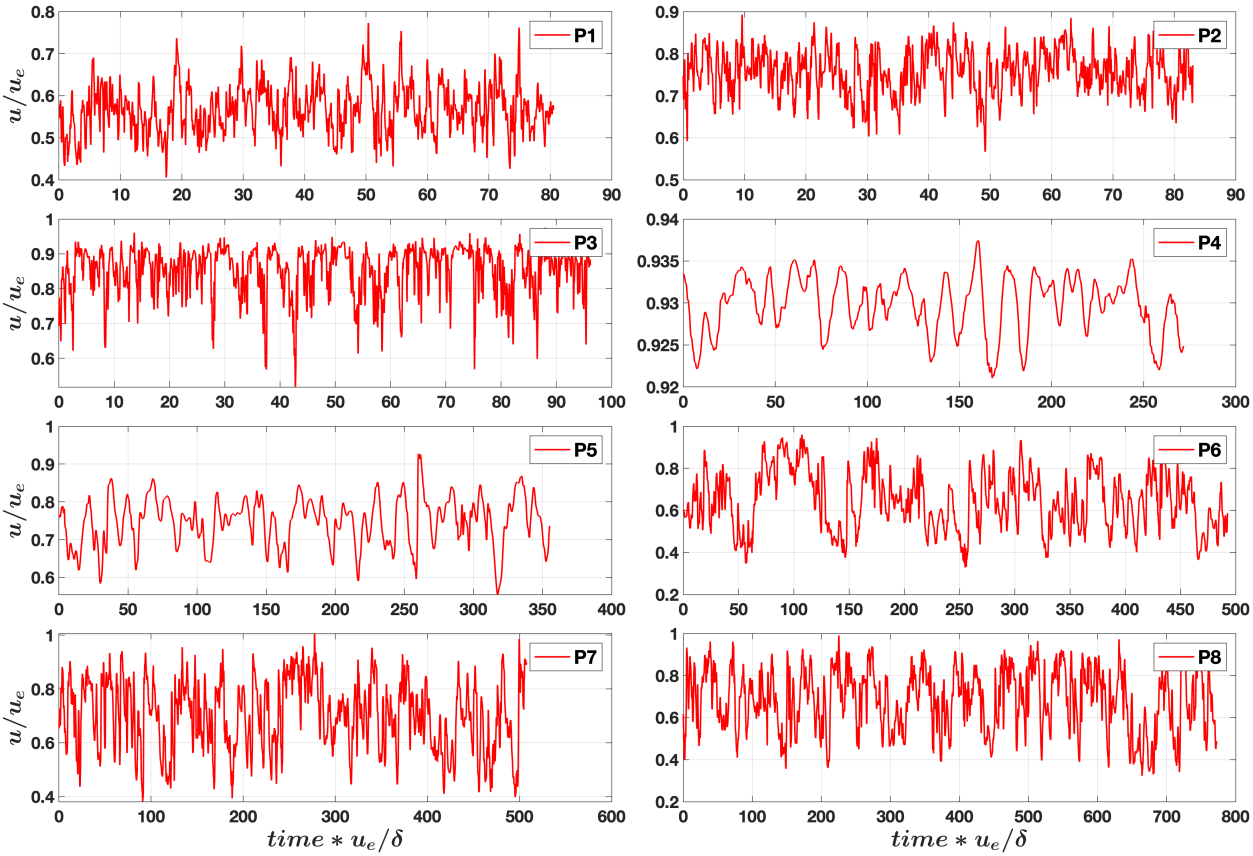


Figure 7.12. Signals of u-velocity at sample location $z/\delta = 0.1$ in the boundary layer.

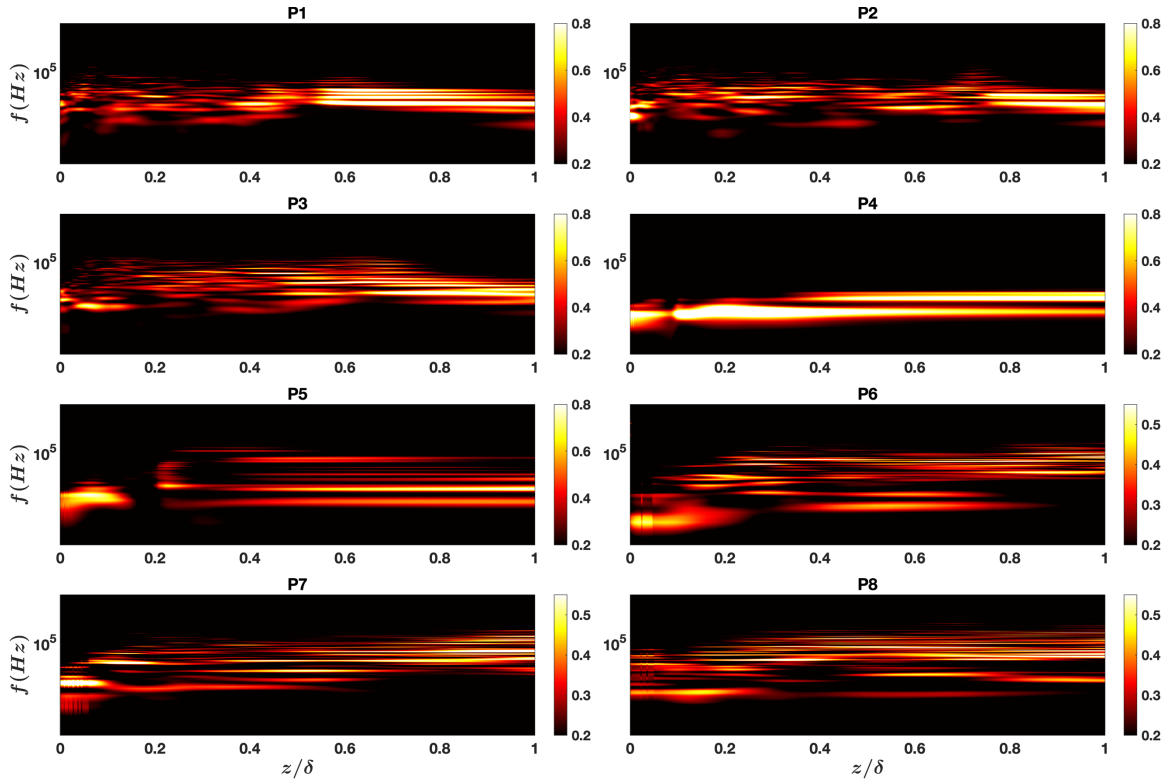


Figure 7.13. Energy spectra through the boundary layer vs. z/δ for probes P1-P8.

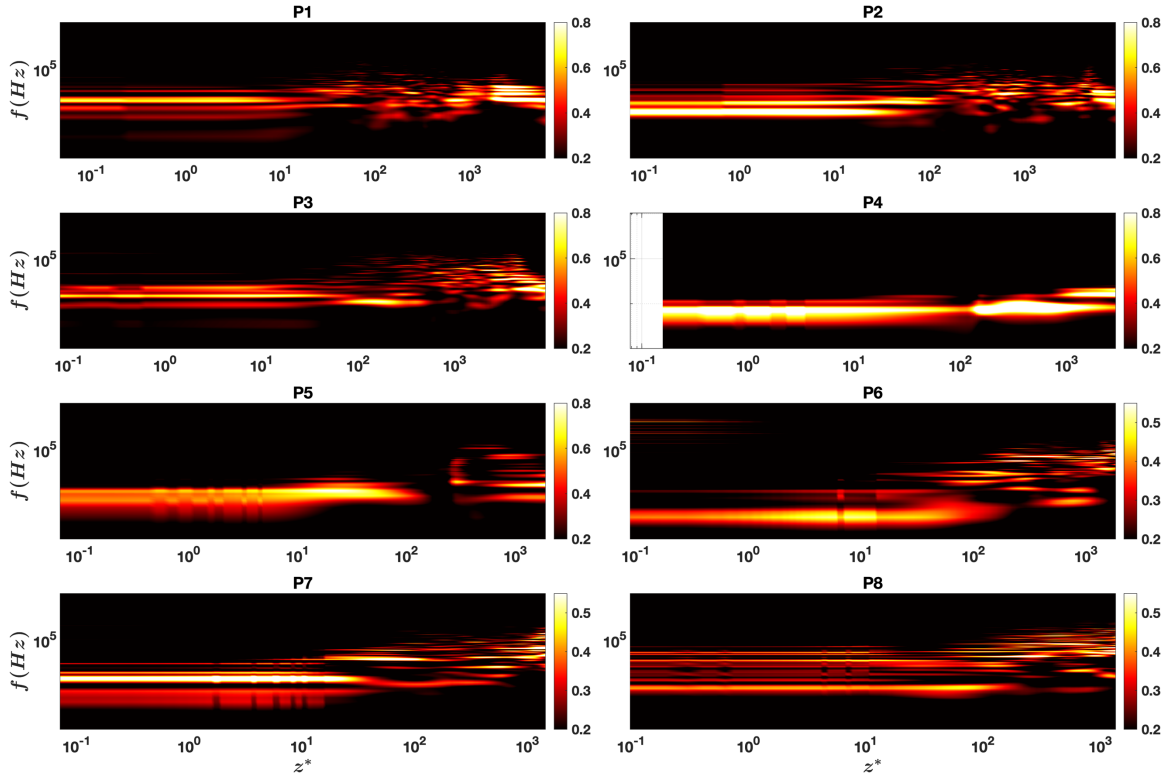


Figure 7.14. Energy spectra through the boundary layer vs. z^* for probes P1-P8.

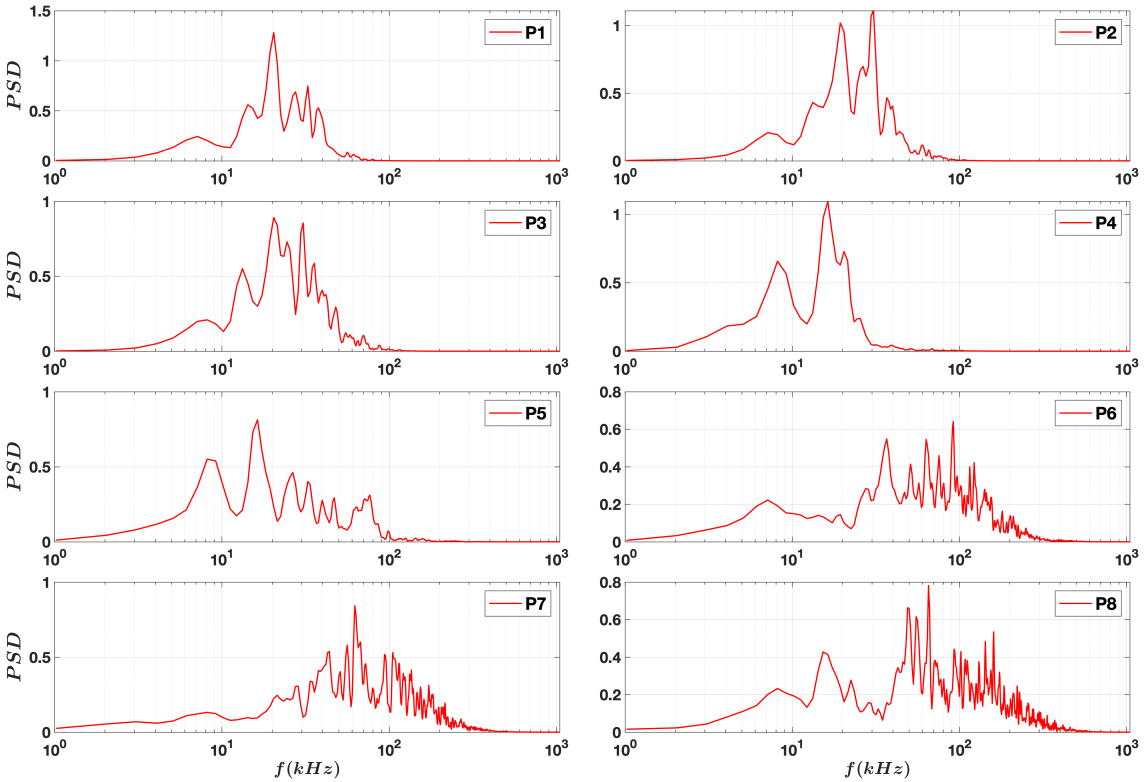


Figure 7.15. Energy spectra at $z/\delta = 0.9$.

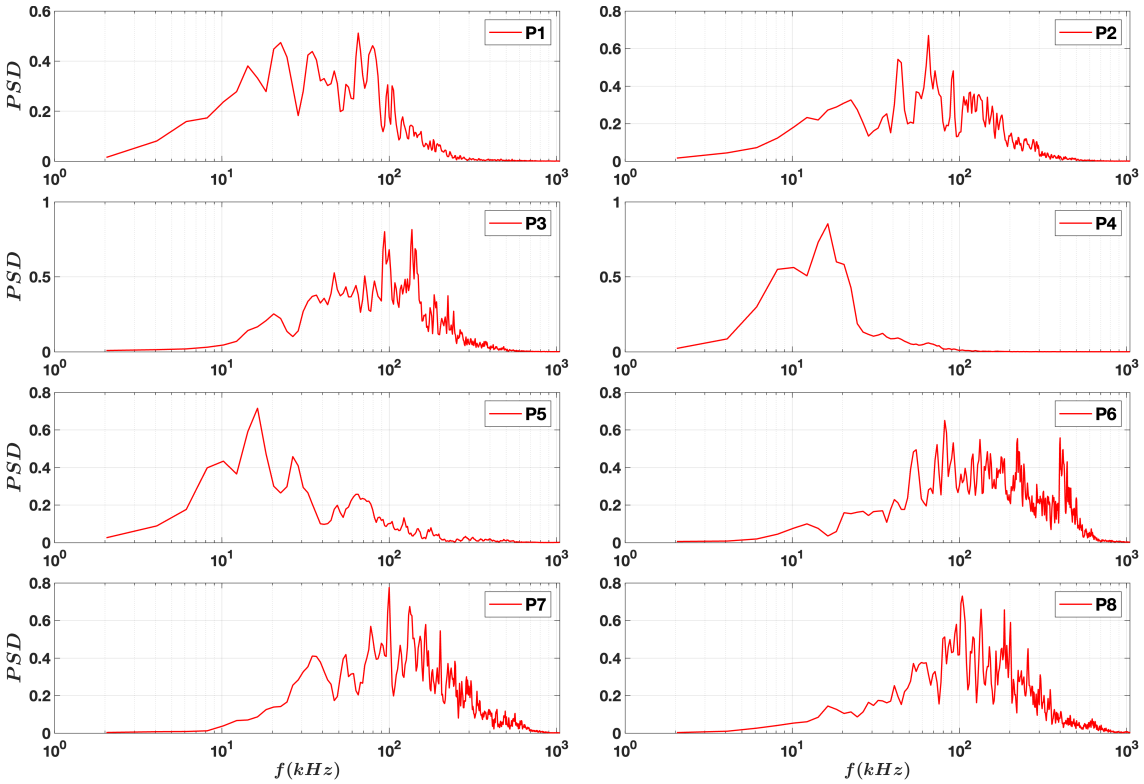


Figure 7.16. Wall pressure spectra.

7.5 Isothermal Wall Case

The isothermal wall case was perturbed at the inlet as described in Section 7.3.4 . Pressure disturbances were applied at the inlet such that the downstream freestream pressure disturbance was measured to be $(p'/\bar{p}_\infty)_{rms} = 0.5\%$. Figure 7.17 shows an instantaneous snapshot of the wall pressure fluctuations p' before and after applying the inlet disturbance. In both cases, wall pressure fluctuations arise down the centerline, starting off as two parallel streaks that appear to coalesce further downstream. Pressure fluctuations also arise in mainly two strips on the outboard regions on either side of the centerline. There is also some pressure fluctuations appearing in a crossflow pattern along the centerline and outboard regions. In the case of the perturbed inlet, larger regions of the downstream end have non-zero pressure fluctuations than the unperturbed case.

Figure 7.18 and Figure 7.19 shows instantaneous wall shear stress and wall heat flux. Also shown in these figures are the locations of some of the wall sensors in the flight experiment organized in three rows labeled R4, R5 and R6. Sensor types included Medtherm Thermocouples (MT, pink dots), Pressure Fluctuation Gauges (PCB, green dots) and Ahmic Skin Friction Gauges (SF, black dots). Table 7.3 summarizes the types of sensors chosen for comparison in this study and their axial locations. In the simulation an additional row of sensors/probe locations were included labeled R7 (yellow dots) located at the downstream end. Both the wall shear stress and wall heat flux exhibit a precipitous rise in the central and outboard regions. At the far downstream end, the entire spanwise extent has higher levels of shear stress and heating.

Figure 7.20 shows the wall shear stress and wall heat flux across the span compared to the sensor flight data extracted at the current simulated flight condition. The CFD results show spikes in shear stress and heat flux in the central and outboard regions for rows R4-R6. Additionally R6 shows spikes in the region between the center and outboard sections. Row R7 at the far

downstream end shows a nearly constant shear stress and heat flux across the span that is generally higher than the upstream region except at the outboard regions. With regards to the flight data, there are only shear stress sensors in middle region between the center and outboard regions, which indicate shear stress levels approaching 300 Pa. This is generally significantly higher than that obtained by the simulations. Only in the outboard regions does the simulated shear stress spike to the level of the flight experiment, that is ~300 Pa. The heat flux from the flight sensors are also generally higher than the CFD predictions, except for a few locations in the center and outboard regions.

From these results, it appears that the sensors in the flight experiment are indicating transition-to-turbulence at this flight condition. The significant cross-stream fluctuations in heat flux in both the experiment and CFD indicates that the transition front varies with axial and spanwise distance, or with Reynolds number based on axial distance as characteristic length. This was also reported in Portoni & Dufrene 2023 [216], among others. The CFD results at R4-R6 appear to indicate delayed transition relative to the flight experiment. A sample time tracking of heat flux from one of the sensors in the descent phase of the trajectory is shown in Figure 7.21. The simulated point in the trajectory is also shown by the black vertical line at flight time 404.5 sec. The flight sensor history indicates that the heat flux is initially laminar at levels between 50-100 kW/m^2, then precipitously jumps to turbulent levels of ~400 kW/m^2 at flight time ~404.4 sec. However, the flow does not remain turbulent at this location. The sensor indicates significant fluctuations in heat flux between laminar and turbulent levels in the range 404.4-405.5 sec, after which the heat flux starts to stabilize at turbulent levels. It may be unfortunate that the flight condition at 404.5 sec was chosen for the simulation herein due to the unstableness of the transitional flow in this flight regime. This was a consequence of the fact that the simulations herein were conducted prior to

obtaining the flight wall sensor data. The unstable transitional flow in this flight regime may explain the discrepancy between CFD and flight experiment, that is, any small difference between simulated flight conditions/Reynolds number and that reported from experiment could easily drive the flow towards a laminar or turbulent state at a given location. To improve confidence in the CFD predictions, a future exercise would simulate a stable flight condition, whether laminar or turbulent, along the trajectory.

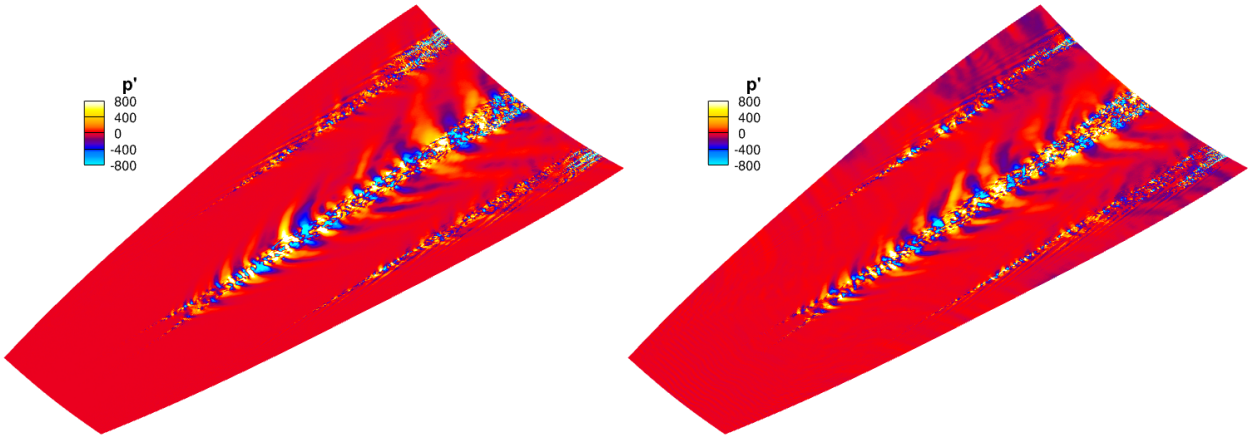


Figure 7.17. Instantaneous wall pressure fluctuations p' (Pa) with no inlet disturbances (left) and with inlet pressure disturbances (right). Freestream disturbance: $(p'/\overline{p}_\infty)_{rms} = 0.5\%$.

Table 7.3. Bolt-II Sensor Types and Locations.

Sensor Type	Row	x-location	Legend Color
Ahmic Skin Friction Sensors (SF)	R4	0.8214	black
	R5	0.8175	
	R6	0.9597	
Medtherm Thermocouples (MT)	R4	0.7960	pink
	R6	0.9470	
Pressure Fluctuation Gauges (PCB)	R5	0.8842	green

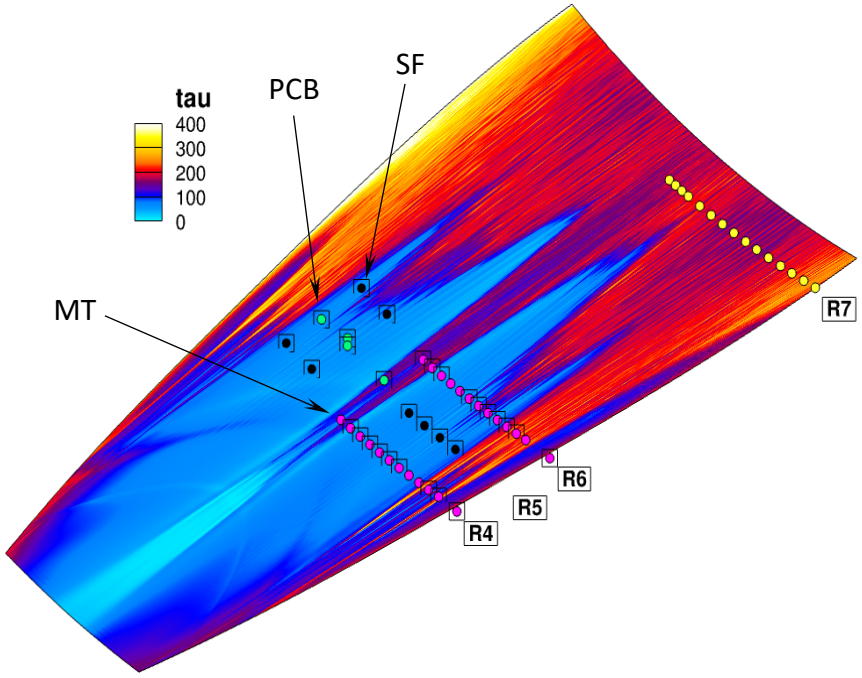


Figure 7.18. Instantaneous surface contours: shear stress τ_w (Pa).

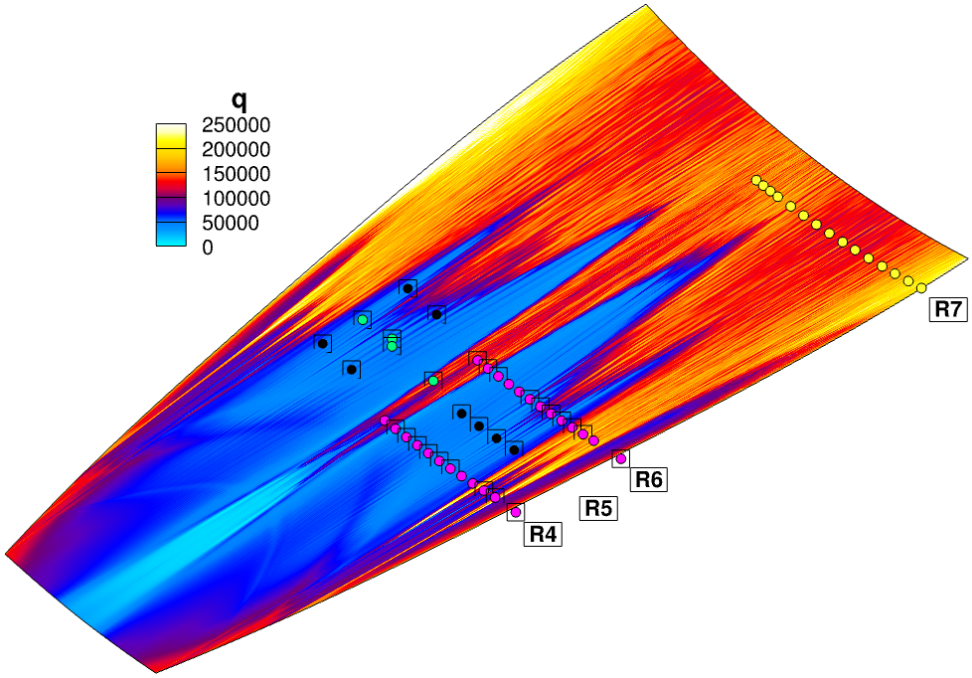


Figure 7.19. Instantaneous surface contours: heat flux q_w (W/m^2).

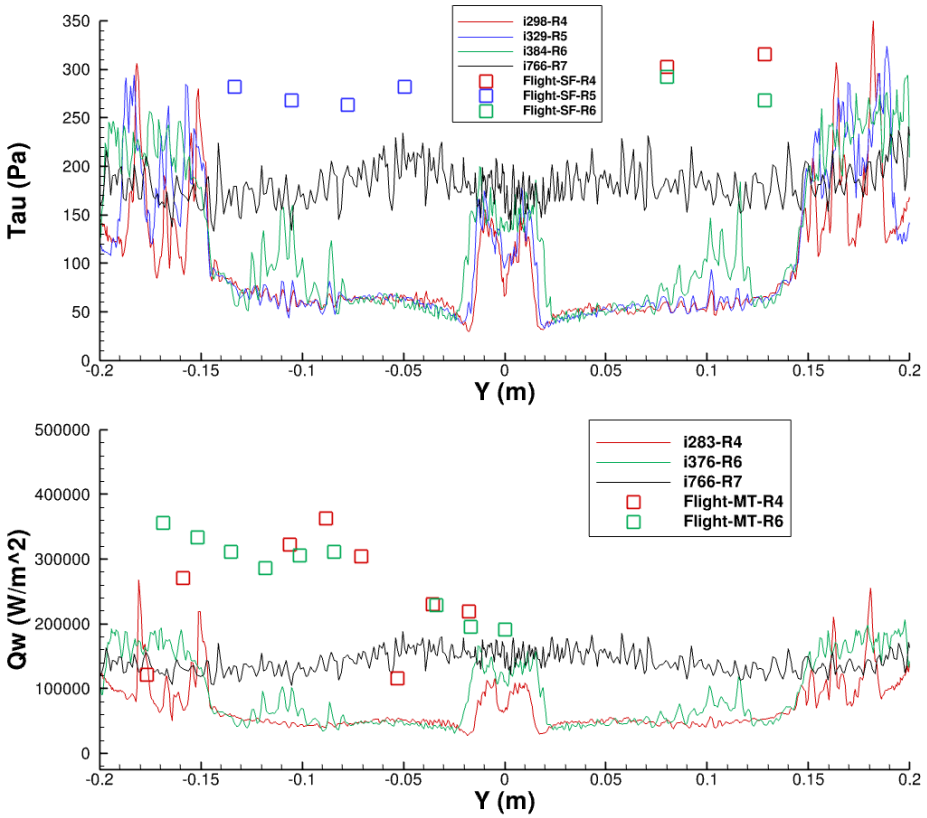


Figure 7.20. Instantaneous cross-stream shear stress τ_w (Pa) (top) and heat flux q_w (W/m^2) (bottom). Solid lines are from CFD, and square symbols are from flight experiment.

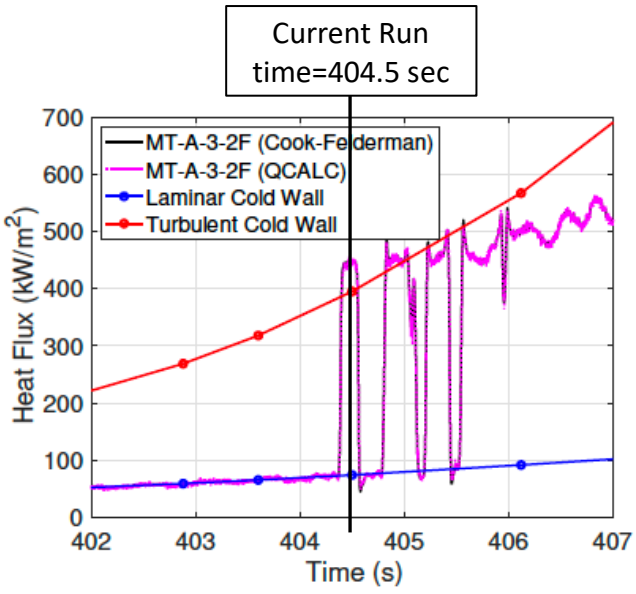


Figure 7.21. Heat flux tracking during flight from thermocouple sensor MT-A-3-2F, and comparisons with CFD. Reproduced from Wheaton & Dufrene 2023 [223]. This figure illustrates the unstable nature of the chosen point in the trajectory for the simulations herein.

7.6 Chapter Conclusion

Wall-resolved large eddy simulations of the BoLT-II flight test vehicle were conducted at a flight condition during the descent phase of the trajectory. The BoLT-II geometry was extended from the flight test configuration of 1.0 m to 1.48 m to allow further development of the turbulent flow. For the *unperturbed adiabatic wall case*, flowfield solutions of the turbulent environment over the vehicle show multiple and distinct large-scale instabilities on top of what is typically seen in broad-frequency turbulence. The present of these structures suggests complex interactions in the boundary layer. Four types of coherent structures were identified. A central pair of vortex streams grows from upstream and coalesces downstream resulting in a region of turbulent eddy-like structures with the highest vorticity, wall temperatures and skin friction on the surface. Although turbulent flow is established, the central vortex pair remains coherent, as shown in the spectral analyses of the data. Energy spectra in this region showed high frequency content, indicative of turbulence, as well as low frequency dynamics through the central boundary layer. The outboard edge of the vehicle incurs crossflow instabilities that grow downstream and show similar behavior to the central region, albeit with lower vorticity, temperatures and skin friction. Between the central and outboard regions, there are two main high vorticity streams that have little to no high frequency content and present only distinct low frequency dynamics. Also observed in this region were flow instabilities with a crisscross pattern. The latter was not explored further in this study. A cursory examination of the velocity profile under similarity transformation for compressible turbulent boundary layers showed that the viscous sublayer remains close to universal, whereas the log layer significantly departs from classical two-dimensional boundary layer turbulence theory.

For the *perturbed isothermal wall* case, the inlet was perturbed according to acoustic wave theory to simulate turbulence in the freestream environment, and the isothermal wall temperature was chosen according to conjugate heat transfer simulations in a recent study which should be more representative of the flight experiment. The simulations predicted precipitous rises in downstream wall shear stress and wall heat flux mainly in the central and outboard regions indicative of transition-to-turbulence. It was observed that the transition front does not occur at a single axial location but instead is two-dimensional where it varies by axial and spanwise location, concurring with experimental observation. Except for some locations across the span, the predictions of wall shear stress and heat flux were generally lower than that reported from the inflight sensors. It was however noted that the particular flight condition simulated in this study fell within a very unstable flight regime where the flow flip-flops multiple times between laminar and turbulent states producing inordinately large fluctuations in the wall heat flux as indicated by flight sensor data. To improve confidence in the CFD predictions, future work may include simulating a more stable flight condition along the trajectory, as well as interrogate the boundary layer on the various regions on the vehicle, its interaction with the vortical instabilities, and its departure from canonical descriptions.

Chapter 8: Conclusion: Significance of Work

Two hypersonic configurations were studied in this thesis, viz, the canonical Mach 10 Hollow-Cylinder Flare (HCF) and the Mach 6 BoLT-II research vehicle. Wall-Resolved Large Eddy Simulations (WRLES) with a high-bandwidth resolving WENO method and explicit third-order Runge-Kutta time advancement was used to obtain detailed solutions of the flowfields, to include mean data, first and second order turbulent statistics and spectral content. The two configurations each presented a different set of flow physics which were interrogated using a variety of processing techniques. The following is a condensation of the Chapter conclusions previously presented, while highlighting the impact of this research.

The Mach 10 HCF presents a strong shock-boundary layer interaction problem with low-frequency unsteadiness and nonequilibrium turbulence, and represents the procurement of a massive, novel, detailed and time-resolved numerical dataset – very rare in the literature at this Mach number. Two key issues were addressed. Firstly was the low-frequency dynamics of the corner shock-interaction responsible for the separation unsteadiness, shock oscillation, and the large fluctuating pressures and heat flux loads, which are all critical vehicle design considerations. Using a sequence of advanced and customized data processing techniques, that includes spectral analysis, 3D lowpass filtering and topological and eigenvalue-based vortex ID methods, the high-resolution LES flow solutions were reduced to reveal the temporal and spatial character of an energy-dominant Görtler-type centrifugal instability manifested as pairs of counter-rotating vortices across the span, evidence of which has also been found in lower speed shock-separated ramp flows. Spatial and temporal correlations demonstrated that the periodic dilation and contraction of the corner separation bubble was statistically linked to the convection and strength of the centrifugal instabilities. This study provided strong visual and statistical evidence that the

unsteady shock-separation dynamics are driven by the centrifugal instabilities and vice versa, creating a low-frequency feedback loop intrinsic to the corner interaction itself, and thus confirming a long debated hypothesis regarding the origin of the low-frequency unsteadiness observed in many shock-separated high-speed junction flows. This study provided a strong understanding of the underpinning physical mechanisms which will inform future control methods, whether passive or active, that can mitigate any adverse effects of the unsteadiness such as the large degree of peak pressure and peak heat flux fluctuations which can impact vehicle flight dynamics and structural integrity.

Secondly, the nonequilibrium turbulence dynamics in the Mach 10 HCF were investigated in detail. The velocity and thermodynamic fluctuation correlations were analyzed as they pertain to Reynolds Stress Transport, Turbulent Kinetic Energy Transport and Turbulent Heat Flux. A priori performance evaluation of classical single-point closures typically used in RANS and other lower-order modeling approaches demonstrated that while several models fared well in the upstream equilibrium boundary layer, many lack the necessary modeling of physics to capture the turbulence in the nonequilibrium post-shock region. The strong shock interaction amplifies the turbulence transport budgets significantly through the interaction and in the post-shock region, far exceeding that of supersonic and lower speed shock-boundary layer interaction flows. Budgets previously ignored or given less attention in modeling played stronger roles in the nonequilibrium post-shock region and therefore warrant modeling considerations. Many models are typically derived from canonical equilibrium flows, and to a much lesser extent from that of simple nonequilibrium flows. Few high-fidelity studies with shock interactions, both computational and experimental, exist in the literature at hypersonic speeds, especially in the Mach 10 range. This study provides a valued

addition to the literature that will inform future model development in high-speed and nonequilibrium turbulent flows.

The Mach 6 BoLT-II hypersonic research vehicle was aimed at studying boundary layer instabilities, transition, turbulence and aerothermal loads. The geometry presented highly three-dimensional flow gradients, significant bow-shock curvature, multiple vortical instabilities and multiple transition mechanisms. This study represented the first high-fidelity turbulent simulation of the Mach 6 Bolt-II hypersonic vehicle at full scale and at a matching flight condition/Reynolds number. The wall temperature was modeled using data from conjugate heat transfer simulations from a previous study to more accurately replicate the in-flight conditions. Furthermore, the freestream disturbance environment was modelled using stochastic broadband forcing to excite acoustic wave modes so that the vehicle "naturally" selects laminar-to-turbulent transition paths. Wall-Resolved LES solutions of the turbulent environment over the vehicle revealed multiple and distinct large-scale instabilities on top of what is typically seen in broad-frequency turbulence. The vehicle surface was characterized by precipitous rises in downstream vorticity, temperature and skin friction and broadband energy spectra, all indicative of turbulence. A cursory examination of the velocity profile under similarity transformation for compressible turbulent boundary layers showed that the viscous sublayer remained close to universal, whereas the log layer significantly departed from classical two-dimensional turbulence scaling exhibiting nonequilibrium energized by the low-frequency instabilities. This study highlights the complexity of flow phenomena on a full-scale, highly three-dimensional hypersonic vehicle and informs future hi-fidelity approaches for simulating and understanding the flow physics of real-world hypersonic vehicles.

Appendix A

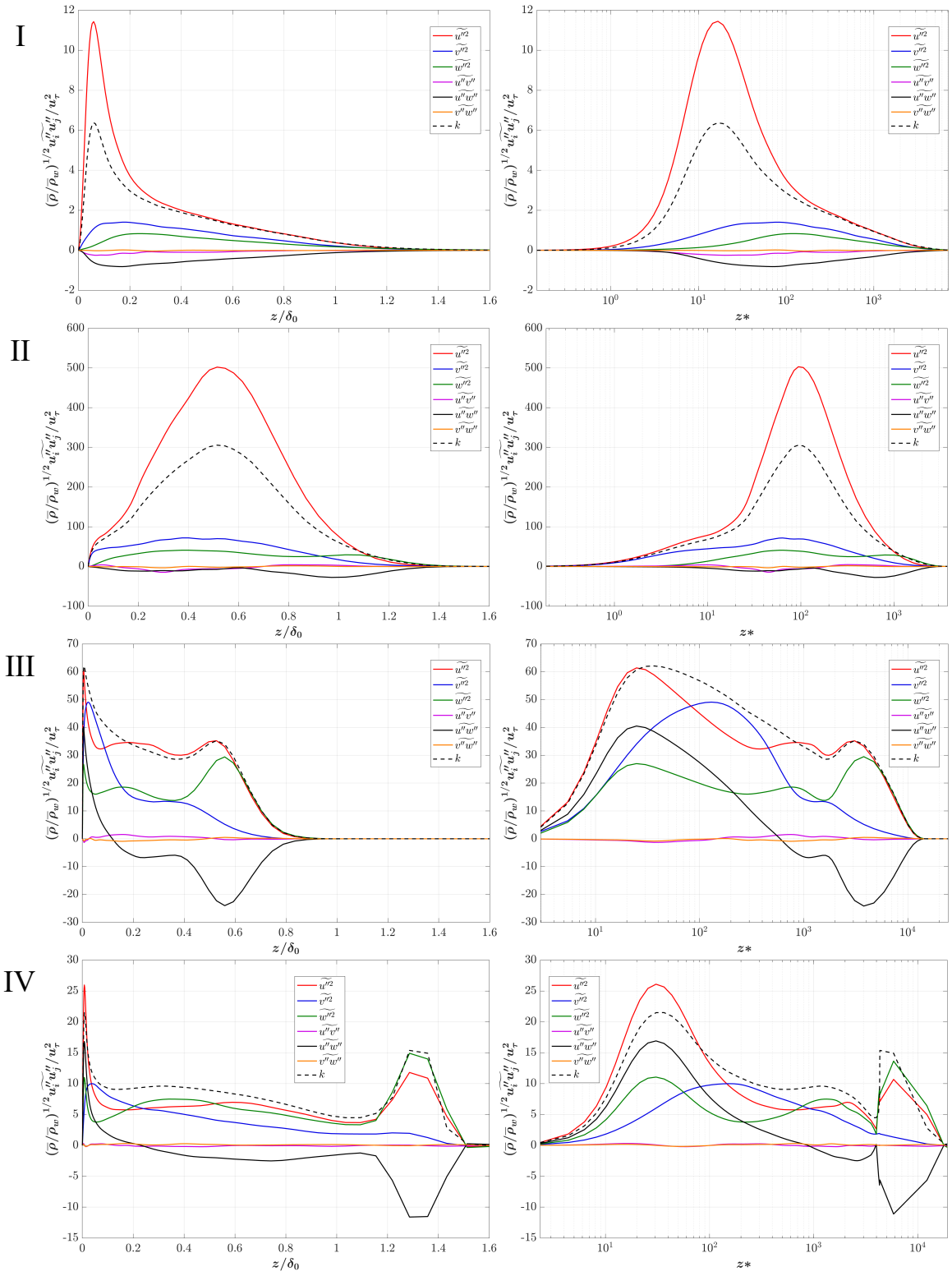


Figure A.1. Reynolds stresses and TKE vs. z/δ (left) and z^* (right), Morkovin scaled.

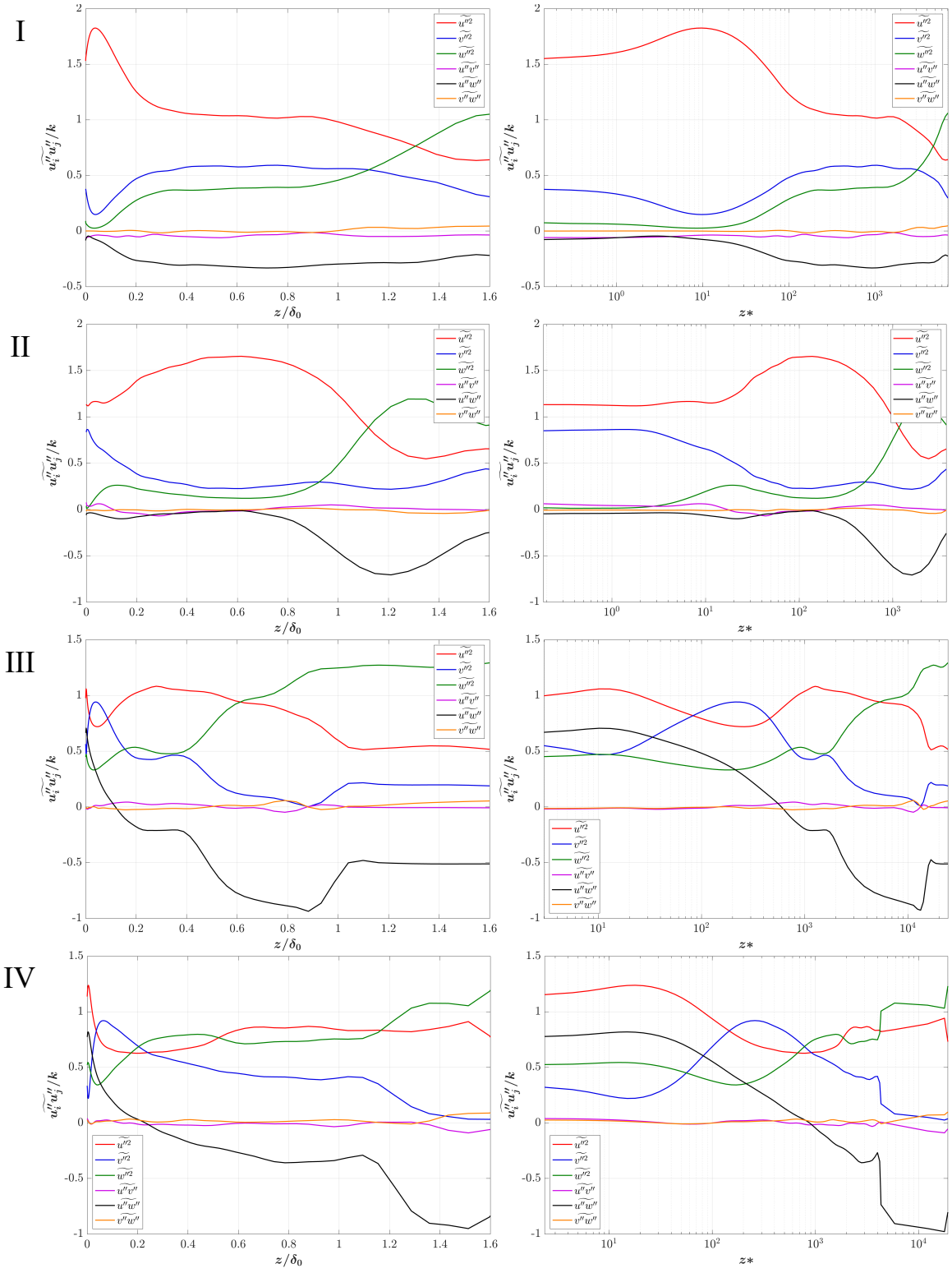


Figure A.2. Reynolds stresses vs. z/δ_0 (left) and z^* (right), TKE scaled.

Appendix B

Several blending functions f_ϵ have been tested for use with dissipation tensor models discussed in Section 6.8.3 . These are listed below. The parameters A_f, E_f, II, III, II_ϵ, III_ϵ and Re_t are as described in Section 6.8.3 . Figure B.1 compares the performance of these blending functions for the three dissipation models compared in this study at the upstream equilibrium station I. Models can be tuned using the empirical constant C_ϵ. Some effort was made to optimize C_ϵ for each model. However, the plots in Figure B.1 used the default values suggested by the references listed below. Nevertheless, the plots indicate the general reliability of the blending functions and the conclusion to use $f_{6\epsilon}$ in this study persisted regardless of optimal C_ϵ. It was also noted that $f_{5\epsilon}$ was not very sensitive to C_ϵ and yielded almost identical results to $f_{6\epsilon}$. The plot denoted by $f_{0\epsilon}$ in the Figure B.1 used no blending, that is, the near-wall correction of the model was applied throughout the wall normal profile without blending to the isotropic condition away from the wall.

No Blending: $f_{0\epsilon} = 1$ [135]

Hanjalić & Launder 1976 [187]: $f_{1\epsilon} = (1 + C_\epsilon Re_t)^{-1}, \quad C_\epsilon = 0.1$ [136]

Lai & So 1990 [188]: $f_{2\epsilon} = e^{-(Re_t/C_\epsilon)^2}, \quad C_\epsilon = 150$ [137]

Launder & Tselipidakis 1991 [168]: $f_{3\epsilon} = e^{-C_\epsilon A_f^2}, \quad C_\epsilon = 20$ [138]

Launder 1996 [189]: $f_{4\epsilon} = (1 + Re_t II/C_\epsilon)^{-2}, \quad C_\epsilon = 150$ [139]

Gerolymos et al. 2012 [160]: $f_{5\epsilon} = 1 - A_f^{\left(1+A_f^2\right)}\left[1 - e^{-\frac{Re_t}{C_\epsilon}}\right], \quad C_\epsilon = 10$ [140]

Hanjalić & Jakirlić 1993 [158]: $f_{6\epsilon} = 1 - A_f^{1/2} E_f^2$ [141]

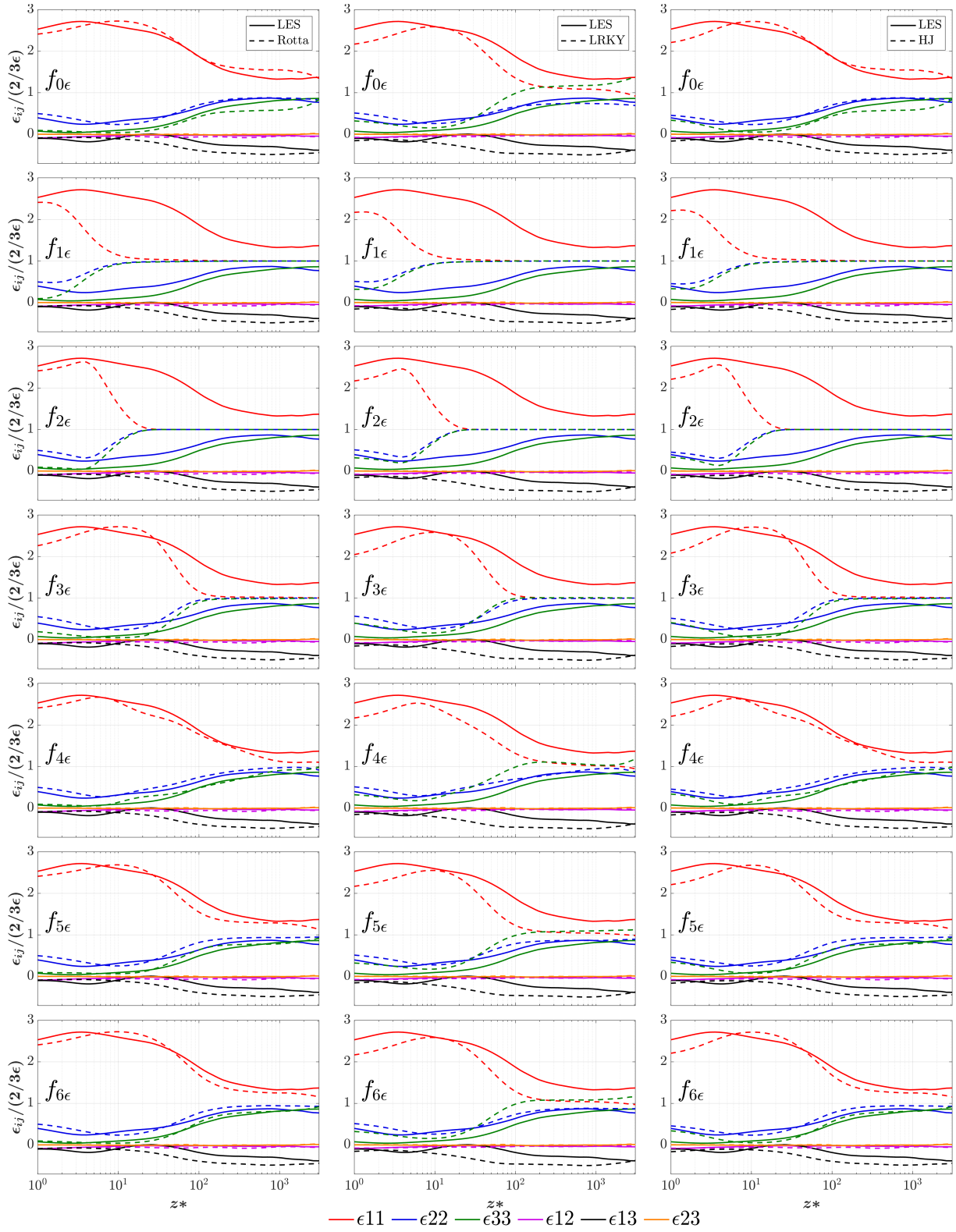


Figure B.1. Blending function f_ϵ assessment for dissipation tensor models at upstream equilibrium station I: Rotta (left), LRKY (middle), HJ (right).

Bibliography

[1] X-43A Development Team, DFRC, NASA, "NASA's X-43A Scramjet Sets Air Speed Record," 29 March 2004, https://apod.nasa.gov/apod/ap040329.html.

[2] NBC News, "Air Force gears up for hypersonic test flight," 9 March 2010, https://www.nbcnews.com/id/wbna35781519.

[3] Leishman, G., "Introduction to Aerospace Engineering," Creative Commons Attribution-NonCommercial-NoDerivatives 4.0 International License, 2022.

[4] Wu, Y., Yi, S., He, L., Chen, Z., and Wang, X., "Experimental Investigations of Supersonic Flow Over a Compression Ramp Based on Nanoparticle-Tracer-Based Plane Laser Scattering Technique," Experimental Techniques, 2014, pp. 651–660.

[5] Boussinesq, J., "Théorie de l'Ecoulement Tourbillant," Mémoires présentés par divers savants à l'Académie des Sciences, France, Vol. 23, pp. 46-50, 1877.

[6] Zuo, F.-Y., Pirozzoli, S., "Recent progress in conical shock wave/boundary layer interaction with spanwise pressure gradient," Propulsion and Power Research, Vol. 13, No. 3, pp. 295-318, 2024.

[7] Gaitonde, D. V., Adler, M. C., "Dynamics of Three-Dimensional Shock-Wave/Boundary-Layer Interactions," Annual Review of Fluid Mechanics, Vol. 55, pp. 291-321, 2023.

[8] Sabnis, K., Zabinsky, H., "A review of three-dimensional shock wave–boundary-layer interactions," Progress in Aerospace Sciences, Vol. 143, 2023.

[9] Gaitonde, D. V., "Progress in shockwave/boundary layer interactions," Progress in Aerospace Sciences, Vol. 72, 2015.

[10] Gnoffo, P. A., Berry, S. A., Norma, J. W. V., "Uncertainty Assessments of Hypersonic Shock Wave–Turbulent Boundary-Layer Interactions at Compression Corners," Journal of Spacecraft and Rockets, Vol. 50, No. 1, 2013.

[11] Blottner, F. G., Roy, C. J., "Review and assessment of turbulence models for hypersonic flows," Progress in Aerospace Sciences, Vol. 42, 2006.

[12] Knight, D., Yana, H., Panarasb, A. G., Zheltovodov, A., "Advances in CFD prediction of shockwave turbulent boundary layer interactions," Progress in Aerospace Sciences, Vol. 39, 2003.

[13] Andreopoulos, Y., Agui, J., Briassulis, G., "Shock wave turbulence interactions," Annual Review of Fluid Mechanics, Vol. 32, pp. 309-345, 2000.

[14] Settles, G. S., Dolling, D. S., "Swept shock-wave/boundary-layer interactions," AIAA Tactical missile aerodynamics: General topics of progress in astronautics and aeronautics, Vol. 141, pp. 505–574, 1992.

[15] Settles, G. S., Dodson, L. J., "Hypersonic shock boundary layer interaction database," NASA Contractor Report 117557, 1991.

[16] Settles, G. S., Dodson, L. J., "Supersonic and hypersonic shock/boundary layer interaction database. AIAA Journal, Vol. 32, pp. 1377–1383, 1994.

[17] Fernholz, H. H., Finley, P. J., Dussauge, J.-P., Smits, A. J., "A survey of measurements and measuring techniques in rapidly distorted compressible turbulent boundary layers," AGARD Report AG-315, 1989.

[18] Fernholz, H. H., Finley, P. J., "A further compilation of compressible turbulent boundary layer data with a survey of turbulence data," AGARD Report AG-263, 1981.

[19] Georgiadis, N. J., Rumsey, C. L., Huang, G. P., "Revisiting Turbulence Model Validation for High-Mach Number Axisymmetric Compression Corner Flows," AIAA Paper 2015-0316, Kissimmee, Florida, 2015.

[20] DeBonis, J. R., Oberkampf, W. L., Wolf, R. T., Orkwis, P. D., Turner, M. G., Babinsky, H., Benek, J. A., "Assessment of Computational Fluid Dynamics and Experimental Data for Shock Boundary-Layer Interactions," AIAA Journal, Vol. 50, No. 4, pp. 891–903, 2012.

[21] Helm, C. M., Martín, M. P., "Large Eddy Simulation of Two Separated Hypersonic Shock/Turbulent Boundary Layer Interactions," Physical Review of Fluids," Vol. 7, No. 7, 2022.

[22] Priebe, S., Martín, M. P., "Turbulence in a hypersonic compression ramp flow," Physical Review of Fluids, Vol. 6, No. 034601, 2021.

[23] Fang, J., Zheltovodov, A., Yao, Y., Moulinec, C., Emerson, D., "On the turbulence amplification in shock-wave/turbulent boundary layer interaction," Journal of Fluid Mechanics, Vol. 897, 2020.

[24] Vyas, M. A., Yoder, D. A., Gaitonde, D. V., "Reynolds-Stress Budgets in an Impinging Shock-Wave/Boundary-Layer Interaction," AIAA Journal, Vol. 57, No. 11, 2019.

[25] Morgan, B., Duraisamy, K., Nguten N., Kawai, S., Lele, S., "Flow physics and RANS modelling of oblique shock/turbulent boundary layer interaction," Journal of Fluid Mechanics, Vol. 729, 2013.

[26] Wu, M., Martín, M. P., "Direct Numerical Simulation of Supersonic Turbulent Boundary Layer over a Compression Ramp," AIAA Journal, Vol. 45, No. 4, 2007.

[27] Pirozzoli, S., Grasso, F., "Direct numerical simulation of impinging shock wave/turbulent boundary layer interaction at M=2.25," Physics of Fluids, Vol. 18, No. 6, 2006.

[28] Loginov, M. S., Adams, N. A., Zheltovodov, A. A., "Large-eddy simulation of shock-wave/turbulent-boundary-layer interaction," Journal of Fluid Mechanics, Vol. 565, 2006.

[29] Dussauge, J.-P., Dupont, P. & Debiève, J.-F., "Unsteadiness in shock wave boundary layer interactions with separation," Aerospace Science Technology, Vol. 10, No. 2, pp. 85–91, 2006.

[30] Humble, R. A., Elsinga, G. E., Scarano, F., and van Oudheusden, B. W., "Three-dimensional instantaneous structure of a shock wave/turbulent boundary layer interaction," Journal of Fluid Mechanics, Vol. 622, pp. 33–62, 2009.

[31] Ganapathisubramani, B., Clemens, N. T., Dolling, D. S., "Effects of upstream boundary layer on the unsteadiness of shock-induced separation," Journal of Fluid Mechanics, Vol. 585, pp. 369–394, 2007.

[32] Ganapathisubramani, B., Clemens, N. T., and Dolling, D. S., "Low-frequency dynamics of shock-induced separation in a compression ramp interaction," Journal of Fluid Mechanics, Vol. 636, pp. 397–425, 2009.

[33] Beresh, S. J., Clemens, N. T., and Dolling, D., "Relationship between upstream turbulent boundary-layer velocity fluctuations and separation shock unsteadiness," AIAA Journal, Vol. 40, No. 12, pp. 2412–2422, 2002.

[34] Priebe, S. and Martín, M. P., "Low-frequency unsteadiness in shock wave-turbulent boundary layer interaction," Journal of Fluid Mechanics, Vol. 699, 2012, pp. 1–49.

[35] Priebe, S., Tu, J., Martín, M. P., and Rowley, C. W., "Low-frequency dynamics in a shock-induced separated flow," Journal of Fluid Mechanics, Vol. 807, 2016, pp. 441–477.

[36] Helm, C. M., Martín, M. P., "Görtler-like vortices in the LES Data of a Mach 7 STBLI," AIAA Paper 2017-0762, 2017.

[37] Martín, M., Helm, C., and Gonzalez-Kosasky, S., "The Centrifugal Instability of Shock- Induced Separated Flows," Symposium on the Frontiers of Turbulent Flows, Denver, Co., 2017.

[38] Trichilo, J., Helm, C. M., Martín, P. M., "Persistence of a Centrifugal Instability in Shock-separated Flows at Mach 3 through 10," AIAA Paper 2019-1130, San Diego, California, 2019.

[39] Martín, M. P., Priebe, S., and Helm, C., "Upstream and Downstream Influence on STBLI Instability," 46th Fluid Dynamics Conference, AIAA Paper No. 2016-3344, 2016.

[40] Görtler, H., "Instabilit¨at laminarer Grenzschichten an konkavenW¨anden gegen¨uber gewissen dreidimensionalen Störungen," ZAMM, Vol. 21, No. 4, 1941, pp. 250–252.

[41] Görtler, H., "On the Three-Dimensional Instability of Laminar Boundary Layers on Concave Walls," NACA-TM-1375, 1955.

[42] Martín, M. P., Piomelli, U., and Candler, G. V., "Subgrid-scale Models for Compressible LES," Theoretical and Computational Fluid Dynamics, Vol. 13, 2000.

[43] Martín, M. P., Taylor, E. M., Wu, M., and Weirs, V. G., "A Bandwidth-Optimized WENO Scheme for the Direct Numerical Simulation of Compressible Turbulence," Journal of Computational Physics, Vol. 220, 2006, pp. 270–289.

[44] Taylor, E. M., Martín, M. P., "Stencil Adaptation Properties of a WENO Scheme in Direct Numerical Simulations of Compressible Turbulence," Journal of Scientific Computing, Vol. 30, No. 3, 2007.

[45] Taylor, E. M., Wu, M., Martín, M. P., "Optimization of nonlinear error for weighted essentially non-oscillatory methods in direct numerical simulations of compressible turbulence," Journal of Computational Physics, Vol. 223, 2007, pp. 384–397.

[46] Grube, N. E., Martín, M. P., "Assessment of WENO Methods with Shock-Confining Filtering for LES of Compressible Turbulence," 18th AIAA Computational Fluid Dynamics Conference, AIAA 2007-4198, 2007.

[47] Grube, N. E., Martín, M. P., "Assessment of Subgrid-Scale Models and Shock-Confining Filters in Large-Eddy Simulation of Highly Compressible Isotropic Turbulence," 47th Aerospace Sciences Meeting, AIAA 2009-947, 2009.

[48] Priebe, S. and Martín, M. P., "Direct Numerical Simulation of a Reflected Shock-Wave/Turbulent Boundary Layer Interaction," AIAA Journal, Vol. 47, No. 5, 2009.

[49] Duan, L., Beekman I., Martín, P., "Direct numerical simulation of hypersonic turbulent boundary layers. Part 2. Effect of wall temperature," Journal of Fluid Mechanics, Vol. 655, 2010, pp. 419-445, 2010.

[50] Duan, L., Beekman I., Martín, P., "Direct numerical simulation of hypersonic turbulent boundary layers. Part 3. Effect of Mach number," Journal of Fluid Mechanics, Vol. 672, 2011, pp. 245-267, 2011.

[51] Leonard, A., "Energy Cascade in Large-Eddy Simulations of Turbulent Fluid Flows," Advances in Geophysics 18A:237-248, 1974.

[52] Sutherland, W., "The Viscosity of Fluids and Molecular Force," Philosophical Magazine, S. 5, Vol 36, pp. 507-531, 1893.

[53] Keyes, F. G., "A summary of viscosity and heat-conduction data for He, A, H2, O2, CO, CO2, H2O, and air," Transactions of the American Society of Mechanical Engineers, Vol. 73, No. 7, 1951, pp. 589–596.

[54] Smagorinsky, J., "General circulation experiments with the primitive equations. I. The basic experiment," Monthly Weather Review, Vol. 91, No. 3, 1963.

[55] Knight, D., Zhou, G., Okong'o, N., and Shukla, V., "Compressible Large Eddy Simulation using Unstructured Grids," AIAA Paper No. 1998-0535, 1998.

[56] Jiang G.-S., Shu, C.W., “Efficient implementation of weighted ENO schemes,” Journal of Computational Physics, Vol. 126, No. 1, pp. 202–228, 1996.

[57] Rusanov V. V., “Calculation of interaction of non-steady shock waves with obstacles,” USSR Journal of Computational Mathematics and Mathematical Physics, Vol 1, pp. 267–79, 1961.

[58] Williamson, J. H., “Low-storage Runge-Kutta schemes,” Journal of Computational Physics, Vol. 35, No. 1, 1980, pp. 48–56.

[59] Adams, N.A., " Direct Numerical Simulation of Turbulent Compression Ramp Flow," Theoretical and Computational Fluid Dynamics, Vol. 12, No. 2, 1998, pp. 109-129.

[60] Martín, M. P., Xu, S., Wu, M., “Preliminary Work on DNS and LES of STBLI,” 33rd AIAA Fluid Dynamics Conference, Orlando FL, AIAA 2003-3464, June 2003.

[61] Wu, M, “Direct Numerical Simulation of Shockwave and Turbulent Boundary Layer Interactions,” PhD Thesis, Princeton University, 2007.

[62] Xu, S., Martín, M. P., “Assessment of inflow boundary conditions for compressible turbulent boundary layers,” Physics of Fluids, Vol. 16, No. 7, July 2004.

[63] Helm, C. M., “Direct and Large-Eddy Simulation and Analysis of Shock-Separated Flows,” PhD Thesis, University of Maryland, 2021.

[64] Brooks, J., Gupta, A., Helm, C., Martín, M., Smith, M., and Marineau, E., “Mach 10 PIV Flow Field Measurements of a Turbulent Boundary Layer and Shock Turbulent Boundary Layer Interaction,” 33rd Aerodynamic Measurement Technology and Ground Testing Conference, AIAA Paper No. 2017-3325, 2017.

[65] Brooks, J., “Development and Application of Mach 10 PIV in a Large Scale Wind Tunnel,” PhD Thesis, University of Maryland, 2018

[66] Van Driest, E. R., “Turbulent Boundary Layer in Compressible Fluids,” Journal of Aeronautical Sciences, Vol. 18, No. 3, 1951, pp. 145-160

[67] Morkovin, M.V., “Effects of compressibility on turbulent flows,” In A. Favre (Ed.), Méchanique de la Turbulence, CNRS, Paris, France, pp. 367–380, 1962.

[68] Huang, P. G., Coleman, G. N., Bradshaw, P., “Compressible turbulent channel flows: DNS results and modeling,” Journal of Fluid Mechanics, Vol. 305, pp. 185–218, 1995.

[69] Coleman, G. T., “Hypersonic Turbulent Boundary Layer Studies,” PhD Thesis, Univ. of London, 1973.

[70] Wu, M. and Martín, M.P., “Analysis of Shock Motion in STBLI using Direct Numerical Simulation Data,” Journal of Fluid Mechanics, 594, 71-83, 2008.

[71] Dupont, P., Haddad, C., and Debieve, J. F., “Space and time organization in a shock-induced separated boundary layer,” Journal of Fluid Mechanics, Vol. 559, 2006, pp. 255–277.

[72] Thomas, F. O., Putnam, C. M., Cho, M. C., “On the mechanism of unsteady shock oscillation in shock wave/turbulent boundary layer interactions,” Experiments in Fluids, Vol. 18, No. 1–2, pp. 69-81, 1994.

[73] Erengil, M. E. and Dolling, D. S., “Unsteady Wave Structure near Separation in a Mach 5 Compression Ramp Interaction,” AIAA Journal, Vol. 29, No. 5, 1991, pp. 728–735.

[74] Piponniau, S., Dussauge, J. P., Debieve, J. F., Dupont, P., “A simple model for low-frequency unsteadiness in shock-induced separation,” J. Fluid Mech., Vol. 629, pp. 87-108, 2009.

[75] Helm C. M., Martín, M. P., “Characterization of the shear layer in separated shock/turbulent boundary layer interactions,” J. of Fluid Mechanics, Vol. 912, A7, 2021.

[76] Cao, S., Klioutchnikov, I., Olivier, H., "Görtler Vortices in Hypersonic Flow on Compression Ramps," AIAA Journal, Vol. 57, No. 9, 2019.

[77] Roghelia, A., Olivier, H., Egorov, I., Chuvakhov, P., "Experimental investigation of Görtler vortices in hypersonic ramp flows," Experimental Fluids, Vol. 58, 2017.

[78] Schülein, E, Trofimov, V. M., "Steady longitudinal vortices in supersonic turbulent separated flows," Journal of Fluid Mechanics, Vol 672, pp. 451-476, 2011.

[79] Brown, L. M., Boyce, R. R., Mudford, N., O'Byrne. S., "Intrinsic three-dimensionality of laminar hypersonic shock wave/ boundary layer interactions," AIAA Paper 2009-7205, Bremen, Germany, 2009.

[80] Navarro-Martínez, S., Tutty, O. R., "Numerical simulation of Go¨ rtler vortices in hypersonic compression ramps," Computers & Fluids, Vol. 34, pp. 225–247, 2005.

[81] Settles. G. S., Fitzpatrick, T. J., Bogdonoff, S. M., "Detailed Study of Attached and Separated Compression Corner Flowfields in High Reynolds Number Supersonic Flow," AIAA Journal, Vol 17, No. 6, 1979.

[82] Welch, P. W., "The use of Fast Fourier Transform for the estimation of power spectra: A method based on time averaging over short, modified periodograms," IEEE Transactions on Audio and Electroacoustics, Vol. AU-15, No. 2, 1967, pp. 70–73.

[83] Rayleigh, Lord, "On the Dynamics of Revolving Fluids," Proceedings of the Royal Society of London, Vol. 93, No. 648, pp. 148-154, 1917.

[84] Bayly, B. J., "Three-dimensional centrifugal-type instabilities in inviscid two dimensional flows," Physics of Fluids Vol. 3, No. 1, pp. 56-64, 1987.

[85] Floryan, J. M., "Gorder Instability of boundary layers over concave and convex walls," Physics of Fluids Vol. 29, No. 8, pp. 2380—2387, 1986.

[86] Saric, W. S., "Görtler Vortices," Annual Review Fluid Mechanics, 1994, 26:379-409.

[87] Taylor, G. I., "Stability of a viscous liquid contained between two rotating cylinders," Proceedings of the Royal Society of London, Vol. 102, No. 178, 1973.

[88] Tagg, R., "A guide to literature related to the Taylor-Couette problem," Proceedings of NATO Adv. Res. Workshop, New York, 1992.

[89] Dean, W. R., "Fluid motion in a curved channel," Proceedings of the Royal Society of London, Vol. 121, No. 787, 1928.

[90] Guo, Y., Finlay, W. H., "Wavenumber selection and irregularity of spatially developing nonlinear Dean and Görtler vortices," J. of Fluid Mechanics, Vol. 264, pp. 1-40, 1994.

[91] Floryan, J. M., "On the Görtler instability of boundary layers," Progress in Aerospace Sciences, Vol. 28, 1991, pp. 235–271.

[92] Tani, I., "Production of longitudinal vortices in the boundary layer along a concave wall," Journal of Geophysical Research, Vol. 67, No. 8, pp. 3075-3080, 1962.

[93] Smits, A. J., Dussauge, J. P., "Turbulent Shear Layers in Supersonic Flow," 2nd Edition, Springer, 2006.

[94] Clauser, F. H., "The Turbulent Boundary Layer," Advances in Applied Mechanics, Vol. 4, pp. 1-51, 1956.

[95] Epps, B. P., "Review of Vortex Identification Methods," AIAA Paper 2017-0989, 2017

[96] Michard, M., Graftieaux, L., Lollini, L., Grosjean, N., "Identification of vortical structures by a non-local criterion - Application to PIV measurements and DNS-LES results of turbulent rotating flows," Symposium on Turbulent Shear Flows, 11th, Grenoble, France, 1997.

[97] Graftieaux, L., Michard, M., and Grosjean, N., “Combining PIV, POD and vortex identification algorithms for the study of unsteady turbulent swirling flows,” Measurement Science and Technology, Vol. 12, 2001, pp. 1422–1429.

[98] Dupont, P., Piponniau, S., Sidorenko, A., Debiève, J. F., “Investigation by particle image velocimetry measurements of oblique shock reflection with separation,” AIAA Journal, Vol. 46 (6), pp. 1365–1370, 2008.

[99] Chong, M. S., Perry, A. E., and Cantwell B. J., “A general classification of three dimensional flowfields," Physics of Fluids, Vol. 2, No. 5, 1990, pp. 765-777.

[100] Haimes, R., Kenwright, D., “On the Velocity Gradient Tensor and Fluid Feature Extraction,” AIAA Paper 99-3288, 1999.

[101] Zhou, J., Adrian, R. J., Balachandar, S., and Kendall, T. M., “Mechanisms for generating coherent packets of hairpin vortices in channel flow," Journal of Fluid Mechanics, Vol. 387, 05 1999, pp. 353-396.

[102] Prandtl, L., “Bericht uber Untersuchungen zur ausgebildeten Turbulenz,” Z. Angew, Math. und Mech., Vol. 5, pp. 136–139, 1925.

[103] Cebeci, T., Smith A. M. O., “Analysis of Turbulent Boundary Layers,” Series in Applied Math. & Mech., Academic Press, Vol. 15, 1974.

[104] Baldwin, B. S., Lomax, H., “Thin-Layer Approximation and Algebraic Model for Separated Turbulent Flows,” AIAA Paper 1978-257, Huntsville, Alabama, 1978.

[105] Johnson, D. A., King, L. S., “A mathematically simple turbulence closure model for attached and separated turbulent boundary layers,” AIAA Journal, Vol. 23, No. 11, 1985.

[106] Johnson, D. A., “Transonic separated flow predictions with an eddy-viscosity/Reynolds-stress closure model,” AIAA Journal, Vol. 25, No. 2, 1987.

[107] Johnson, D. A., Coakley, T. J., “A mathematically simple turbulence closure model for attached and separated turbulent boundary layers,” AIAA Journal, Vol. 28, No. 11, 1990.

[108] Prandtl, L., “Über ein neues Formelsystem für die ausgebildete Turbulenz,” Akademie der Wissenschaften, Göttingen, Math-Phys. Kl., Vol. 5, pp, 6-19, 1945.

[109] Emmons, H. W., “Shear Flow Turbulence,” Proceedings of the 2nd U.S. Congress of Applied Mechanics, ASME, 1954.

[110] Glushko, G., “Turbulent Boundary Layer on a Flat Plate in an Incompressible Fluid,” Izvestia Academy Nauk. SSSR Mekh., No. 4, pp. 13, 1965.

[111] Wolfshtein, M., “Convection Processes in Turbulent Impinging Jets,” Imperial College, Heat Transfer Section Report SF/R/2.

[112] Bradshaw P., Ferriss D. H., Atwell N. P., “Calculation of Boundary-Layer Development using the Turbulent Energy Equation,” AIAA Journal of Fluid Mechanics, Vol. 28, pp. 593-616, 1967.

[113] Goldberg, U. C., “Derivation and testing of a one-equation model based on two time scales,” AIAA Journal, Vol. 29, No. 8, 1991.

[114] Baldwin, B. S., Barth, T. J., “A One-Equation Turbulence Transport Model for High Reynolds Number Wall-Bounded Flows,” NASA TM-102847.

[115] Spalart, P., Allmaras, S., “A One-Equation Turbulence Model for Aerodynamic Flows,” AIAA Paper 1992-439, Reno, Nevada, 1992.

[116] Han, X., Rahman, M. M., Agarwal, R. K., “Development and Application of a Wall Distance Free Wray-Agarwal Turbulence Model (WA2018),” AIAA Paper 2018-0593, Kissimmee, Florida, 2018.

[117] Jones, W., Launder, B., "The Prediction of Laminarization with a Two-Equation Model of Turbulence," International Journal of Heat and Mass Transfer, Vol. 15, pp. 301-314, 1972.

[118] Launder, B. E., Sharma, B. I., "Application of the energy-dissipation model of turbulence to the calculation of flow near a spinning disc," Letters in Heat and Mass Transfer, Vol. 1, No. 2, pp. 131-138, 1974.

[119] Chien, K.-Y., "Predictions of Channel and Boundary-Layer Flows with a Low-Reynolds-Number Turbulence Model," AIAA Journal, Vol. 20, No. 1, 1982.

[120] Shih, T. H., Liou, W. W., Shabir, A., Yang, Z., Zhu, J., "A New k-e Eddy Viscosity Model for High Reynolds Number Turbulent Flows-Model Development and Validation", NASA TM-106721, ICOMP-94-21, CMOTT-94-6, 1994.

[121] Yakhot, V., Orszag, S.A., Thangam, S., Gatski, T.B. & Speziale, C.G., "Development of turbulence models for shear flows by a double expansion technique," Physics of Fluids, Vol. 4, No. 7, pp. 1510-1520, 1992.

[122] Menter, F. R., "Two-Equation Eddy-Viscosity Turbulence Models for Engineering Applications," AIAA Journal, Vol. 32, No. 8, pp. 1598-1605, 1994.

[123] Wilcox, D. C., "Formulation of the k-omega Turbulence Model Revisited," AIAA Journal, Vol. 46, No. 11, pp. 2823-2838, 2008.

[124] Goldberg, U., Peroomian, O., Batten, P., Chakravarthy, S., "The k-ϵ-R_t Turbulence Closure," Engineering Applications of Computational Fluid Mechanics Vol. 3, No. 2, pp. 175–183, 2009.

[125] Durbin, P. A., "Separated Flow Computations with the k-ϵ-v^2 Model," AIAA Journal, Vol. 33, No. 4, 1995.

[126] Hanjalic, K., Popovac, M., Hadziabdic, M., "A robust near-wall elliptic-relaxation eddy-viscosity turbulence model for CFD," International Journal of Heat and Fluid Flow, Vol. 25, pp. 1047–1051, 2004.

[127] Hamlington, P. E., Dahm, W. J. A., "Reynolds stress closure for nonequilibrium effects in turbulent flows," Physics of Fluids Vol. 20, No. 11, 2008.

[128] Lien, F. S., Chen, W.L., Leschziner, M. A., "Low-Reynolds-Number Eddy-Viscosity Modelling Based on Non-Linear Stress-Strain/Vorticity Relations," Engineering Turbulence Modelling and Experiments 3, pp. 91–100, 1996.

[129] Olsen, M., Coakley, T., "The lag model, a turbulence model for nonequilibrium flows," AIAA Paper 2001-2564, Anaheim, California, 2001.

[130] Hellsten, A., "New Advanced k-omega Turbulence Model for High-Lift Aerodynamics," AIAA Journal, Vol. 43, No. 9, pp. 1857-1869, 2005.

[131] Abdol-Hamid, K. S., "Development and Documentation of kL-Based Linear, Nonlinear, and Full Reynolds Stress Turbulence Models," NASA TM-2018-219820, 2018.

[132] Chou, P. Y., "On the Velocity Correlations and the Solution of the Equations of Turbulent Fluctuation," Quart. Appl. Math, Vol. 3, pp. 38, 1945.

[133] Rotta, J., "Statistische Theorie nichthomogener Turbulenz," Zeitschrift fur Physik, Vol. 129, pp. 547-572, 1951.

[134] Wilcox, D. C., "Turbulence Modeling for CFD," 3rd Edition, DCW Industries, Inc., La Canada CA, 2006.

[135] Pope, S. B., "Turbulent Flows," Cambridge university Press, UK, 2000.

[136] Coleman, G. N., Kim, J., Moser, R. D., "A numerical study of turbulent supersonic isothermal-wall channel flow," Journal of Fluid Mechanics, Vol. 305, pp. 159–183, 1995.

[137] Maeder, T., Adams, N. A., Kleiser, L., "Direct simulation of turbulent supersonic boundary layers by an extended temporal approach," Journal of Fluid Mechanics, Vol. 429, pp. 187-216, 2001.

[138] Morinishi, Y., Tamano, S., Nakabayashi, K., "Direct numerical simulation of compressible turbulent channel flow between adiabatic and isothermal walls," Journal of Fluid Mechanics, Vol. 502, pp. 273-308, 2004.

[139] Lumley, J., Newman, G., "The return to isotropy of homogeneous turbulence," Journal of Fluid Mechanics, Vol. 82, Part 1, pp. 161-178, 1977.

[140] Lumley, J., "Pressure–strain correlation," Physics of Fluids, Vol. 18, No. 750, 1975.

[141] Sarkar, S., Lakshmanan, B., "Application of a Reynolds stress turbulence model to the compressible shear layer," AIAA Journal, Vol. 29, pp. 743–749, 1991.

[142] Gatski, T. B., Bonnet, J.-P., "Compressibility Turbulence and High Speed Flow," 2nd Edition, Elsevier Inc., UK, 2013.

[143] Sarkar, S., Erlebacher, G., Hussaini, M. Y., "Compressible Homogeneous Shear: Simulation and Modeling," Turbulent Shear Flows 8, Springer-Verlag, Berlin, Heidelberg, pp. 249-267, 1992.

[144] Blaisdell, G. A., Mansour, N. N., Reynold, W. C, "Compressibility effects on the growth and structure of homogeneous turbulent shear flow," Journal of Fluid Mechanics, Vol. 256, pp. 443-485, 1993.

[145] Zhang, C., Duan, L., "Direct Numerical Simulation Database for Supersonic and Hypersonic Turbulent Boundary Layers," AIAA Journal, Vol. 56, No. 11, 2018.

[146] Vreman, A. W., Sandham, N. D., Luo, K. H., "Journal of Fluid Mechanics, Vol. 320, pp. 235-258, 1996.

[147] Zeman, O., "Dilatation dissipation: The concept and application in modeling compressible mixing layers," Physics of Fluids, Vol. 2, 178-188, 1990.

[148] Sarkar, S., Erlebacher, G., Hussaini, M. Y., Kreiss, H. O., "The analysis and modelling of dilatational terms in compressible turbulence," Journal of Fluid Mechanics, Vol. 227, pp. 473-493, 1991.

[149] Wilcox, D. C., "Dilatation-dissipation corrections for advanced turbulence models," AIAA Journal, Vol. 30, 1992.

[150] Pirozzoli, S., Grasso, F., "Direct numerical simulations of isotropic compressible turbulence: Influence of compressibility on dynamics and structures," Physics of Fluids, Vol. 16, No. 12, 2004.

[151] Ristorcelli, J. R., "A pseudo-sound constitutive relationship for the dilatational covariances in compressible turbulence," Journal of Fluid Mechanics, Vol. 347, pp. 37-70, 1997.

[152] Barone, M. F., Oberkampf, W. L., Blottner, F. G., "Validation case study: Prediction of compressible turbulent mixing layer growth rate," AIAA Journal, Vol. 44, pp. 1488–1497, 2006.

[153] Sarkar, S., "The stabilizing effect of compressibility in turbulent shear flow," Journal of Fluid Mechanics, Vol. 282, pp. 163-186, 1995.

[154] Lumley, J. L., "Computational Modeling of Turbulent Flows," Advances in Applied Mechanics, Vol. 18, pp. 123–176, 1979.

[155] Spalart, P. R., "Direct simulation of a turbulent boundary layer up to R_θ=1410," Journal of Fluid Mechanics, Vol. 187, pp. 61–98, 1988.

[156] Launder, B. E., Reynolds, W. C., "Asymptotic near-wall stress dissipation rates in a turbulent flow," Physics of Fluids, Vol. 26, pp. 1157–1158, 1983.

[157] Kebede, W., Launder, B. E., Younis, B. A., "Large-amplitude periodic pipe flow: a second-moment closure study," Proceedings of 5th Symposium on Turbulent Shear Flows, pp. 16.23–16.29, Ithaca, NY, 1985.

[158] Hanjalić, K. and S. Jakirlić, "A model of stress dissipation in second moment closures," Applied Scientific Research, Vol. 51, pp. 513–518, 1993.

[159] Craft, T. J. and B. E. Launder, "A Reynolds stress closure designed for complex geometries," International Journal of Heat Fluid Flow, Vol. 17, pp. 245–254, 1996.

[160] Gerolymos, G. A., Lo, C., Vallet, I., Younis, B. A., "Term-by-Term Analysis of Near-Wall Second-Moment Closures," AIAA Journal, Vol. 50, No. 12, 2012.

[161] Zeman, O., "The role of pressure-dilatation correlation in rapidly compressed turbulence and in boundary layers," Annual Research Briefs, Center for Turbulence Research, Stanford University, pp. 105–117, 1991.

[162] Durbin, P.A., Zeman, O. "Rapid distortion theory for homogeneous compressed turbulence with application to modeling," Journal of Fluid Mechanics, Vol. 242, 1992.

[163] Zeman, O., Coleman, G. N., "Compressible turbulence subjected to shear and rapid compression," Proceedings of the 8th Symposium on Turbulent Shear Flows, pp. 283–296, Heidelberg, Germany, Springer-Verlag, 1993.

[164] Zeman, O., "A New Model for Super/Hypersonic Turbulent Boundary Layers," AIAA Paper 1993-0897, Reno, Nevada, 1993.

[165] Simone, A., Coleman, G. N., Cambon, C., "The effect of compressibility on turbulent shear flow: a rapid-distortion-theory and direct-numerical-simulation study," Journal of Fluid Mechanics, Vol. 330, pp. 307-338, 1997.

[166] Launder, B. E., G. J. Reece, and W. Rodi, "Progress in the development of a Reynolds-stress turbulence closure," Journal of Fluid Mechanics, Vol 68, pp. 537–566, 1975.

[167] Speziale, C. G., Sarkar, S., Gatski, T. B., "Modelling the pressure–strain correlation of turbulence: an invariant dynamical systems approach, Journal of Fluid Mechanics, Vol. 227, pp. 245–272, 1991.

[168] Launder, B., Tselepidakis, D., "Directions in second-moment modelling of near-wall turbulence," AIAA Paper 1991-219, Reno, Nevada, 1991.

[169] Gibson, M. M., B. E. Launder, "Ground effects on pressure fluctuations in the atmospheric boundary layer," Journal of Fluid Mechanics, Vol. 86, pp. 491–511, 1978.

[170] Launder, B. E., Shima, N., "Second-Moment Closure for the Near-Wall Sublayer: Development and Application," AIAA Journal, Vol. 27, No. 10, pp. 1319–1325, 1989.

[171] Gerolymos, G. A., and Vallet, I., "Wall-Normal-Free Near-Wall Reynolds-Stress Closure for 3-D Compressible Separated Flows," AIAA Journal, Vol. 39, No. 10, pp. 1833–1842, 2001.

[172] So, R. M. C., Aksoy, H., Yuan, S. P., and Sommer, T. P., "Modeling Reynolds-Number Effects in Wall-Bounded Turbulent Flows," Journal of Fluids Engineering, Vol. 118, pp. 260–267, 1996.

[173] Suga, K., "Modeling the Rapid Part of the Pressure-Diffusion Process in the Reynolds Stress Transport Equation," Journal of Fluids Engineering, Vol. 126, July 2004, pp. 634–641.

[174] Jakirlić, S., Eisfeld, B., Jester-Zürker, R., and Kroll, N., "Near-Wall Reynolds-Stress Model Calculations of Transonic Flow Configurations Relevant to Aircraft Aerodynamics," International Journal of Heat and Fluid Flow, Vol. 28, pp. 602–615, 2007.

[175] Durbin, P. A., "A Reynolds stress model for near-wall turbulence," Journal of Fluid Mechanics, Vol. 249, pp. 465–498, 1993.

[176] Pirozzoli, S., Grasso, F., Gatski, T. B., "Direct numerical simulation and analysis of a spatially evolving supersonic turbulent boundary layer at M=2.25," Physics of Fluids, Vol. 16, pp. 530-545, 2004.

[177] Gaviglio, J., "Reynolds analogies and experimental study of heat transfer in the supersonic boundary layer," International Journal of Heat and Mass Transfer, Vol. 30, pp. 911–926, 1987.

[178] Rubesin, M. W., "Extra compressibility terms for Favre-averaged two-equation models of inhomogeneous turbulent flows," NASA Contractor Report 177556, 1990.

[179] Kolmogorov, A. N., "Dissipation of energy in locally isotropic turbulence," Doklady Akademii Nauk SSSR, Vol. 32, pp. 16-18, 1941.

[180] Durbin, P. A., "Near-Wall Turbulence Closure Modeling Without Damping Functions," Theoretical Computational Fluid Dynamics, Vol. 3, pp. 1-13, 1991.

[181] Rodi, W. and N. N. Mansour, "Low Reynolds number k–ε modelling with the aid of direct numerical simulation data," Journal of Fluid Mechanics, Vol. 250, pp. 509–529, 1993.

[182] Figueiredo, J. R., "A Statistical Dynamic Model for the Turbulent Transport of Kinetic Energy in Shear Layers," Journal of Aerospace Technology Management, Vol. 10, 2018.

[183] Daly, B. J., Harlow, F. H., "Transport Equations in Turbulence," Physics of Fluids, Vol. 13, Issue 11, pp. 2634-2649, 1970.

[184] Hanjalić, K., Launder, B. E., "A Reynolds stress model of turbulence and its application to thin shear flows Journal of Fluid Mechanics, Vol. 52, pp. 609–638, 1972.

[185] Younis, B. A., Gatski, T. B., Speziale, C. G., "Towards a rational model for the triple velocity correlations of turbulence," Proceedings of the Royal Society of London A, Vol. 456, Issue 1996, 2000.

[186] Abe, K., Suga, K., "Towards the Development of a Reynolds-averaged Algebraic Turbulent Scalar-Flux Model," International Journal of Heat and Fluid Flow, Vol. 22, pp. 19-29, 2001.

[187] Hanjalić, K., Launder, B. E., "Contribution towards a Reynolds-stress closure for low-Reynolds-number turbulence," Journal of Fluid Mechanics, Vol. 74, pp. 593–610, 1976.

[188] Lai, Y. G., So, R. M. C., "Near-wall modelling of turbulent heat fluxes," International Journal of Heat and Mass Transfer, Vol. 33, pp. 1429–1440, 1990.

[189] Launder, B. E., "An introduction to single-point closure methodology," Simulation and Modeling of Turbulent Flows, Chapter 6, pp. 243–310, Oxford University Press, New York, 1996.

[190] Leyva, I. A., Cummings, R. M., "Introduction to the Special Section on the Boundary Layer Transition (BoLT) Flight Experiment," Journal of Spacecraft and Rockets, Vol. 58, No. 1, 2021, pp. 4–5. doi:10.2514/1.A34872.

[191] Wheaton, B. M., Berridge, D. C., Wolf, T. D., Araya, D. B., Stevens, R. T., McGrath, B. E., Kemp, B. L., Adamczak, D. W., "Final Design of the Boundary Layer Transition (BoLT) Flight Experiment," Journal of Spacecraft and Rockets, Vol. 58, No. 1, 2021, pp. 6–17. doi:10.2514/1.A34809.

[192] McKiernan, G. R., Chynoweth, B. C., Schneider, S. P., Berridge, D. C., Wheaton, B. M., "Boundary Layer Transition Preflight Experiments in a Mach-6 Quiet Tunnel," Journal of Spacecraft and Rockets, Vol. 58, No. 1, 2021, pp. 54–66. doi:10.2514/1.A34772.

[193] Kostak, H. E., Bowersox, R. D. W., "Preflight Ground Test Analyses of the Boundary Layer Transition (BoLT) Flight Geometry," Journal of Spacecraft and Rockets, Vol. 58, No. 1, 2021, pp. 67–77. doi:10.2514/1.A34858.

[194] Rieken, E. F., Berry, S. A., Mason, M. L., Greene, F. A., "Aerothermodynamic Ground Tests in Support of the Boundary Layer Transition Flight Experiment," Journal of Spacecraft and Rockets, Vol. 58, No. 1, 2021, pp. 38–53. doi:10.2514/1.A34803.

[195] Berry, S. A., Wheaton, B. M., Chynoweth, B. C., "Secondary Side Considerations for Boundary Layer Transition Flight Experiment," Journal of Spacecraft and Rockets, Vol. 58, No. 1, 2021, pp. 18–25. doi:10.2514/1.A34778.

[196] Hörschgen-Eggers, M., Kirchhartz, R. M., Jung, W., Schoppmann, K., Ettl, J., and Wittkamp, M., "Boundary Layer Transit Flight Experiment: Mission Overview, Launch Vehicle and Payload Subsystems," Journal of Spacecraft and Rockets, Vol. 58, No. 1, 2021, pp. 26–37. doi:10.2514/1.A34877.

[197] Wheaton, B. M., Butler, C., McKiernan, G., Berridge, D., "Initial Results from the BoLT Flight Experiment," AIAA 2022-0345, AIAA SciTech 2022. doi:10.2514/6.2022-0345.

[198] Butler, C. S., Araya D. B., McKiernan, G. R., Wheaton, B. M., "Supersonic Transition Measurements During the BoLT Flight Experiment Descent Phase," AIAA-2022-4099, AIAA Aviation 2022

[199] Kutty, P. M., Butler, C. S., Wheaton, B. M., Fortier, J. B., "6DOF Simulation Analysis for the Post-Flight Investigation of the Boundary Layer Transition (BoLT) Experiment," AIAA-2022-3884, AIAA Aviation 2022.

[200] Melcher, J. T., Radcliffe, E. J., Butler, C. S., Wheaton, B. M., "Effects of Aeroelasticity on Flight Stability of the Boundary Layer Transition (BoLT) Experiment," AIAA-2022-3748, AIAA Aviation 2022.

[201] Thome J. S., Dwivedi A., Nichols J. W., Candler G. V., "Direct numerical simulation of BoLT hypersonic flight vehicle", AIAA-2018-2894, AIAA Fluids Dynamics Conference, 2018.

[202] Thome J. S., Knutson A. L., Candler G. V., "Boundary layer instabilities on BoLT subscale geometry," AIAA-2019-0092, AIAA SciTech 2019.

[203] Knutson, A. L., Thome, J. S., Candler, G. V., "Numerical Simulation of Instabilities in the Boundary-Layer Transition Experiment Flowfield," Journal of Spacecraft and Rockets, Vol. 58, No. 1, 2021, pp. 90–99. doi:10.2514/1.A34599.

[204] Cook D. A., Thome J. S., Nichols J. W., Candler G. V., "Receptivity analysis of BoLT to distributed surface roughness using input-output analysis," AIAA-2019-0089, AIAA SciTech 2019.

[205] Thome J. S., Reinert J. D., Candler G. V., "Effect of steady forcing on BoLT flowfield for flight Reynolds numbers," AIAA-2020-1042, AIAA SciTech 2020.

[206] Johnston, Z. M., Candler, G. V., "Hypersonic simulations of the BoLT-II subscale geometry," AIAA-2021-0366, AIAA SciTech 2021.

[207] Johnston, Z. M., Hemati, M. S., Candler, G. V., "Modal Analysis of Instabilities in the BoLT-II Flowfield," AIAA-2022-0348, AIAA SciTech 2022.

[208] Moyes, A. J., Reed, H. L., "Preflight Boundary-Layer Stability Analysis of BoLT Geometry," Journal of Spacecraft and Rockets, Vol. 58, No. 1, 2021, pp. 78–89. doi:10.2514/1.A34792.

[209] Mullen D., Moyes A., Kocian T., Reed H., "Heat Transfer and Boundary-Layer Stability Analysis of Subscale BoLT and the Fin Cone," AIAA 2019-3081, 2019.

[210] Moyes A., Reed H., "Nonlinear Boundary-Layer Stability Analysis of BoLT and HIFiRE-5," AIAA 2019-2972, 2019.

[211] Mullen, C. D., Reed, H. L., "Linear Parabolized Stability Analysis of the BoLT Flight Geometry at Off-Nominal Conditions," AIAA 2020-3027, AIAA Aviation 2020.

[212] Mullen, C. D., Reed, H. L., "Analysis of the BoLT Flight Geometry At Off-Nominal Conditions," AIAA 2021-1093, AIAA SciTech 2021.

[213] Mullen, C. D., Reed, H. L., "Analysis of the BoLT II - Holden Mission Flight and Wind Tunnel Geometries," AIAA 2021-0852, AIAA SciTech 2021.

[214] Morreale, B. J., Swinny, E. L., Kostak-Teplicek, H. E., Bowersox, R. D., White, E. B., Dufrene, A., Wadhams, T., Popkin, S., Adamczak, D., Tancred, J., "Boundary Layer Turbulence Flight Experiment in Memory of Mike Holden: Pre-Flight Mission Design," AIAA-2023-0477, AIAA SciTech 2023.

[215] Dufrene, A., Portoni, P. P., Maclean, M., Wadhams, T., Kostak-Teplicek, H. E., Bowersox, R. D., "Boundary Layer Turbulence Flight Experiment in Memory of Mike Holden: Vehicle Design, Instrumentation, and Ground Test Results," AIAA-2023-0478, AIAA SciTech 2023.

[216] Portoni, P. P., Dufrene, A., "Boundary Layer Turbulence Flight Experiment in Memory of Mike Holden: Ground-to-Flight Comparisons," AIAA-2023-0683, AIAA SciTech 2023.

[217] Kostak-Teplicek, H. E., Bowersox, R. D., "Hypersonic Stability and Breakdown Measurements on the AFRL/AFOSR BOLT II Geometry," AIAA-2023-0085, AIAA SciTech 2023.

[218] Butler, C. S., Bitter, N. P., Wheaton, B. M., "Initial BiGlobal Stability Analysis of the BOLT II Flight Experiment," AIAA-2023-0291, AIAA SciTech 2023.

[219] Johnston, Z. M., Candler, G. V., "Hypersonic Boundary Layer Transition of the BoLT-II Flowfield at Flight Conditions," AIAA-2023-0084, AIAA SciTech 2023.

[220] Wirth, J., Morreale, B., Kostak, H., Bowersox, R., Dufrene, A., Portoni, P., Wadhams, T., "Boundary Layer Turbulence Flight Experiment in Memory of Mike Holden: Side A Flight Data," AIAA SciTech Forum, AIAA Paper 2023-0682, Jan 2023.

[221] Wirth, J., Morreale, B., Bowersox, R., Wheaton, B. M., "Boundary Layer Turbulence Flight Experiment in Memory of Mike Holden: Side A Flight Data 2," AIAA SciTech Forum, AIAA Paper 2023-3440, June 2023.

[222] Damm, K. A., Curran, D. R., Gollan, R. J., Veeraragavan, A., "Trajectory-Based Conjugate Heat Transfer Simulation of the BoLT-II Flight Experiment," AIAA-2023-0292, AIAA SciTech 2023.

[223] Wheaton, B. M., Dufrene, A. T., "Thermal and Structural Analysis of BoLT-2: The Holden Mission," AIAA SciTech Forum, AIAA 2023-0685, Jan 2023.

[224] Fidelity Pointwise, Cadence Design Systems, Inc. URL https://www.pointwise.com/.

[225] FUN3D 13.7 Manual, NASA Langley Research Center, Hampton, VA. URL https://fun3d.larc.nasa.gov/.

[226] Hader, C., Fasel, H. F., "Towards simulating natural transition in hypersonic boundary layers via random inflow disturbances," Journal of Fluid Mechanics, Vol. 847, 2018.

[227] Goparaju, H., Gaitonde, D., "Transition to turbulence on hypersonic flat plates induced by stochastic forcing," AIAA SciTech Forum, AIAA Paper 2021-1738, Jan 2021.

[228] Balakumar, P., Kegerise, M. A., "Receptivity of Hypersonic Boundary Layers to Acoustic and Vortical Disturbances," 49th AIAA Aerospace Sciences Meeting, AIAA 2011-371, Jan 2011.

[229] Kovasznay, L. S. G., "Turbulence in supersonic flow," Journal of Aerospace Sciences, Vol. 20, No. 10, pp. 657–674, 1953.

[230] Fedorov, A.V., "Receptivity of a High-Speed Boundary Layer to Acoustic Disturbances," Journal of Fluid Mechanics, Vol. 491, pp. 101-129, 2003.